

**Gas-Phase Negative Ion Chemistry: Photoelectron Spectroscopy,
Reactivity, and Thermochemical Studies**

by

Stephanie M. Villano

B. S., University of Colorado at Denver, 2001

A thesis submitted to the Faculty of the Graduate School
of the University of Colorado in partial fulfillment
of the requirements for the degree of
Doctor of Philosophy
Department of Chemistry and Biochemistry
2008


This thesis entitled:

Gas-Phase Negative Ion Chemistry: Photoelectron Spectroscopy,
Reactivity, and Thermochemical Studies

Written by Stephanie M. Villano

has been approved for the
Department of Chemistry and Biochemistry

by



Veronica M. Bierbaum



W. Carl Lineberger



G. Barney Ellison

Date: December 2, 2008

A final copy of this thesis has been examined by all signatories, and we find that both the content and the form meet acceptable presentation standards of scholarly work in the above mentioned discipline.

Villano, Stephanie M. (Ph.D. Physical Chemistry)

Gas-Phase Negative Ion Chemistry: Photoelectron Spectroscopy, Reactivity, and Thermochemical Studies

Thesis directed by Professors Veronica M. Bierbaum and W. Carl Lineberger

Abstract:

This thesis describes the reactive and spectroscopic characterization of several anions. An overview of gas-phase ion-molecule reactivity and photoelectron spectroscopy is given in Chapters I-IV.

In Chapter V the competition between nucleophilic substitution and base-induced elimination for the reactions of BrO^- and ClO^- with a series of alkyl chlorides is investigated. These results are in stark contrast to prior theoretical work, and they indicate that the elimination channel becomes the dominant pathway as the neutral reagent becomes more sterically hindered. Additionally, the highly debated α -nucleophilicity of these two anions and of HO_2^- is examined; no enhanced reactivity is displayed suggesting that the α -effect is not due to an intrinsic property of the anion.

The reactivity of simple halogen substituted carbene anions is investigated with a series of oxygen, sulfur, and halogen containing neutral reagents in Chapter VI. These carbanions display diverse reactivity that includes substitution, elimination, proton transfer, and electron transfer reactions. In addition to these classic transformations, isotopic labeling studies indicate that these carbanions can undergo an insertion-elimination mechanism. Such reactivity has been observed in neutral carbenes; however, this is the first report of such gas-phase anion reactivity.

Spectroscopic studies of SF_6^- and $c\text{-C}_4\text{F}_8^-$ are reported in Chapter VII. The photoelectron spectra of both anions are consistent with a large geometry change

between anionic and neutral species. The photoelectron spectrum of $c\text{-C}_4\text{F}_8^-$ is composed of combination bands of two symmetric ring-breathing modes. The photoelectron spectrum of SF_6^- is dominated by an extended progression in the S–F stretching mode as well as a strong overtone/combination progression.

In Chapter VIII we report the photoelectron spectra of the *N*-methyl-5-pyrazolide and *N*-methyl-5-imidazolide anions, which provide electron affinities for the corresponding radicals. The gas-phase acidities of *N*-methylpyrazole and *N*-methyimidazole are also measured, and these measurements are used to determine the C-H bond strengths.

The thermochemistry of peroxyformic acid and peroxyacetic acid is investigated in Chapter IX. The electron affinities of the peroxyformyl and peroxyacetyl radicals are determined from the photoelectron spectra of the corresponding anion. The gas-phase acidities of both acids are determined, and these measurements are used to determine the O-H bond strengths.

Dedicated to my parents:
Denise Thornton and Steve E. Villano.

Acknowledgements:

There are so many people who have supported me in this journey. I am foremost grateful to both Veronica Bierbaum and Carl Lineberger for their guidance, patience, and commitment over the years. I am very appreciative for the opportunities that they have given me and for the scientific freedom to work on projects that interested me. I especially need to thank Veronica for the enormous amounts of time that she has given me and for putting up with me on a daily basis; it has really meant a lot to me!

Barney Ellison and Chuck DePuy in many ways have been surrogate advisors to me, and I am appreciative of that. Shuji Kato has also been of immense help to me, and I am grateful for his time and patience. There have been many visitors to CU during my time here, of these, John Stanton, Kent Ervin, and Steve Blanksby stand out for their excellent advice and suggestions. I also need to thank Don David and the CIRES Machine Shop Crew for all of their damage control and help over the years.

I am grateful to Nicole Eyet, for the help that she has given me, daily commiseration, and for her friendship. I need to thank Adam Gianola for teaching me about PES experiments and Scott Wren and Kristen Vogelhuber for their excellent job in running the PES lab. There have been a number of wonderful people who have in one way or another helped me: Brad Flowers, Tim D'Andrea, A. J. Vasiliou, Al Maccarone, Django Andrews, Jeff Rathbone, Katy Plath, and Nabilah Rontu-Carlton. I need to thank Jack Barbera and Heather Meylemans for their friendship and help. Lastly, I need to thank my husband, Todd Kreutzian, and my family for their love and support.

Publications:

- (1) Villano, S. M.; Kato, S.; Bierbaum, V. M. Deuterium Kinetic Isotope Effects in Gas-Phase S_N2 and E2 Reactions: Comparison of Experiment and Theory, *Journal of the American Chemical Society*, **2006**, *128*, 736-737.
- (2) Bopp, J. C.; Roscioli, J. R.; Johnson, M. A.; Miller, T. M.; Viggiano, A. A.; Villano, S. M.; Wren, S. W.; Lineberger, W. C. Spectroscopic Characterization of the Isolated SF_6^- and $C_4F_8^-$ Anions: Observation of a Very Long Harmonic Progression in Symmetric Deformation Modes upon Photodetachment, *Journal of Physical Chemistry A*, **2007**, *111*, 1214-1221.
- (3) Eyet, N.; Villano, S. M.; Kato, S.; Bierbaum, V. M. Deuterium Kinetic Isotope Effects in Microsolvated Gas-Phase E2 Reactions, *Journal of the American Society of Mass Spectrometry*, **2007**, *18*, 1046-1051.
- (4) Villano, S. M.; Gianola, A. J.; Eyet, N.; Ichino, T.; Kato, S.; Bierbaum, V. M.; Lineberger, W. C. Thermochemical Studies of *N*-methylpyrazole and *N*-methylimidazole, *Journal of Physical Chemistry A*, **2007**, *111*, 8579-8587.
- (5) Villano, S. M.; Eyet, N.; Lineberger, W. C.; Bierbaum, V. M. Gas-Phase Carbene Radical Anions: New Mechanistic Insight, *Journal of the American Chemical Society*, **2008**, *130*, 7214-7215.
- (6) Eyet, N.; Villano, S. M.; Bierbaum, V. M. Deuterium Kinetic Isotope Effects in Microsolvated E2 Reactions; Methanol and Ethanol as Solvents, *Journal of the American Society of Mass Spectrometry*, **2008**, *19*, 1296-1302.
- (7) Martinez, O.; Betts, N. B.; Villano, S. M.; Eyet, N.; Snow, T. P.; Bierbaum, V. M. Gas-Phase Study of C^+ Reactions of Interstellar Relevance, *The Astrophysical Journal*, **2008**, *686*, 1486-1492.
- (8) Villano, S. M.; Eyet, N.; Lineberger, W. C.; Bierbaum, V. M. Gas-Phase Reactions of Halogenated Radical Carbene Anions with Sulfur and Oxygen Containing Species, *International Journal of Mass Spectrometry*, **2009**, *In Press*.
- (9) Eyet, N.; Villano, S. M.; Bierbaum, V. M. Anchoring the Gas-Phase Acidity Scale: Formic Acid to Methanethiol, *International Journal of Mass Spectrometry*, **2009**, *In Press*.
- (10) Villano, S. M.; Eyet, N.; Lineberger, W. C.; Bierbaum, V. M. Reactions of α -Nucleophiles with Alkyl Chlorides: The Competition Between S_N2 and E2 Mechanisms and the Gas-Phase α -Effect, *Submitted to Journal of the American Chemical Society*.
- (11) Villano, S. M.; Eyet, N.; Wren, S. W.; Ellison, G. B.; Bierbaum, V. M.; Lineberger, W. C. Thermochemical Studies of the Peroxyformyl and Peroxyacetyl Radicals, *In Preparation*.
- (12) Eyet, N.; Villano, S. M.; Bierbaum, V. M. E2 Reactions of Microsolvated Fluoride Ion Using Deuterium Kinetic Isotope Effects, *In Preparation*.

TABLE OF CONTENTS

Chapter I: Gas-Phase Anion Chemistry Overview	1
1.1 Introduction	1
1.2 Gas-Phase Ion-Molecule Potential Energy Surface	2
1.3 Collision Rate Theory	4
1.4 Kinetic Isotope Effects	9
1.5 Thermochemistry	11
1.6 References	17
Chapter II: Anion Photoelectron Spectroscopy Overview	19
2.1 Introduction	19
2.2 Atomic Species	19
2.3 Molecular Species	20
2.4 Selection Rules	25
2.5 Photoelectron Angular Distributions	27
2.6 References	30
Chapter III: Flowing Afterglow-Selected Ion Flow Tube Triple Quadrupole Mass Spectrometer: Instrument Description.	32
3.1 Introduction	32
3.2 Flowing Afterglow Ion Source	33
3.3 Ion Optics and Mass Selection	38
3.4 Reaction Flow Tube	40
3.5 Triple Quadrupole Detection	43
3.6 Data Acquisition	45
3.7 Rate Constant Determination and Error Analysis	46
3.8 Branching Ratio Determinations	54
3.9 References	58
Chapter IV: Negative Ion Flowing Afterglow Photoelectron Spectrometer: Instrument Description	60
4.1 Introduction	60
4.2 Flowing Afterglow Ion Source	63
4.3 Ion Optics and Mass Selection	66
4.4 Ultraviolet Laser System	70

4.5 Photoelectron Kinetic Energy Analyzer	73
4.6 Data Acquisition and Analysis	76
4.7 Franck-Condon Simulations	78
4.8 References	80
Chapter V: Reactions of BrO^- and ClO^- with Alkyl Halides: The Competition Between $\text{S}_{\text{N}}2$ and E2 Mechanisms and the Gas-Phase α -Effect.	83
5.1 Introduction	83
5.2 Experimental Methods	87
5.3 Results and Discussion	89
5.3.1 Reaction Trend and Product Distributions	89
5.3.2 Kinetic Isotope Effects	94
5.3.3 ClO^- with EtCl: Comparison of Experiment and Theory	100
5.3.4 α -Nucleophilic Character	102
5.4 Conclusions	106
5.5 Acknowledgments	106
5.6 References	108
Chapter VI: Gas-Phase Carbene Radical Anions: New Mechanistic Insights	114
6.1 Introduction	114
6.2 Experimental Methods	117
6.3 Results and Discussion	119
6.3.1 Reactions of Carbene Anions with Sulfur/Oxygen Containing Species	119
6.3.2 Reactions of $\text{CHX}^{\bullet-}$ and $\text{CCIX}^{\bullet-}$ ($\text{X}=\text{Cl}$ and Br) with Halogenated Species	134
6.4 Conclusions	148
6.5 Acknowledgments	148
6.6 References	150
Chapter VII: Spectroscopic Characterization of the $c\text{-C}_4\text{F}_8^-$ and SF_6^- Anions	159
7.1 Introduction	159
7.2 Experimental Methods	161
7.3 Results and Discussion	161
7.3.1 Photoelectron Spectrum of the $c\text{-C}_4\text{F}_8^-$ Anion	161
7.3.2 Photoelectron Spectrum of the SF_6^- Anion	168
7.4 Conclusions	175

7.5 Acknowledgements	176
7.6 References	177
Chapter VIII: Thermochemical Studies of <i>N</i> -methylpyrazole and <i>N</i> -methylimidazole	182
8.1 Introduction	182
8.2 Experimental Methods	185
8.2.1 Negative Ion Photoelectron Spectroscopy	187
8.2.2 Flowing Afterglow-Selected Ion Flow Tube Measurements	187
8.3 Results and Discussion	189
8.3.1 Computational Results	189
8.3.2 Photoelectron Spectroscopy of the <i>N</i> -methyl- 5-pyrazolide Anion	189
8.3.3 Photoelectron Spectroscopy of the <i>N</i> -methyl- 5-imidazolide Anion	199
8.3.4 Gas-Phase Acidity Measurements	206
8.3.5 H/D Exchange of the <i>N</i> -methylimidazolide Anion	208
8.3.6 Thermochemistry	209
8.4 Conclusions	213
8.5 Acknowledgements	214
8.6 References	215
Chapter IX: Thermochemical Studies of the Peroxyformyl and Peroxyacetyl Radicals	221
9.1 Introduction	221
9.2 Experimental Methods	224
9.2.1 Negative Ion Photoelectron Spectroscopy	224
9.2.2 Flowing Afterglow-Selected Ion Flow Tube Measurements	225
9.2.3 Electronic Structure Calculations	226
9.3 Results and Discussion	227
9.3.1 Computational Results	227
9.3.2 Photoelectron Spectroscopy of the Peroxyformate Ion	234
9.3.3 Photoelectron Spectroscopy of the Peroxyacetate Ion	241
9.3.4 Collision Induced Dissociation Studies	246
9.3.5 Gas-Phase Acidity Measurements	250
9.3.6 Thermochemistry	256

9.4 Conclusions	260
9.5 Acknowledgements	261
9.6 References	262
Bibliography	268

List of Tables

5.01	Reaction rate constants ($10^{-10} \text{ cm}^3 \text{ s}^{-1}$), kinetic isotope effects and product ion branching ratios for the reactions of $^{79}\text{BrO}^-$ and $^{35}\text{ClO}^-$ with RCl (R = methyl, ethyl, <i>i</i> -propyl, and <i>t</i> -butyl).	91
5.02	Reaction exothermicities (kcal mol^{-1}) for the reactions of BrO^- and ClO^- with RCl (R = methyl, ethyl, <i>i</i> -propyl, and <i>t</i> -butyl).	95
6.01	Reaction rate constants ($10^{-10} \text{ cm}^3 \text{ s}^{-1}$) for the reactions of $\text{CXY}^{\bullet-}$ with CS_2 , COS, CO_2 , O_2 , CO, and N_2O .	120
6.02	Product ion distributions for the reactions of $\text{CXY}^{\bullet-}$ with CS_2 , COS, CO_2 , and O_2 .	121
6.03	Calculated and experimental reaction exothermicities (kcal mol^{-1}) for the reactions of $\text{CHCl}^{\bullet-}$, $\text{CCl}_2^{\bullet-}$, and $\text{CF}_2^{\bullet-}$.	123
6.04	Reaction rate constants ($10^{-10} \text{ cm}^3 \text{ s}^{-1}$) for the reactions of $\text{CXY}^{\bullet-}$ with CCl_4 , CHCl_3 , CH_2Cl_2 , CH_3Cl , CH_3Br , and $(\text{CH}_3)_3\text{CBr}$.	135
6.05	Product ion branching fractions for the reactions of $\text{CXY}^{\bullet-}$ with CCl_4 , CHCl_3 , and CH_2Cl_2 .	136
6.06	Reaction rate constants ($10^{-10} \text{ cm}^3 \text{ s}^{-1}$) and product ion branching ratios for the reactions of $\text{CH}^{35}\text{Cl}^{\bullet-}$ with $\text{CH}_n\text{Cl}_{4-n}$ ($n=0-3$) and product ion isotope distributions for the reactions of $\text{CH}^{35}\text{Cl}^{\bullet-}$ and $\text{CH}^{37}\text{Cl}^{\bullet-}$ with $\text{CH}_n\text{Cl}_{4-n}$ ($n=0-3$).	137
7.01	Theoretical frequencies (cm^{-1}), calculated using the MP2/TZVPP level of theory for both <i>c</i> - C_4F_8 anion and neutral along with the experimental values for neutral <i>c</i> - C_4F_8 .	165
7.02	Theoretical frequencies (cm^{-1}), calculated using the MBPT(2) level of theory for SF_6 anion and neutral and the experimental values for SF_6 neutral.	173
8.01	B3LYP/6-311++G(d,p) Optimized Geometries for <i>N</i> -methylpyrazole, <i>N</i> -methyl-5-pyrazolide and <i>N</i> -methyl-5-pyrazolyl.	190
8.02	B3LYP/6-311++G(d,p) Harmonic Frequencies (cm^{-1}) of <i>N</i> -methyl-5-pyrazolide and <i>N</i> -methyl-5-pyrazolyl.	191
8.03	B3LYP/6-311++G(d,p) Optimized Geometries for <i>N</i> -methylimidazole, <i>N</i> -methyl-5-imidazolide and <i>N</i> -methyl-5-imidazolyl.	192
8.04	B3LYP/6-311++G(d,p) Harmonic Frequencies (cm^{-1}) of <i>N</i> -methyl-5-imidazolide and <i>N</i> -methyl-5-imidazolyl.	193

8.05	B3LYP/6-311++G(d,p) $\Delta_{\text{acid}}G_{298}$ and BDE of <i>N</i> -methylpyrazole and <i>N</i> -methylimidazole and the EA of the corresponding radicals.	194
8.06	Thermochemical Parameters.	211
9.01	Experimental and Calculated (G3MP2B3) Electron Affinities, Enthalpies of Deprotonation and Bond Dissociation Enthalpies for Alkyl Peroxides and Carboxylic Acids.	229
9.02	Relative Energies (kcal mol ⁻¹) of the <i>cis</i> - and <i>trans</i> -conformers.	230
9.03	B3LYP/6-311++G(d,p) Optimized Geometries for Peroxyformic Acid, Peroxyformate Anion and Peroxyformyl Radical.	232
9.04	B3LYP/6-311++G(d,p) Optimized Geometries for Peroxyacetic Acid, Peroxyacetate Anion and Peroxyacetyl Radical.	233
9.05	B3LYP/6-311++G(d,p) Harmonic Frequencies (cm ⁻¹) of Peroxyformate Anion and Peroxyformyl Radicals. Experimental values are provided in parentheses.	237
9.06	B3LYP/6-311++G(d,p) Harmonic Frequencies (cm ⁻¹) of Peroxyacetate Anion and Peroxyacetyl Radical. Experimental values are provided in parentheses.	243
9.07	Thermochemical Parameters.	258

LIST OF FIGURES

1.01	Representative reaction coordinate diagrams for the S _N 2 reaction of BrO ⁻ + CH ₃ Cl in the gas-phase and in solution.	3
1.02	Schematic diagram of ion-neutral molecule trajectories.	6
1.03	Schematic diagrams of potential energy surfaces for a vibration in the reactant and in the transition state for a) a loose transition state where E _H < E _D and k _H /k _D > 1 and for b) a tight transition state where E _H > E _D and k _H /k _D < 1.	12
1.04	Schematic diagram that shows the relationship of the thermochemical quantities that compose the proton affinity cycle, negative ion cycle, and the appearance energy cycle.	16
2.01	The 351.1 nm photoelectron spectrum of the O ^{*-} anion. The solid line is the experimental spectrum while the sticks are the calculated transitions.	21
2.02	Schematic representation of the photodetachment from the ground state of AB ⁻ to the ground state and first excited state of AB.	22
3.01	Photograph of the Flowing Afterglow-Selected Ion Flow Tube Mass Spectrometer (FA-SIFT) at CU Boulder	34
3.02	Schematic of Flowing Afterglow-Selected Ion Flow Tube Mass Spectrometer (FA-SIFT).	35
3.03	Schematic of the flowing afterglow source and mass selection region.	36
3.04	Schematic of triple quadrupole detection.	44
3.05	a) Spectrum of the SIFT-injected ⁷⁹ BrO ⁻ anion (m/z 95). b) Spectrum of the S _N 2 reaction of ⁷⁹ BrO ⁻ + CH ₃ Cl.	47
3.06	Reactant ion depletion and product ion formation for the reaction ⁷⁹ BrO ⁻ + CD ₃ Cl.	49
3.07	Sample branching ratio determination for the reaction ⁷⁹ BrO ⁻ + CD ₃ Cl.	56
4.01	Photograph of the JILA Negative Ion Flowing Afterglow Photoelectron Spectrometer.	61
4.02	Schematic representation of the JILA Negative Ion Flowing Afterglow Photoelectron Spectrometer.	62
4.03	Schematic representation of the flowing afterglow source.	65
4.04	Schematic representation of the ion optics and Wien filter.	68
4.05	Schematic of Ar-ion laser system and external buildup cavity.	71

4.06	Schematic representation of ion-photon interaction region and of the electron kinetic energy analyzer.	74
5.01	a) Reaction coordinate diagram for the reaction of ClO^- with CH_3Cl . b) Transition state structures are provided.	96
5.02	Anion basicity versus reaction efficiency for the $\text{S}_{\text{N}}2$ reactions of Nu^- with CH_3Cl . The normal nucleophiles are indicated by the closed circles and the α -nucleophiles are indicated by the open circles.	104
6.01	Reaction efficiency versus anion basicity.	122
6.02	Reaction efficiency versus the number of chlorine atoms in the neutral reagent.	144
7.01	The 351.1 nm photodetachment spectrum of $c\text{-C}_4\text{F}_8^-$ taken at the magic angle.	163
7.02	Optimized geometries of $c\text{-C}_4\text{F}_8$ neutral and anion.	164
7.03	Calculated photoelectron spectra of the $c\text{-C}_4\text{F}_8^-$ anion reproduced from Borrelli, R.; Peluso, A. <i>J. Chem. Phys.</i> 2008 , <i>128</i> , 044303/1-044303/7 with permission copyright 2008, American Institute of Physics, where a) only the ν_5 and ν_1 modes were considered and b) where all modes were considered.	167
7.04	The 351.1 nm photodetachment spectrum of SF_6^- taken under cold flow tube conditions at the magic angle.	170
7.05	Comparison of the a) 351.1 nm photodetachment spectrum of SF_6^- reproduced from Figure 7.04, and (b and c) the SF_6^- photoelectron spectrum taken by Mark A. Johnson's group at Yale University using a double focusing tandem time of flight pulsed spectrometer.	171
7.06	Calculated photoelectron spectra of the SF_6^- anion reproduced from Borrelli, R. <i>Chem. Phys. Lett.</i> 2007 , <i>445</i> , 84-88 with permission copyright 2008, Elsevier.	174
8.01	(a) The 351.1 nm magic-angle photoelectron spectrum of the <i>N</i> -methyl-5-pyrazolide anion. (b) Simulations of the spectrum for the transitions from $\tilde{X}^1\text{A}'$ <i>N</i> -methyl-5-pyrazolide anion to $\tilde{X}^2\text{A}'$ and $\tilde{\text{A}}^2\text{A}''$ <i>N</i> -methyl-5-pyrazolyl radical.	195
8.02	Relative atomic displacements in the activated normal modes of the $\tilde{X}^2\text{A}'$ state of <i>N</i> -methyl-5-pyrazolyl and their frequencies.	198
8.03	The 351.1 nm magic-angle photoelectron spectrum of the <i>N</i> -methyl-imidazolide anion.	201

8.04	a) The 351.1 nm magic-angle photoelectron spectrum of the <i>N</i> -methylimidazolide anion, reproduced from Figure 8.03. Simulations of the spectrum for the transitions of b) \tilde{X}^1A' <i>N</i> -methyl-5-imidazolide to \tilde{X}^2A' <i>N</i> -methyl-5-imidazolyl, c) \tilde{X}^1A' <i>N</i> -methyl-2-imidazolide to \tilde{X}^2A' <i>N</i> -methyl-2-imidazolyl, and d) \tilde{X}^1A <i>N</i> -imidazolymethyl anion to \tilde{X}^2A' <i>N</i> -imidazolymethyl radical.	202
8.05	The 351.1 nm magic-angle photoelectron spectrum of the <i>N</i> -methylimidazolide anion (black), reproduced from Figure 8.03 and the simulated 10 meV Gaussian convoluted and stick spectra, reproduced from Figure 8.04b.	203
8.06	Relative atomic displacements in the activated normal modes for the \tilde{X}^2A' state of <i>N</i> -methyl-5-imidazolyl.	204
9.01	Potential energy surface ($E + E_{zpt}$) calculated at the G3MP2B3 level of theory for the <i>cis</i> - to <i>trans</i> -isomerization of the peroxyformate anion and the peroxyformyl radical.	231
9.02	a-b) The 351.1 nm magic-angle photoelectron spectrum of the peroxyformate anion reproduced from Figure 9.02. c-f) Franck-Condon simulations for transitions from \tilde{X}^1A' state of the <i>trans</i> -peroxyformate anion to the \tilde{X}^2A'' state of the <i>trans</i> -peroxyformyl radical.	238
9.03	a) The 351.1 nm magic-angle photoelectron spectrum of the peroxyformate anion reproduced from Figure 9.02a. b) Franck-Condon simulation for transitions from \tilde{X}^1A' state of the <i>cis</i> -peroxyformate anion to the \tilde{X}^2A'' state of the <i>cis</i> -peroxyformyl radical.	239
9.04	a) The 351.1 nm magic-angle photoelectron spectrum of the peroxyacetate anion. b) Simulations of the spectrum for transitions from \tilde{X}^1A' <i>trans</i> -peroxyacetate anion to \tilde{X}^2A'' and \tilde{A}^2A' <i>trans</i> -peroxyacetyl radical.	244
9.05	a) The 351.1 nm magic-angle photoelectron spectrum of the peroxyacetate anion reproduced from Figure 9.04a. Franck-Condon simulation based on the B3LYP/6-311++G(d,p) optimized geometries and harmonic frequencies for transitions from b) \tilde{X}^1A' <i>cis</i> -peroxyacetate anion to \tilde{X}^2A'' <i>cis</i> -peroxyacetyl radical and c) \tilde{X}^1A' state of the hydrogenperoxide ethylenolate anion to \tilde{X}^2A'' state of the hydrogenperoxide ethylenolyl radical.	245
9.06	Collision Energy (E_{COM}) dependence of the relative yields of the parent and daughter ions in the CID of a) the peroxyformate anion and b) the peroxyacetate anion.	248
9.07	a-d) Representative potential energy surfaces for the proton transfer reaction of the <i>trans</i> -conformer of the peroxyacyl ion with a reference acid.	254

CHAPTER I

GAS-PHASE ANION CHEMISTRY OVERVIEW

1.1) Introduction

While anions are not as prevalent in nature as cations, their reactions are important in the atmosphere and other environments.¹ The primary source of anions in the atmosphere is due to electron attachment to molecular oxygen and dissociative electron attachment to ozone. These anions eventually go on to react with other trace gases to form a variety of anions. Additionally, while the chemistry of the interstellar medium is dominated by cation-atom/molecule chemistry, the recent discovery of carbon chain anions, C_nH^- , may indicate that anions also play an important role in interstellar processes.^{2,3} The study of gas-phase anion chemistry is particularly relevant to condensed-phase synthetic organic chemistry. Many common synthetic organic schemes (such as substitutions, eliminations, Grignard additions, aldol condensations, hydrolysis of esters, etc.) involve anions; in contrast to cations, anions seldom undergo unimolecular rearrangement. Gas-phase studies provide insight into the intrinsic nature of a reaction without the interference of solvent effects and the presence of counter ions.

Studying reactions in a solvent free environment provides insight into the role of the solvent. For example, in the gas-phase the alcohols become more acidic as the size of the alkyl group increases ($t\text{-C}_4\text{H}_9\text{OH} > i\text{-C}_3\text{H}_7\text{OH} > \text{C}_2\text{H}_5\text{OH} > \text{CH}_3\text{OH} > \text{H}_2\text{O}$), which is the opposite of the acidity ordering in protic solutions.⁴ Additionally, in solution polarizable nucleophiles are more reactive than nonpolarizable nucleophiles ($\text{CH}_3\text{S}^- > \text{CH}_3\text{O}^-$ and $\text{I}^- > \text{Br}^- > \text{Cl}^- > \text{F}^-$). However, in the gas-phase this enhanced nucleophilicity is not observed.⁵ In both cases the trends observed in solution do not reflect an intrinsic property of the molecules. Instead the ordering of the aliphatic

alcohol acidity series in solution is due to the steric hindrance to solvation for the larger alkoxides, while the enhanced reactivity of polar nucleophiles in solution stems from their ability to better facilitate charge reorganization as the reaction proceeds from the reactants to the transition state.

Another stark difference between gas-phase studies and solution phase studies is the rates at which reactions occur in the two media. For example, in the gas-phase the S_N2 reaction of hydroxide with methyl bromide is sixteen orders of magnitude faster than in solution.⁶ The decrease in reactivity is attributed to the reorganization of the solvent, as well as the greater thermodynamic stability of the solvated ion relative to the transition state. Stepwise hydration of the nucleophile indicates that the solvent reorganization effects become evident with the attachment of only two solvent molecules. In order to understand the differences between gas-phase and condensed phase ion-molecule reactions it is important to understand the energetic factors that influence gas-phase processes.

1.2) Gas-Phase Ion-Molecule Potential Energy Surface

The potential energy surface of a typical gas-phase ion-molecule reaction has a double well shape, where the transition state is flanked by two stable ion-molecule complexes.⁵ This is qualitatively shown for the S_N2 reaction of $\text{BrO}^- + \text{CH}_3\text{Cl}$, in Figure 1.01a. The collision of BrO^- with CH_3Cl , results in a reactant ion-dipole complex that is stabilized (by $\sim 10\text{-}20 \text{ kcal mol}^{-1}$) relative to the separated reactants. Initially, this energy is in the form of translational energy. However, as the reactants come together the energy is equilibrated among the various rotational and vibrational modes, resulting in a relatively long-lived complex. Eventually this energy will return to the translational degrees of freedom and the reactants will separate, or the energy will concentrate along the reaction coordinate thereby allowing the reaction to

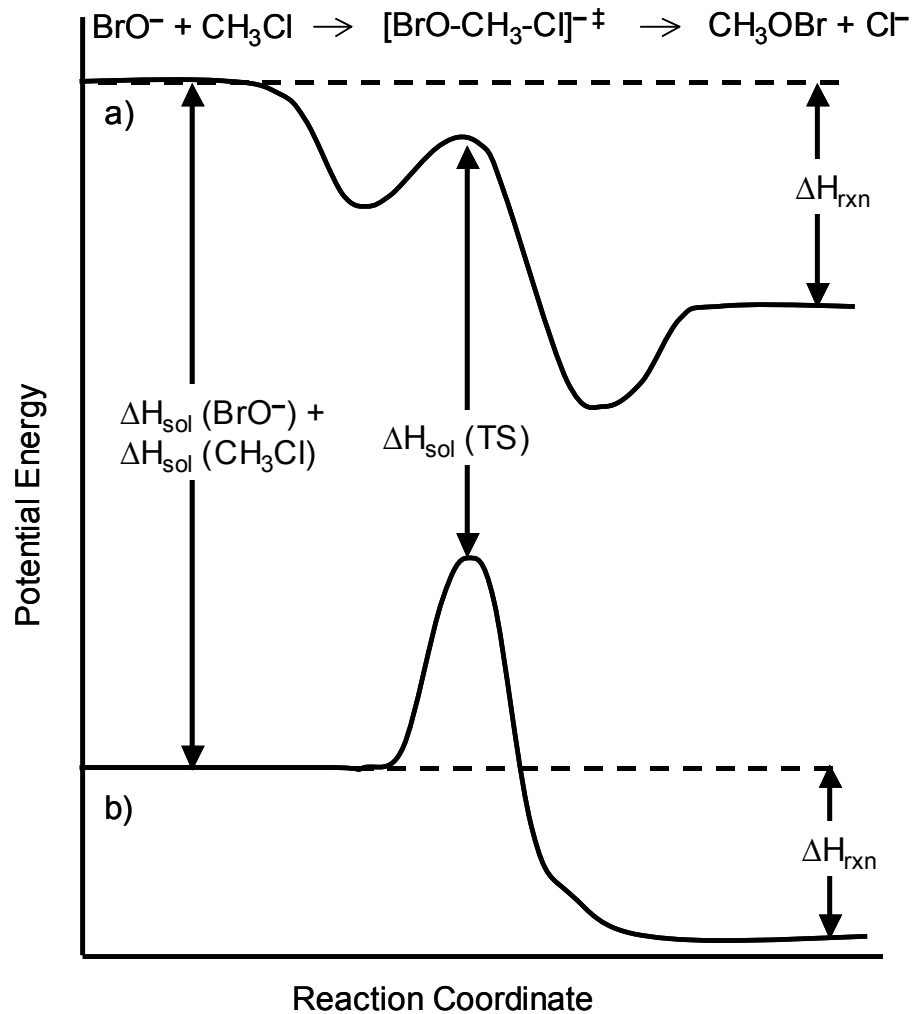


Figure 1.01: Representative reaction coordinate diagrams for the $\text{S}_{\text{N}}2$ reaction of $\text{BrO}^- + \text{CH}_3\text{Cl}$ in a) the gas-phase and b) in solution.

overcome the activation barrier to form a product ion-dipole complex. Similarly the excess energy contained in the product ion-dipole complex must concentrate into the translation modes for the complex to dissociate into the free products. While there is ample energy to cross over the barrier, the transition state is an ordered structure limiting the rate of the reaction. In other words, dissociation of the reactant ion-dipole complex into the free reactants is entropically favored over crossing the barrier.

The gas-phase ion-molecule potential energy surface is qualitatively very different from that in solution, shown in Figure 1.01a and b. The solvent stabilizes the reactants, products, and transition state compared to those species in the gas-phase. The enthalpy of solvation of the reactants is greater than that of the transition state structure since the charge is more localized in the reactants than in the transition state. Additionally, the solvent shields the attractive ion-dipole/ion-induced dipole forces, therefore, the double well shape is absent in solution. In solution the activation energy is positive, thus most collisions are unreactive. For a reaction to proceed, the reactants must come together with enough energy to surmount the activation barrier, and therefore only the high-energy tail of the Maxwell-Boltzmann energy distribution reacts. Since the reactants are in thermal equilibrium with the solvent the reactants are activated through collisions with the surrounding solvent.

1.3) Collision Rate Theory

In the gas-phase, an ion and a neutral molecule approach one another on an attractive potential surface, which results from the interaction of the ion charge with any permanent dipoles or multipoles and any induced dipoles or multipoles. This potential is represented by a sum of terms, one for each interaction. For relatively simple potentials, the collision rate constant can easily be evaluated. However, as the number of terms in the potential increases, it becomes increasingly more complicated to solve for the collision rate constant. Two common scenarios are

discussed below: 1) the collision of an ion and a non-polar molecule where the attractive potential is due to an ion-induced dipole force and 2) the collision of an ion and a molecule with a permanent dipole where the attractive potential is due both to ion-induced dipole and ion-dipole forces.

In the simplest case, the ion is described by a point charge that interacts with a structureless, isotropically polarizable molecule that does not have a permanent dipole. The potential between the two species results from the charge-induced dipole that arises from the interaction of the neutral molecule with the electric field of the ion, shown in eq 1.01.

$$V(r) = \frac{-q^2\alpha}{2r^4} \quad (1.01)$$

Here, q is the anion charge, α is the isotropic polarizability, and r is the distance between the ion and the neutral species. The total energy of the system is given by eq 1.02, where the dot represents the derivative with respect to time, μ is the reduced mass of the colliding pair, and L is the angular momentum.

$$E = \frac{\mu\dot{r}^2}{2} + \frac{L^2}{2\mu r^2} + V(r) \quad (1.02)$$

Because the potential depends only on the distance between the ion and the neutral, r , this motion is confined to a plane, shown in Figure 1.02, where v_0 is the initial velocity of the molecule and b is the distance between the ion and the trajectory of the neutral molecule before it is influenced by the electric field of the ion; v_0 and b are perpendicular to one another and θ is the angle between r and v_0 . As the ion and molecule approach one another the radial kinetic energy decreases, then increases again as the ion and molecule move away from one another. At a certain value of b , the radial kinetic energy becomes zero and the ion-induced dipole force is equal but

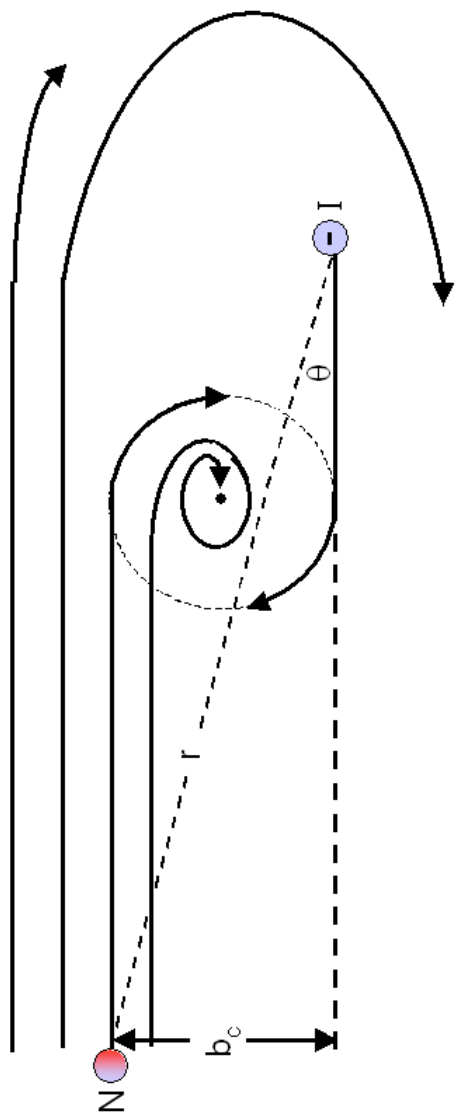


Figure 1.02: Schematic diagram of ion-neutral molecule trajectories. The critical impact factor, b_c , is shown. Trajectories where $b > b_c$ are scattered. Trajectories where $b < b_c$ are captured.

opposite to the centrifugal force, where $L = \mu v_0 b$. The critical impact factor, b_c , can be found, eq 1.03.⁷

$$b_c = \left(\frac{4q^2\alpha}{\mu v_0} \right)^{1/4} \quad (1.03)$$

At this critical impact factor, b_c , the ion and molecule enter a metastable orbit. Any trajectories where $b > b_c$ will be deflected by the attractive potential but not captured; for large values of b , the initial trajectory of the molecule remains unchanged. Any trajectories where $b < b_c$ will spiral towards the ion and be captured. The collision cross section is given by $\sigma_c = \pi b_c^2$. Using a classical cross section treatment and averaging over the Maxwell-Boltzmann energy distribution gives the Langevin-Gioumouisis-Stevenson equation,⁸ k_L in eq 1.04.

$$k_L = 2\pi q \left(\frac{\alpha}{\mu} \right)^{1/2} \quad (1.04)$$

This theory adequately predicts collision rate constants, when the neutral species does not have a permanent dipole. For collision of an ion with a neutral molecule that does have a permanent dipole, k_L provides a lower limit to the true collision rate constant.

The calculation of the collision rate constant is more complicated when an ion interacts with a neutral molecule that has a permanent dipole. In this case the potential is described by eq 1.05, where μ_D is the dipole moment of the neutral molecule and θ is the angle between the dipole moment vector and r (shown in Figure 1.02). The first term describes the ion-induced dipole potential and the second term describes the ion-dipole potential.

$$V(r) = \frac{-q^2\alpha}{2r^4} + \frac{-q\mu_D \cos\theta}{r^2} \quad (1.05)$$

In the same manner as above, the collision rate constant can be derived if one assumes that the dipole is locked in the direction of the approaching ion.⁹ In this case $\theta=0$, thereby giving a potential that depends only on r . The resulting rate constant is given in eq 1.06.

$$k = \left(\frac{2\pi q}{\mu^{1/2}} \right) \left[\alpha^{1/2} + \mu_D \left(\frac{2}{\pi k_b T} \right)^{1/2} \right] \quad (1.06)$$

Neglecting the rotation of the dipole, however, leads to an overestimation of the collision rate, since the complete alignment of the dipole is prevented by the rotational energy and forbidden quantum mechanically. To compensate for this, an effective-locking constant, c , is placed in front of the ion-dipole term in eq 1.06. This constant is between 0 and 1 and is estimated from a plot of calculated c versus $\mu_D/\alpha^{1/2}$; this approach is referred to as average dipole orientation (ADO) theory.^{10,11}

Through trajectory calculations, Su and Chesnavich¹² have derived an empirical function to determine the collision rate constant based on the ratio of the dipole moment of the neutral species to the square root of the polarizability. The collision rate constant is determined from $k_c = k_L K_{cap}$, where k_L is found in eq 1.04 and K_{cap} is found from either eq 1.07 or eq 1.08, depending upon the value of x , which is defined in eq 1.09.

$$K_{cap} (x \geq 2) = 0.4767x + 0.6200 \quad (1.07)$$

$$K_{cap} (x \leq 2) = \frac{(x + 0.5090)^2}{10.526} + 0.9754 \quad (1.08)$$

$$x = \frac{\mu_D}{(2\alpha k_b T)^{1/2}} \quad (1.09)$$

This theory is referred to as parameterized trajectory theory. It is important to note that at high temperatures or for molecules without a permanent dipole, the collision

rate constant reduces to the Langevin-Gioumouis-Stevenson equation. This theory has been shown to calculate the collision rate constant to within 3% of the true value.

The calculated collision rate constants provided in this thesis are calculated using parameterized trajectory theory.¹² The ratio of the reaction rate constant to the collision rate constant gives the reaction efficiency, $\text{Eff} = k_{\text{rxn}}/k_{\text{col}}$. This ratio expresses the percentage of collisions that cross over the activation barrier. It is often more appropriate to compare the reaction efficiencies of ion-molecule reactions, since the collision rates may vary significantly for different reactions.

1.4) Kinetic Isotope Effects

For reactions whose rate is controlled by the crossing of an activation barrier, isotopic substitution of a deuterium for a hydrogen atom can change the reaction rate.¹³ Deuterium kinetic isotope effects (KIE), defined as the ratio of perprotio to perdeuterio rate constants ($\text{KIE} = k_{\text{H}}/k_{\text{D}}$), can provide insight into the reaction mechanism. A classic example is the competing nucleophilic substitution ($\text{S}_{\text{N}}2$) and base-induced elimination (E2) mechanisms. Since these two mechanisms have the same ionic reactants and products, they are not readily distinguished using mass spectrometric techniques. These mechanisms, however, are distinguishable by their distinct KIE. For an $\text{S}_{\text{N}}2$ mechanism, deuteration of the neutral reactant increases the reaction rate giving an inverse KIE ($k_{\text{H}}/k_{\text{D}} < 1$).^{14,15} For an E2 mechanism deuteration of the neutral reactant decreases the reaction rate giving a normal KIE ($k_{\text{H}}/k_{\text{D}} > 1$).

The total KIE can be factored into a collisional (η_{col}), translational (η_{tran}), rotational (η_{rot}), and vibrational (η_{vib}) contribution, eq 1.10.

$$k_{\text{H}}/k_{\text{D}} = \eta_{\text{col}} \eta_{\text{tran}} \eta_{\text{rot}} \eta_{\text{vib}} \quad (1.10)$$

The origin of the KIE for each component is given in eq 1.11-1.14.

$$\eta_{\text{col}} = \left(\frac{\mu^{\text{D}}}{\mu^{\text{H}}} \right)^{1/2} \quad (1.11)$$

$$\eta_{\text{tran}} = \left(\frac{\mu^{\text{D}}}{\mu^{\text{H}}} \right)^{3/2} \quad (1.12)$$

$$\eta_{\text{rot}} = \left(\frac{I^{\text{H,TS}} I^{\text{D,R}}}{I^{\text{D,TS}} I^{\text{H,R}}} \right)^{1/2} \quad (1.13)$$

$$\eta_{\text{vib}} = \frac{q_{\text{vib}}^{\text{H,TS}} q_{\text{vib}}^{\text{D,R}}}{q_{\text{vib}}^{\text{D,TS}} q_{\text{vib}}^{\text{H,R}}} \quad (1.14)$$

The collisional and translational contributions (eq 1.11 and 1.12, respectively) are determined by the ratio of the reduced mass, μ , for the perdeuterio reactants (superscript D) to the perprotio reactants (superscript H). This ratio gives a normal effect that is generally small. The rotational component (eq 1.13) is a spatial effect, where I is the determinant of the moment of inertia tensor and the superscripts R and TS indicate the reactants and the transition state, respectively. The ratio of $I^{\text{H,TS}}$ to $I^{\text{D,TS}}$ gives an inverse effect while the ratio of $I^{\text{D,R}}$ to $I^{\text{H,R}}$ gives a normal effect. The total rotational effect is normal since the change in the moments of inertia upon deuteration is greater for the reactants than for the transition state. The magnitude of the rotational effect can range from small to large depending on the structure of the transition state. The vibrational component (eq 1.14) is given by the ratio of vibrational partition function, q_{vib} , for the reactants and transition state. Depending upon changes in vibrational frequencies in the reactants and in the transition state upon deuteration, this effect can vary from inverse to normal and from small to large in size.

The rotational and vibrational components provide insight into the reaction mechanism since they probe the structure of the transition state. The vibrational

component is more sensitive, and typically provides the distinguishing factor in determining a reaction mechanism since deuterium results in either a normal or inverse effect.¹⁶ Normal effects are observed when the transition state is loose (i.e., the bonds are lengthened in the transition state) whereas inverse effects are observed when the transition state is tight (i.e., the bonds are shortened in the transition state). This is schematically shown in Figure 1.03a and 1.03b, respectively. Deuterium lowers the vibrational frequencies in both the reactants and transition states relative to the hydrogenated compounds. For a reaction proceeding through a loose transition state a) the frequencies for the hydrogenated species are lowered more substantially than for the deuterated species in the transition state, thus the activation energy for the perprotio reaction is lower than that of the perdeuterio reaction, $E_{\text{H}}^{\ddagger} < E_{\text{D}}^{\ddagger}$. For a reaction proceeding through a tight transition state b) the frequencies for the hydrogenated species are raised more substantially than for the deuterated species in the transition state, thus the activation energy for the perprotio reaction is greater than that of the perdeuterio reaction, $E_{\text{H}}^{\ddagger} > E_{\text{D}}^{\ddagger}$.

1.5) Thermochemistry

The gas-phase acidity of AH, ($\Delta_{\text{a}}G_0(\text{AH})$), is the free-energy change for the heterolytic cleavage of $\text{AH} \rightarrow \text{A}^- + \text{H}^+$. Typical gas-phase acidities are $\sim 300\text{-}400 \text{ kcal mol}^{-1}$; thus, these quantities are difficult to measure directly and instead are measured relative to a reference acid (RH) of known acidity. Proton transfer equilibrium experiments determine the free energy difference between an acid of unknown acidity and a reference acid via eq 1.15.

$$\Delta(\Delta_{\text{a}}G_{298}) = -RT \ln K_{\text{eq}} \quad (1.15)$$

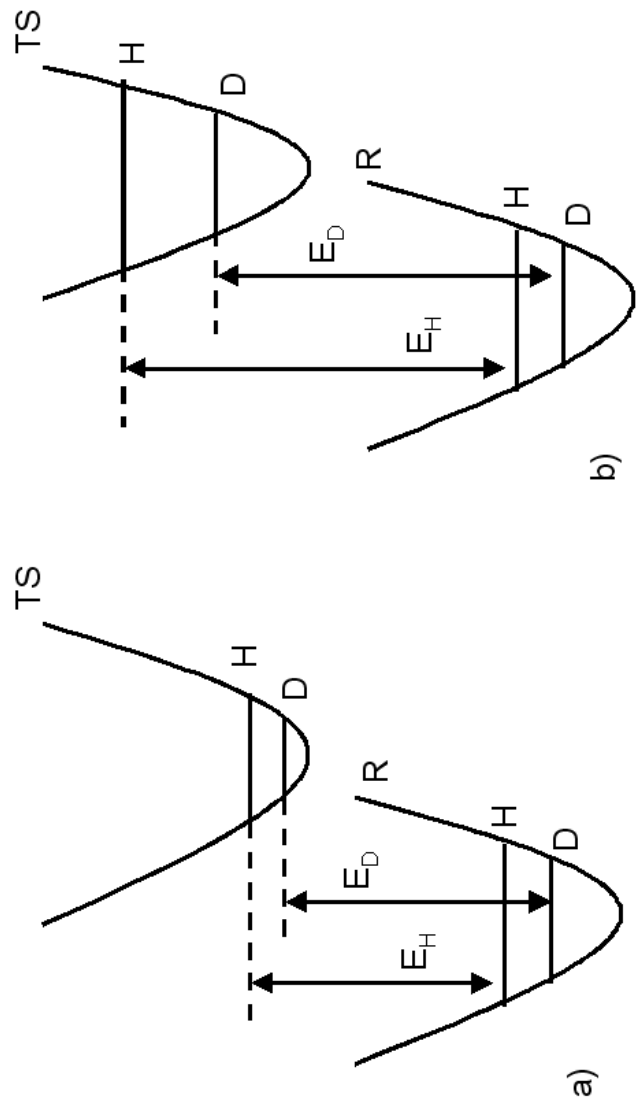


Figure 1.03: Schematic diagrams of potential energy surfaces where R indicates a vibration in the reactant and TS indicates the vibration in the transition state. The activation barriers for hydrogen and deuterium labeled compounds are shown for a) a loose transition state where $E_H < E_D$ and $k_H/k_D > 1$ and for b) a tight transition state where $E_H > E_D$ and $k_H/k_D < 1$.

Here $\Delta(\Delta_a G_{298}) = \Delta_a G_{298}(\text{AH}) - \Delta_a G_{298}(\text{RH})$, where $\Delta_a G_{298}(\text{RH})$ is a known quantity.

The equilibrium constant can be directly determined by measuring the relative intensities of two conjugate bases and the relative concentrations of the acids in an equilibrium mixture. This technique requires sufficiently long residence times so that equilibrium is established. A more common approach is to separately determine the forward and reverse proton transfer rate constants (k_f and k_r) for the reactions shown in eq 1.16; the rate constant ratio gives the proton transfer equilibrium constant,

$$K_{\text{eq}} = k_f/k_r.$$



Gas-phase ion-molecule bracketing experiments are employed when the more desirable equilibrium method is not feasible. Complications in measuring the proton transfer equilibrium constant arise when one of the conjugate bases cannot readily be formed or when the neutral acid is not available in pure form. Ion-molecule bracketing experiments overcome these difficulties by only examining one direction of the proton transfer equilibrium, either k_f or k_r . This method provides a semiquantitative estimate of the gas-phase acidity by examining the occurrence or non-occurrence of proton transfer with several reference acids, RH. For the case of $\text{A}^- + \text{RH}$, if rapid proton transfer is observed then the acidity of the reference acid is a lower bound, while if proton transfer is not observed then the acidity of the reference acid is an upper bound. Conversely, for the reaction of $\text{R}^- + \text{AH}$, the occurrence of rapid proton transfer sets an upper bound while the non-occurrence of proton transfer sets a lower bound.

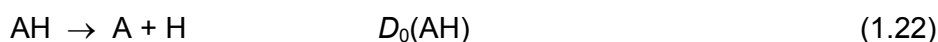
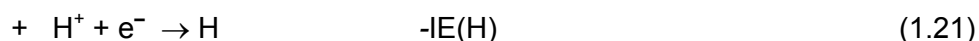
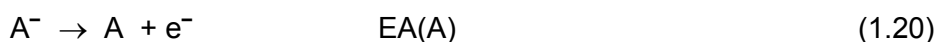
The enthalpy of deprotonation of AH, ($\Delta_a H_{298}(\text{AH})$), is determined from gas-phase acidity measurements via eq 1.17, where $\Delta_a S_{298}(\text{AH})$, is the entropy of deprotonation.

$$\Delta_a H_{298}(AH) = \Delta_a G_{298}(AH) + T \Delta_a S_{298}(AH) \quad (1.17)$$

The entropy of deprotonation can be determined by measuring the gas-phase acidity as a function of temperature; however, more often this value is found from electronic structure calculations. A small thermal correction ($\sim 1.5 \text{ kcal mol}^{-1}$) is applied to convert the 298 K enthalpy of deprotonation to 0 K (eq 1.18). Often, the integrated heat capacities are not available in the literature and therefore these values are also approximated from electronic structure calculations.

$$\Delta_a H_0(AH) = \Delta_a H_{298}(AH) - \int_0^{298} [C_p(A^-) + C_p(H^+) - C_p(AH)] dT \quad (1.18)$$

The enthalpy of dissociation can be related to other important thermodynamic quantities. Of particular importance, the bond dissociation energy (BDE, $D_0(AH)$) is the enthalpy required to homolytically cleave the AH bond, shown in eq 1.22. Since the making and breaking of bonds is the basis of all chemical transformation, knowledge of BDEs provides insight into whether or not a given chemical process can occur. BDEs can be determined from the enthalpy of deprotonation of AH ($\Delta_a H_0(AH)$), the electron affinity of the A radical ($EA(A)$), and the ionization energy of the hydrogen atom ($IE(H)$) via a negative ion thermochemical cycle:^{17,18}



The sum of eq 1.19-1.21, gives the bond dissociation energy at 0 K, eq 1.23.

$$D_0(AH) = \Delta_a H_0(AH) + EA(A) - IE(H) \quad (1.23)$$

Electron affinity measurements are discussed in Chapter 2 and the ionization energy of the hydrogen atom is well-known (13.59844 eV).¹⁹ If the heat of formation of AH is

known, then the heat of formation of the A radical, $\Delta_f H_0(A)$, can be determined from the BDE of the AH, using eq 1.24.

$$\Delta_f H_0(A) = D_0(AH) + \Delta_f H_0(AH) - \Delta_f H_0(H) \quad (1.24)$$

Here, $\Delta_f H_0(H)$ is the heat of formation of hydrogen atom ($52.103 \pm 0.001 \text{ kcal mol}^{-1}$)²⁰

This relationship is significant since radicals are highly unstable species, and their heats of formation cannot be determined directly from more traditional methods.

The thermodynamic quantities that make up the negative ion cycle are connected to other important thermodynamic quantities. Figure 1.04 shows the relationship between the negative ion cycle, the appearance energy cycle, and the proton affinity cycle. Through the appearance energy cycle, the BDE of AH is found from the difference of the ionization energy of A and the appearance energy of A^+/AH . The ionization energy of the A radical, $IE(A)$, is the energy required to remove an electron from A to form A^+ and a free electron. The appearance energy, $AE(A^+,AH)$ is the energy at which A^+ is observed in the photodissociation of AH. In the proton affinity cycle, the sum of $EA(A)$ and $\Delta_a H_0(AH)$ equals the sum of the ionization energy of AH and the proton affinity of A. The ionization energy of the AH, $IE(AH)$, is the energy required to remove an electron from AH to form AH^+ and a free electron. The proton affinity of A, $PA(A)$, is the energy required to remove a proton from AH^+ to form A and H^+ .

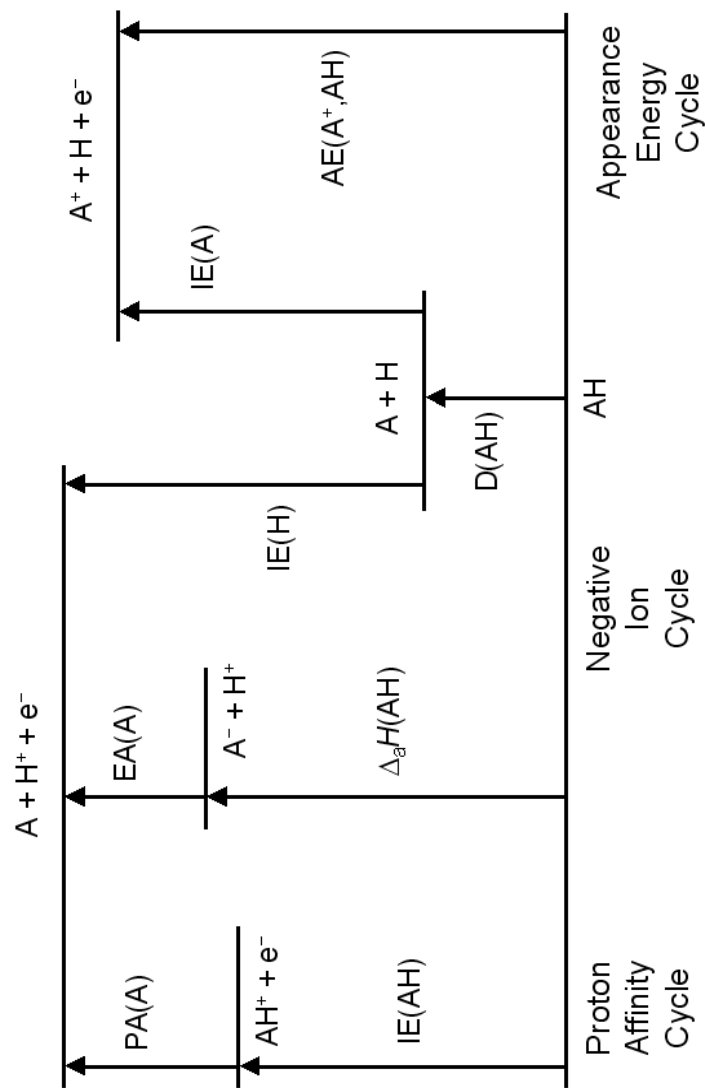


Figure 1.04: Schematic diagram that shows the relationship of the thermochemical quantities that compose the proton affinity cycle, negative ion cycle, and the appearance energy cycle.

1.6) Chapter 1 References

- (1) Wayne, R. P. Chemistry of Atmospheres; Oxford: Clarendon, 1991.
- (2) McCarthy, M. C.; Gottlieb, C. A.; Gupta, H.; Thaddeus, P. Laboratory and Astronomical Identification of the Negative Molecular Ion C_6H^- . *Astrophysical Journal* **2006**, 652, L141-L144.
- (3) Cernicharo, J.; Guelin, M.; Agundez, M.; Kawaguchi, K.; McCarthy, M.; Thaddeus, P. Astronomical Detection of C_4H^- , the Second Interstellar Anion. *Astronomy & Astrophysics* **2007**, 467, L37-L40.
- (4) Brauman, J. I.; Blair, L. K. Gas-Phase Acidities of Alcohols. *Journal of the American Chemical Society* **1970**, 92, 5986-5992.
- (5) Olmstead, W. N.; Brauman, J. I. Gas-Phase Nucleophilic Displacement-Reactions. *Journal of the American Chemical Society* **1977**, 99, 4219-4228.
- (6) Mackay, G. I.; Bohme, D. K. Bridging the Gap between Gas-Phase and Solution - Transition in Relative Acidity of Water and Methanol at $296 \pm 2K$. *Journal of the American Chemical Society* **1978**, 100, 327-329.
- (7) Langevin, P. A Fundamental Formula of Kinetic Theory. *Annales De Chimie Et De Physique* **1905**, 5, 245-288.
- (8) Gioumouzis, G.; Stevenson, D. P. Reactions of Gaseous Molecule Ions with Gaseous Molecules .5. Theory. *Journal of Chemical Physics* **1958**, 29, 294-299.
- (9) Moran, T. F.; Hamill, W. H. Cross Sections of Ion-Permanent-Dipole Reactions by Mass Spectrometry. *Journal of Chemical Physics* **1963**, 39, 1413-1422.
- (10) Su, T.; Bowers, M. T. Theory of Ion-Polar Molecule Collisions - Comparison with Experimental Charge-Transfer Reactions of Rare-Gas Ions to Geometric Isomers of Difluorobenzene and Dichloroethylene. *Journal of Chemical Physics* **1973**, 58, 3027-3037.
- (11) Bass, L.; Su, T.; Chesnavich, W. J.; Bowers, M. T. Ion-Polar Molecule Collisions - Modification of Average Dipole Orientation Theory: The $\cos\theta$ Model. *Chemical Physics Letters* **1975**, 34, 119-122.
- (12) Su, T.; Chesnavich, W. J. Parametrization of the Ion-Polar Molecule Collision Rate-Constant by Trajectory Calculations. *Journal of Chemical Physics* **1982**, 76, 5183-5185.
- (13) Melander, L.; Saunders, J. H., Jr. Reaction Rates of Isotopic Molecules; John Wiley and Sons: New York, 1980.

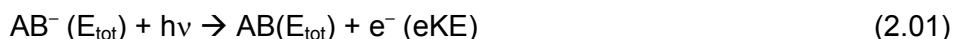
- (14) Kato, S.; Davico, G. E.; Lee, H. S.; DePuy, C. H.; Bierbaum, V. M. Deuterium Kinetic Isotope Effects in Gas-Phase S_N2 Reactions. *International Journal of Mass Spectrometry* **2001**, *210*, 223-229.
- (15) Viggiano, A. A.; Morris, R. A.; Paschkewitz, J. S.; Paulsen, J. F. Kinetics of the Gas-Phase Reactions of Chloride Anion, Cl⁻ with CH₃Br and CD₃Br: Experimental Evidence for Nonstatistical Behavior? *Journal of the American Chemical Society* **1992**, *114*, 10477-10482.
- (16) Poirier, R. A.; Wang, Y. L.; Westaway, K. C. A Theoretical-Study of the Relationship between Secondary α-Deuterium Kinetic Isotope Effects and the Structure of S_N2 Transition-States. *Journal of the American Chemical Society* **1994**, *116*, 2526-2533.
- (17) Berkowitz, J.; Ellison, G. B.; Gutman, D. Three Methods to Measure RH Bond-Energies. *Journal of Physical Chemistry* **1994**, *98*, 2744-2765.
- (18) Blanksby, S. J.; Ellison, G. B. Bond Dissociation Energies of Organic Molecules. *Accounts of Chemical Research* **2003**, *36*, 255-263.
- (19) Chase Jr., M. W.; Davies, C. A.; Downey Jr., J. R.; Frurip, D. J.; McDonald, R. A.; Syverud, A. N. JANAF Thermochemical Tables, 3rd ed. *Journal of Physical and Chemical Reference Data* **1985**, *14*.
- (20) *NIST Chemistry WebBook, NIST Standard Reference Database Number 69*; Linstrom, P. J.; Mallard, W. G., Eds.; National Institute of Standards and Technology: Gaithersburg MD, 20899 June 2005 (<http://webbook.nist.gov>).

CHAPTER II

ANION PHOTOELECTRON SPECTROSCOPY OVERVIEW

2.1) Introduction

In negative ion photoelectron spectroscopy¹⁻³ an anion beam (AB^-) is bombarded with a photon beam ($h\nu$) of fixed frequency. If the energy of the photon beam is greater than the electron binding energy, electrons will be ejected to yield neutral molecules (AB) and free electrons (e^-). This process is described by eq 2.01.



Conservation of energy requires that the internal energy of the neutral molecule plus the kinetic energy of the neutral molecule and of the ejected electron equals the photon energy. Since the electron is so much lighter than the neutral molecule, nearly all of the kinetic energy is imparted to the electron. As a result, measurement of the electron kinetic energy (eKE) distribution gives the internal energy of the neutral molecule. As will be discussed below, anion photoelectron spectroscopy provides thermodynamic information such as electron affinities (EA) and term splitting energies (T_e), allows for the measurement of vibrational frequencies and anharmonicities, and gives insight into the molecular structure of both the anion and the neutral species. Furthermore, by selectively choosing the anionic species, electron detachment yields unique or unstable radical and transition state species, which are difficult to study by other techniques.⁴

2.2) Atomic Species

Electron detachment from an atomic species, to form the corresponding neutral, results in purely electronic transitions. Consider for example, the photoelectron spectrum of $O^{\bullet-}$ collected at 351.1 nm (3.531 eV) photon energy

(shown in Figure 2.01). Photodetachment yields electrons with six different discrete kinetic energies (peaks *a-f*), which represent transitions from the two lowest spin-orbit states of $O^{\bullet-}$ ($^2P_{3/2,1/2}$) to the three lowest states of O ($^3P_{2,1,0}$);⁵⁻⁷ the corresponding energy diagram is included in the inset of Figure 2.01. The next electronic state of atomic oxygen is 1.96 eV higher in energy than the 3P_2 state and is not accessible with a 3.531 eV photon. Peak *c* corresponds to the EA of the oxygen atom (1.461112 eV), which is the transition from the ground state of the anion ($^2P_{3/2}$) to the ground state of the neutral (3P_2). The difference of peak *a* and *c* gives a term energy splitting of 177.13 cm^{-1} for the anion, while the differences of peak *c* and *e* and of peak *c* and *f* represent the energy differences between the ground state and the first and second excited states term energies of neutral oxygen (158.27 cm^{-1} and 226.98 cm^{-1} , respectively). For atomic transitions, the line width of the spectrum (fwhm) is determined by the instrument resolution (7 meV in Figure 2.01) and the relative intensities are determined by the population of the various levels of the anion.

2.3) Molecular Species

Electron detachment from molecular anions is more complicated since each electronic transition is composed of vibrational bands, which in turn are composed of rotational bands, eq 2.02.^{1,2}



In this process, an anion, which has an internal energy distribution of electronic, vibrational, and rotational energies ($E_{\text{ele}'} + E_{\text{vib}}(v') + E_{\text{rot}}(J')$) interacts with a photon to yield a neutral species with an internal energy distribution ($E_{\text{ele}''} + E_{\text{vib}}(v'') + E_{\text{rot}}(J'')$) and a free electron with discrete amounts of kinetic energy $e^-(eKE)$. Typically, using this experimental method, rotational frequencies cannot be resolved and are

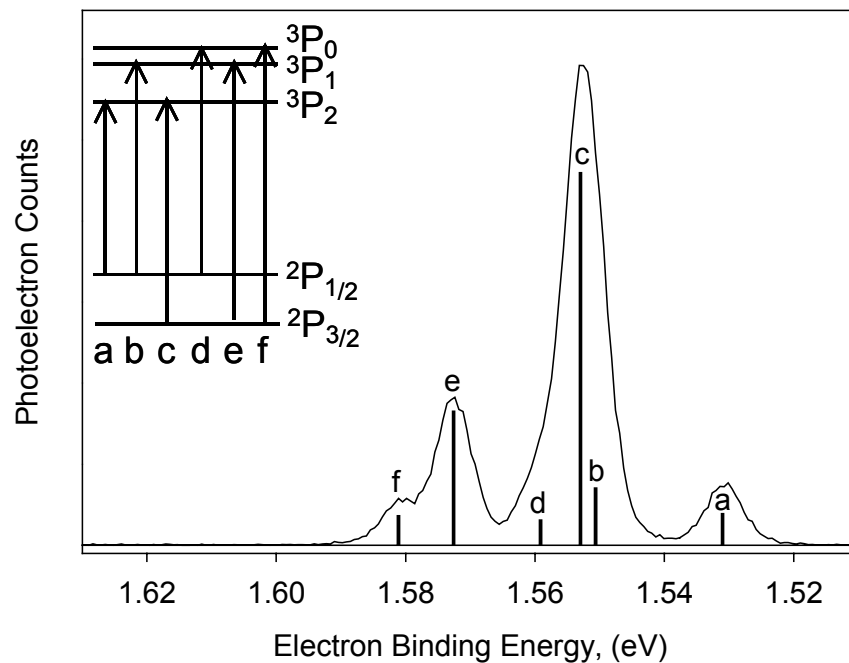


Figure 2.01: The 351.1 nm photoelectron spectrum of the $\text{O}^{\bullet-}$ anion. The solid line is the experimental spectrum while the sticks are the calculated transitions. Peak c is the electron affinity of atomic oxygen. An energy diagram for the two lowest spin-orbit states of the anion (bottom) to the three lowest states of the neutral atom (top) is provided in the inset.

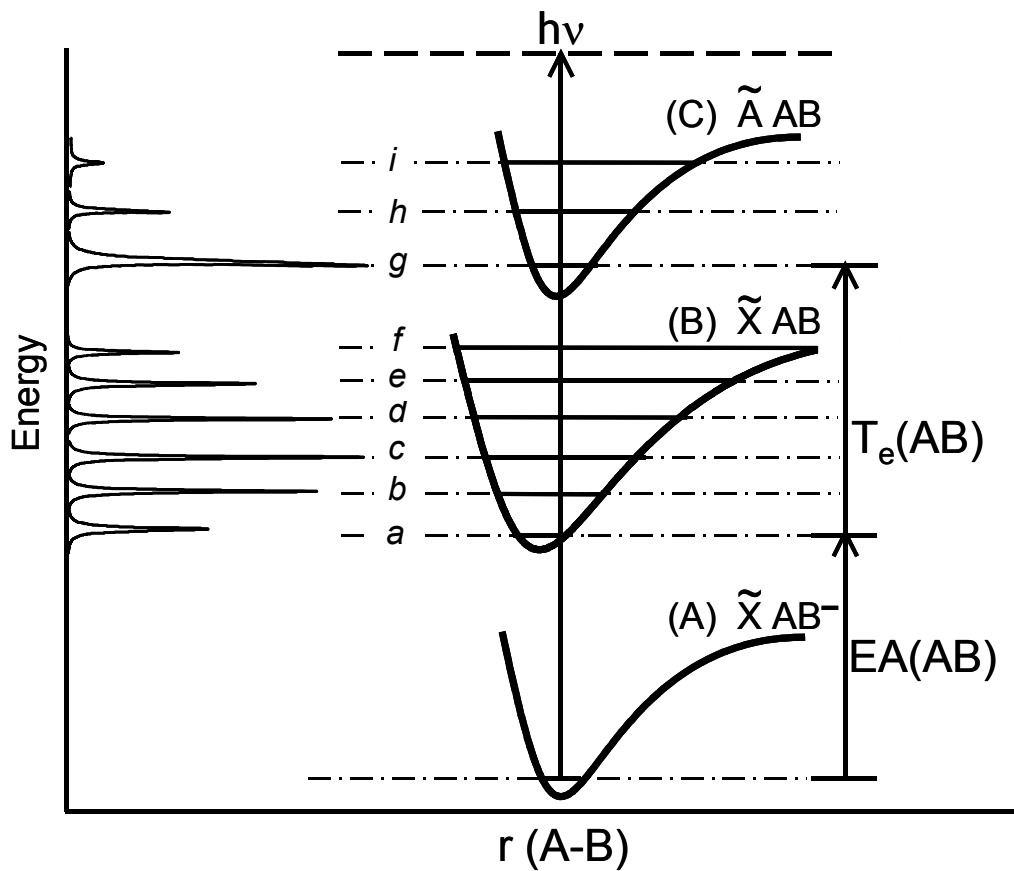


Figure 2.02: Schematic representation of the photodetachment from the ground state of AB^- (curve A) to the ground state (curve B) and first excited state (curve C) of AB.

only considered as corrections⁸ to final energies (discussed below); therefore, for the following discussion only vibrational transitions are considered, eq 2.03.

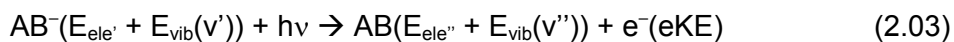


Figure 2.02 is a schematic representation of photodetachment from a hypothetical system, AB^- . This figure shows the potential energy curves and vibrational levels of the ground state of the anion (curve A) and the ground state (curve B) and first excited state (curve C) of the neutral AB. For a diatomic molecule the x-axis represents the A-B stretching motion. For a polyatomic molecule with n atoms (and $3n-5$ or $3n-6$ normal modes), the x-axis is a cut through one of the active modes. The transition from the ground electronic and vibrational state of the anion to the ground electronic and vibrational state of the neutral is the electron affinity (EA) of the neutral species (peak *a*). Vibrational levels of the neutral are seen as peaks at higher binding energies than the EA or origin peak (peaks *b-f*), while the peaks at binding energies lower than the origin represent vibrations of the anion; these transitions are referred to as hot bands (not shown in spectra on Figure 2.02). The spacing between these peaks gives the vibrational frequencies and anharmonicities. If the neutral molecule has a low-lying electronic state, it is also possible to observe a transition to this state. As in the ground state progression, the difference in the peaks, observed at higher binding energies than the excited state band origin (peak *g*), gives vibrational frequencies and anharmonicities of the neutral excited state. The difference between the electronic band origin of the ground state and the excited state (peaks *a* and *g*) gives the neutral term energy splitting (T_e).

For molecular anions, the intensities of the various transitions are determined by three factors: the intrinsic strength of the electronic transition, the population of the various levels, and the square of the vibrational overlap integral (i.e., Franck-Condon overlap). For a given electronic transition, the relative intensities of the

various vibrational levels can be explained by the Franck-Condon (FC) principle. This principle is based on the idea that electronic transitions occur very fast ($\sim 10^{-15}$ sec) relative to nuclear motion and, therefore, the nuclear positions do not change.

Quantitatively the Frank-Condon principle can be derived from the transition dipole moment, shown in eq 2.04.

$$\mathbf{M}_{ev} = \langle \Psi_{e'v'} | \boldsymbol{\mu} | \Psi_{e''v''} \rangle \quad (2.04)$$

where $\Psi_{e'v'}$ is the wavefunction for the initial state of the anion (single prime) and for the final state of the neutral plus a free electron (double prime) and $\boldsymbol{\mu}$ is the dipole moment operator. According to the Born-Oppenheimer approximation, the electronic and nuclear motions of the molecule are separable and the wavefunction can be written as a product of the two parts, $\Psi_{ev} = \Psi_e \Psi_v$. Additionally, the dipole moment operator, which is the sum over all the electrons (index i) and nuclei (index I) in the molecule, can be broken into an electronic part and a nuclear part, eq 2.05.

$$\boldsymbol{\mu} = -e \sum_i \mathbf{r}_i + e \sum_I Z_I \mathbf{R}_I = \boldsymbol{\mu}_e + \boldsymbol{\mu}_N \quad (2.05)$$

The transition dipole moment can be rewritten as:

$$\mathbf{M}_{ev} = \langle \Psi_{e'} | \boldsymbol{\mu}_e | \Psi_{e''} \rangle \langle \Psi_{v'} | \Psi_{v''} \rangle + \langle \Psi_{e'} | \Psi_{e''} \rangle \langle \Psi_{v'} | \boldsymbol{\mu}_N | \Psi_{v''} \rangle \quad (2.06)$$

The second half of eq 2.06 is zero, since the electronic wavefunctions of two different states are orthogonal; further simplification gives:

$$\mathbf{M}_{ev} = \langle \Psi_{e'} | \boldsymbol{\mu}_e | \Psi_{e''} \rangle \langle \Psi_{v'} | \Psi_{v''} \rangle = \mathbf{R}_e \langle \Psi_{v'} | \Psi_{v''} \rangle \quad (2.07)$$

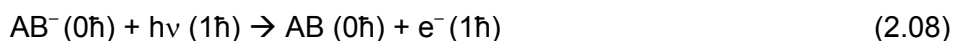
The intensity of a given transition is proportional to the square of the transition moment dipole^{9,10}, $I \propto |\mathbf{M}_{ev}|^2$. Therefore, for a given electronic transition the relative intensities of the vibrational peaks are proportional to the square of the vibrational overlap integral of the anion vibrational wavefunctions and the neutral species vibrational wavefunctions, $I \propto |\langle \Psi_{v'} | \Psi_{v''} \rangle|^2$, which are the Franck-Condon factors.

The intensity profile of the peaks within a given Franck-Condon envelope is a result of the difference in geometry between the anion and neutral. This has important implications, especially in our experimental setup, since typically the anion is in its ground electronic and ground vibrational state. The removal of an electron is rapid when compared to atomic nuclear motion, thus electron detachment results in the projection of the anion geometry and hence the anion wavefunction onto the neutral molecule potential energy surface. In other words, electron detachment results in a vertical transition, which corresponds to the most intense peak in the Franck-Condon envelope. For example in Figure 2.02, peak *c* is the most intense peak in the ground state envelope, this indicates that there is a significant change in the AB equilibrium bond length upon photodetachment thus, the transition from the ground vibrational state of the anion to the $v=2$ vibrational level of the \tilde{X} state of AB has the best Franck-Condon overlap. On the other hand, peak *g* is the most intense peak in the excited electronic state manifold, indicating that there is only a modest change in the AB equilibrium bond length upon photodetachment; thus, the transition from the ground vibrational level of the anion to the ground vibrational level of the \tilde{A} state of AB has the best Franck-Condon overlap.

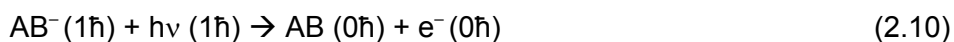
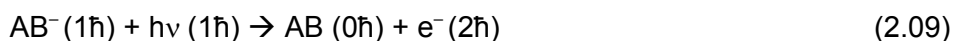
2.4) Selection Rules

Equation 2.07 allows us to define a set of selection rules. The selection rules for photodetachment are slightly different than those that govern the transitions in optical electronic spectroscopy. These differences arise since optical electronic spectroscopy involves a bound process, whereas photoelectron spectroscopy involves an unbound process; the initial state wavefunction describes the anion while the final state wavefunction describes the neutral molecule and the detached electron.

- 1) *Electronic Selection Rule* - Only single electron processes are allowed. Two electron processes occur when there is a detached electron with the simultaneous promotion of another electron to an excited molecular orbital. These processes are rare, but can occur if there is configuration mixing to produce a weak transition.
- 2) *Spin Selection Rule* - The total spin of the system (molecule and unbound electron) is conserved. Because the electron detaches with a spin $\pm \frac{1}{2}\hbar$ and only one electron is ejected, the spin of the molecule must also change by the same amount. This yields a selection rule for the molecule of $\Delta S = \pm \frac{1}{2}$, which is distinctly different from traditional electronic spectroscopy. Photodetachment from an anion that is a doublet ($2s+1=2$) results in a neutral molecule that is either a singlet ($2s+1=1$) or triplet ($2s+1=3$), allowing for direct determination of singlet-triplet splitting energies.
- 3) *Angular Momentum Selection Rule* - The angular momentum of the system must be conserved. The incident photon has an angular momentum of $1\hbar$, which is imparted to the outgoing electron. For example, if an electron is detached from an atomic s-orbital, as in the case of H^- , the electron will detach as a p-wave, eq 2.08.



If an electron is detached from an atomic p-orbital, as in the case of $O^{\bullet-}$, the photon angular momentum adds or subtracts, and the electron will leave as an d-type or s-type wave, respectively, eq 2.09 and 2.10.



Thus, there is a selection rule for the system (molecule and unbound electron) of $\Delta L = 0, \pm 1$. This rule is analogous to optical electronic spectroscopy, except that in a bound process, absorption of a photon will promote an electron from an s-orbital to a p-orbital and from a p-orbital to either an s- or d-orbital.

4) *Vibrational Selection Rule - Only vibrations that correspond to the changes in geometries between the anion and the neutral molecule are activated in the photoelectron spectra.* In the simplest approximation, all $3n-5$ (or $3n-6$) normal modes are separable and can be approximated as harmonic oscillators. Under this simple approximation, only totally symmetric vibrational modes will yield a non-zero Franck-Condon factor, hence only totally symmetric stretches are active in the photoelectron spectrum for any Δv . In practice, however, vibrations are not harmonic and non-totally symmetric modes can be active. Typically non-totally symmetric modes only have significant Franck-Condon factors for $\Delta v = 0$, unless there is a significant difference in the frequency between the anion and the neutral molecule. In this case, non-totally symmetric vibrations the Franck-Condon factors are non-zero for even quanta, $\Delta v = 0, \pm 2, \pm 4 \dots$ and zero for odd quanta, $\Delta v = 1, \pm 3, \pm 5 \dots$

2.5) Photoelectron Angular Distributions

Photoelectrons are not ejected isotropically, instead the intensity is dependent upon the relative polarity of the incoming linearly polarized photon.^{11,12} For linearly polarized light, photoelectron intensity is proportional to the differential photodetachment cross-section, which is described by eq 2.11.

$$I \propto \frac{\partial \sigma}{\partial \Omega}(\mathbf{E}) = \frac{\sigma_{\text{tot}}}{4\pi} \left[1 + \frac{\beta(\mathbf{E})}{2} (3\cos^2\theta - 1) \right] \quad (2.11)$$

Here, σ_{tot} is the total photodetachment cross-section, β is the asymmetry parameter ($-1 \leq \beta \leq +2$), and θ is the angle between the electric field vector of the incident

photon and the photoelectron collection axis. If the spectrum is collected at the “magic angle” ($\theta = 54.7^\circ$), then $3\cos^2\theta - 1 = 0$, and the photoelectron intensity is proportional to the photodetachment cross-section. Thus, the relative intensities of the various final vibrational states for a given initial vibrational state are proportional to the Franck-Condon factors only.

The anisotropy parameter (β) can be estimated by relative intensity measurements collected at laser polarizations perpendicular ($\theta=90^\circ$) and parallel ($\theta=0^\circ$) to the photoelectron collection axis as shown in eq 2.12.

$$\beta = \frac{I_{0^\circ} - I_{90^\circ}}{\frac{1}{2}I_{0^\circ} + I_{90^\circ}} \quad (2.12)$$

The anisotropy parameter (β) provides valuable information about the symmetry of the orbital from which the electron was ejected. Consider for example, ejection of an s-orbital electron, as the case of H^- , versus ejection of a p-orbital, as in the case of O^- . Electron detachment from an s-orbital results in a p-wave, which is polarized in the same direction as the photon. The angular distribution is $\cos^2\theta$ and $\beta=2$; additionally, the electron angular distribution is independent of the electron kinetic energy. Ejection of an electron from a p-orbital results in both an s- and d-wave. The photodetachment cross-sections for s- and d-waves are dependent upon the electron kinetic energy. For slow electrons, ejected just above threshold, the photodetachment cross-section of an s-wave is much larger than that of a d-wave, thus the photoelectron angular distribution is isotropic ($\beta=0$). As the electron kinetic energy increases, the d-wave cross-section becomes larger and the relative contributions of the s- and d-waves change. The asymmetry parameter is a measure of the interference between the s- and d-wave and, depending on the amount of interference, β is between 0 and 1.

While detachment of an electron from a molecular orbital is more complicated, β can still provide valuable information. It has been shown that $\beta < 0$ for electron detachment from π -orbitals and $\beta > 0$ for electron detachment from σ -orbitals.^{13,14} Additionally, dramatic changes in β are indicative of photodetachment of an electron from a different molecular orbital and therefore β can be used to identify different electronic states within the same spectrum.

2.6) Chapter 2 References

- (1) Eland, J. H. D. Molecular Photoelectron Spectroscopy. *Journal of Physics E - Scientific Instruments* **1978**, *11*, 969-977.
- (2) Ervin, K. M.; Lineberger, W. C. Photoelectron Spectroscopy of Negative Ions. In *Advances in Gas-Phase Ion Chemistry*; N. G. Adams and L. M. Babcock, Eds. Greenwich, 1992; pp 121-166.
- (3) Chen, P. Photoelectron Spectroscopy of Reactive Intermediates. In *Unimolecular and Bimolecular Reaction Dynamics*; C. Y. Ng, T. Baer and I. Powis, Eds.; John Wiley and Sons: New York, 1994; pp 371-425.
- (4) Wenthold, P. G.; Lineberger, W. C. Negative Ion Photoelectron Spectroscopy Studies of Organic Reactive Intermediates. *Accounts of Chemical Research* **1999**, *32*, 597-604.
- (5) Moore, C. E. Atomic Energy Levels. NSRDS-NBS; Washington: US GPO Circular No. 467, 1952.
- (6) Neumark, D. M. Laser Photodetachment Measurement of the Electron-Affinity of Atomic Oxygen. *Physical Review A* **1985**, *32*, 1890-1892.
- (7) Ervin, K. M.; Anusiewicz, I.; Skurski, P.; Simon, J.; Lineberger, W. C. The Only Stable State of O_2^- is the $X^2\Pi_g$ Ground State and It (Still!) Has an Adiabatic Electron Detachment Energy of 0.45 eV. *Journal of Physical Chemistry A* **2003**, *107*, 8521-8529.
- (8) Engelking, P. C. Approximate Rotational Band Shifts. *Journal of Physical Chemistry* **1986**, *90*, 4544-4545.
- (9) Bernath, P. F. Spectra of Atoms and Molecules; Oxford University Press: New York, 1995.
- (10) Harris, D. C.; Bertolucci, M. D. Symmetry and Spectroscopy: An Introduction to Vibrational and Electronic Spectroscopy; Oxford University Press: New York, 1978.
- (11) Cooper, J.; Zare, R. N. Angular Distributions of Photoelectrons. *Journal of Chemical Physics* **1968**, *48*, 942-943.
- (12) Hall, J. L.; Siegel, M. W. Angular Dependence of the Laser Photodetachment of the Negative Ions of Carbon, Oxygen, and Hydrogen. *Journal of Chemical Physics* **1968**, *48*, 943-945.
- (13) Gunion, R. F.; Gilles, M. K.; Polak, M. L.; Lineberger, W. C. Ultraviolet Photoelectron-Spectroscopy of the Phenide, Benzyl and Phenoxide Anions, with *Ab Initio* Calculations. *International Journal of Mass Spectrometry and Ion Processes* **1992**, *117*, 601-620.

(14) Wenthold, P. G.; Polak, M. L.; Lineberger, W. C. Photoelectron Spectroscopy of the Allyl and 2-Methylallyl Anions. *Journal of Physical Chemistry* **1996**, *100*, 6920-6926.

CHAPTER III

FLOWING AFTERGLOW-SELECTED ION FLOW TUBE TRIPLE QUADRUPOLE MASS SPECTROMETER: INSTRUMENT DESCRIPTION

3.1) Introduction

The Flowing-Afterglow technique was developed by E. E. Ferguson, F. C. Fehsenfeld, and A. L. Schmeltekopf at NOAA in 1963 as a means of studying atmospherically relevant ion-molecule reactions.¹ In this early technique, helium gas was directed down a glass flow tube by a high capacity pump and ionized by a discharge. Trace amounts of neutral reagents were added to the He flow and ions were observed with a quadrupole mass analyzer coupled to a particle multiplier. Kinetic measurements were made by monitoring the falloff of ion intensity as a function of neutral reagent concentration. Since its advent, several modifications including temperature variability,^{2,3} drift capability,⁴ inclusion of an atomic and radical species generator,⁵⁻⁸ and selected ion injection⁹ have been made. This powerful technique provides several advantages for studying the kinetics and thermochemistry of gas-phase ion-molecule reactions: 1) ionic and neutral reactants have a well-defined thermal energy distribution, 2) high ion densities are obtained, 3) a variety of ions can be formed by coupling several different ionization techniques and through multi step ion-molecule syntheses, 4) energy variability is possible, and 5) the kinetic analysis is relatively straightforward. Over the past four decades, this technique has been applied to study atmospheric and interstellar chemistry, gas-phase thermochemistry, fundamental and mechanistic physical organic chemistry, organometallic chemistry, and a variety of analytical problems.

The Flowing Afterglow-Selected Ion Flow Tube mass spectrometer (FA-SIFT) at the University of Colorado Department of Chemistry incorporates selected ion

injection, drift capabilities, and triple quadrupole detection. In this instrument ions are formed in a flowing afterglow source through a series of ion-molecule reactions. Ions of a certain polarity are extracted from the source region, mass selected by a quadrupole mass filter and injected into the reaction flow tube where they are thermalized to ~298 K through multiple collisions with He buffer gas. Measured flows of neutral reagents are introduced into the reaction flow tube through a series of fixed inlets along the reaction flow tube and the reactant and product ions are analyzed by a triple quadrupole mass filter coupled to an electron multiplier. Neutral reactant flow rates are measured by monitoring the pressure change versus time in a calibrated volume system. Reaction rate constants are determined by changing the neutral addition inlet, thereby changing the reaction distance and time, while monitoring the change in reactant ion intensity. Figure 3.01 is a photograph of the CU chemistry FA-SIFT mass spectrometer and Figure 3.02 is a schematic diagram of this instrument. The following sections provide an overview of this instrument: Flowing Afterglow Ion Source, Ion Optics and Mass Selection, Reaction Flow Tube, Triple Quadrupole Detection, Data Acquisition, Rate Constant Determination and Error Analysis, and Branching Ratio Determination. Several other sources have described this technique in more detail.¹⁰⁻¹³

3.2) Flowing Afterglow Ion Source

Reactant ions are formed in a flowing afterglow source by passing helium buffer gas, which has been purified by passage through a liquid nitrogen-cooled molecular sieve trap, over a heated filament. The filament assembly, shown in Figure 3.03, is composed of a repeller plate, a rhenium filament, and an acceleration grid. The filament is typically biased at approximately ± 70 V relative to the flow tube and grid. One side of the filament is biased 5 V higher than the other side; the filament is resistively heated and electrons are boiled off and accelerated towards



Figure 3.01: Photograph of the Flowing Afterglow-Selected Ion Flow Tube mass spectrometer (FA-SIFT) at CU Boulder

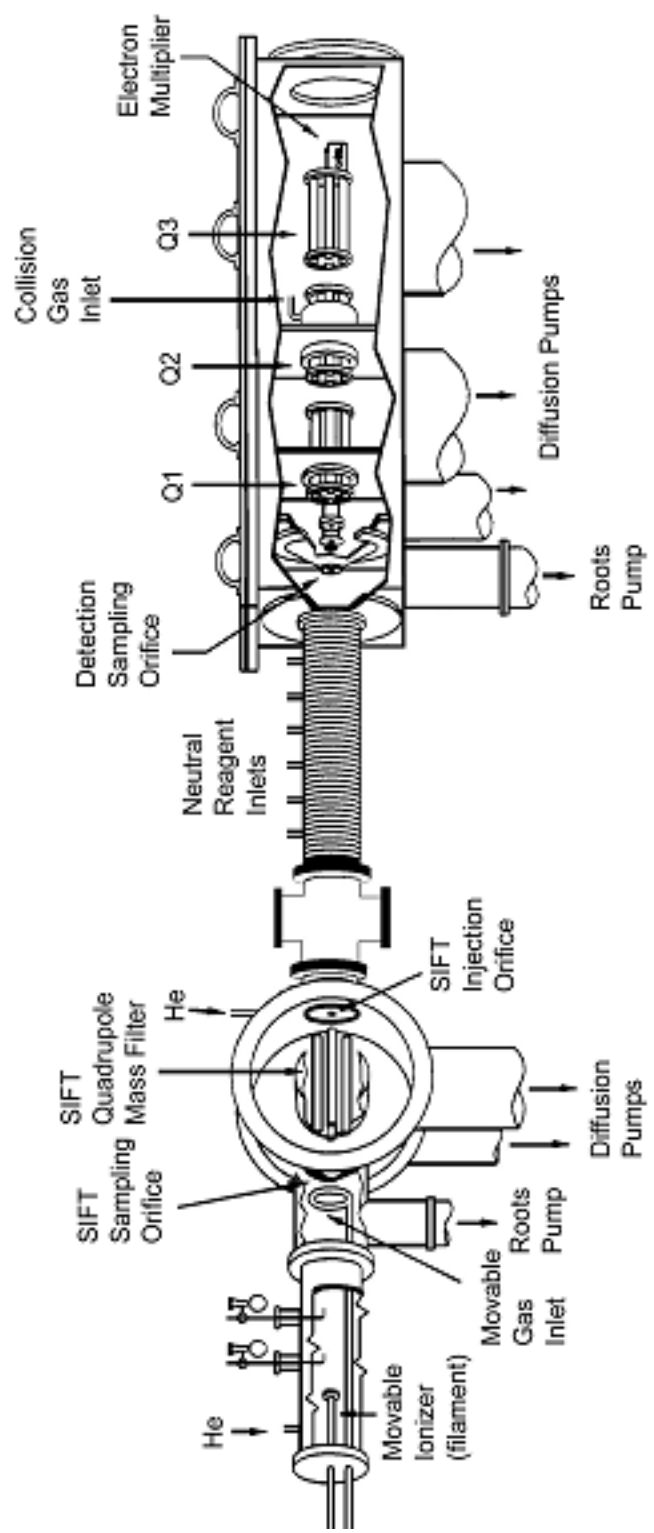


Figure 3.02: Schematic of Flowing Afterglow-Selected Ion Flow Tube mass spectrometer (FA-SIFT).

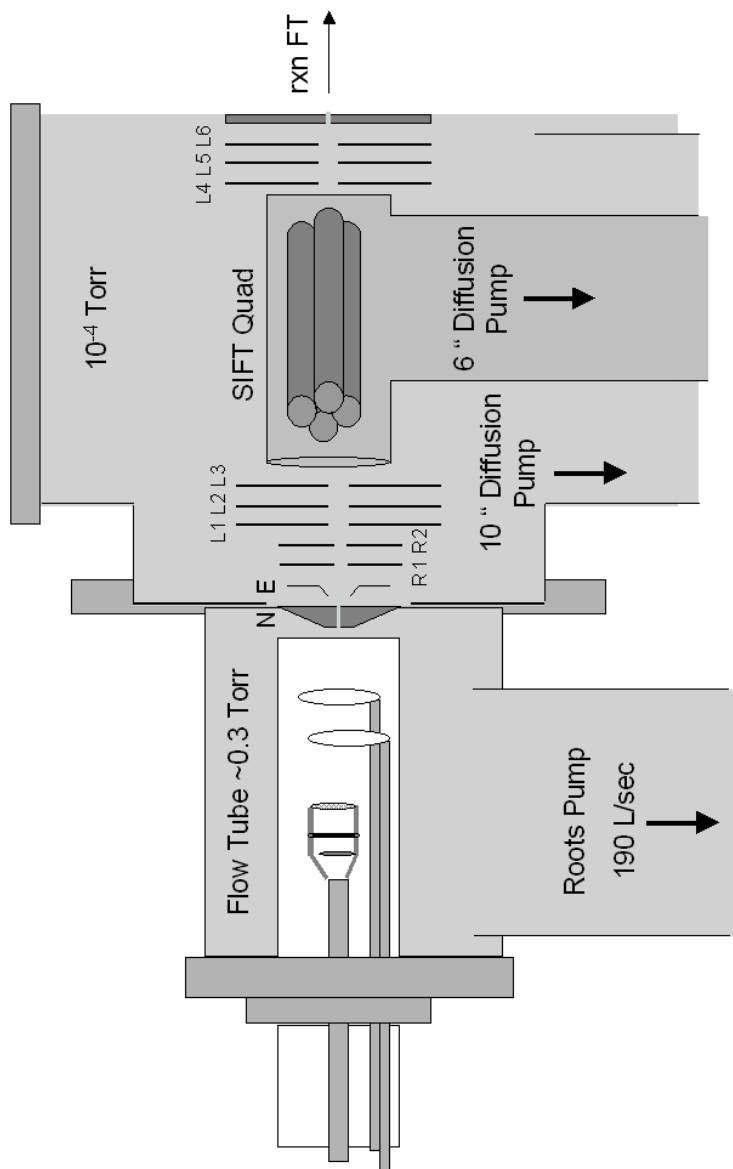


Figure 3.03: Schematic of the flowing afterglow source and mass selection region.

the grid. The emission current is typically set to 60 μA and is regulated by a feedback loop. The resulting helium plasma contains He 2^3S and 2^1S metastable species, He^+ , He_2^+ , and free electrons. The addition of trace amounts of neutral gases allows for a variety of ions to be produced from a wide range of mechanisms. In this source, both positive and negative ions are produced; however, only the mechanisms relevant to negative ion formation are discussed here. In general, negative ions are more difficult to produce than positive ions. The conditions, however, in the flowing afterglow source are ideal for producing negative ions since there are multiple collisions and an abundance of thermal energy electrons. Equations 3.01a-d summarize several routes to anion formation: (a) collisional electron attachment, (b) dissociative electron attachment, and (c and d) chemical ionization processes.



Since both the filament and two neutral inlets are movable, it is possible to perform an *in situ* ion synthesis through multiple, sequential ion-molecule reactions. For example $\text{O}^{\bullet-}$ is produced from dissociative electron attachment of N_2O (eq 3.01b), a subsequent H atom abstraction reaction with methane forms OH^- (eq 3.01c). Further downstream, introduction of an alcohol can lead to the formation of RO^- from a proton transfer reaction (eq 3.01d)

Since the plasma contains equal numbers of negatively and positively charged species, high ion densities ($\sim 10^7$ ions cm^{-3}) are achieved due to shielding effects. Ions are lost by recombination reactions and by ambipolar diffusion to the

walls of the flow tube. To minimize the diffusive loss of ions, the flow tube was constructed with a relatively large diameter (4.75 cm ID) and operated under high neutral gas flow rates and densities. The ions undergo multiple collisions ($\sim 10^6$ collisions s^{-1}) with the He buffer gas (~ 0.3 torr, 3-10 ms residence time). As a result, the ions are collisionally cooled to approximately room temperature. The He buffer gas and any neutral precursor gases are pumped away by a high capacity Stokes roots blower pump (190 L s^{-1}) while anions (or cations) are extracted from the source region into a low pressure region through a molybdenum nose cone with a 2 mm diameter orifice.

3.3) Ion Optics and Mass Selection

The ions are extracted from the source flow tube by biasing the source nose cone at an attractive potential relative to the source flow tube. A cone shaped extractor with an aperture of 4 mm sits directly behind the nose cone. The extractor is designed so that the electric field applied to it penetrates through the nose cone orifice into the source flow tube. Typically $< 20 \text{ V}$ is placed on this element, however, occasionally it is floated. The ion beam is focused into a SIFT quadrupole mass filter by a series of five lenses. These lenses are mounted on a common assembly with the extractor. The voltage applied to each element can be independently adjusted to tune the ion beam. The last three lenses in this assembly can operate as an Einzel lens, which allows for ion focusing without acceleration. A 10-inch diffusion pump maintains a pressure of approximately 10^{-4} torr in the lensing region. The SIFT quadrupole is mounted in a separate chamber which is pumped by a 6-inch diffusion pump to approximately 10^{-6} torr. A voltage is applied to the quadrupole case and to an entrance plate, which is mounted on the front of the quadrupole case. The SIFT quadrupole (Extrel # 4-270-9) rods are 1.6 cm in diameter and 22 cm long, allowing for transmission of ions up to 500 amu. The system is powered by an Extrel Power

Supply # 011-1. For the work presented in this thesis, a 2.2 MHz High-Q head (Extrel # 011-13) was employed, which allows for transmission of ions up to 180 amu.

A quadrupole consists of four parallel rods, and each set of opposite rods is electrically connected. An equal but opposite polarity RF potential ($V\cos(\omega t)$) is applied between each set of rods causing the ions to oscillate. Superimposed on the RF potential is an equal but opposite polarity DC voltage (U), shown in eq 3.02a and 3.02b.

$$\Phi_0 = U - V\cos(\omega t) \quad \text{and} \quad \Phi_0 = -U + V\cos(\omega t) \quad (3.02a-b)$$

In the absence of an RF voltage a negative ion will be attracted to the pair of positive rods, and a collision with the rods will neutralize the ion. Application of an RF voltage offsets this movement. For lighter ions this offset will be greater than for heavier ions, hence this pair of rods acts as a high-mass filter. The other pair of rods acts as a low-mass filter. In the absence of an RF voltage the negative pair of rods repels a negative ion and therefore the ion remains near the center. Application of an RF voltage will deflect the anions off the center axis. Lighter ions are displaced more than heavier ions, eventually resulting in neutralization from a collision with the rods. Only ions within a certain mass window will pass through the quadrupole. Increasing both the RF and DC voltages simultaneously allows for the mass range to be scanned. In these experiments, the SIFT quadrupole is set to pass an ion with a specific mass to charge ratio, rather than to scan the mass range.

Following mass selection, the ion beam is focused through three electrostatic lenses, which can also be used as an Einzel lens, into the reaction flow tube. These lenses are mounted on a common assembly and the voltage on each element can be applied separately. Injection of the ion beam from the source selection region into

the reaction flow tube requires the ions to travel from a low-pressure region into a high-pressure region. A Venturi inlet is employed for efficient injection of the ion beam into the reaction flow tube and to minimize backstreaming of neutral gases into the source selection region.^{9,14,15} This inlet is composed of an inner and outer annulus (0.007 cm² and 0.6 cm², respectively), which are positioned symmetrically about the injection orifice. The Venturi effect results from forcing gas through the smaller inner annulus by supplying a large backing pressure. The gas flow is hypersonic and the gas is compressible. A missile-shaped jet is formed, where there is high gas density at the edges and low gas-density in the interior, near the orifice.

3.4) Reaction Flow Tube

He buffer gas flows through the reaction flow tube at a rate of 12.0 SLPM (maintained by Tylan flow controller). The pressure in the flow tube is approximately 0.5 torr and is maintained by a high capacity Stokes roots blower pump (755 L s⁻¹). The reaction flow tube is ~117 cm long and is composed of two distinct parts, an entry region and a reaction region. Introduction of He buffer gas through the Venturi inlet results in turbulent flow. The entry region provides the necessary distance for the gas flow to relax and for collisional cooling of the ions. The entry region is composed of a stainless steel cross and bellows. The cross is equipped with several neutral gas inlets and a filament, which allows the instrument to operate in traditional flow afterglow mode. This option is useful since higher ion densities are achieved. The anions undergo multiple collisions with the He buffer gas (~0.5 torr, 10⁴ cm s⁻¹). As a result the ions are vibrationally and rotationally relaxed to a room temperature Boltzmann distribution; the excited electronic states of most negative ions in general are repulsive and lead to dissociation.¹⁶

The reaction region is approximately 68 cm long. It is constructed from multiple segments of 7.30 cm inner diameter stainless steel cylinders. Neutral

reagents are introduced into the flow tube through a manifold containing seven fixed radial inlets that are spaced 9.7 cm from one another. Each radial inlet contains seventeen (0.37 mm diameter) holes concentrically spaced around the flow tube diameter. This design allows for efficient mixing of the neutral reagent into the buffer gas. A capacitance manometer measures the pressure at approximately the center of the reaction region.

The fluid properties of the He buffer gas in the reaction region are very well defined. The flow of He gas is viscous (i.e., $\lambda/d \ll 1$, the mean free path of a particle is much smaller than the flow tube diameter).¹⁷ Therefore, a given particle will undergo more collisions with other particles than with the walls of the instrument. Thus, within a given mean free path gas properties such as temperature, velocity, and density remain constant and the gas is described as a continuous medium. Gas flowing through a cylindrical reaction vessel experiences resistance to flow and a velocity gradient is established across the cylinder radius. If the velocity gradient is smooth then the flow is laminar, while if the velocity profile is irregular then the flow is turbulent.¹⁸ The flow is characterized by a dimensionless parameter called a Reynolds number (R_e),¹⁸ (eq 3.03), where ρ is the fluid density, v is the fluid velocity, d is the flow tube diameter, and η is the fluid viscosity.

$$R_e = \frac{\rho v d}{\eta} \quad (3.03)$$

Laminar flow is described by $R_e < 1200$, while turbulent flow is described by $R_e > 2200$. In the entry region of the flow tube, the gas flow is turbulent; however, these instabilities are damped out in the first ~15 cm of the entry region and the flow in the reaction region is laminar ($R_e \sim 40$). Additionally the flow in the reaction region is Poiseuille,¹⁷ hence the gas is incompressible and the flow is stable. The velocity gradient of a viscous, laminar medium flowing in a cylindrical reaction vessel is

parabolic. Equation 3.04 describes the parabolic velocity gradient ($v(r)$),¹⁸ where r is the radial distance from the center, v_0 is the velocity at the center of the flow tube, and R is the flow tube radius.

$$v(r) = v_0 \left(1 - \frac{r^2}{R^2} \right) \quad (3.04)$$

At the chamber walls ($r=R$) the velocity is zero; at the center of the flow tube ($r=0$) the velocity is the maximum velocity (v_0). It can be shown that the average velocity (v_{ave}) is one-half the maximum velocity.

The density of He in the flow tube is $\sim 10^{16}$ particles cm^{-3} . The density of neutral reagents introduced into the flow tube is $\sim 10^{11}$ molecules cm^{-3} , thus the neutral reagents have the same velocity profile as the He buffer gas. On the other hand, ionic species travel slightly faster than neutral species in the flow tube. Ions that collide with the walls of the flow tube are neutralized resulting in a radial concentration gradient. Fick's law of diffusion, eq 3.05, describes the diffusive flux of the ions in the flow tube,

$$J = -D\nabla[A^-] \quad (3.05)$$

where $\nabla[A^-]$ is the ion concentration gradient, D is the diffusion coefficient, and the negative sign indicates that ions are transported from high to low concentration. The concentration of ions is greatest at the center of the flow tube, where the He velocity is at its maximum. As a result, the average ion velocity is larger than the average He velocity ($v_{ions} = \alpha v_{ave}$, where α is a correction factor between 1 and 2). For this system, the average ion velocity was experimentally determined to be 1.6 times greater than the average He velocity.^{1,19-21} The well-defined velocity profile in the reaction region means that reaction distance can be related to the reaction time

($v = z/t$, where z is distance and t is time) allowing for rate constant determinations, as described in section 3.7.

3.5) Triple Quadrupole Detection

The reaction region of the flow tube ends ~4 cm before the detection nose cone; a thin molybdenum plate with a 0.5 mm orifice is mounted on a stainless steel carrier plate that separates the flow tube from the detection region. Anions are gently extracted into the detection region (shown in Figure 3.04) by placing a slightly positive voltage (< 10 V) on the nose cone while neutral species are pumped away. The carrier plate voltage is applied separately and is set to transmit the maximum number of ions. The current on the nose cone is measured by an electrometer; typical currents range between 0.5-30 pA in the SIFT mode of operation. The ion beam is focused into a triple quadrupole mass filter by a stack of five electrostatic lenses. The five lenses are mounted on a common assembly, which sits on the front plate of the triple quadrupole case. The lens stack is housed in the first differentially pumped chamber that is maintained at a pressure of $\sim 10^{-5}$ torr by an Edwards 6-inch diffusion pump (805 L s^{-1}). The voltage on each lens can be controlled separately and is gradually increased to more attractive voltages from the first lens to the third lens. The first lens is a cone shaped extractor, which operates similarly to the source region extractor. The last three lenses are designed to operate as an Einzel lens. A voltage is also applied to the quadrupole entrance plate.

The triple quadrupole consists of a series of three identical stainless steel quadrupoles that are housed in one common assembly. The triple quadrupole is part of the Extrel C50 TQMS system (1.2 MHz RF oscillator, 300 W DC Power level for Q1 and Q3, and 200 W Power level for Q2). The rods are 1.9 cm in diameter

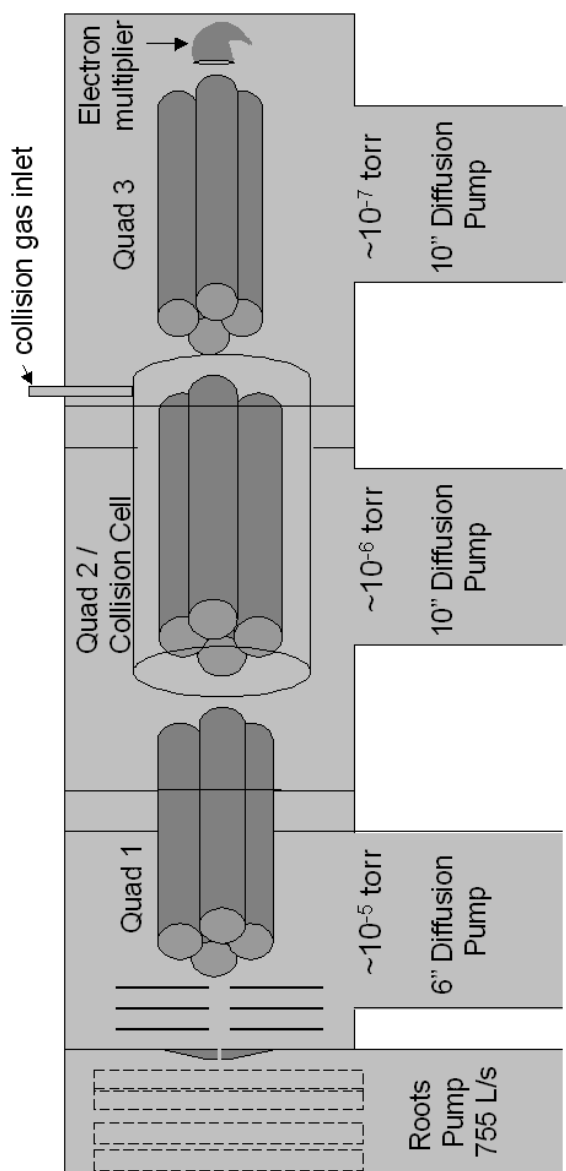


Figure 3.04: Schematic of triple quadrupole detection.

allowing for the transmission of ions up to 500 amu. Each quadrupole is electrically isolated from one another and from lenses (five total), which sit at the entrance and exit of each set of rods. The entire assembly spans the three differentially pumped regions. The second and third chambers are maintained at $\sim 10^{-6}$ and $\sim 10^{-7}$ torr, respectively, by two Edwards 10-inch diffusion pumps (2300 L s^{-1}).

The triple quadrupole assembly can operate in two distinct modes, MS-MS and MS. In MS-MS mode both Q1 and Q3 are mass resolving while Q2 acts as an ion pipe (RF voltage only). This arrangement allows for selection of a single mass-to-charge ratio ion by Q1, collision induced dissociation in Q2, followed by mass analysis of the fragment ions by Q3. The fragment ions formed from CID can provide structural information about the parent ion, thus MS-MS mode is used to elucidate the identity of an unknown ion. For the experiments described in this thesis, the instrument was operated in MS mode only. In this setup, Q1 and Q2 are used as ion pipes, while Q3 is a mass analyzer. The mass selected ion beam impinges on an electron multiplier that has a gain of 10^8 .

3.6) Data Acquisition

The current collected by the electron multiplier is converted to pulses by a capacitor and passed through a pulse amplifier and discriminator. The TTL pulses are fed into an Ortec ACE-MCS board that contains an array of 4096 channels. The voltage output is sent to the Extrel quadrupole controller, which specifies the specific mass-to-charge ratio to transmit. As the ACE-MCS voltage is ramped, the channel array is scanned and the Extrel quadrupole controller scans the RF and DC quadrupole voltages. The data acquisition time is specified and the number of counts per channel is collected. A plot of counts per second versus channel number corresponds to ion intensity versus mass-to-charge ratio; hence a mass spectrum is collected. Figure 3.05a is a mass spectrum of the SIFT-injected BrO^- anion. A

portion of this anion fragments to form Br^- upon injection into the reaction flow tube. Figure 3.05b is a mass spectrum for the reaction of BrO^- with CH_3Cl .

Kinetics measurements are collected using a separate program that controls the opening and closing of the neutral reagent solenoid valves and a series of voltages, which are sent to the Extrel quad controller. For each neutral reagent inlet, the program jumps through a series of voltages corresponding to different mass ions and collects the number of counts per second. The user inputs certain experimental parameters (temperature, flow tube pressure, and neutral reagent flow) and the program calculates a reaction rate constant and product ion branching ratios as described below.

3.7) Rate Constant Determination and Error Analysis

One of the benefits of this technique is that it affords a relatively straightforward kinetic analysis. Bimolecular reaction rate constants are measured under pseudo first order conditions (i.e., the concentration of one of the reactants is much greater than the concentration of the other reactant and therefore does not appreciably change over the course of the reaction). Under our experimental conditions, the neutral reagent concentration is $\sim 10^{11}$ molecules cm^{-3} , while the ion concentration is $\sim 10^5$ ions cm^{-3} . For a given bimolecular reaction: $\text{A}^- + \text{B} \rightarrow \text{C}^- + \text{D}$, the loss of A^- is described by eq 3.06, where k^{II} is the bimolecular rate constant, $[\text{B}]$ is the neutral reagent concentration, $[\text{A}^-]$ is the ion concentration, and t is the reaction time. Since there is a well-defined velocity profile, reaction time and distance are related ($t = z/\alpha v_{\text{He}}$, where z is the reaction distance, α is the ion velocity correction factor of 1.6,^{1,19-21} and v_{He} is the average helium velocity).

$$\frac{d[\text{A}^-]}{dt} = \alpha v_{\text{He}} \frac{d[\text{A}^-]}{dz} = -k^{\text{II}} [\text{A}^-] [\text{B}] \quad (3.06)$$

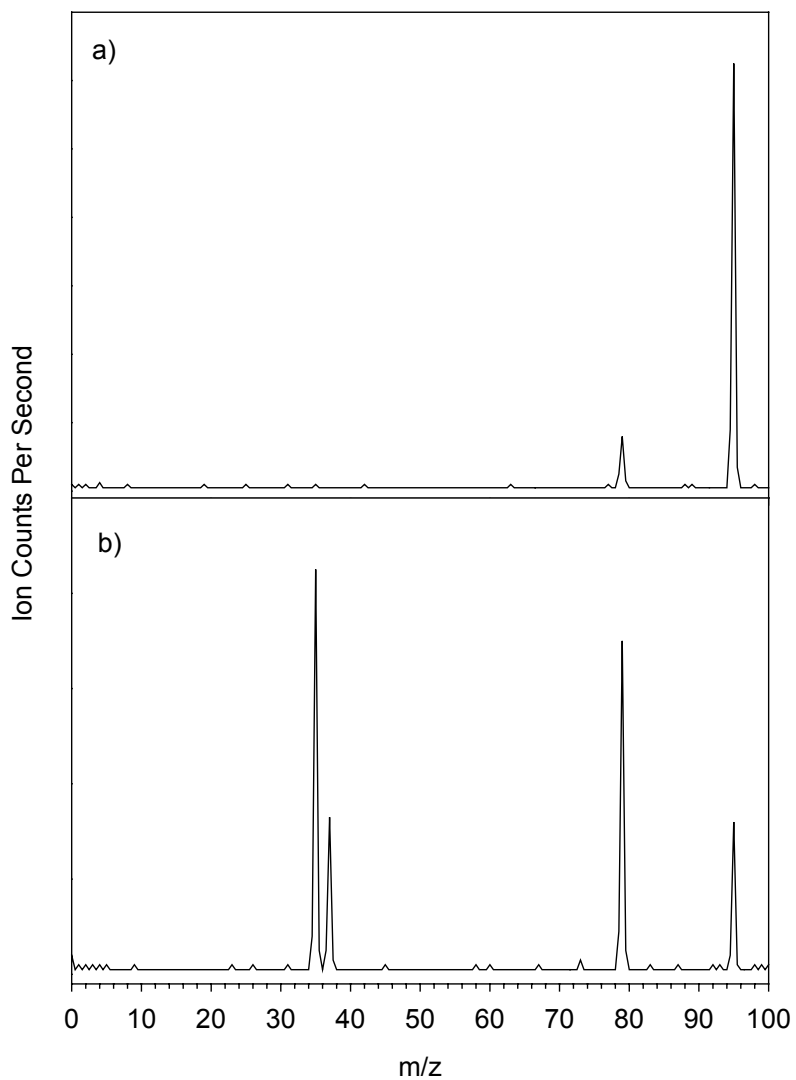


Figure 3.05: a) Spectrum of the SIFT-injected $^{79}\text{BrO}^-$ anion (m/z 95); the Br^- anion (m/z 79) is also present due to collision induced dissociation upon SIFT injection of the parent ion. b) Spectrum of the $\text{S}_{\text{N}}2$ reaction of $\text{BrO}^- + \text{CH}_3\text{Cl}$; both Br^- (m/z 79) and Cl^- (m/z 35 and m/z 37) are products of this reaction.

The integrated rate expression is given in eq 3.07, where $[A^-]_0$ is the initial ion concentration and $[A^-]_z$ is the ion concentration at distance z .

$$[A^-]_z = [A^-]_0 \exp\left[\frac{-k''[B]z}{\alpha v_{\text{He}}}\right] \quad (3.07)$$

Ions injected into the reaction flow tube also undergo diffusive losses in addition to reactive losses. Incorporation of radial diffusion and of the parabolic radial velocity profile leads to the solution shown in eq 3.08.

$$[A^-]_z = [A^-]_0 \exp\left[-\left(\frac{\partial D}{R^2} + \frac{k''[B]}{\alpha}\right)\frac{z}{v_{\text{He}}}\right] \quad (3.08)$$

where ∂ is a constant equal to 3.7,^{1,19-21} R is the flow tube radius, and D is the diffusion coefficient of the reactant ion through He buffer gas; a detailed derivation of this solution can be found in reference 11. The ion density at any given axial position can be found from this equation. The first term describes the diffusive loss while the second term describes the reactive loss. Diffusive loss occurs over the entire flow tube length (L) and is independent of the neutral reagent concentration. Thus, the diffusive loss term is a constant for a given measurement and can be neglected when measuring the reactive loss.

A plot of the logarithmic falloff of ion intensity versus reaction distance is linear; the slope is a result of the reactive loss and the intercept is a result of the diffusion loss as shown in eq 3.09. A representative kinetics plot (i.e., reactant and product ion intensities versus reaction distance for given neutral reagent concentration) is shown in Figure 3.06 for the reaction of $\text{BrO}^- + \text{CD}_3\text{Cl}$ (discussed in chapter 5).

$$\ln\left(\frac{[A^-]_z}{[A^-]_0}\right) = -\frac{\partial D z}{R^2 v_{\text{He}}} - \frac{k''[B]z}{\alpha v_{\text{He}}} \quad (3.09)$$

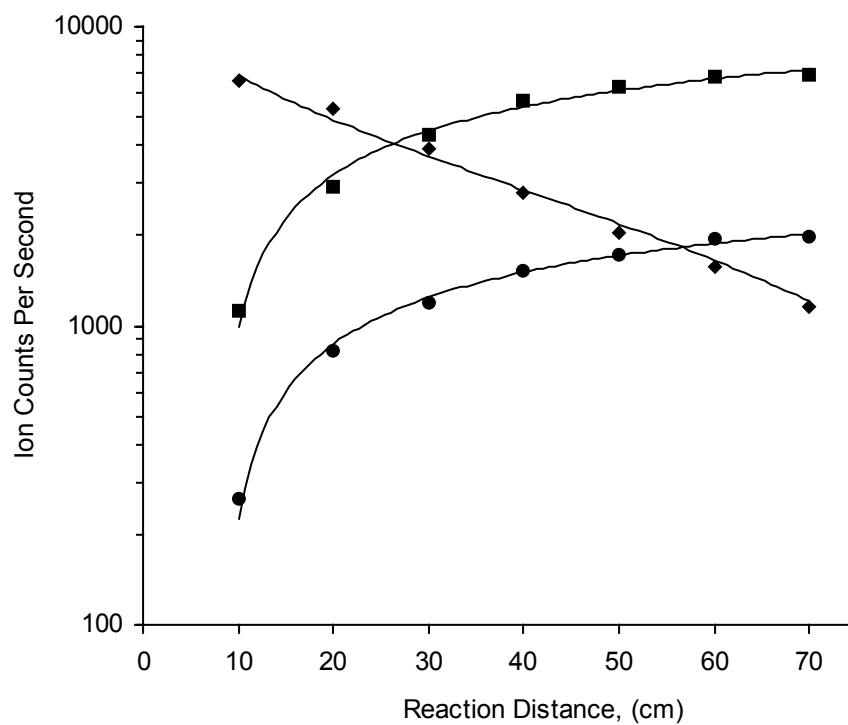


Figure 3.06: Reactant ion depletion and product ion formation for the reaction $\text{BrO}^- + \text{CD}_3\text{Cl}$. Symbols: \blacklozenge BrO^- , \blacksquare Cl^- , and \bullet Br^- .

The reaction rate constants can be determined from the slope of the plot of $\ln([A^-]_z/[A^-]_0)$ versus z . The velocity of He buffer gas (v_{He}) is determined from the flow of He (F_{He}), the pressure of He (P_{He}), and the cross sectional area of the flow tube (πR^2), eq 3.10.

$$v_{\text{He}} (\text{cm/s}) = \frac{F_{\text{He}} (\text{STP} \cdot \text{cm}^3/\text{s})}{\pi R^2 (\text{cm}^2) P_{\text{He}} (\text{torr})} \times \frac{760 (\text{torr})}{\text{atm}} \times \frac{T (\text{K})}{273.16 (\text{K})} \quad (3.10)$$

The concentration of B is determined using a calibrated volume technique. In this technique, the neutral reagent flow (F_{B}) is determined by measuring a change in pressure (ΔP) per unit time (Δt) for a given volume (V).

$$[B] (\text{part./cm}^3) = \frac{F_{\text{B}} (\text{atm} \cdot \text{cm}^3/\text{s})}{\pi R^2 (\text{cm}^2) v_{\text{He}} (\text{cm/s})} \times \frac{760 \text{torr}}{\text{atm}} \times 3.535 \cdot 10^{16} \text{ part./cm}^3 \cdot \text{torr} \quad (3.11)$$

Equation 3.12 expresses the reaction rate constant in terms of measurable experimental quantities.

$$k^{\text{II}} (\text{cm}^3/\text{part.} \cdot \text{s}) = \frac{-\text{dln}[A^-]}{\text{dz} (\text{cm})} \frac{\alpha F_{\text{He}}^2 (\text{atm}^2 \cdot \text{cm}^6/\text{s}^2) T^2 (\text{K}^2)}{P_{\text{He}}^2 (\text{torr}^2) F_{\text{B}} (\text{atm} \cdot \text{cm}^3/\text{s}) \pi R^2 (\text{cm}^2)} \quad (3.12)$$

$$\times \frac{1}{3.535 \cdot 10^{16} \text{ part./cm}^3 \cdot \text{torr}} \times \frac{760 \text{torr}}{\text{atm} \cdot 273.16^2 (\text{K}^2)}$$

The units of the bimolecular rate constant, k^{II} , are the inverse of the product of concentration and time. When the flow is given in $\text{atm cm}^3 \text{ s}^{-1}$, velocity in cm s^{-1} , temperature in K, and pressure in atmospheres, then k^{II} is in $\text{cm}^3 \text{ s}^{-1} \text{ particle}^{-1}$.

Additionally, rate constants for three-body processes such as association reactions, can also be determined since the He buffer gas density is in excess, hence $k^{\text{II}} = [\text{He}]k^{\text{III}}$. Given the above dimensions, termolecular rate constants, k^{III} , are given in $\text{cm}^6 \text{ s}^{-1} \text{ particle}^{-2}$.

The systematic and random errors for a given rate constant measurement must be considered. The random error is determined by propagating the error associated with each individual measurement, as shown in eq 3.13.

$$\frac{\sigma(k^{\parallel})}{k^{\parallel}} = \left[\frac{\sigma^2(\text{slope})}{\text{slope}^2} + \frac{\sigma^2(\alpha)}{\alpha^2} + \frac{4\sigma^2(F_{\text{He}})}{F_{\text{He}}^2} + \frac{4\sigma^2(T)}{T^2} + \frac{4\sigma^2(P_{\text{He}})}{P_{\text{He}}^2} + \frac{4\sigma^2(R)}{R^2} + \frac{\sigma^2(F_{\text{B}})}{F_{\text{B}}^2} \right]^{\frac{1}{2}} \quad (3.13)$$

$$\frac{\sigma(F_{\text{B}})}{F_{\text{B}}} = \left[\frac{\sigma^2(\Delta P)}{(\Delta P)^2} + \frac{\sigma^2(V)}{V^2} + \frac{\sigma^2(\Delta t)}{(\Delta t)^2} + \frac{\sigma^2(T)}{T^2} \right]^{\frac{1}{2}} \quad (3.14)$$

The error in the slope is the standard deviation determined by a least squares analysis, typically 1-3%; the error in α is 12.5%; the error in the He buffer gas flow (F_{He}) is 0.9%, this is a combination of the precision of the Tylan flow controller and the standard deviation determined by a least squares analysis for the Tylan flow calibration curve; the error in the temperature (T) is conservatively estimated to be 0.4%, this encompasses a 2°C change in temperature over the course of a measurement and an accuracy of $\pm 0.5^\circ\text{C}$; the error in the He pressure (P_{He}) is 0.3%, this is the accuracy of the capacitance manometer; and the error in the flow tube radius (R) is 0.7%. The error in the neutral reactant flow (F_{B}) encompasses individual errors in time (t), volume (V), pressure (P), and temperature (T), as shown in eq 3.14. The error in time is the standard deviation of multiple measurements, typically ~3%; the error in the volume is <0.9%; the error in the pressure measurements is estimated to be 0.75%; and the error in the temperature is 0.4%. Propagating each error results in a $\pm 13.4\%$ error bar for each rate constant measurement; if a rate constant is measured three separate times the error is reduced to $\pm 7.7\%$. Typically, a more conservative error bar of $\pm 20\%$ is reported. This propagated error reflects the accuracy of each measurement. For the rate constant measurements in this thesis, the reported error bar is one standard

deviation of at least three separate measurements. This error reflects the reproducibility of each measurement and is usually smaller than the propagated error.

In addition to random error, the systematic error must be evaluated. The working equation, eq 3.09, embodies several important assumptions. The effect of each assumption has been rigorously evaluated in reference 11 and, therefore, will only be briefly discussed here.

- 1) *There are no other production or loss mechanisms for the ions other than diffusive and reactive losses.* Since reaction rate constants are measured under pseudo first order conditions, the concentration of neutral products is small and, therefore, the back reaction to reform the reactant ion does not occur in any significant amount. On the other hand, secondary reactions between the product ions and the neutral reactant may occur. Secondary reactions of this sort do not affect the rate constant measurement, but need to be accounted for in determining a product branching ratio. One additional complication is the occurrence of side reactions with trace contaminants contained in the neutral reagent. If the reaction of the anion with the contaminant is fast compared to that of the anion with the neutral reagent of interest then measured rate constants will be larger than the true value.
- 2) *The ion density is determined by diffusion rather than by reactive loss.* When the magnitude of the reactive loss is comparable to diffusive loss, higher order diffusive terms must be considered. This results in a ~1% deviation from the true rate constant.
- 3) *For viscous, laminar gas flow through a cylinder, the velocity at the chamber walls is assumed to be zero.* Non-zero velocity at the chamber walls (termed slip flow) flattens the parabolic velocity profile, lowering the average ion velocity. A

more rigorous treatment of the velocity profile would result in a rate constant that is 1-3% lower than the true value.

- 4) *Ions are continually lost in the flow tube from diffusion.* This radial loss is described by Fick's law of diffusion (eq 3.05), where the diffusion coefficient depends on both the ion structure and the nature of the medium through which the ion moves. This diffusive loss is assumed to be constant along the flow tube and, therefore, is neglected when determining the rate constant. This assumption is reasonable since the concentration of He is much greater than the concentration of the neutral reagent and therefore the diffusion coefficient does not significantly change upon introduction of neutral reagent into the flow tube. However, for large neutral flows the diffusion coefficient may change. The resulting error may be as large as a ~5% underestimation of the rate constant. In addition to a radial density gradient, there is an axial density gradient. This axial density gradient results from the continual radial loss of ions to the chamber walls in combination with reactive loss of ions. The axial ion density gradient is small and therefore neglected; however, consideration of axial diffusion would result in a rate constant that is ~1% higher than the true value.
- 5) *The pressure drop across the reaction flow tube of ~12% is negligible.* This axial pressure gradient results in an axial velocity gradient; thus, as an ion travels down the flow tube its velocity increases. By measuring the flow tube pressure at the center of the reaction region, the effects of the velocity gradient are minimized since the magnitude of error that results from evaluating the reaction with the inlets upstream of the center position is approximately equal in magnitude and opposite in direction to the error resulting from the inlets that are downstream of the center position. In actuality, these errors do not quite cancel one another, since the flow tube pressure is measured slightly upstream of the

center position. This results in a slight overestimation of the rate constant by ~1%. In practice, the error that results from the axial velocity gradient is less important when rate constants are determined by changing the neutral flow rather than changing the neutral inlet position. However, comparison of rate constant measurements collected by changing the neutral flow compare well with measurements collected by changing the reaction distance. However, it is more practical to change the reaction distance, since the distance can be more accurately determined and since some neutral reagent flows are difficult to stabilize.

- 6) *The introduction of neutral reagents into the reaction flow tube is planar, uniform, and occurs with instantaneous mixing.* In our experimental design neutral reagents are introduced into the instrument from the edges of the flow tube. Introduction of neutral reagents is symmetric but not instantaneous nor uniform. In general several centimeters are required for complete mixing to occur. The seven radial inlets are designed to allow for efficient mixing. The effect of mixing is minimized since each inlet is identical and, therefore, changes in reaction distances are not affected.

3.8) Branching Ratio Determinations

The reaction of an ion with a neutral molecule may occur by multiple reaction pathways. In this case, the measured reaction rate constant is the sum of the reaction rate constants for each channel, $k_{\text{tot}} = k_1 + k_2$.



The product branching ratios (BR) are determined from the ratio of concentration of a given ionic product (C^- or E^-) to the total ionic products ($\text{C}^- + \text{E}^-$) or equivalently to

the ratio of the individual reaction rate constant to the total rate constant, as shown in eq 3.16a and 3.16b. The branching ratio is a measure of the fraction of A^- that reacts to form a given product.

$$BR_1 = \frac{[C^-]}{[C^-] + [E^-]} = \frac{k_1}{k_1 + k_2} \quad \text{and} \quad BR_2 = \frac{[E^-]}{[C^-] + [E^-]} = \frac{k_2}{k_1 + k_2} \quad (3.16a-b)$$

Branching ratios are experimentally determined by measuring the intensities of the product ions for introduction of the neutral reactant at each inlet. A branching ratio is determined at each inlet. A plot of branching ratio as a function of inlet distance is constructed; the actual branching ratio is determined by extrapolating to “zero reaction distance”, where there are no contributions from any secondary reactions. Figure 3.07 shows the product ion branching fractions for the two product channels for the reaction of $BrO^- + CD_3Cl$.

One major experimental complication in determining product branching is mass discrimination. Ideally, the sum of the product ion intensity plus the remaining reactant ion intensity should equal the initial reactant ion intensity. This, however, rarely occurs since different mass ions are detected with different efficiency. Mass discrimination is the result of differences in diffusion and transmission efficiency for different mass ions. In the reaction flow tube ions of different masses or different cross sections diffuse at different rates; typically heavier ions diffuse at a slower rate than lighter ions. Additionally, different mass ions are transmitted through the ion optics and quadrupole with different efficiencies; typically lighter ions are transmitted more efficiently. The mass biases from diffusion and from transmission are opposite to one another. However, under most experimental conditions some mass discrimination still exists and must be considered. Typically the relative detection sensitivity is estimated by examining a series of exothermic ion-molecule reactions

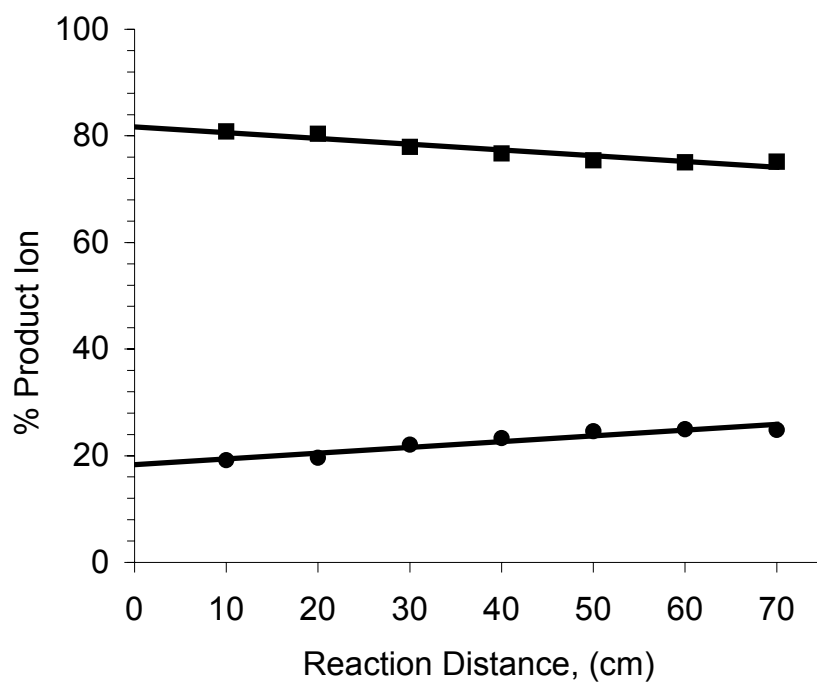


Figure 3.07: Sample branching ratio determination for the reaction $\text{BrO}^- + \text{CD}_3\text{Cl}$. Symbols: ■ Cl^- and • Br^- .

where only one ionic product is formed and the reactant and product ions are similar in mass to the ions of interest. In this method, a reactant ion is SIFT-injected into the reaction flow tube and allowed to react with a neutral reagent. The reactant and product ion intensities were measured and a correction factor is applied to the product ion so that the sum of the product and reactant ion intensities is equal to that of the initial reactant ion intensity.

3.9) Chapter 3 References

- (1) Ferguson, E. E.; Fehsenfeld, F. C.; Schmeltekopf, A. L. Flowing Afterglow Measurements of Ion-Neutral Reactions. In *Advances in Atomic and Molecular Physics*; Academic Press, Inc: New York, 1969; Vol. 5; pp 1-56.
- (2) Dunkin, D. B.; Fehsenfeld, F. C.; Schmeltekopf, A. L.; Ferguson, E. E. Ion-Molecule Reaction Studies from 300 to 600 K in a Temperature-Controlled Flowing Afterglow System. *Journal of Chemical Physics* **1968**, *49*, 1365-1371.
- (3) Hierl, P. M.; Friedman, J. F.; Miller, T. M.; Dotan, I.; Menendez-Barreto, M.; Seeley, J. V.; Williamson, J. S.; Dale, F.; Mundis, P. L.; Morris, R. A.; Paulson, J. F.; Viggiano, A. A. Flowing Afterglow Apparatus for the Study of Ion-Molecule Reactions at High Temperatures. *Review of Scientific Instruments* **1996**, *67*, 2142-2148.
- (4) McFarland, M.; Albritton, D. L.; Fehsenfeld, F. C.; Ferguson, E. E.; Schmeltekopf, A. L. Flow-Drift Technique for Ion Mobility and Ion-Molecule Reaction Rate Constant Measurements. I Apparatus and Mobility Measurements. *Journal of Chemical Physics* **1973**, *59*, 6610-6619.
- (5) Fehsenfeld, F. C.; Albritton, D. L.; Bush, Y. A.; Fournier, P. G.; Govers, T. R.; Fournier, J. Ion-Atom Interchange Reactions Using Isotopic-Species. *Journal of Chemical Physics* **1974**, *61*, 2150-2155.
- (6) Fehsenfeld, F. C. Ion Reactions with Atomic Oxygen and Atomic Nitrogen of Astrophysical Importance. *Astrophysical Journal* **1976**, *209*, 638-639.
- (7) Viggiano, A. A.; Howorka, F.; Albritton, D. L.; Fehsenfeld, F. C.; Adams, N. G.; Smith, D. Laboratory Studies of Some Ion-Atom Reactions Related to Interstellar Molecular Synthesis. *Astrophysical Journal* **1980**, *236*, 492-497.
- (8) Zhang, X.; Kato, S.; Bierbaum, V. M.; Nimlos, M. R.; Ellison, G. B. Use of a flowing afterglow SIFT apparatus to study the reactions of ions with organic radicals. *Journal of Physical Chemistry A* **2004**, *108*, 9733-9741.
- (9) Adams, N. G.; Smith, D. Selected Ion Flow Tube (SIFT) - Technique for Studying Ion-Neutral Reactions. *International Journal of Mass Spectrometry and Ion Processes* **1976**, *21*, 349-359.
- (10) Van Doren, J. M.; Barlow, S. E.; DePuy, C. H.; Bierbaum, V. M. The Tandem Flowing Afterglow-SIFT-DRIFT. *International Journal of Mass Spectrometry and Ion Processes* **1987**, *81*, 85-100.
- (11) Van Doren, J. M. Developments and Applications to Gas-Phase Ion Chemistry. Ph.D. Thesis, Department of Chemistry and Biochemistry, University of Colorado at Boulder, 1987.
- (12) Grabowski, J. J. Studies of Gas Phase Ion-Molecule Reactions using a Selected Ion Flow Tube. Ph.D. Thesis, Department of Chemistry and Biochemistry, University of Colorado at Boulder 1983.

- (13) Hankin, J. J. Gas-Phase Chemistry of Silicone and Boron Ions. Ph.D. Thesis, Department of Chemistry and Biochemistry, University of Colorado at Boulder 1995.
- (14) Dupeyrat, G.; Rowe, B. R.; Fahey, D. W.; Albritton, D. L. Diagnostic Studies of Venturi Inlets for Flow Reactors. *International Journal of Mass Spectrometry and Ion Processes* **1982**, *44*, 1-18.
- (15) Mackay, G. I.; Vlachos, G. D.; Bohme, D. K.; Schiff, H. I. Studies of Reactions Involving $C_2H_x^+$ Ions with HCN Using a Modified Selected Ion Flow Tube. *International Journal of Mass Spectrometry and Ion Physics* **1980**, *36*, 259-270.
- (16) Simon, J. Molecular Anions. *Journal of Physical Chemistry A* **2008**, *112*, 6401-6511.
- (17) Dushman, S.; Lafferty, J. M. Scientific Foundations of Vacuum Techniques; John Wiley and Sons: New York, 1962.
- (18) Tritton, D. J. Physical Fluid Dynamics; Van Nostrand Reinhold Company: New York, 1977.
- (19) Stock, H. M. P. Theory of Flowing Afterglow. *Journal of Physics B - Atomic Molecular and Optical Physics* **1973**, *6*, L86-L88.
- (20) Huggins, R. W.; Cahn, J. H. Metastable Measurements in Flowing Helium Afterglow. *Journal of Applied Physics* **1967**, *38*, 180-188.
- (21) Bolden, R. C.; Hemsworth, R. S.; Shaw, M. J.; Twiddy, N. D. Measurements of Thermal-Energy Ion-Neutral Reaction Rate Coefficients for Rare-Gas Ions. *Journal of Physics Part B - Atomic and Molecular Optical Physics* **1970**, *3*, 45-60.

CHAPTER IV

NEGATIVE ION FLOWING AFTERGLOW PHOTOELECTRON SPECTROMETER: INSTRUMENT DESCRIPTION

4.1) Introduction

Over the past forty years, photoelectron spectroscopy has provided valuable insight into the chemical physics of negative ions. Currently there are several different types of photoelectron spectrometers, each with their own advantages and disadvantages. In general, however, each one of these techniques involves the formation and mass selection an anion beam, which is then crossed with a photon beam; the resulting photoelectrons are collected and energy analyzed.

The negative ion flowing afterglow photoelectron spectrometer (NIPES) at JILA is pictorially shown in Figure 4.01 and schematically shown in Figure 4.02. In this instrument, ions are created in a flowing afterglow source and extracted and focused into a Wien velocity filter. The mass selected ion beam is refocused and decelerated into an interaction region, where the ion beam is crossed with the 351 nm line of a cw Ar-ion laser in an external buildup cavity. Photoelectrons that are ejected perpendicular to the ion and photon beams are collected, energy analyzed by a hemispherical kinetic energy analyzer, and imaged onto a position sensitive detector. Photoelectron spectra are obtained by measuring photoelectron counts as a function of electron kinetic energy (eKE); the energy scale can be converted to electron binding energy (eBE) by subtracting the eKE from the photon energy. An overview of this technique is discussed in six sections below: flowing afterglow ion source, ion optics and mass selection, ultraviolet laser system, photoelectron kinetic energy analyzer, data acquisition and analysis, and Franck-



Figure 4.01: Photograph of the JILA Negative Ion Flowing Afterglow Photoelectron Spectrometer.

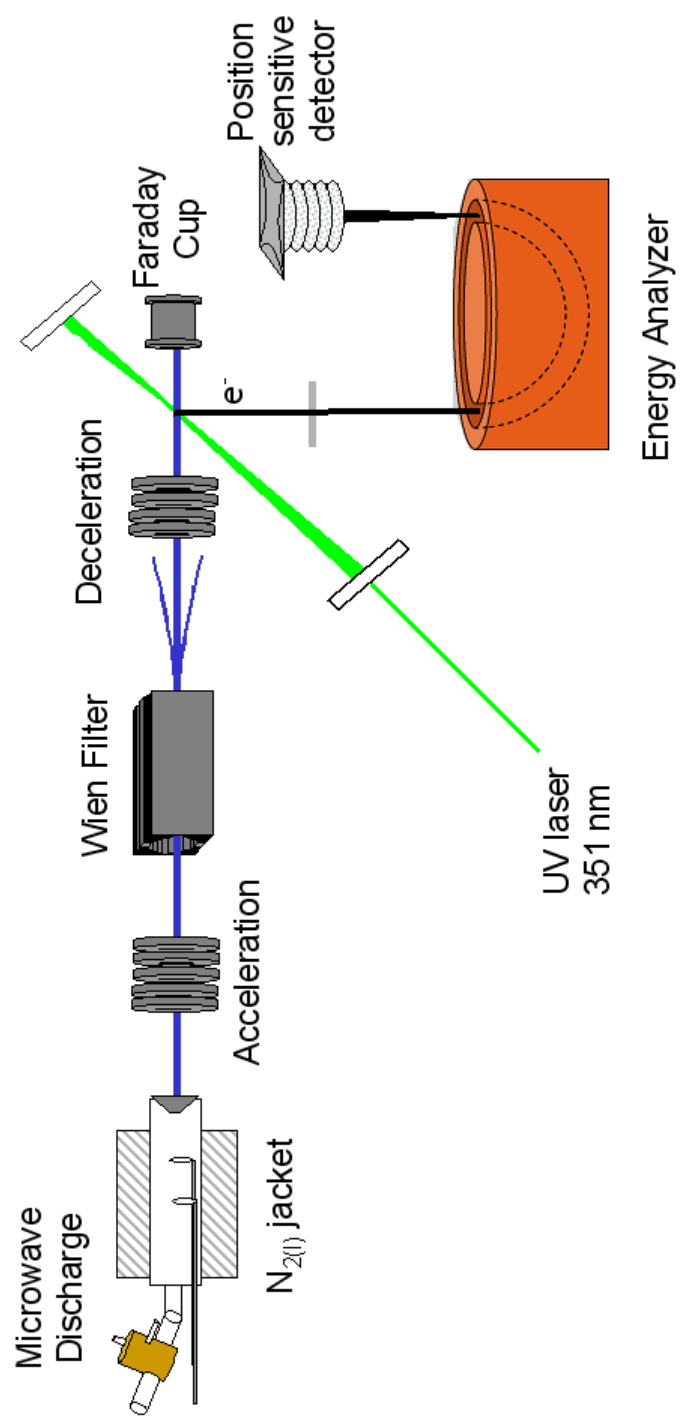


Figure 4.02: Schematic representation of the JILA Negative Ion Flowing Afterglow Photoelectron Spectrometer.

Condon simulations. A more detailed discussion of this instrument is provided in several other sources.¹⁻⁴

4.2) Flowing Afterglow Ion Source

The flowing afterglow source is very similar to the flowing afterglow source in the FA-SIFT instrument described in Chapter 3. Because these sources are so similar, these techniques can provide complementary information to one another; the union of these techniques is discussed in Chapter 1. Despite the similarities, the two sources are not identical and these differences must be kept in mind when comparing data between the two instruments.

The NIPES instrument flowing afterglow source is shown in Figure 4.03. The work presented in this thesis utilizes a microwave discharge to initiate ionization. Other types of sources such as a heated filament and a metal cathode discharge have previously been used; however, since these sources were not utilized they are not discussed here. The microwave discharge source consists of an Evenson-type brass cavity⁵ and a one-inch diameter quartz tube. Helium gas, which has been purified by passage through a molecular sieve trap immersed in liquid nitrogen, is passed through the microwave discharge source at a rate of ~7-10 standard liters per minute (maintained by a Tylan flow controller). The plasma is ignited by a spark from a Tesla coil, which ionizes He to produce free electrons. These free electrons absorb the 2.45 GHz microwave radiation at ~10-100 W of input power (provided by an Opthos MPG 4 microwave power generator) to maintain the plasma.⁵

The properties of the NIPES source plasma are similar to the FA-SIFT source plasma and, therefore, a detailed discussion is not provided. The discharge contains free electrons, He 2³S and 2¹S metastable species, He⁺, and He₂⁺.^{6,7} Since the plasma contains equal amounts of negatively and positively charged species, high ion densities (~10⁸ ions cm⁻³) are achieved due to shielding effects and the diffusion

is ambipolar. Trace amounts of neutral gases are either passed through or introduced directly downstream of the discharge source. Oxygen anion is the most commonly produced ion since it can be formed in high densities and it displays diverse ion chemistry that can be utilized to synthesize other target ions; moreover since its electron binding energy is well-known,⁸ it is often therefore used to calibrate the energy scale. Oxygen anion is produced from dissociative electron attachment (eq 4.01a) by introducing a controlled flow of O₂ gas (7-10 cm³ per minute) through the discharge. Further downstream in the source flow tube, other precursor gases can be introduced to synthesize a target anion. For example, hydroxide is produced from an H atom abstraction reaction (eq 4.01b) by introducing methane into the source downstream of the ion production region.



The flowing afterglow source allows for a variety of ions to be produced, from a wide range of ion-molecule reactions, some of which were outlined in Chapter 3. The flow tube is constructed from multiple segments of 4.8 cm inner diameter stainless steel so that its length can be changed from 25 – 100 cm. Additionally, two movable inlets make it possible to introduce neutral precursor gases at various distances along the source flow tube.

The ions undergo multiple collisions ($\sim 10^6$ collisions s⁻¹) with the He buffer gas (~ 0.5 torr, 3-10 ms residence time). As a result the ions are vibrationally and rotationally cooled to approximately room temperature. Vibrational and rotational cooling is important, since anion hot bands can significantly congest and complicate the resulting photoelectron spectrum. Surrounding the source flow tube with a liquid

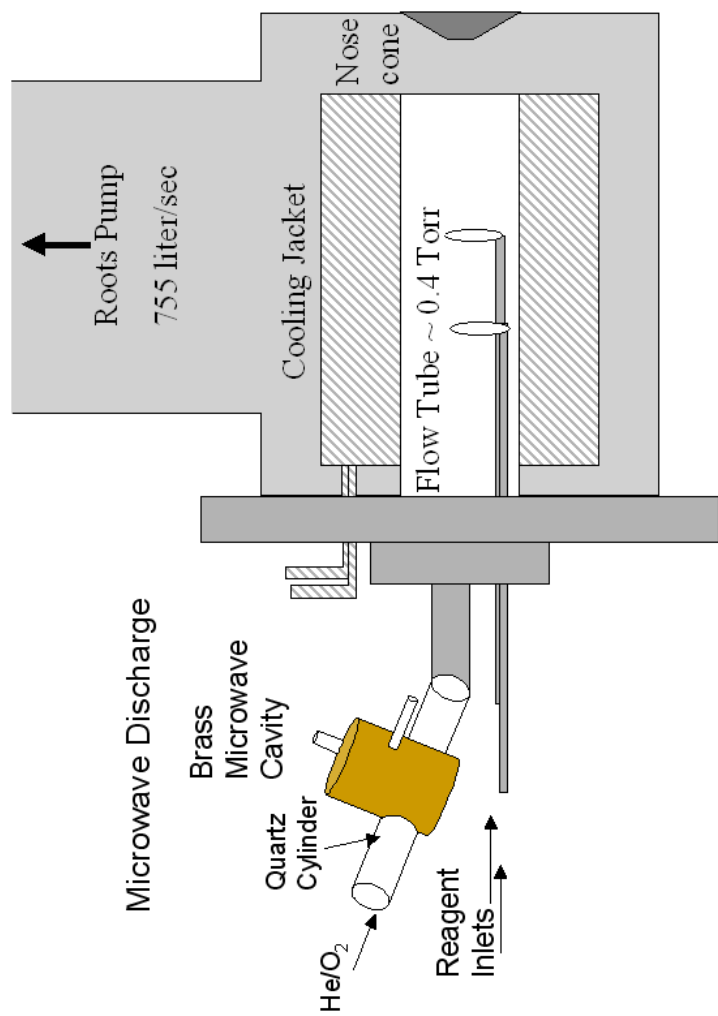


Figure 4.03: Schematic representation of the flowing afterglow source.
Figure from Dr. Adam J. Gianola.

nitrogen jacket can further cool the ions. Prior experience with this arrangement suggests that the resulting ions are prepared in the 150-200 K range;⁹ typically ion densities in the source are also reduced. Comparison of photoelectron spectra collected both at room temperature and under liquid nitrogen conditions can help identify anion hot bands and aid in the assignment of the origin peak. The He buffer gas and any neutral precursor gases are pumped away by a high capacity Stokes roots blow pump (755 L s^{-1}) while anions are extracted from the source region into the first differentially pumped region through a molybdenum nose cone with a 1 mm diameter orifice.

4.3) Ion Optics and Mass Selection

It is important to gently extract the anions from the source region. The nose cone is held at a small positive voltage ($<+3 \text{ V}$). The first differentially pumped region is maintained at a pressure of $\sim 10^{-4}$ torr by a 6-inch diffusion pump (805 L s^{-1}). At these pressures an ion still may collide with a neutral background molecule; if the ion is accelerated with too much energy it can be excited through ion-molecule collisions.¹⁰ The ion beam is focused and gradually accelerated through a series of ion optics, which are referred to as the afterglow lenses (L1-L6, shown in Figure 4.04). The voltage of the first four lenses (L1-L4) can be independently adjusted to tune the ion beam. The first and second deflectors (D1 and D2) electrostatically move the ion beam both vertically and horizontally; however, they float on the L3 and L4 voltages, respectively. The voltages of L5 and L6 are held at fixed potentials of 500 and 735 V, respectively. Lenses 1-3 and the first set of deflectors are mounted on one assembly, while Lenses 4-6 and the second set of deflectors are on a separate assembly mounted behind an aperture plate (A1).

After L6, the ion beam is steered around a 10° bend by a third set of deflectors (D3) into the second differentially pumped region, maintained at a

pressure of $\sim 10^{-6}$ Torr by a 8-inch diffusion pump (2000 L s^{-1}); at this point any neutral species or photons from the source region collide with the walls of the instrument. The ion beam, now traveling at 735 V, is focused by a three-element quadrupole Einzel lens (Q1).¹¹ After Q1 the ion beam passes through a second aperture (A2), where an electrometer measures the ion current (typical currents are 0.5-6 pA), and a fourth set of deflectors (D4). After D4 there is a gate valve, which separates the front half of the instrument from the back half of the instrument; this allows the back half of the instrument to remain under vacuum when the instrument is not in operation and when performing routine maintenance and cleaning in the source region. Following this gate valve there is a second three-element quadrupole Einzel lens, which focuses the ion beam into a Wien velocity filter.

Up to this point, the ion beam is composed several different anions. A Wien filter serves to select a narrow window of mass-to-charge ratio anions. A Wien filter is composed of perpendicular electric and magnetic fields (E and B) that are also perpendicular to the incoming ion beam (z-axis). The forces (F) that result from the electric field ($F_E = qE$) and from the magnetic field ($F_B = qv \times B$) are opposite to one another; the net result is the deflection of the ion along the y-axis, where q is the particle charge and v is the velocity of the ion. An ion will pass through the Wien filter only if the forces from the electric and the magnetic fields are equal and opposite to each other, $F_E = -F_B$. Kinetic energy (KE) is related to the velocity and mass of an ion ($KE = \frac{1}{2}mv^2$), therefore ions of a different mass (hence velocity) require a different set of forces to pass through the filter. Ions that are too heavy or too light will be deflected into the walls of the instrument. Different mass ions are allowed to pass through the filter either by holding the electric field constant and scanning the magnetic field or vice versa.

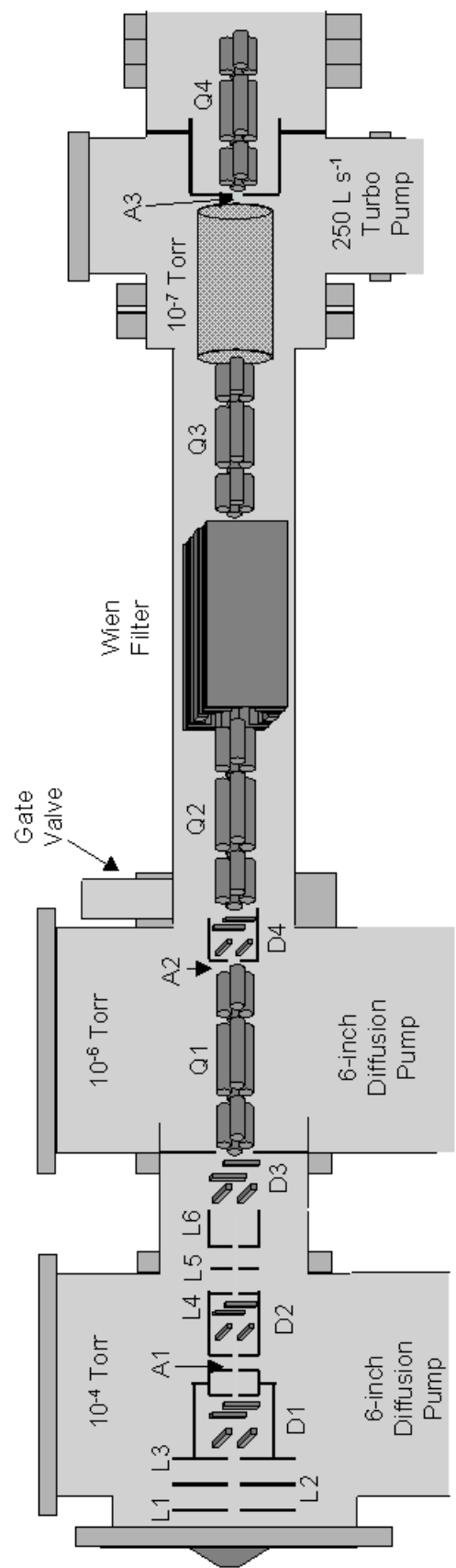


Figure 4.04: Schematic representation of the ion optics and Wien filter. Figure from Dr. Adam J. Gianola.

The magnetic field is established by a water-cooled electromagnet powered by a Kepco regulated DC voltage supply. The electric field is produced by applying equal but opposite polarity voltages (along the y-axis) on a series of ten electrically-isolated stainless steel shims. The voltage on each shim is symmetrically stepped up (along the x-axis) so that the outer shims are at the lowest voltage and the inner shims are at the highest voltage; this arrangement minimizes the fringe fields at the entrance and exit of the Wien filter. The electric field is supplied by a voltage divider circuit powered by a 0-40 mA / 0-5000 V Kepco power supply. The Wien filter resolution ($m/\Delta m$) is approximately 40; therefore, as the mass scale is increased, ions that differ by 1-2 amu cannot be resolved from one another. Despite having poor resolution at higher masses, use of a Wien filter is advantageous because of its high ion transmission. The Wien filter sits in a common assembly with Q2 and Q3; the pressure is maintained at 10^{-7} torr by a Varian turbomolecular pump (250 L s^{-1}).

Following mass selection, the ion beam passes through several more ion optics. First is another three-element quadrupole Einzel lens (Q3), which focuses the ion beam through a short field-free region and a third aperture (A3). The ion beam then passes through the fourth and last three-element quadrupole Einzel lens (Q4), which focuses the ions into a deceleration lens stack (DL1-4). The deceleration stack is composed of four lenses, which gradually slow the ions to 35 V and focus the ion beam into an ion-photon interaction region. A faraday cup collects the ions that pass through the interaction region. The current is measured by a second electrometer; typical ion currents range from 10-2000 pA. The pressure in the interaction region is maintained at 10^{-8} torr by a Varian turbomolecular pump (280 L s^{-1}).

4.4) Ultraviolet Laser System

The ion beam is perpendicularly crossed with either the 351.1 or the 363.8 nm line of a Spectra Physics cw argon-ion laser coupled to an external build-up cavity producing ~100 W of circulating power; a diagram of this setup is provided in Figure 4.05. A detailed description of the optical build-up cavity is provided elsewhere.¹² Additionally, during the fall of 2007, the Ar-ion laser was replaced with a newer model and some minor modifications were made to the optics table. These changes do not change the fundamental operation of the laser or optical build-up cavity; they are outlined in the thesis of Mr. Scott W. Wren.

The Ar-ion laser is composed of a plasma tube, a broadband high reflector back mirror, an output coupler (either 351.1 nm or 363.8 nm), and an etalon. The plasma tube is filled with argon gas; an electric discharge doubly ionizes the argon atoms. The distance between the broadband high reflector back mirror and the front output coupler define the length (L_A) of the resonant optical cavity. These two mirrors select a single Doppler broadened lasing transition of Ar^{2+} and provide feedback to the Ar medium. Only standing waves (or longitudinal modes) of $\nu_n = nc/2L_A$, where ν_n is a frequency, n is an integer, c is the speed of light, and L_A is the cavity length, will oscillate within the cavity. An etalon selects one of these longitudinal modes (ν). Output powers of ~1 W are typically obtained.

The output of the laser is a single monochromatic beam that is vertically polarized. Several mirrors (M) and optical components direct the laser beam into an external build-up cavity.¹² M1 and M2 adjust the beam to the height of the optical table and additionally rotate the laser polarization by 90°. The laser is directed to the back of the optics table by M3 where it hits a partial reflector, M4. From M4, the beam passes through a telescope lens, and an acoustical-optical modulator (AOM).

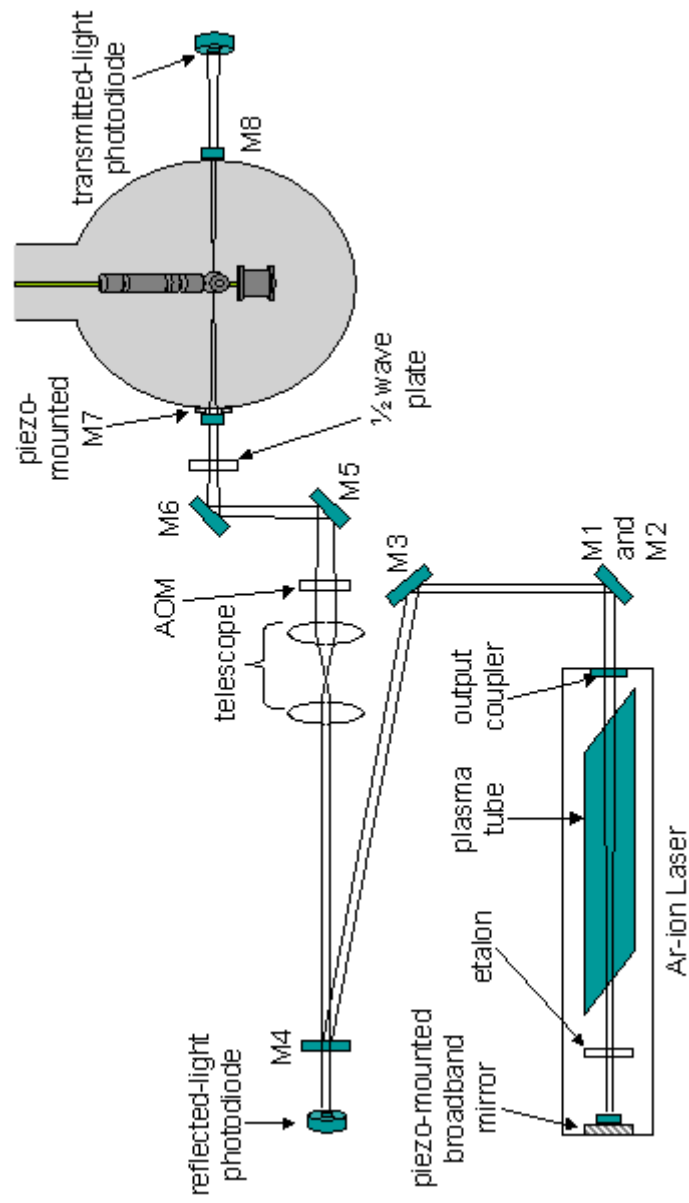


Figure 4.05: Schematic of Ar-ion laser system and external buildup cavity. Figure from Dr. Adam J. Gianola.

The telescope lens serves to minimize the wave front curvature of the beam entering the build-up cavity; the purpose of the AOM will be discussed shortly. Prior to entering the build-up cavity through M7, the light is reflected off two additional steering mirrors, M5 and M6, and passed through a half-wave plate, which allows the beam polarization to be rotated. A small portion of light reflects off M7 back through the AOM and telescope lens onto M4. A fraction of this reflected light passes through M4 into a reflected-light photodiode. The external build-up cavity is composed of two highly reflective curved mirrors (M7 = 99.6% and M8 = 99.8%) mounted on either side of the vacuum chamber; a transmitted light photodiode is positioned after M7. The external cavity operates on the same principle as the Ar-ion laser cavity. For build-up to occur, the length of the external cavity (defined by the distance between M7 and M8) must match the laser wavelength, $L_E = nc/2v$. However, since the length of the cavity is affected by a variety of external sources such as acoustic noise, air current, and temperature fluctuations, active steps must be taken to maintain this condition.

An electronic servo amplifier system is employed to actively match the external build-up cavity length and the laser wavelength.¹² To accomplish this, both the laser cavity back mirror and the external build-up cavity front mirror are mounted on a stack of piezoelectric transducers and an AOM is placed in the beam path. An AOM is composed of a transducer that is connected to a quartz crystal. A voltage applied to the crystal vibrates it back and forth, producing a standing wave, which acts like a Bragg's diffraction grating. The light passing through the crystal is shifted by an amount equal to the acoustical frequency of the glass. The first order diffraction is shifted by ~55 MHz; this serves to frequency isolate the two cavities so that any reflected light from the build-up cavity will not return to the laser cavity and interfere. Additionally, a small 1 MHz frequency dither is placed on top of the ~55

MHz shift; this dither varies the frequency around the resonance frequency producing an error function. When the two cavities are off resonance, the intensity of light reflected from M7 increases. The servo system electronics monitor the RF signal from the reflected light photodiode and respond by either changing the length of the laser cavity, changing the length of the build-up cavity, or by varying the frequency of the AOM shift to regain the resonance condition. The piezo-mounted external build-up cavity mirror corrects for noise at 0-100 Hz, the piezo-mounted laser cavity mirror corrects for noise at 0.1-10 kHz, while the AOM frequency shift corrects for noise that is greater than 5 kHz. When resonance is achieved the laser power is increased by a factor of 100.

4.5) Photoelectron Kinetic Energy Analyzer

Figure 4.06 schematically depicts the ion-photon interaction region, the analyzer entrance and exit lenses, the hemispherical analyzer, and the position sensitive detector.³ Photoelectrons are ejected over 4π steradians; however, only the photoelectrons that are ejected perpendicular (along the y-axis) into a 5° half-angle acceptance cone are energy analyzed. Prior to entering the hemispherical analyzer the photoelectrons are passed through a series of lenses (V1-3 and V_{HC}). Lenses 1 and 2 serve to accelerate the electrons by a factor of 5-10 times their initial kinetic energy. Acceleration is necessary since the kinetic energy of the ejected photoelectrons is between 0-3.5 eV, while the transmission energy (TE) of the hemispherical analyzer is 4 eV. Lens 3 serves to focus the photoelectrons to the center of the hemispherical analyzer entrance, while V_{HC} (Herzog corrector voltage) compensates for fringe fields, which are present at the entrance of the analyzer. The hemispherical analyzer is composed of an inner and an outer hemisphere, which are made of OFHC copper. The transmission energy of the analyzer is defined by

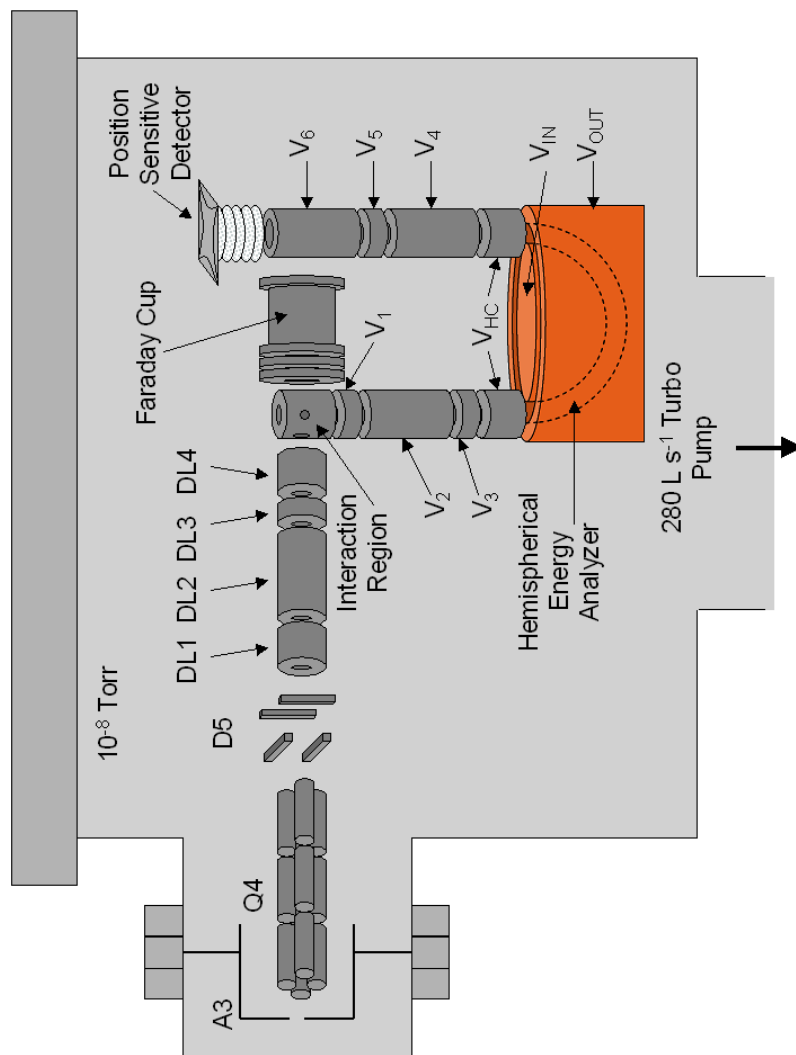


Figure 4.06: Schematic representation of ion-photon interaction region and of the electron kinetic energy analyzer. Figure from Dr. Adam J. Gianola.

the difference in voltage between the inner and outer hemispheres. Only electrons that are at $4 \text{ eV} \pm 2 \%$ will pass through the analyzer. Photoelectrons with energy lower than the transmission window will collide with the inner hemisphere, while those with energy higher than the transmission window will collide with the outer hemisphere. The photoelectron energy scale (0-3.5 eV) is scanned by sweeping the acceleration voltages on the entrance lens stack.

After passing through the analyzer, the photoelectrons pass through an exit lens stack prior to impacting a position sensitive detector. Lens 4 (V4) compensates for fringe fields at the exit of the analyzer. Lenses 4-6 (V4-6) accelerate the photoelectrons to 300 eV for efficient detection and to magnify their image so that the entire area of the detector is utilized. The detector is composed of a stack of five microchannel plates coupled to a resistive anode encoder (Quantar Technology 3318A). Each microchannel plate has 10^6 channels per plate. The five microchannel plates are connected through a series of resistors so that each plate is held at a successively higher voltage; the last plate is held at $\sim 3400 \text{ V}$. For every one electron that impinges upon this detector, a gain of $\sim 10^7$ electrons is obtained. The resistive anode is a curved rectangular shaped plate with a circular effective detection area. Each corner of the plate (A,B,C, and D) is electrically connected to a position sensitive analyzer (Quantar 2401B). When an electron cloud hits the detector, a current is measured at each of the four detector corners; the detector registers each electron cloud as a single event. The x-y position of the electron is determined from eq 4.02a and 4.02b.

$$x = \frac{B + C}{A + B + C + D} \quad \text{and} \quad y = \frac{A + B}{A + B + C + D} \quad (4.02a-b)$$

Here the y-axis represents photoelectron counts per second and the x-axis represents kinetic energy. The resolution of the detector is 5 meV; however, the

limiting resolution of the instrument (typically 7-15 meV) is determined by the size of the ion-photon interaction region and its position relative to photoelectron extraction.

4.6) Data Acquisition and Analysis

The position sensitive analyzer outputs digitized pulses of x-y coordinates; the x-position indicates electron kinetic energy, while the y-position indicates the number of counts for a given electron kinetic energy. This signal is sent to an oscilloscope for real-time observation of the electron flux, and a 2412 B Histogram Memory Card (HMC) coupled to a PC.¹³ The HMC alternates between data collection and data writing (to the PC). The HMC has 12 bits, 8 bits for the x-axis and 4 bits for the y axis; thus the detector area is divided into $2^8=256$ channels along the x-axis and $2^4=16$ channels along the y-direction. Electrons hit the detector and the number of events per channel is counted. After a given accumulation time the HMC outputs this information to the computer. A LabView program (PESDAT) controls the data collection process. Data are sampled over the entire energy range in small overlapping segments, which are defined by their center eKE. The PESDAT program sends the center eKE value and the corresponding V3 voltage of the first segment to a voltage controller (JILA LC036), which sets the analyzer input lens stack voltages. Electrons are collected for 0.5 seconds; after this time the data are sent from the HMC to the computer. This collection process is repeated for each segment over the course of multiple scans. A more detailed description of the data acquisition components is given in reference 13.

In order to convert the data file into counts versus electron kinetic energy, a separate calibration spectrum is collected. The absolute energy scale is calibrated by measuring the photoelectron spectrum of an atomic species with a well-known electron affinity (typically oxygen atom¹⁴⁻¹⁶). This spectrum additionally provides the magnification (i.e., the energy width of each detector channel, meV/channel) of the

energy scale. Since the energy scale is not linear, a small compression factor ($\gamma < 1\%$) is measured (typically from the term energies of tungsten¹⁴). Lastly, since the ions are traveling at 35 V through the interaction region, eq 4.03 converts the electron kinetic energies, which are measured in the lab frame, to the center-of-mass frame of the ion.

$$eKE = h\nu - \left[EA_{\text{ref}} + \gamma (eKE_{\text{ref}} - eKE_{\text{lab}}) + W_{\text{ion}} M_e \left(\frac{1}{M_{\text{ref}}} + \frac{1}{M} \right) \right] \quad (4.03)$$

Here $h\nu$ is the photon energy, EA_{ref} is the calibration ion electron affinity, W_{ion} is the ion beam kinetic energy, γ is the electron kinetic energy scale compression factor, eKE_{ref} is the measured electron kinetic energy of the calibration ion origin peak in the lab frame, eKE_{lab} is the measured electron kinetic energy of the molecule of interest in the lab frame, M_{ref} is the mass of the calibration ion, M_e is the mass of an electron and M is the mass of the molecule under investigation.

Each resolvable transition in the spectrum is fit with a Gaussian curve to find the center of the peak. Since photoelectron spectroscopy cannot typically resolve rotational transitions, the measured electron band origins (EA_{exp}) are rotationally uncertain and must be corrected (EA_{cor}).

$$EA_{\text{cor}} = EA_{\text{exp}} + E_{\text{rot}}(J'') + E_{\text{rot}}(J') = EA_{\text{exp}} + \Delta_{\text{rot}} \quad (4.04)$$

In eq 4.04, $E_{\text{rot}}(J'')$ and $E_{\text{rot}}(J')$ are the mean rotational energies of the anion and neutral, respectively. The difference in rotational energies (Δ_{rot}) for an asymmetric rotor can be approximated by eq 4.05, where A , B , and C are rotational constants for the anion and neutral molecule.¹⁷ The single prime denotes the anion and the double prime denotes the neutral species. These rotational constants are either measured by a separate experimental technique or estimated from electronic structure calculations. A typical rotational correction is < 0.005 eV.

$$\Delta_{\text{rot}} = k_{\text{B}}T \left(\frac{A'}{2A''} + \frac{B'}{2B''} + \frac{C'}{2C''} - \frac{3}{2} \right) + \left(\frac{B'' - B'}{3} \right) \quad (4.05)$$

The error associated with electronic band origin measurements is the sum of the rotational correction, the energy scale compression factor, and the error associated with fitting the data with a Gaussian function. The error associated with a vibrational band is the sum of the error for the electronic band origin and the error associated with fitting the vibrational band with a Gaussian function. Statistical errors can be assessed by collecting multiple spectra; an error bar is assigned from the standard deviation of multiple measurements of the peak positions. In general, the statistical error is larger and, therefore, this value is typically reported.

4.7) Franck-Condon Simulation

Electronic structure calculations and spectral simulations are performed to aid in the interpretation of the photoelectron spectra. Optimized geometries and harmonic vibrational frequencies for the neutral parent, anion, and radical are determined from either density functional or *ab initio* calculations using the Gaussian 03 suite of programs.¹⁸ Electronic structure calculations can predict the electron affinity and identify which normal modes will be active in the spectrum. For more complicated systems, calculations can predict the lowest energy isomer and possible excited states.

Spectral simulations are performed by calculating the Franck-Condon (FC) factors using the PESCAL program,^{19,20} using the calculated geometries, normal modes, and electron binding energies for the anion and neutral species. A separate Fortran program (FCFGAUS)²¹ extracts the necessary information from the Gaussian 03 output files for the anion and neutral species. FCFGAUS outputs the Duschinsky rotation matrices, normal mode displacement vectors, geometries, and normal mode frequencies in a usable format for the PESCAL program. The PESCAL program

calculates the Franck-Condon (FC) factors by assuming that each normal mode is an independent harmonic oscillator and by transforming the normal modes of the anion into linear combinations of the normal modes of neutral species.^{19,22-25} The resulting stick spectra can be convoluted with a 7-15 meV fwhm Gaussian function, which represents the instrument resolution. For most systems that are free of nonadiabatic effects, the PESCAL program provides excellent reproduction of the experimental spectra.

4.8) Chapter 4 References

- (1) Leopold, D. G.; Murray, K. K.; Lineberger, W. C. Laser Photoelectron-Spectroscopy of Vibrationally Relaxed CH_2^- - A Reinvestigation of the Singlet Triplet Splitting in Methylene. *Journal of Chemical Physics* **1984**, *81*, 1048-1050.
- (2) Leopold, D. G.; Murray, K. K.; Miller, A. E. S.; Lineberger, W. C. Methylene: A Study of the X^3B_1 and a^1A_1 States by Photoelectron-Spectroscopy of CH_2^- and CD_2^- . *Journal of Chemical Physics* **1985**, *83*, 4849-4865.
- (3) Feigerle, C. S. Laser Photoelectron Spectroscopy Studies of Transition Metal Negative Ions. Ph.D. Thesis, Department of Chemical Physics, University of Colorado at Boulder, 1983.
- (4) Ervin, K. M.; Lineberger, W. C. Photoelectron Spectroscopy of Negative Ions. In *Advances in Gas-Phase Ion Chemistry*; N. G. Adams and L. M. Babcock, Eds. Greenwich, 1992; pp 121-166.
- (5) Fehsenfeld, F. C.; Evenson, K. M.; Broida, H. P. Microwave Discharge Cavities Operating at 2450 MHz. *Review of Scientific Instruments* **1965**, *36*, 294-298.
- (6) Fehsenfeld, F. C.; Schmeltekopf, A. L.; Goldan, H. I.; Schiff, H. I.; Ferguson, E. E. Thermal Energy Ion - Neutral Reaction Rates. I. Some Reactions of Helium Ions. *Journal of Chemical Physics* **1966**, *44*, 4087-4094.
- (7) Schmeltekopf, A. L.; Fehsenfeld, F. C. De-excitation Rate Constants for Helium Metastable Atoms with Several Atoms and Molecules. *Journal of Chemical Physics* **1970**, *53*, 3173-3177.
- (8) Neumark, D. M.; Lykke, K. R.; Andersen, T.; Lineberger, W. C. Laser Photodetachment Measurement of the Electron-Affinity of Atomic Oxygen. *Physical Review A* **1985**, *32*, 1890-1892.
- (9) Wenthold, P. G.; Polak, M. L.; Lineberger, W. C. Photoelectron Spectroscopy of the Allyl and 2-Methylallyl Anions. *Journal of Physical Chemistry* **1996**, *100*, 6920-6926.
- (10) Duncan, M. A.; Bierbaum, V. M.; Ellison, G. B.; Leone, S. R. Laser-Induced Fluorescence Studies of Ion Collisional Excitation in a Drift Field: Rotational Excitation of N_2^+ in Helium. *Journal of Chemical Physics* **1983**, *79*, 5448-5456.
- (11) Marynowski, M.; Franzen, W.; Elbatouny, M. Analysis of the Properties of an Electrostatic Triplet Quadrupole Lens Used as an Electron-Beam Transport Device. *Review of Scientific Instruments* **1994**, *65*, 3718-3723.
- (12) Ho, J. Negative Ion Laser Photoelectron Spectroscopy of Mass Selected Small Metal Clusters. Ph.D. Thesis, Department of Physics, University of Colorado at Boulder, 2001.

- (13) Ramond, T. Negative Ion Photoelectron Spectroscopy of Alkyl Peroxides, Alkoxides, and Group VIII Transition Metal Oxides. Ph.D. Thesis, Department of Physics, University of Colorado at Boulder, 2001.
- (14) Moore, C. E. Atomic Energy Levels. NSRDS-NBS; Washington: US GPO Circular No. 467, 1952.
- (15) Ervin, K. M.; Anusiewicz, I.; Skurski, P.; Simon, J.; Lineberger, W. C. The Only Stable State of O_2^- is the $X^2\Pi_g$ Ground State and It (Still!) Has an Adiabatic Electron Detachment Energy of 0.45 eV. *Journal of Physical Chemistry A* **2003**, *107*, 8521-8529.
- (16) Neumark, D. M. Laser Photodetachment Measurement of the Electron-Affinity of Atomic Oxygen. *Physical Review A* **1985**, *32*, 1890-1892.
- (17) Engelking, P. C. Approximate Rotational Band Shifts. *Journal of Physical Chemistry* **1986**, *90*, 4544-4545.
- (18) Frisch, M. J.; Trucks, G. W.; Schlegel, H. B.; Scuseria, G. E.; Robb, M. A.; Cheeseman, J. R.; Montgomery, J. A.; Vreven, T.; Kudin, K. N.; Burant, J. C.; Millam, J. M.; Iyengar, S. S.; Tomasi, J.; Barone, V.; Mennucci, B.; Cossi, M.; Scalmani, G.; Rega, N.; Petersson, G. A.; Nakatsuji, H.; Hada, M.; Ehara, M.; Toyota, K.; Fukuda, R.; Hasegawa, J.; Ishida, M.; Nakajima, T.; Honda, Y.; Kitao, O.; Nakai, H.; Klene, M.; Li, X.; Knox, J. E.; Hratchian, H. P.; Cross, J. B.; Adamo, C.; Jaramillo, J.; Gomperts, R.; Stratmann, R. E.; Yazyev, O.; Austin, A. J.; Cammi, R.; Pomelli, C.; Ochterski, J. W.; Ayala, P. Y.; Morokuma, K.; Voth, G. A.; Salvador, P.; Dannenberg, J. J.; Zakrzewski, V. G.; Dapprich, S.; Daniels, A. D.; Strain, M. C.; Farkas, O.; Malick, D. K.; Rabuck, A. D.; Raghavachari, K.; Foresman, J. B.; Ortiz, J. V.; Cui, Q.; Baboul, A. G.; Clifford, S.; Cioslowski, J.; Stefanov, B. B.; Liu, G.; Liashenko, A.; Piskorz, P.; Komaromi, I.; Martin, R. L.; Fox, D. J.; Keith, T.; Al-Laham, M. A.; Peng, C. Y.; Nanayakkara, A.; Challacombe, M.; Gill, P. M. W.; Johnson, B.; Chen, W.; Wong, M. W.; Gonzalez, C.; Pople, J. A. Gaussian 03, revision B.05; I. Gaussian, Ed. Pittsburgh, PA, 2003.
- (19) Ervin, K. M.; Ramond, T. M.; Davico, G. E.; Schwartz, R. L.; Casey, S. M.; Lineberger, W. C. Naphthyl radical: Negative Ion Photoelectron Spectroscopy, Franck-Condon Simulation, and Thermochemistry. *Journal of Physical Chemistry A* **2001**, *105*, 10822-10831.
- (20) Ervin, K. M. PESCAL, Fortran program; University of Nevada, Reno, 2008.
- (21) Ervin, K. M. FCFGAUS, Fortran program; University of Nevada, Reno, 2003.
- (22) Chen, P. Photoelectron Spectroscopy of Reactive Intermediates. In *Unimolecular and Bimolecular Reaction Dynamics*; C. Y. Ng, T. Baer and I. Powis, Eds.; John Wiley and Sons: New York, 1994; pp 371-425.

(23) Ozkan, I. Franck-Condon Principle for Polyatomic-Molecules - Axis-Switching Effects and Transformation of Normal Coordinates. *Journal of Molecular Spectroscopy* **1990**, *139*, 147-162.

(24) Botter, R.; Dibeler, V. H.; Walker, J. A.; Rosenstock, H. M. Experimental and Theoretical Studies of Photoionization-Efficiency Curves for C₂H₂ and C₂D₂. *Journal of Chemical Physics* **1966**, *44*, 1298-1299.

(25) Sharp, T. E.; Rosenstock, H. M. Franck-Condon Factors for Polyatomic Molecules. *Journal of Chemical Physics* **1964**, *41*, 3453-3463.

CHAPTER V

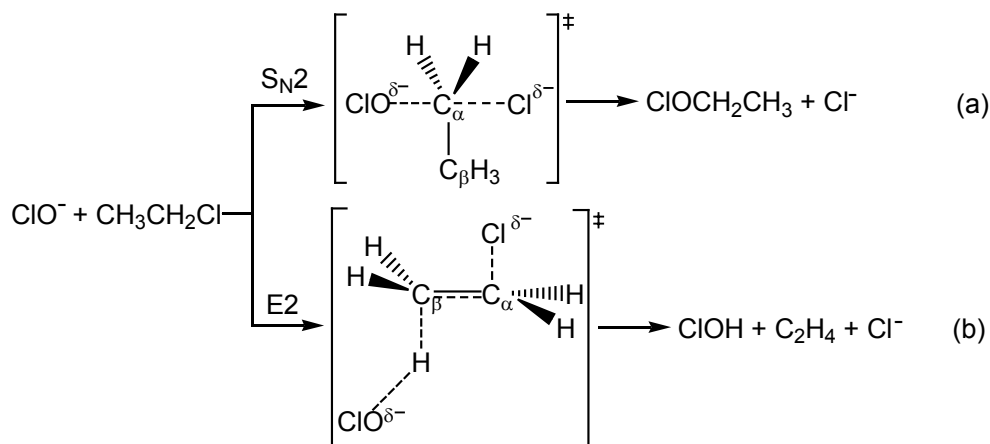
REACTIONS OF BrO^- AND ClO^- WITH ALKYL CHLORIDES: THE COMPETITION BETWEEN $\text{S}_{\text{N}}2$ AND $\text{E}2$ MECHANISMS AND THE GAS-PHASE α -EFFECT

5.1) Introduction

Gas-phase ion-molecule studies provide a route to understanding the intrinsic factors that affect a reaction in an environment free from solvent effects. These studies, therefore, provide important insight into the role of the solvent in a given reaction. Several notable differences between the intrinsic gas-phase reactivity and the reactivity in solution have been observed.¹⁻⁴ This work focuses on two areas where solvent effects are important: 1) the competition between nucleophilic substitution ($\text{S}_{\text{N}}2$) and base-induced elimination ($\text{E}2$) and 2) the α -effect or enhanced reactivity due to a lone pair of electrons adjacent to the nucleophilic center.

It has been shown theoretically that the reaction of ClO^- with ethyl chloride proceeds by both an $\text{S}_{\text{N}}2$ and an $\text{E}2$ reaction,⁵ as shown in Scheme 5.01.

Scheme 5.01:



In the $\text{S}_{\text{N}}2$ pathway (a), ClO^- attacks the α -carbon of ethyl chloride, displacing Cl^- . Since the attack by the nucleophile occurs from the opposite direction of the leaving group, the transition state is characterized by an sp^2 -like hybridized

α -carbon, where there is simultaneous formation of the C_{α} -OCl bond and breaking of the C_{α} -Cl bond; the two α -hydrogen atoms lie approximately in the same plane as the β -carbon. As the reaction proceeds the substituents around the α -carbon are inverted. In the E2 pathway (b), ClO^{-} abstracts a proton from the β -carbon of ethyl chloride, forming a double bond, and simultaneously displacing Cl^{-} . In the transition state the two leaving groups are coplanar, with the lower energy antiperiplanar transition state structure being highly favored over the synperiplanar transition state structure.

Since these two mechanisms generate the same ionic product and since the detection of the distinct neutral products presents serious analytical challenges, gas-phase experiments that address this competition are severely limited.⁶⁻¹⁸ One distinguishing difference, however, is that S_N2 mechanisms generally display inverse deuterium kinetic isotope effects ($KIE < 1$), while E2 mechanisms display normal deuterium kinetic isotope effects ($KIE > 1$).^{10,19,20} Deuterium kinetic isotope effects are defined as the ratio of perprotio to perdeuterio rate constants ($KIE = k_H/k_D$). Deuteration of the neutral reactant changes the rate of the reaction, providing insight into the transition state structure and hence the reaction mechanism. The origin of these effects is primarily the result of changes in vibrational frequencies as the reaction proceeds from the reactants to the transition state structure.²¹ In an S_N2 reaction (Scheme 5.01a), the C_{α} -H bonds are shortened in going from the sp^3 hybridized orbitals in the reactants to the sp^2 -like hybridized orbitals in the transition state, thus raising these frequencies relative to reactants. Since the frequencies for the hydrogenated species are raised more substantially than for the deuterated species in the transition state, the threshold energy for the hydrogenated reaction is greater than that of the deuterated reaction, $E_H^{\ddagger} > E_D^{\ddagger}$. In an E2 mechanism

(Scheme 5.01b), the C_β-H bond is lengthened in going from the reactants to transition state, thus lowering these frequencies relative to reactants. Since the frequencies for the hydrogenated species are lowered more substantially than for the deuterated species in the transition state, the threshold energy for the hydrogenated reaction is smaller than that of the deuterated reaction, $E_H^\ddagger < E_D^\ddagger$. When both reaction pathways are viable an overall KIE is measured, which provides qualitative insight into the competition between these two mechanisms.

Hu and Truhlar⁵ have calculated reaction rate constants and deuterium KIEs as a function of temperature for both the S_N2 and E2 pathways of ClO⁻ with ethyl chloride using correlated electronic structure calculations (MP2/ADZP) and dual-level direct dynamical calculations based on variational transition state theory and a competitive canonical unified statistical model. Their work has provided us the unique opportunity to compare experiment and theory. Their computations predict that, although the classical E2 barrier height is 3.2 kcal mol⁻¹ higher than the S_N2 barrier, the vibrational zero point energy for the E2 reaction is 3.5 kcal mol⁻¹ lower than the S_N2 vibrational zero point energy; thus, the zero point corrected barrier heights are approximately equal to each other. While both mechanisms are predicted to occur, the E2 pathway is highly favored (by a factor of 10) over the S_N2 pathway by entropic effects at room temperature.

Nucleophiles such as ClO⁻ have been the subject of intense study for another reason. Nucleophiles of this type, where there is a lone pair of electrons on the atom that is adjacent to the nucleophilic center, have been shown to display an enhanced reactivity relative to that expected from a Bronsted-type correlation. This type of nucleophile is known as an “α-nucleophile”, and the enhanced reactivity is termed an “α-effect”.²² In solution, this effect has been observed in several different types of

reactions including substitution reactions.²³⁻²⁹ However, in gas-phase reactions there has been continuing controversy about whether or not the α -effect exists,^{27,30-38} prompting the question: is an α -effect really a solvent-induced effect?

Only a limited number of gas-phase experiments have addressed this question. In an early study, DePuy *et al.*³⁶ found that the reactivity of HO_2^- was similar to that of HO^- in the reaction with methyl formate. These reactions proceed via three channels: proton abstraction, $\text{B}_{\text{AC}}2$ addition to the carbonyl center, and $\text{S}_{\text{N}}2$ substitution at the methyl group. The product branching fractions for these anions were found to be similar; thus, HO_2^- does not show an enhanced reactivity towards addition or substitution. In a similar approach, McAnoy *et al.*³⁰ have recently studied the reactions of HO_2^- and CD_3O^- with dimethyl methylphosphonate. These reactions proceed by proton abstraction and by $\text{S}_{\text{N}}2$ substitution at a methyl group. The HO_2^- anion reacts primarily via substitution while the CD_3O^- anion reacts preferentially via proton abstraction. The difference in the reactivity of the two anions is attributed to the α -nucleophilicity of the HO_2^- anion. This conclusion is supported by computations (B3LYP/aug-cc-pVTZ// B3LYP/ 6-31+G(d)), which find that the $\text{S}_{\text{N}}2$ barrier is lower (by $\sim 1.9 \text{ kcal mol}^{-1}$) for the reaction of HO_2^- . While these two studies come to conflicting conclusions, the later study may be more compelling since the basicity of the HO_2^- and CD_3O^- anions are comparable.

Recent theoretical work predicts that the α -effect results from an intrinsic property of a nucleophile and, therefore, this effect should be manifested in the gas-phase. Ren and Yamataka^{31,32} have investigated a series of $\text{S}_{\text{N}}2$ reactions, including the reactions of ClO^- and BrO^- with methyl, ethyl, and *i*-propyl chloride, using G2(+) calculations. In this work, the authors plot the barrier heights for the reactions of normal nucleophiles versus basicity to obtain a linear correlation curve. The barrier

heights for the reactions of the α -nucleophile were projected onto this plot and were found to be smaller than predicted for a hypothetical normal nucleophile of similar basicity, thus providing evidence for a gas-phase α -effect. The size of this α -effect is proportional to the amount of the deviation from the correlation curve and scales with the size of the neutral substrate and with the electronegativity of the α -atom.

In this work we report overall reaction rate constants and deuterium KIEs for the reactions of BrO^- and ClO^- with RCl , where R = methyl, ethyl, *i*-propyl, and *t*-butyl.^{18,39} As the extent of substitution in the neutral reagent increases, the KIEs become increasing more normal. This result indicates that the E2 pathway becomes the dominant pathway as the neutral reagent becomes more sterically hindered. The reactions of methyl chloride, ethyl chloride, and *i*-propyl chloride also proceed by an additional reaction pathway besides $\text{S}_{\text{N}}2$ substitution and elimination; two potential reaction mechanisms are investigated using electronic structure calculations. The overall reaction efficiency and KIE for the reaction of ClO^- with ethyl chloride is compared to the calculated results of Hu and Truhlar. Lastly, the α -nucleophilicity of the ClO^- and BrO^- anions is investigated by comparing their reactivity to that of other nucleophiles including the HO_2^- anion.

5.2) Experimental Methods

The overall reaction rate constants and KIE for the reactions of BrO^- and ClO^- with RCl were measured with a flowing afterglow-selected ion flow tube (FA-SIFT) mass spectrometer, which was described in Chapter 3. BrO^- and ClO^- are ideal nucleophiles for this type of study since the rate constants for the entire neutral series, methyl through *t*-butyl, are within the measurable kinetic window of 10^{-9} – 10^{-13} $\text{cm}^3 \text{s}^{-1}$ and are all below the calculated collision rate so the KIEs are evident. These two reactant ions were formed in the source flow tube from electron impact on

N₂O to produce O⁺, which was then allowed to react with CCl₃Br or CCl₄, respectively. Ions of a single isotopomer, ⁷⁹BrO⁻ and ³⁵ClO⁻, were mass selected by a quadrupole mass filter and injected into the reaction flow tube where they were thermalized to 302 ± 2 K by collisions with He buffer gas (~0.5 torr, 10⁴ cm s⁻¹). Despite injecting the reactant ions with minimal energy, ⁷⁹Br⁻ or ³⁵Cl⁻ ions produced from collision-induced dissociation were also present in the reaction flow tube; the presence of these additional ions was considered in the data analysis below.

Measured flows of neutral reagents are introduced into the reaction flow tube through a series of fixed inlets along the reaction flow tube and the reactant and product ions are analyzed by a quadrupole mass filter coupled to an electron multiplier. Neutral reactant flow rates were measured by monitoring the pressure change versus time in a calibrated volume system. Reaction rate constants and product branching ratios were determined by changing the neutral addition inlet, thereby changing the reaction distance and time, while monitoring the change in reactant ion intensity. The ratio of perprotio to perdeuterio rate constants gives the KIE (KIE = k_H/k_D). Product branching ratios were determined by plotting the percentage of each ion at each neutral inlet; extrapolation to “zero distance” gives the branching ratio. Efforts were made to minimize mass discrimination; however, it was necessary to estimate the relative detection sensitivities when calculating product branching ratios. The relative detection sensitivity was estimated by examining a series of exothermic ion-molecule reactions where only one ionic product was formed.

The error reported for the reaction rate constants is one standard deviation of at least three consecutive measurements. The systematic error is generally ±20%; however, KIEs are more accurately determined because some of the systematic

errors (pressure, temperature, He flow rate, etc.) cancel in the rate ratio. The estimated error in the product branching fractions is $\pm 25\%$ of the smaller product channel; this is mostly attributed to mass discrimination and to the fact that X^- results both from the collision-induced dissociation (CID) of the reactant ion and from the reaction. Neutral reagents were purchased from commercial sources and used without further purification.⁴⁰ However, it was verified that HCl was not a significant contaminant by mass selecting $^{35}\text{Cl}^-$ and allowing it to react with the neutral reagents. It has previously been shown that the reaction rates of Cl^- with these alkyl halides are below the detection limits of our instrument, while the $\text{Cl}^- + \text{HCl}$ exchange reaction proceeds at approximately half of the collision rate.⁴¹ Thus, the absence of $^{37}\text{Cl}^-$ as a product ion demonstrates that HCl is not a significant contaminant. An HCl impurity would complicate the rate measurements due to a rapid proton transfer pathway, which could not be distinguished from the $\text{S}_{\text{N}}2$ and E2 channels.

Optimized geometries and harmonic vibrational frequencies for the reactants, products, and transition state structures were determined from electronic structure calculations using the Gaussian 03 suite of programs⁴² at the MP2/aug-cc-pVDZ level of theory.^{43,44} Transition state structures were identified to have only one imaginary frequency and this frequency was animated to verify that its motion corresponds to the transition state reaction coordinate.

5.3) Results and Discussion

5.3.1) Reaction Trend and Product Distributions

The experimental reaction rate constants, product branching fractions, and deuterium kinetic isotope effects are reported in Table 5.01 for the reactions of BrO^- and ClO^- with RCI (R = methyl, ethyl, *i*-propyl, *t*-butyl or abbreviated as Me, Et, *i*-Pr, and *t*-Bu). For a given neutral reagent, the reactions of BrO^- are slightly less efficient than those of ClO^- and the kinetic isotope effects are more pronounced.

This trend reflects the weaker basicity of the BrO^- anion ($353.5 \text{ kcal mol}^{-1}$) relative to the ClO^- anion ($355.6 \text{ kcal mol}^{-1}$).

For the reactions of BrO^- with RCl , the formation of Cl^- is the major product channel. The reactions of BrO^- with MeCl , EtCl and $i\text{-PrCl}$ also produce minor amounts of Br^- ; this product was not observed for the reaction of BrO^- with $t\text{-BuCl}$. Additionally, the reactions of BrO^- with $i\text{-PrCl}$ and $t\text{-BuCl}$ produce trace amounts (<1%) of an E2 product cluster, $\text{Cl}^-(\text{BrOH})$ or $\text{Cl}^-(\text{BrOD})$, and minor amounts of an association product, $\text{BrO}^-(\text{RCl})$. For the reaction with $i\text{-PrCl}$ the amount of association that occurs is negligibly small. For the reaction with $t\text{-BuCl}$ the association channel is less than 5% of the total reaction; this contribution is removed from the rate constants and KIEs in Table 5.01. The reactions of ClO^- with MeCl and EtCl , exclusively produce the displaced halide, Cl^- . For the reactions of ClO^- with $i\text{-PrCl}$ and $t\text{-BuCl}$, trace amounts of an association cluster, $\text{ClO}^-(\text{RCl})$, were observed in addition to Cl^- ; the occurrence of this association channel is negligible.

The formation of Br^- in the reactions of BrO^- with MeCl , EtCl and $i\text{-PrCl}$ is rather unexpected. The analogous pathway in the reactions of ClO^- would produce the same product as an $\text{S}_{\text{N}}2$ or E2 mechanism, except that, in these classic mechanisms, Cl^- is produced with an isotope distribution that reflects the natural Cl atom abundance in RCl (76:24). This is not the case, however, for the reactions of ClO^- with MeCl , EtCl and $i\text{-PrCl}$, where the Cl^- isotope distribution is slightly skewed towards the $^{35}\text{ClO}^-$ reactant ion isotopomers. For the reaction of ClO^- with $t\text{-BuCl}$, the Cl^- isotope distribution reflects that of the natural abundance of Cl in $t\text{-BuCl}$. This additional pathway is not readily obvious since CID of the $^{35}\text{ClO}^-$ reactant ion upon SIFT-injection results in the formation of $^{35}\text{Cl}^-$. The presence of this fragment ion results in the appearance of a skewed $^{35}\text{Cl}/^{37}\text{Cl}$ isotope distribution. However, by subtracting the amount of initial $^{35}\text{Cl}^-$ due to CID from the product distribution, we

Table 5.01: Reaction rate constants ($10^{-10} \text{ cm}^3 \text{ s}^{-1}$), kinetic isotope effects, and product ion branching ratios for the reactions of $^{79}\text{BrO}^-$ and $^{35}\text{ClO}^-$ with RCl (R = methyl, ethyl, *i*-propyl, and *t*-butyl).

Reaction	k^a	KIE	Ionic products	branching ratios
$^{79}\text{BrO}^- + \text{CH}_3\text{Cl}$	1.08 ± 0.03		Cl^- , $^{79}\text{Br}^-$	0.82, 0.18
$^{79}\text{BrO}^- + \text{CD}_3\text{Cl}$	1.31 ± 0.04	0.82 ± 0.03	Cl^- , $^{79}\text{Br}^-$	0.86, 0.14
$^{79}\text{BrO}^- + \text{CH}_3\text{CH}_2\text{Cl}$	1.07 ± 0.01		Cl^- , $^{79}\text{Br}^-$	0.91, 0.09
$^{79}\text{BrO}^- + \text{CD}_3\text{CD}_2\text{Cl}$	1.11 ± 0.03	0.96 ± 0.03	Cl^- , $^{79}\text{Br}^-$	0.92, 0.08
$^{79}\text{BrO}^- + \text{CH}_3\text{CD}_2\text{Cl}$	1.05 ± 0.04	1.02 ± 0.04	Cl^- , $^{79}\text{Br}^-$	0.91, 0.09
$^{79}\text{BrO}^- + \text{CD}_3\text{CH}_2\text{Cl}$	1.12 ± 0.02	0.95 ± 0.02	Cl^- , $^{79}\text{Br}^-$	0.93, 0.07
$^{79}\text{BrO}^- + (\text{CH}_3)_2\text{CHCl}^b$	0.934 ± 0.157		Cl^- , $^{79}\text{Br}^-$, $\text{Cl}^-(\text{HO}^{79}\text{Br})$	0.97, 0.03, trace
$^{79}\text{BrO}^- + (\text{CD}_3)_2\text{CDCl}^b$	0.352 ± 0.137	2.65 ± 0.11	Cl^- , $^{79}\text{Br}^-$, $\text{Cl}^-(\text{DO}^{79}\text{Br})$	0.92, 0.08, trace
$^{79}\text{BrO}^- + (\text{CH}_3)_3\text{CCl}^c$	1.93 ± 0.11		Cl^- , $\text{Cl}^-(\text{HO}^{79}\text{Br})$	1.00, trace
$^{79}\text{BrO}^- + (\text{CD}_3)_3\text{CCl}^c$	0.638 ± 0.023	3.03 ± 0.22	Cl^- , $\text{Cl}^-(\text{DO}^{79}\text{Br})$	1.00, trace
$^{35}\text{ClO}^- + \text{CH}_3\text{Cl}$	2.01 ± 0.01		Cl^- , $^{35}\text{Cl}^-$	0.73, 0.27
$^{35}\text{ClO}^- + \text{CD}_3\text{Cl}$	2.36 ± 0.01	0.85 ± 0.01	Cl^- , $^{35}\text{Cl}^-$	0.78, 0.22
$^{35}\text{ClO}^- + \text{CH}_3\text{CH}_2\text{Cl}$	2.25 ± 0.01		Cl^- , $^{35}\text{Cl}^-$	0.90, 0.10
$^{35}\text{ClO}^- + \text{CD}_3\text{CD}_2\text{Cl}$	2.27 ± 0.01	0.99 ± 0.01	Cl^- , $^{35}\text{Cl}^-$	0.90, 0.10
$^{35}\text{ClO}^- + \text{CH}_3\text{CD}_2\text{Cl}$	2.17 ± 0.02	1.04 ± 0.01	Cl^- , $^{35}\text{Cl}^-$	0.89, 0.11
$^{35}\text{ClO}^- + \text{CD}_3\text{CH}_2\text{Cl}$	2.35 ± 0.01	0.96 ± 0.01	Cl^- , $^{35}\text{Cl}^-$	0.90, 0.10
$^{35}\text{ClO}^- + (\text{CH}_3)_2\text{CHCl}^b$	1.74 ± 0.03		Cl^- , $^{35}\text{Cl}^-$	0.94, 0.06
$^{35}\text{ClO}^- + (\text{CD}_3)_2\text{CDCl}^b$	1.01 ± 0.02	1.71 ± 0.05	Cl^- , $^{35}\text{Cl}^-$	0.90, 0.10
$^{35}\text{ClO}^- + (\text{CH}_3)_3\text{CCl}^b$	2.33 ± 0.03		Cl^-	1.00
$^{35}\text{ClO}^- + (\text{CD}_3)_3\text{CCl}^b$	1.01 ± 0.05	2.31 ± 0.12	Cl^-	1.00

^a The error is the standard deviation of at least three measurements. ^b A negligible amount of an association product was observed. ^c An association channel of 0.01 for the perprotio reaction and 0.04 for the perdeuterio reaction was observed; this component was removed from the overall reaction rate constant.

were able to determine the product ion $^{35}\text{Cl}/^{37}\text{Cl}$ isotope distribution; the deviation from the Cl natural abundance gives the branching ratio for the two pathways (Table 5.01).

For both anions, the occurrence of this additional reaction pathway is most significant for the reaction with MeCl and gradually diminishes as the size of the neutral substrate increases. This trend correlates with the anticipated falloff of the $\text{S}_{\text{N}}2$ channel as steric factors become more important, indicating that this additional product channel may result from a transformation within the $\text{S}_{\text{N}}2$ product ion-dipole complex. It is well established that $\text{S}_{\text{N}}2$ reactions are characterized by a double well potential energy surface, where two stable ion-dipole complexes flank the transition state.² Depending on the thermodynamics of the system, the lifetime of these complexes can be relatively long, allowing for additional chemistry to occur.⁴⁵ The complex retains all of its initial energy since there are no collisions during its lifetime; thus, endothermic processes can be driven by the complexation energy and as long as the overall process is exothermic, the complex can dissociate into products.

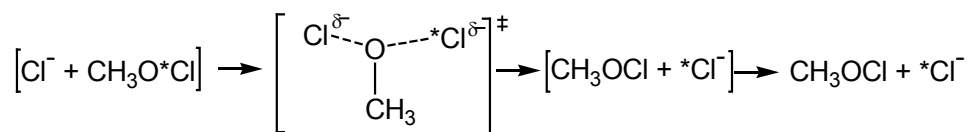
A possible reaction that would account for the formation of these products is shown in eq 5.01 for the reactions of ClO^- with CH_3Cl ; the Cl atom that originates from ClO^- is indicated with an asterisk.



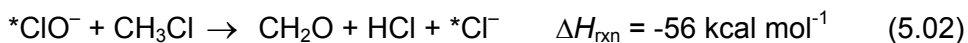
This reaction presumably is initiated by the $\text{S}_{\text{N}}2$ reaction of $^*\text{ClO}^- + \text{CH}_3\text{Cl}$, where $^*\text{ClO}^-$ attacks the carbon atom of methyl chloride to displace Cl^- (analogous to Scheme 5.01a). A second substitution step within the $[\text{Cl}^- + \text{CH}_3\text{O}^*\text{Cl}]$ ion-dipole complex, would scramble the chlorine atoms. This second substitution reaction presumably would proceed in a concerted step, as shown Scheme 5.02, where Cl^- attacks the oxygen atom of $\text{CH}_3\text{O}^*\text{Cl}$ displacing $^*\text{Cl}^-$. For the reaction of the ClO^- anion, this mechanism produces the same products as the traditional $\text{S}_{\text{N}}2$ reaction,

however, the chlorine atom are exchanged in a thermoneutral process. For the reactions of the BrO^- anion, a substitution step that exchanges Cl for Br is slightly more exothermic. These exothermicities ($\text{S}_{\text{N}}2$ -induced substitution) are summarized in Table 5.02.

Scheme 5.02:

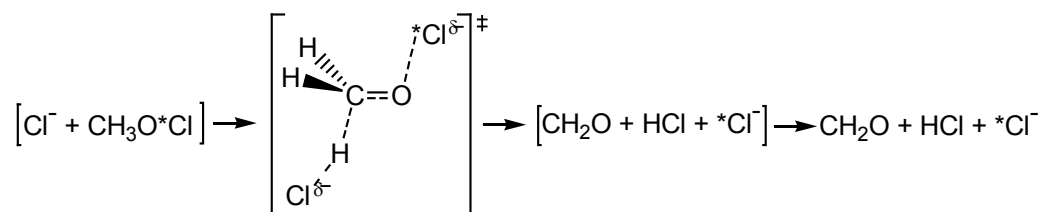


A second possible reaction that would account for the formation of these products is shown in eq 5.02. These exothermicities ($\text{S}_{\text{N}}2$ -induced elimination) are also summarized in Table 5.02.



This reaction is consistent with an elimination reaction that occurs following the initial substitution step, within the $\text{S}_{\text{N}}2$ product ion-dipole complex as shown in Scheme 5.03. This second transformation likely occurs in a concerted step where Cl^- abstracts an H atom from $\text{CH}_3\text{O}^*\text{Cl}$, displacing $* \text{Cl}^-$ and forming a C-O double bond; similar elimination reactions have previously been reported.⁴⁶ The transition state for this reaction resembles that of a typical E2 transition state, where the two leaving groups are antiperiplanar to one another.

Scheme 5.03:



Because we cannot detect the neutral products we are not able to distinguish between these two proposed mechanisms. Electronic structure calculations were

employed to explore whether or not these two potential mechanisms are thermodynamically feasible. These results are summarized in Figure 5.01 for the reaction of ClO^- with CH_3Cl . For both potential reactions the highest energy point, once the reactants come together, is the first $\text{S}_{\text{N}}2$ barrier, TS1; passage over this barrier is the rate-limiting step. If the reaction occurs according to Scheme 5.02, the reaction proceeds through TS2 into a second product ion-dipole well. Passage over the second substitution barrier requires more energy than for the initial $\text{S}_{\text{N}}2$ products to separate. If the reaction occurs according to Scheme 5.03, the reaction proceeds through TS3. This elimination barrier is below the second substitution barrier (TS2) and below the energy required for the initial $\text{S}_{\text{N}}2$ products to separate. While both proposed mechanisms are thermodynamically viable, the $\text{S}_{\text{N}}2$ -induced elimination channel (Scheme 5.03) is energetically more feasible and the overall reaction is considerably more exothermic.

A similar computational study was done for the reaction of BrO^- with CH_3Cl . In this case, the relative energetics for the substitution-elimination pathway were found to be similar to the corresponding reaction of ClO^- . However, for this reaction we were unable to locate a saddle point corresponding to the second substitution transition state, TS2. This provides additional support for the occurrence of the $\text{S}_{\text{N}}2$ -induced elimination mechanism rather than the double substitution mechanism. However, without performing a more exhaustive computational investigation, which is beyond the scope of this work, we cannot state with certainty which mechanism is responsible for this additional channel.

5.3.2) Kinetic Isotope Effects

For a given neutral reagent, the reactions of BrO^- with RCl are less efficient than those of ClO^- with RCl and, as the reaction efficiency decreases, the magnitude

Table 5.02: Reaction exothermicities^a (kcal mol⁻¹) for the reactions of BrO⁻ and ClO⁻ with RCl (R = methyl, ethyl, *i*-propyl, and *t*-butyl).

Reaction	E2 ^b	S _N 2 ^c	S _N 2-induced substitution ^d	S _N 2-induced elimination ^e
BrO ⁻ + CH ₃ Cl	-	-21 ^f	-59	-23
BrO ⁻ + CH ₃ CH ₂ Cl	-4	-23 ^f	-69	-25
BrO ⁻ + (CH ₃) ₂ CHCl	-5	-23 ^f	-66	-25
BrO ⁻ + (CH ₃) ₃ CCl	-4	-24 ^f	-	-26
ClO ⁻ + CH ₃ Cl	-	-20	-56	-20
ClO ⁻ + CH ₃ CH ₂ Cl	-6	-22	-66	-22
ClO ⁻ + (CH ₃) ₂ CHCl	-6	-22	-69	-22
ClO ⁻ + (CH ₃) ₃ CCl	-6	-23	-	-23

^a Enthalpies of formation are determined from the thermochemical data on the NIST WebBook⁴⁷ or from the JANAF thermochemical tables.⁴⁸ ^b See Scheme 5.01b in text for example. The formation of the E2 cluster is not considered. ^c See Scheme 5.01a in text for example. ^d See Scheme 5.02 in text for example. ^e See Scheme 5.03 in text for example. ^f Enthalpy of formation of CH₃OBr is calculated in reference 49; for C₂H₅OBr, C₃H₇OBr, and C₄H₉OBr, enthalpies of formation are estimated.

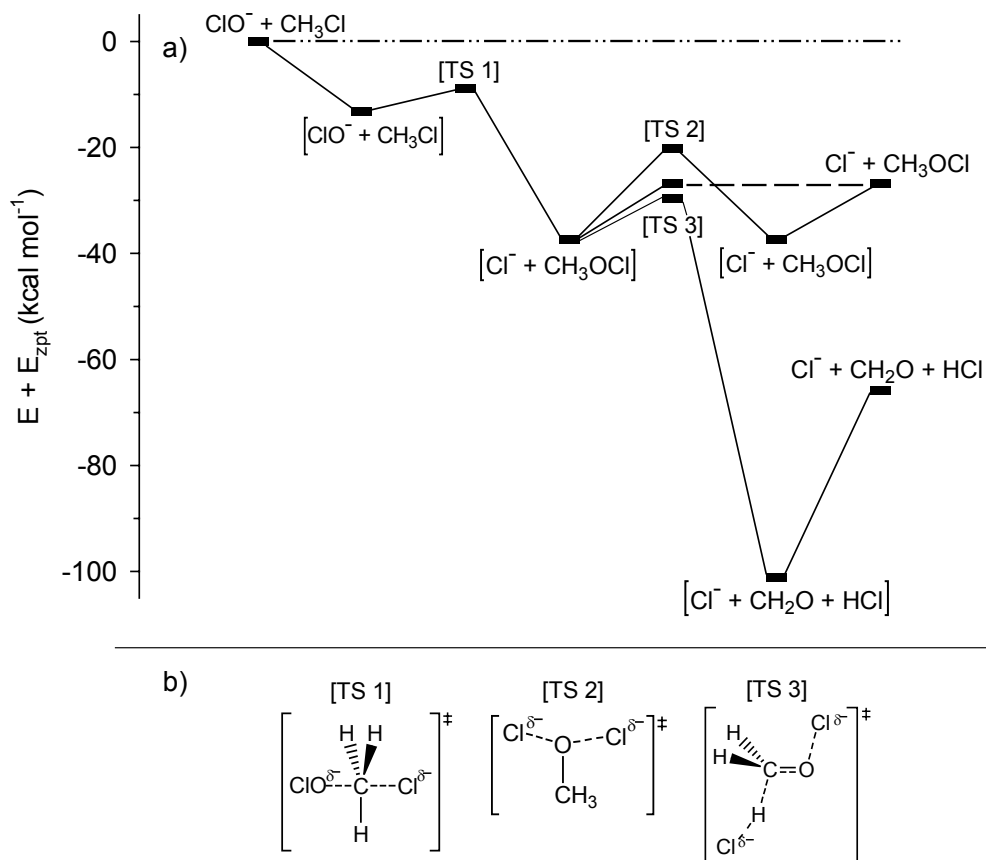


Figure 5.01: a) Reaction coordinate diagram for the reaction of ClO^- with CH_3Cl . The relative energies (electronic + zero point energy) were calculated at the MP2/aug-cc-pVDZ level of theory; b) the transition state structures are provided.

(deviation from unity) of the KIE increases. This is consistent with slower reactions having larger reaction barriers, hence larger KIEs. However, the efficiencies of these reactions are all well below the collision-controlled limit, therefore, the KIE is expected to accurately reflect the transition state. As a point of clarification, when the magnitude of a KIE is discussed as large or small, this refers to the absolute value of the displacement from unity. The terms inverse and normal indicate whether the KIE is less than one or greater than one, respectively.

With both sets of reactions, the KIE becomes increasingly more normal as the size of the alkyl substrate increases. These results indicate that the E2 pathway becomes the dominant channel as the neutral reagent becomes more sterically hindered. The reactions with *t*-BuCl are expected to exclusively occur via an E2 mechanism. Previous results have shown that the sterically bulky *t*-butyl group inhibits the S_N2 pathway.¹¹ The normal effect observed for these reactions is consistent with other E2 isotope effects reported in the literature.¹⁰

The reactions of CH₃Cl proceed by two pathways; for the remainder of this discussion, the major, prototypical S_N2 substitution channel will be referred to as the “direct substitution” channel and the minor channel will be referred to as the “substitution-induced displacement” channel. Since the rate-limiting step in both pathways is crossing the initial S_N2 barrier (Figure 5.01), the KIEs for these reactions are exclusively attributed to the prototypical S_N2 mechanism. The inverse KIEs measured for these reactions are consistent with the KIEs of other S_N2 reactions reported in the literature.^{19,20} For a given anion, the substitution-induced displacement product branching fraction is larger for the perdeuterio reaction than for the perprotio reaction. The change in branching fraction upon deuteration is most likely due to dynamical factors within the S_N2 product ion-dipole complex. In general, heavier systems have more low-frequency vibrational modes that better facilitate

vibrational coupling and increase the density of states. Thus, the lifetime of the S_N2 product ion-dipole complex is longer for the perdeuterio reaction, increasing the likelihood that the complexation energy can concentrate in the reaction coordinate of the second transformation.

The KIEs measured for the reactions of EtCl and *i*-PrCl are larger than the KIEs measured in the MeCl reactions but smaller than the KIEs measured for the *t*-BuCl reactions, indicating that these reactions proceed by competing S_N2 and E2 mechanisms. For these reactions, the substitution-induced displacement channel is small. However, the occurrence of this mechanism provides evidence that these reactions proceed partially by an S_N2 mechanism, since this channel results from a second reaction step within the S_N2 product ion-dipole complex. The reaction of BrO^- with *i*-PrCl additionally produces trace amounts of a clustered product, Cl^- (HOBr), providing evidence that this reaction proceeds partially through an elimination mechanism since HOBr is a neutral product of this mechanism. This E2 cluster is also observed for the reaction of BrO^- with *t*-BuCl. For these larger systems the formation of this cluster is likely promoted by the lower reaction efficiencies, hence a longer lifetime of the product ion-dipole complex.

To further verify that the EtCl systems proceed by both an S_N2 and an E2 mechanism, we have measured kinetic isotope effects that arise from the selective deuteration at the α and β positions of the EtCl (termed *d*2-KIE and *d*3-KIE, respectively). The *d*2-KIEs are slightly more inverse than the *d*5-KIEs, consistent with the occurrence of an S_N2 mechanism. Deuteration at the α -position is expected to be more sensitive to the S_N2 pathway since the inverse effect is predominantly the result of changes in the C_α -H umbrella bending motion. The *d*3-KIEs are slightly more normal than the *d*5-KIEs, reflecting the occurrence of an E2 mechanism.

Deuteration at the β -position is expected to be more sensitive to the E2 pathway since the normal effect is mainly the result of changes in the C_{β} -H stretching frequency. These results indicate that both mechanisms do indeed occur. While the $d2$ - and $d3$ -effects provide a more sensitive probe of the S_N2 and E2 pathways, respectively, they are still an overall effect and do not reflect the absolute magnitude of the KIEs for the respective pathways. For example, the KIE for the reaction of $BrO^- + MeCl$ is 0.82. Since the reaction of BrO^- with EtCl proceeds with approximately the same efficiency as the reaction with MeCl, we may expect that the transition state for these two S_N2 pathways is similar and, therefore, the S_N2 -KIE for the EtCl system would be closer to 0.88, since this system contains two α -hydrogen atoms. Likewise, the E2-KIE is expected to be larger than $d3$ -KIE, being closer in magnitude to the KIE measured for the t -BuCl system.

For each anion series, the trend in the KIEs indicates that the E2 channel becomes more important for larger systems, where steric effects inhibit the S_N2 channel. In a *crude* approximation, the E2 branching fraction (BR) for the reactions of EtCl and i -PrCl can be estimated by assuming that the E2-KIE for these reactions is approximately equal to the KIE observed in the t -BuCl systems and that the S_N2 -KIE is approximately equal to the KIE observed for the MeCl system when scaled for number of α -hydrogen atoms, given that:

$$KIE_{tot} = KIE_{E2} \times BR_{E2} + KIE_{SN2} \times BR_{SN2} \quad (5.03)$$

$$BR_{E2} + BR_{SN2} = 1 \quad (5.04)$$

Here, BR_{SN2} is the combined substitution channels. The KIE for the t -BuCl system is not scaled for the number of hydrogen atoms, since to a first order approximation, only one C_{β} -H bond is elongated in the E2 transition state (see Scheme 1b). This analysis, of course, relies on many assumptions and is only intended to provide an

estimate of which pathway is dominant. For the reaction of BrO^- with EtCl the overall KIE is 0.96. If the E2-KIE and $\text{S}_{\text{N}}2$ -KIE are taken to be 3.03 and 0.88, respectively, then the E2 channel only accounts for ~10% of the reaction and the combined substitution channels account for ~90% of the total reaction. Applying this same analysis to the reaction of ClO^- with EtCl , the E2 mechanism represents only ~10% of the reaction. About 80% of the reaction of BrO^- with *i*-PrCl proceeds by the E2 channel, while ~60% of the reaction of ClO^- with *i*-PrCl proceeds by the E2 channel. While this analysis is qualitative in nature, it does identify the major and minor channels.

5.3.3) ClO^- with *EtCl*: Comparison of Experiment and Theory

Hu and Truhlar⁵ have quantitatively evaluated the competition between $\text{S}_{\text{N}}2$ and E2 pathways for ClO^- with $\text{C}_2\text{H}_5\text{Cl}$ and with $\text{C}_2\text{D}_5\text{Cl}$ using dual-level generalized transition state theory and statistical calculations based on high-level, correlated electronic structure calculations using extended basis sets (MP2/ADZP). Their computations predict that, despite the nearly equal zero point corrected barrier heights, the E2 pathway is highly favored (by a factor of 10) over the $\text{S}_{\text{N}}2$ pathway by entropic effects at room temperature; the reaction proceeds 93% of the time by an E2 mechanism with an overall reaction efficiency of 0.28. This is in striking contrast to experimental results in which the E2 channel is only estimated to occur ~10% of the time. Additionally, Hu and Truhlar predict that the overall reaction has a KIE of 2.42, which disagrees with the experimentally determined KIE of 0.99.

It is difficult to account for the discrepancies between experiment and theory. The treatment of the reaction between ClO^- and ethyl chloride assumes that the reaction is statistical. Statistical theories are based on the assumption that energy is randomized among different modes as the reaction proceeds from reactants to the transition state. Non-statistical effects⁵⁰ have been observed for $\text{S}_{\text{N}}2$ reactions of

monatomic nucleophiles with methyl halides, and these effects have been extensively documented in the literature.⁵¹⁻⁵⁵ However, the use of statistical theories has been successful for slightly larger systems.⁵⁶⁻⁵⁸ Furthermore, Hu and Truhlar have previously calculated the KIE for the S_N2 reaction of F⁻(H₂O) with CH₃Cl using a statistical approach.⁵⁹ Their results show excellent agreement with experimental values of O'Hair *et al.*⁶⁰ Thus the assumption that the ClO⁻ + C₂H₅Cl reaction behaves statistically is reasonable.

Hu and Truhlar's calculations predict that the S_N2 channel has a KIE of 0.60 while the E2 channel has a KIE of 3.1. These individual KIEs are combined with the theoretically determined product branching fractions to give an overall KIE of 2.4. However, it should be noted that these KIE effects are likely incorrect. The calculated KIEs are based on the optimized geometries, rotational constants, and harmonic vibrational frequencies from MP2/ADZP calculations. For both C₂H₅Cl and C₂D₅Cl, ν_{18} was reported to be 279 cm⁻¹. This mode corresponds to a methyl rocking motion and should be lowered upon deuteration. Calculations performed here (MP2/aug-cc-pVDZ) found that the frequency of ν_{18} is 271 cm⁻¹ for C₂H₅Cl and 197 cm⁻¹ for C₂D₅Cl. If these newly calculated ν_{18} frequencies are used rather than the suspect ν_{18} frequencies, the calculated S_N2-KIE changes from 0.60 to 0.89. This value is very close to the experimental KIE of 0.85 for the S_N2 reaction of ClO⁻ + MeCl and the estimated S_N2-KIE of 0.88 for ClO⁻ + EtCl (see above). Additionally the calculated E2-KIE would also become slightly more normal upon inclusion of the new ν_{18} value. If the vibrational modes are treated as harmonic oscillators, then the corrected E2-KIE is 4.6. Hu and Truhlar, however, treat the low frequency modes of the E2 channel with a hindered rotor model and, therefore, this value is an upper bound.

While this error in the calculated individual KIEs certainly contributes to the discrepancy between experiment and theory, it can be argued that the errors in the branching ratio calculations are the primary cause for the large deviation from the experimental results. It should be noted that the suspect value of v_{18} in C_2D_5Cl does not need to be considered in the branching ratios, since only the perprotio reactions were evaluated. Likewise errors in the barrier heights do not affect the individual KIEs since the contributions from the electronic energy cancel in the rate ratio. Assuming that the branching ratios predicted by Hu and Truhlar are correct, then the E2-KIE would need to be less than 1.0 or the S_N2 -KIE would need to be less than 0.13 to be consistent with the measured overall KIE. These values are not reasonable based on previous results. On the other hand assuming that the individual KIEs are correct (provided that the corrected value of v_{18} for C_2D_5Cl is used) and that the discrepancy lies in the calculation of the branching ratios, we can use these individual KIEs (S_N2 -KIE = 0.89 and E2-KIE = 4.6) along with the experimentally measured overall rate constant and KIE to predict the reaction efficiencies for the S_N2 and E2 channels. This analysis gives $k = 2.12 \times 10^{-10} \text{ cm}^3 \text{ s}^{-1}$ and $\text{eff} = 0.10$ for the S_N2 channel, and $k = 0.13 \times 10^{-10} \text{ cm}^3 \text{ s}^{-1}$ and $\text{eff} = 0.0062$ for the E2 channel for the perprotio reaction. Thus, the E2 channel represents 6% of the overall reaction, very close to the above experimental estimates.

5.3.4) α -Nucleophilic Character

Both BrO^- and ClO^- are prototypical α -nucleophiles. It has been shown in solution that α -nucleophiles display an enhanced reactivity relative to that expected from a Bronsted-type correlation. Figure 5.02 is a plot of reaction efficiency (k/k_{col} , where k_{col} is calculated using parameterized trajectory theory⁶¹) as a function of anion basicity over a 40 kcal mol^{-1} range for the S_N2 reactions of various oxy anions with

CH₃Cl. As expected, the general trend displayed by the normal nucleophiles (open circles) is that reaction efficiency increases with anion basicity. Unfortunately, there are few oxygen anions in the lower basicity range of ClO⁻ and BrO⁻ (closed circles) whose reactions with CH₃Cl have been reported. However, by fitting a linear trend line to this data set, the efficiency of normal nucleophiles in this lower basicity region can be estimated. The reaction efficiencies of the α -nucleophiles, ClO⁻ and BrO⁻, are consistent with the predictions of the basicity-reactivity correlation. In fact, the trend line predicts the reaction efficiency for these anions within the error bars of their measurement. This is in contrast to G2(+) calculations, which predict the barriers for the reactions of BrO⁻ and ClO⁻ with CH₃Cl to be 2.5 and 3.8 kcal mol⁻¹ lower than those of normal nucleophiles of comparable basicity, respectively.³¹ Based on these results, we would expect the reaction efficiency of the BrO⁻ and ClO⁻ anions to be enhanced by one to two orders of magnitude.

It perhaps can be argued that the BrO⁻ and ClO⁻ anions are poor α -nucleophiles, since the halogen-oxygen bond is relatively long resulting in poor orbital overlap of the lone pairs on the halogen and oxygen atoms. We, therefore, have additionally studied the reaction of HO₂⁻ with CH₃Cl ($k = 1.23 \times 10^{-9} \text{ cm}^3 \text{ s}^{-1}$), and this result is also included in Figure 5.02. The HO₂⁻ anion is an excellent α -nucleophile whose reactivity has been extensively studied in solution. In one study, HO₂⁻ was found to undergo S_N2 substitution on a methyl group ten times faster than HO⁻, despite the greater basicity of the HO⁻ anion.²⁹ In the gas-phase, however, this anion does not display enhanced reactivity with CH₃Cl. Again, the trend line predicts the reaction efficiency for this anion within the error bars of the measurement. In further support of these findings, the S_N2 reaction of HO₂⁻ with MeF ($k = 6.0 \times 10^{-12} \text{ cm}^3 \text{ s}^{-1}$; eff = 0.0025)⁶² is slower than that of HO⁻ and CH₃O⁻

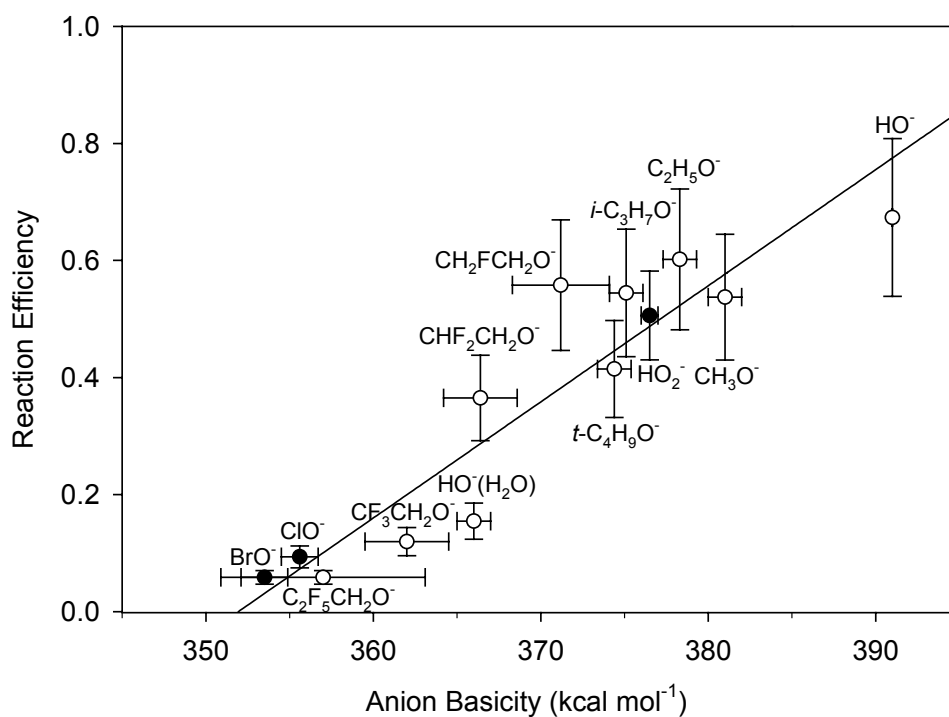


Figure 5.02: Anion basicity versus reaction efficiency for the S_N2 reactions of Nu⁻ with CH₃Cl. The normal nucleophiles are indicated by the open circles and the α-nucleophiles are indicated by the closed circles. The vertical error bars represent the absolute uncertainty of ±20%. Reactivities: references 11, 63, and 64; Anion basicities: reference 47.

($k = 2.5 \times 10^{-11} \text{ cm}^3 \text{ s}^{-1}$; $\text{eff} = 0.0087$ and $k = 1.4 \times 10^{-11} \text{ cm}^3 \text{ s}^{-1}$; $\text{eff} = 0.0058$, respectively).⁶⁵ Since these reactions proceed at rates well below the collision rate, the α -effect would likely be more apparent. However, the rates of these reactions scale with anion basicity and are inconsistent with a gas-phase α -effect.

This result also contradicts theoretical results, which predict that the barrier for the reaction of HO_2^- with MeCl is lower (by $\sim 5.4 \text{ kcal mol}^{-1}$) than that of a nucleophile of similar basicity.⁶⁶ It is difficult to account for the discrepancies between experiment and theory. However, it is possible that these nucleophiles have different entropic factors, which would influence their reactivity. Additionally, these results disagree with the experimental findings of McAnoy *et al.*,³⁰ which find a larger propensity for the reaction of HO_2^- with dimethyl methylphosphonate to proceed via an $\text{S}_{\text{N}}2$ substitution rather than proton transfer, whereas the corresponding reaction of CD_3O^- proceeds primarily by proton transfer. The difference in the product branching fractions was attributed to the α -nucleophilicity of HO_2^- . In this study, however, the overall reaction rate constants for HO_2^- and CD_3O^- with dimethyl methylphosphonate could not be evaluated and, therefore, it is not known if the overall reaction rates for the two reactions are comparable.

These results cast serious doubt on the existence of a gas-phase α -effect. This implies that the α -effect is not due to an intrinsic property of the anion and instead due to solvent effects. These findings are complemented by the solution studies of Um and Bunce,³⁷ which demonstrate the important and complicated role of the solvent in the destabilization/stabilization of the α -nucleophile and the transition state. However, as stated above, the calculations of Ren and Yamsataka³¹ predict that the α -effect in $\text{S}_{\text{N}}2$ reactions becomes more pronounced as the size of the neutral substrate increases. Unfortunately, given the limitations of gas-phase

experiments, a similar analysis for the S_N2 reactions of larger alkyl halides (EtCl and *i*-PrCl) is not feasible since the E2 pathway is competitive. Additionally, further investigation of the gas-phase reactivity of α -nucleophiles with sp²-hybridized carbon centers is a clear target for future studies.

5.4) Conclusions

The competition between S_N2 and E2 channels for the reactions of BrO⁻ and ClO⁻ with RCl (R = methyl, ethyl, *i*-propyl, and *t*-butyl) was explored through deuterium kinetic isotope effect measurements. These kinetic isotope effects become increasingly more normal as the extent of substitution in the neutral reactant increases. This indicates that the E2 channel becomes the dominant pathway as the neutral reagent becomes more sterically hindered. For the reactions of ethyl chloride, elimination is estimated to be a minor channel, while for the reactions of *i*-propyl chloride, elimination is estimated to be the major channel. The reactions of MeCl, EtCl, and *i*-PrCl proceed by an additional minor reaction pathway, which is likely due to a novel elimination step that occurs within the S_N2 product ion-dipole complex.

Additionally, the gas-phase substitution reactions of ClO⁻ and BrO⁻ with CH₃Cl occur as predicted by a basicity-reactivity relationship. The same result is observed for the S_N2 reaction of HO₂⁻ with CH₃Cl and CH₃F. The lack of enhanced reactivity of these α -nucleophiles implies that the α -effect is not manifested in the gas-phase but instead is due to solvent effects.

5.5) Acknowledgements

This work benefited from the contributions of Ms. Nicole Eyet, Dr. Shuji Kato, Prof. Veronica M. Bierbaum, and Prof. Charles H. DePuy. Additionally gratitude is expressed towards Dr. Gustavo Davico, Prof. Stephen J. Blanksby, and Prof. W. Carl

Lineberger. This work was supported by the AFOSR (FA9550-06-1-006) and NSF (CHE-0647088). The computational results are based upon work supported by the National Science Foundation under the following NSF programs: Partnerships for Advanced Computational Infrastructure, Distributed Terascale Facility (DTF) and Terascale Extensions: Enhancements to the Extensible Terascale Facility.

5.6) Chapter 5 References

- (1) Mackay, G. I.; Bohme, D. K. Bridging the Gap between the Gas-Phase and Solution - Transition in the Relative Acidity of Water and Methanol at 296 ± 2 K. *Journal of the American Chemical Society* **1978**, *100*, 327-329.
- (2) Olmstead, W. N.; Brauman, J. I. Gas-Phase Nucleophilic Displacement-Reactions. *Journal of the American Chemical Society* **1977**, *99*, 4219-4228.
- (3) Brauman, J. I.; Blair, L. K. Gas-Phase Acidities of Alcohols. *Journal of the American Chemical Society* **1970**, *92*, 5986-5992.
- (4) Brodbelt, J. S.; Isbell, J.; Goodman, J. M.; Secor, H. V.; Seeman, J. I. Gas Phase Versus Solution Chemistry: On the Reversal of Regiochemistry of Methylation of sp^2 - and sp^3 -Nitrogens. *Tetrahedron Letters* **2001**, *42*, 6949-6952.
- (5) Hu, W. P.; Truhlar, D. G. Factors affecting competitive ion-molecule reactions: $ClO^+ + C_2H_5Cl$ and C_2D_5Cl via E2 and S_N2 channels. *Journal of the American Chemical Society* **1996**, *118*, 860-869.
- (6) Lieder, C. A.; Brauman, J. I. Technique for Detection of Neutral Products in Gas-Phase, Ion-Molecule Reactions. *International Journal of Mass Spectrometry and Ion Processes* **1975**, *16*, 307-319.
- (7) Wladkowski, B. D.; Brauman, J. I. Substitution Versus Elimination in Gas-Phase Ionic Reactions *Journal of the American Chemical Society* **1992**, *114*, 10643-10644.
- (8) Lum, R. C.; Grabowski, J. J. Substitution Competes with Elimination in a Gas-Phase Anion Molecule Reaction. *Journal of the American Chemical Society* **1988**, *110*, 8568-8570.
- (9) Jones, M. E.; Ellison, G. B. A Gas-Phase E2 Reaction - Methoxide Ion and Bromopropane. *Journal of the American Chemical Society* **1989**, *111*, 1645-1654.
- (10) Gronert, S.; DePuy, C. H.; Bierbaum, V. M. Deuterium-Isotope Effects in Gas-Phase Reactions of Alkyl-Halides: Distinguishing E2 and S_N2 Pathways. *Journal of the American Chemical Society* **1991**, *113*, 4009-4010.
- (11) DePuy, C. H.; Gronert, S.; Mullin, A.; Bierbaum, V. M. Gas-Phase S_N2 and E2 Reactions of Alkyl-Halides. *Journal of the American Chemical Society* **1990**, *112*, 8650-8655.
- (12) Gronert, S.; Pratt, L. M.; Mogali, S. Substituent Effects in Gas-Phase Substitutions and Eliminations: β -Halo Substituents. Solvation Reverses S_N2 Substituent Effects. *Journal of the American Chemical Society* **2001**, *123*, 3081-3091.

- (13) Gronert, S.; Fagin, A. E.; Okamoto, K.; Mogali, S.; Pratt, L. M. Leaving Group Effects in Gas-Phase Substitutions and Eliminations. *Journal of the American Chemical Society* **2004**, *126*, 12977-12983.
- (14) Gronert, S. Gas phase Studies of the Competition Between Substitution and Elimination Reactions. *Accounts of Chemical Research* **2003**, *36*, 848-857.
- (15) Lum, R. C.; Grabowski, J. J. The Intrinsic Competition between Elimination and Substitution Mechanisms Is Controlled by Nucleophile Structure. *Journal of the American Chemical Society* **1992**, *114*, 9663-9665.
- (16) Noest, A. J.; Nibbering, N. M. M. Negative Ion-Molecule Reactions of Aliphatic Nitrites Studied by Ion Cyclotron Resonance. *Advances in Mass Spectrometry* **1980**, *8*, 227-237.
- (17) Bartmess, J. E.; Hays, R. L.; Khatri, H. N.; Misra, R. N.; Wilson, S. R. Elimination, Fragmentation, and Proton-Transfer in 1,3-Dithianes and 1,3-Dithiolanes in the Gas-Phase. *Journal of the American Chemical Society* **1981**, *103*, 4746-4751.
- (18) Villano, S. M.; Kato, S.; Bierbaum, V. M. Deuterium kinetic isotope effects in gas-phase S_N2 and E2 reactions: Comparison of experiment and theory. *Journal of the American Chemical Society* **2006**, *128*, 736-737.
- (19) Kato, S.; Davico, G. E.; Lee, H. S.; DePuy, C. H.; Bierbaum, V. M. Deuterium Kinetic Isotope Effects in Gas Phase S_N2 Reactions. *International Journal of Mass Spectrometry* **2001**, *210*, 223-229.
- (20) Viggiano, A. A.; Morris, R. A.; Paschkewitz, J. S.; Paulsen, J. F. Kinetics of the Gas-Phase Reactions of Chloride Anion, Cl^- with CH_3Br and CD_3Br : Experimental Evidence for Nonstatistical Behavior? *Journal of the American Chemical Society* **1992**, *114*, 10477.
- (21) Poirier, R. A.; Wang, Y. L.; Westaway, K. C. A Theoretical-Study of the Relationship Between Secondary α -Deuterium Kinetic Isotope Effects and the Structure of S_N2 Transition-States. *Journal of the American Chemical Society* **1994**, *116*, 2526-2533.
- (22) Edwards, J. O.; Pearson, R. G. Factors Determining Nucleophilic Reactivities. *Journal of the American Chemical Society* **1962**, *84*, 16-24.
- (23) Fountain, K. R.; Felkerson, C. J.; Driskell, J. D.; Lamp, B. D. The α -Effect in Methyl Transfers from S-Methyldibenzothiophenium Fluoroborate to Substituted N-Methylbenzohydroxamates. *Journal of Organic Chemistry* **2003**, *68*, 1810-1814.
- (24) Fountain, K. R.; Hutchinson, L. K.; Mulhearn, D. C.; Xu, Y. B. α -Effect in Menschutkin Alkylations. *Journal of Organic Chemistry* **1993**, *58*, 7883-7890.
- (25) Fountain, K. R.; Tad-y, D. B.; Paul, T. W.; Golynskiy, M. V. The α -Effect in Benzyl Transfers from Benzyphenylmethyl Sulfonium Salts to N-

Methylbenzohydroxamate Anions. *Journal of Organic Chemistry* **1999**, *64*, 6547-6553.

(26) McIsaac, J. E.; Mulhausen, H. A.; Behrman, E. J.; Subbaram, J.; Subbaram, L. R. Nucleophilic Reactivity of Peroxy Anions. *Journal of Organic Chemistry* **1972**, *37*, 1037-1041.

(27) Dixon, J. E.; Bruice, T. C. α -Effect. IV. Additional Observation on the α -Effect Employing Malachite Green as Substrate. *Journal of the American Chemical Society* **1971**, *93*, 6592-6597.

(28) Gregory, M. J.; Bruice, T. C. Alpha Effect. II. Displacements on sp^3 Carbon. *Journal of the American Chemical Society* **1967**, *89*, 4400-4402.

(29) Buncl, E.; Wilson, H. R.; Chuaqui, C. Reaction-Selectivity Correlations. 4. The α -Effect in S_N2 Reactions at sp^3 Carbon. The Reactions of Hydrogen Peroxide Anion with Methyl Sulfates. *Journal of the American Chemical Society* **1982**, *1982*, 4896-4900.

(30) McAnoy, A. M.; Paine, M. R. L.; Blanksby, S. J. Reactions of the Hydroperoxide Anion with Dimethyl Methylphosphonate in an Ion Trap Mass Spectrometer: Evidence for a Gas-Phase α -Effect. *Organic and Biomolecular Chemistry* **2008**, *6*, 2316-2326.

(31) Ren, Y.; Yamataka, H. The α -Effect in Gas-Phase S_N2 Reactions: Existence and the Origin of the Effect. *Journal of Organic Chemistry* **2007**, *72*, 5660-5667.

(32) Ren, Y.; Yamataka, H. G2(+) Investigation on the α -Effect in the S_N2 Reactions at Saturated Carbon. *Chemistry-A European Journal* **2007**, *13*, 677-682.

(33) Patterson, E. V.; Fountain, K. R. On Gas Phase α -Effects. I. The Gas-Phase Manifestation and Potential SET Character. *Journal of Organic Chemistry* **2006**, *71*, 8121-8125.

(34) Evanseck, J. D.; Blake, J. F.; Jorgensen, W. L. *Ab Initio* Study of the S_N2 Reactions of Hydroxide and Hydroperoxide with Chloromethane. *Journal of the American Chemical Society* **1987**, *109*, 2349-2353.

(35) Hupe, D. J.; Wu, D. The Effect of Solvation on Bronsted β Values for Proton Transfer Reactions. *Journal of the American Chemical Society* **1977**, *99*, 7653-7659.

(36) DePuy, C. H.; Della, E. W.; Filley, J.; Grabowski, J. J.; Bierbaum, V. M. Absence of an α -Effect in the Gas-Phase Nucleophilic Reactions of HOO^- . *Journal of the American Chemical Society* **1983**, *105*, 2481-2482.

(37) Buncl, E.; Um, I.-H. The α -Effect and Its Modulation by Solvent. *Tetrahedron* **2004**, *60*, 7801-7825.

- (38) Hoz, S. The α -Effect - on the Origin of Transition-State Stabilization. *Journal of Organic Chemistry* **1982**, *47*, 3545-3547.
- (39) Villano, S. M.; Eyet, N.; Lineberger, W. C.; Bierbaum, V. M. Reactions of α -Nucleophiles with Alkyl Chlorides: The Competition Between S_N2 and E2 Mechanisms and the Gas-Phase α -Effect. *Submitted to Journal of the American Chemical Society* **2009**.
- (40) CH_3Cl 99.4%, CD_3Cl 98%, C_2H_5Cl >99%, C_2D_5Cl 98%, *i*- C_3H_7Cl 99%, *i*- C_3D_7Cl 99.4%, *t*- C_4H_9Cl 99%, *t*- C_4D_9Cl 99.1%.
- (41) Van Doren, J. M.; DePuy, C. H.; Bierbaum, V. M. Gas-Phase Isotope-Exchange Reactions with Chloride-Ion. *Journal of Physical Chemistry* **1989**, *93*, 1130-1134.
- (42) Frisch, M. J.; Trucks, G. W.; Schlegel, H. B.; Scuseria, G. E.; Robb, M. A.; Cheeseman, J. R.; Montgomery, J. A.; Vreven, T.; Kudin, K. N.; Burant, J. C.; Millam, J. M.; Iyengar, S. S.; Tomasi, J.; Barone, V.; Mennucci, B.; Cossi, M.; Scalmani, G.; Rega, N.; Petersson, G. A.; Nakatsuji, H.; Hada, M.; Ehara, M.; Toyota, K.; Fukuda, R.; Hasegawa, J.; Ishida, M.; Nakajima, T.; Honda, Y.; Kitao, O.; Nakai, H.; Klene, M.; Li, X.; Knox, J. E.; Hratchian, H. P.; Cross, J. B.; Adamo, C.; Jaramillo, J.; Gomperts, R.; Stratmann, R. E.; Yazyev, O.; Austin, A. J.; Cammi, R.; Pomelli, C.; Ochterski, J. W.; Ayala, P. Y.; Morokuma, K.; Voth, G. A.; Salvador, P.; Dannenberg, J. J.; Zakrzewski, V. G.; Dapprich, S.; Daniels, A. D.; Strain, M. C.; Farkas, O.; Malick, D. K.; Rabuck, A. D.; Raghavachari, K.; Foresman, J. B.; Ortiz, J. V.; Cui, Q.; Baboul, A. G.; Clifford, S.; Cioslowski, J.; Stefanov, B. B.; Liu, G.; Liashenko, A.; Piskorz, P.; Komaromi, I.; Martin, R. L.; Fox, D. J.; Keith, T.; Al-Laham, M. A.; C. Y. Peng; Nanayakkara, A.; Challacombe, M.; Gill, P. M. W.; Johnson, B.; Chen, W.; Wong, M. W.; Gonzalez, C.; Pople, J. A. Gaussian 03, revision B.05; I. Gaussian, Ed.; Gaussian, Inc.: Pittsburgh, PA, 2003.
- (43) Hehre, W. J.; Radom, L.; Schleyer, P. v. R.; Pople, J. A. *Ab Initio Molecular Orbital Theory*; Wiley: New York, 1986.
- (44) Woon, D. E.; Dunning, T. H. Gaussian-Basis Sets for Use in Correlated Molecular Calculations. III. The Atoms Aluminum through Argon. *Journal of Chemical Physics* **1993**, *98*, 1358-1371.
- (45) DePuy, C. H.; Bierbaum, V. M. Gas-Phase Elimination-Reactions of Ethers Induced by Amide and Hydroxide Ions. *Journal of the American Chemical Society* **1981**, *103*, 5034-5038.
- (46) King, G. K.; Maricq, M. M.; Bierbaum, V. M.; Depuy, C. H. Gas-Phase Reactions of Negative-Ions with Alkyl Nitrites. *Journal of the American Chemical Society* **1981**, *103*, 7133-7140.
- (47) *NIST Chemistry WebBook, NIST Standard Reference Database Number 69*; Linstrom, P. J.; Mallard, W. G., Eds.; National Institute of Standards and Technology: Gaithersburg MD, 20899 June 2005 (<http://webbook.nist.gov>).

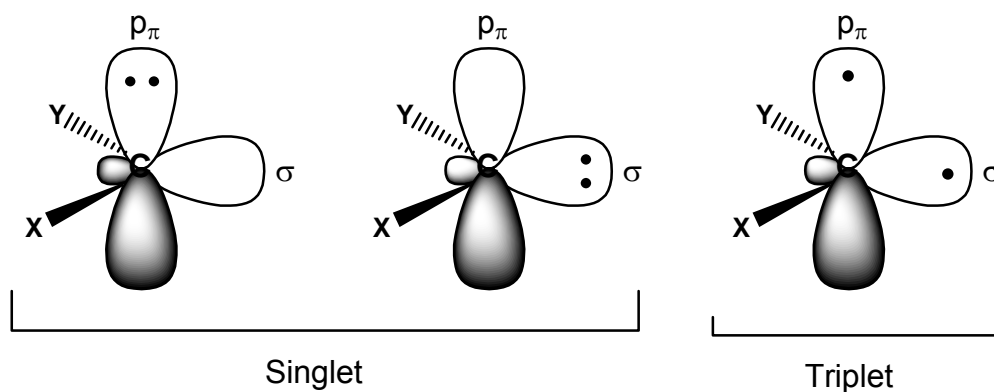
- (48) Chase Jr., W. M.; Davies, C. A.; Downey, J. J. R.; Frurip, D. J.; McDonald, R. A.; Syverud, A. N. JANAF Thermochemical Tables, 3rd ed. Parts I and II. In *J. Phys. Chem. Ref. Data*; 3rd Parts I and II ed., 1985; pp Suppl 1.
- (49) Espinosa-Garcia, J. Theoretical Enthalpies of Formation of ROX (R = H, CH₃; X = F, Cl, Br) Compounds. *Chemical Physics Letters* **1999**, *315*, 239-247.
- (50) Baer, T.; Hase, W. L. Unimolecular Reaction Dynamics: Theory and Experiment; Oxford University Press: New York, 1996.
- (51) Angel, L. A.; Ervin, K. M. Gas-phase S_N2 and Bromine Abstraction Reactions of Chloride Ion with Bromomethane: Reaction Cross Sections and Energy Disposal Into Products. *Journal of the American Chemical Society* **2003**, *125*, 1014-1027.
- (52) Sun, L.; Hase, W. L.; Song, K. Trajectory Studies of S_N2 Nucleophilic Substitution. 8. Central Barrier Dynamics for Gas-Phase Cl⁻+CH₃Cl. *Journal of the American Chemical Society* **2001**, *123*, 5753-5756.
- (53) Sun, L.; Song, K.; Hase, W. L. A S_N2 Reaction That Avoids Its Deep Potential Energy Minimum. *Science* **2002**, *296*.
- (54) Tonner, D. S.; McMahon, T. B. Non-statistical Effects in the Gas-Phase S_N2 Reaction. *Journal of the American Chemical Society* **2000**, *122*, 8783-8784.
- (55) Graul, S. T.; Bowers, M. T. Vibrational-Excitation in Products of Nucleophilic-Substitution - The Dissociation of Metastable X⁻(CH₃Y) in the Gas-Phase. *Journal of the American Chemical Society* **1994**, *116*, 3875-3883.
- (56) Midey, A. J.; Viggiano, A. A. Rate Constants as a Function of Temperature and Kinetic Energy for the Reactions of Cl⁻ with C₂H₅Br and *n*-C₃H₇Br. *Journal of Physical Chemistry A* **200**, *104*, 6786-6790.
- (57) Chabinyk, M. L.; Craig, S. L.; Regan, C. K.; Brauman, J. I. Gas-Phase Ionic Reactions: Dynamics and Mechanism of Nucleophilic Displacements. *Science* **1998**, *279*, 1882-1886.
- (58) Morris, R. A.; Viggiano, A. A. Kinetics of the Reactions of F⁻ with CF₃Br and CF₃I as a Function of Temperature, Kinetic-Energy, Internal Temperature, and Pressure. *Journal of Physical Chemistry* **1994**, *98*, 3740-3746.
- (59) Hu, W. P.; Truhlar, D. G. Modeling Transition-State Solvation at the Single-Molecule Level - Test of Correlated *Ab-Initio* Predictions against Experiment for the Gas-Phase S_N2 Reaction of Microhydrated Fluoride with Methyl-Chloride. *Journal of the American Chemical Society* **1994**, *116*, 7797-7800.
- (60) O'Hair, R. A. J.; Davico, G. E.; Hacaloglu, J.; Dang, T. T.; DePuy, C. H.; Bierbaum, V. M. Measurements of Solvent and Secondary Kinetic Isotope Effects for the Gas-Phase S_N2 Reactions of Fluoride with Methyl Halides. *Journal of the American Chemical Society* **1994**, *116*, 3609-3610.

- (61) Su, T.; Chesnavich, W. J. Parametrization of the Ion-Polar Molecule Collision Rate-Constant by Trajectory Calculations. *Journal of Chemical Physics* **1982**, *76*, 5183-5185.
- (62) Grabowski, J. J. Studies of Gas Phase Ion-Molecule Reactions using a Selected Ion Flow Tube. Ph.D. Thesis, Department of Chemistry and Biochemistry, University of Colorado at Boulder 1983.
- (63) Villano, S. M.; Eyet, N.; Bierbaum, V. M. Unpublished Results: $k=7.50 \times 10^{-10} \text{ cm}^3 \text{ s}^{-1}$ for $\text{CFH}_2\text{CH}_2\text{O}^- + \text{CH}_3\text{Cl}$ and $k=4.59 \times 10^{-10} \text{ cm}^3 \text{ s}^{-1}$ for $\text{CF}_2\text{HCH}_2\text{O}^- + \text{CH}_3\text{Cl}$.
- (64) Bohme, D. K.; Young, L. B. Kinetic Studies of Reactions of Oxide, Hydroxide, Alkoxide, Phenyl, and Benzylic Anions with Methyl Chloride in Gas Phase at 22.5°. *Journal of the American Chemical Society* **1970**, *92*, 7354-7358.
- (65) Tanaka, K.; Mackay, G. I.; Payzant, J. D.; Bohme, D. K. Gas-Phase Reactions of Anions with Halogenated Methanes at $297 \pm 2 \text{ K}$. *Canadian Journal of Chemistry* **1976**, *54*, 1643-1659.
- (66) Ren, Y.; Yamataka, H. The α -Effect in Gas-Phase $\text{S}_{\text{N}}2$ Reactions Revisited. *Organic Letters* **2005**, *8*, 119-121.

CHAPTER VI
GAS-PHASE CARBENE RADICAL ANIONS:
NEW MECHANISTIC INSIGHTS

6.1) Introduction

Carbenes are highly reactive organic species that have the general structure $:CXY$, where the central carbon atom has two substituents (X and Y) and two electrons, which can either be paired in a singlet state or unpaired in a triplet state. These molecules have been the focus of intense study, the results of which demonstrate that the structure, thermochemical properties, and reactivity depend upon the ground state multiplicity and the singlet-triplet energy gap.¹⁻⁴ The ground state spin multiplicity of a carbene depends on the nature of the substituents. For example, electron-withdrawing groups stabilize singlet states, while electropositive and sterically bulky groups stabilize triplet states.⁵⁻⁸



Simple halogen substituted carbenes ($:CXY$, where X=F, Cl, and Br and Y=H, F, Cl, and Br) have singlet ground states.⁹⁻¹¹ In solution, these molecules are highly reactive and undergo characteristic reactions such as insertion into single bonds and cycloaddition to double bonds,^{1,2} making them useful synthetic organic chemistry reagents. In the atmosphere, these compounds are likely photofragments of chlorofluoro compounds and other halons,¹²⁻¹⁶ the role of halogenated compounds in

ozone depletion has been well documented.¹⁷⁻²⁰ In addition, the reactions of halocarbenes are important to the plasma chemistry of halogenated compounds²¹ and to organometallic chemistry.²²⁻²⁴

There has been an extensive effort, both experimentally and theoretically, aimed at determining the fundamental physical properties of halocarbenes. These studies have been employed to determine the electronic and molecular structure of the ground and first excited state, vibrational frequencies, ionization energies, electron affinities, and the singlet-triplet splittings.^{9-11,25-52} Additionally, heats of formation, gas-phase acidities, and bond dissociation energies have been determined either directly or indirectly through gas-phase ion-molecule bracketing experiments and collision-induced dissociation threshold energy measurements.^{8,53-57}

While halogen substituted neutral carbenes have been extensively investigated, only a few studies have addressed the chemistry of the corresponding anions. Addition of an electron to a halocarbene forms a π -radical anion.⁹⁻¹¹ In solution, radical anions are of interest since these species are often reactive intermediates. In the gas-phase, the chemistry of radical anions has important implications for reactions in the upper atmosphere,⁵⁸ negative ion chemical ionization mass spectrometry,^{59,60} and electron capture detectors.⁶¹

The majority of the studies involving $CXY^{\bullet-}$ anions have focused on electron and proton transfer reactions;⁵⁵⁻⁵⁷ these studies have provided valuable thermodynamic information about the corresponding neutral carbenes. Beyond this, Born, Ingemann, and Nibbering^{55,62} have investigated the reactivity of a series of mono-halocarbene anions with methyl halides, organic esters, and aliphatic alcohols. Their results show that reactions with methyl halides proceed solely by an S_N2 mechanism, while the reactions with the esters proceed by competing S_N2 and $B_{AC}2$

mechanisms.⁶² The reactions with the alcohol series (ROH) indicate that, in addition to proton transfer, an S_N2 reaction to produce X⁻ also occurs. This S_N2 process must occur within the [RO⁻ + •CH₂X] complex before the initial products separate.⁵⁵

The first part of this chapter focuses on the gas-phase reactions of carbene radical anions with a series of oxygen and sulfur containing neutral reagents (CS₂, COS, CO₂, O₂, CO, and N₂O).⁶³ In past studies from this laboratory, it has been shown that these sulfur and oxygen containing neutral reagents can provide insight into the structure of an anion as well as form interesting product ions from diverse chemistry.⁶⁴⁻⁷² Additionally, the reactivity of methylene anion, CH₂^{•-}, has been studied with this neutral series,⁷⁰ which allows for direct comparison to the results presented here. Since there is very little thermochemical information available in the literature for these systems, electronic structure calculations are employed to evaluate the reaction exothermicities for several proposed pathways. The second half of the chapter evaluates the gas-phase reactivity of carbene radical anions with a series of halogenated neutral reagents (CCl₄, CHCl₃, CH₂Cl₂, CH₃Cl, CH₃Br, and (CH₃)₃CBr). For the reactions of CHCl₂^{•-} with CCl₄, CHCl₃, CH₂Cl₂, and CH₃Cl, careful quantitative isotope labeling studies were performed; the results of these labeling studies provide insight into the reaction mechanism.⁷³ For the reactions of CCl₂^{•-} with CCl₄, CHCl₃, CH₂Cl₂, and CH₃Cl, isotope labeling studies only provide qualitative insight. Additionally for the reactions with CH₃Br and (CH₃)₃CBr, deuterium isotope effects were measured. In this work we present reaction rate constants as well as product ion branching ratios. Additionally, we suggest reaction mechanisms, which account for the observed product ions.

6.2) Experimental Methods

The reactivities of mono- and dihalocarbene anions ($\text{CHCl}^{\bullet-}$, $\text{CHBr}^{\bullet-}$, $\text{CF}_2^{\bullet-}$, $\text{CCl}_2^{\bullet-}$, and $\text{CBrCl}^{\bullet-}$) were studied using a tandem flowing afterglow-selected ion flow tube instrument (FA-SIFT), which was described in Chapter 3. Reactant ions were formed in a flowing afterglow source from the $\text{H}_2^{\bullet+}$ abstraction reactions of $\text{O}^{\bullet-}$.^{74,75}



Ions of a single isotopomer were mass-selected and injected into a reaction flow tube where they were thermalized to 302 ± 2 K by collisions with He buffer gas (0.5 torr, $\sim 10^4$ cm s⁻¹). Despite injecting the reactant ions with minimal energy, $\text{X}^{\bullet-}$ ions produced from collision-induced dissociation were also present in the reaction flow tube; the presence of these additional ions was considered in the data analysis below.

Measured flows of neutral reagents were introduced into the reaction flow tube through a manifold of inlets and the reactant and product ions were analyzed by a quadrupole mass filter coupled to an electron multiplier. Reaction rate constants were determined by changing the neutral reagent inlet position, thereby varying the reaction distance and time, while monitoring the change in reactant ion intensity. Product branching fractions were measured at each neutral inlet and averaged together; secondary reactions in general do not occur for these systems. Efforts were made to minimize mass discrimination; however, it was necessary to estimate the relative detection sensitivities when calculating product branching ratios. The relative detection sensitivity was estimated by examining a series of exothermic ion-molecule reactions where only one ionic product was formed. For reactions of $\text{CBrCl}^{\bullet-}$, we were unable to cleanly separate the $\text{CBrCl}^{\bullet-}$ anion from the $\text{CHBrCl}^{\bullet-}$ anion in the injection process. The presence of this additional ion does not interfere

with measurements of the overall reaction rate constant since $\text{CBrCl}^{\bullet-}$ can be resolved and monitored with the mass detection system. The presence of $\text{CHBrCl}^{\bullet-}$, however, does complicate the determination of the product branching ratios. For this same reason, the $\text{CBr}_2^{\bullet-}$ anion was not included in this study. Additionally the $\text{CHF}^{\bullet-}$ anion was not studied since it occurs at the same mass as $\text{O}_2^{\bullet-}$, which is also present in the ion source.

For the perchloro and perbromo reactions, isotopic labeling studies were performed by alternately SIFT-injecting different isotopomers of the reactant ion while monitoring the product isotope distributions; these studies aided in the identification of the product ions and of the reaction mechanism. For the reactions of $\text{CHCl}^{\bullet-}$ with CCl_4 , CHCl_3 , CH_2Cl_2 , and CH_3Cl , careful, quantitative isotope labeling studies were performed. For the reactions of $\text{CCl}_2^{\bullet-}$ with CCl_4 , CHCl_3 , CH_2Cl_2 , and CH_3Cl and for the reactions of $\text{CHBr}^{\bullet-}$ with CH_3Br and $(\text{CH}_3)_3\text{CBr}$, only qualitative results were obtained.

The error reported for the reaction rate constants is one standard deviation of at least three measurements. The uncertainty in the reaction rate constants due to systematic error is $\pm 20\%$ and the uncertainty in the product branching ratios is $\pm 30\%$. Helium buffer gas (99.995%) was purified by passage through a liquid nitrogen-cooled molecular sieve trap. Neutral reagents were purchased from commercial sources and used without further purification. The reactions of $\text{CXY}^{\bullet-}$ with COS indicate that the neutral sample contains a trace amount of H_2S impurity; as a result, the measured rate constants represent an upper bound value. The reported reaction efficiencies are the measured rate constant divided by the calculated collision rate constant ($\text{eff} = k/k_{\text{col}}$). Collision rate constants were calculated from parametrized trajectory collision rate theory.⁷⁶

Electronic structure calculations were performed using the G3 composite technique⁷⁷ provided in the Gaussian 03 suite of programs.⁷⁸ The electronic energy, harmonic frequencies, and rotational constants were determined for the optimized geometries of the reactants and products of the fluorinated and chlorinated reactions. These results were used to evaluate the exothermicities of the proposed mechanisms; a more detailed investigation to include the reaction intermediates and transition states is beyond the scope of this work. The exothermicities for the brominated reactions are not provided since the G3 method does not include fourth row elements.

6.3) Results and Discussion

6.3.1) Reactions of Carbene Anions with Sulfur/Oxygen Containing Species

Table 6.01 displays the experimentally measured reaction rate constants for the reactions of $CXY^{\bullet-}$ with each neutral reagent; Table 6.02 presents product ion branching fractions. Figure 6.01 is a plot of reaction efficiency as a function of anion basicity for the reactions of $CXY^{\bullet-}$ with CS_2 , COS , CO_2 , O_2 , and CO ; N_2O is excluded from this plot since it only reacts with $CF_2^{\bullet-}$. In this figure each trace represents a different neutral reagent and the data points are connected to guide the eye only. The reaction trends presented in this plot are not readily observed in Table 6.01 since the collision rate constants for the reactions of CO_2 and CS_2 are smaller than for COS . The $CHCl^{\bullet-}$ and $CHBr^{\bullet-}$ anions react with similar efficiencies and trends. As expected, replacing a hydrogen atom with a chlorine atom to form $CCl_2^{\bullet-}$ and $CBrCl^{\bullet-}$ substantially decreases the reaction efficiency. The reaction efficiencies and trends for the $CCl_2^{\bullet-}$ and $CBrCl^{\bullet-}$ anions are similar to one another but differ from those of the $CHCl^{\bullet-}$ and $CHBr^{\bullet-}$ anions. The $CF_2^{\bullet-}$ anion displays unique reactivity. This difference in reactivity is, in part, not surprising since the $CF_2^{\bullet-}$ anion has a

Table 6.01: Reaction rate constants ($10^{-10} \text{ cm}^3 \text{ s}^{-1}$) for the reactions of $\text{CXY}^{\bullet-}$ with CS_2 , COS , CO_2 , O_2 , CO , and N_2O .

Neutral reagent	$\text{CHCl}^{\bullet-}$ (384.8; 1.210) ^a	$\text{CHBr}^{\bullet-}$ (380.7; 1.454)	$\text{CF}_2^{\bullet-}$ (377.4; 0.180)	$\text{CCl}_2^{\bullet-}$ (364.2; 1.590)	$\text{CBrCl}^{\bullet-}$ (361; 1.84)
CS_2	10.5 ± 0.7^b	9.14 ± 0.22	10.7 ± 0.3	0.400 ± 0.080	0.162 ± 0.009
COS^c	6.87 ± 0.25	5.27 ± 0.14	5.02 ± 0.17	1.31 ± 0.03	0.850 ± 0.038
CO_2	5.62 ± 0.17	5.13 ± 0.02	$<0.070 \pm 0.002$	<0.001	<0.001
O_2	2.11 ± 0.04	1.80 ± 0.05	2.65 ± 0.03	0.946 ± 0.025	0.748 ± 0.014
CO	1.42 ± 0.25	0.943 ± 0.013	<0.001	<0.001	<0.001
N_2O	<0.001	<0.001	0.178 ± 0.030	<0.001	<0.001

^a The enthalpy of protonation in kcal mol^{-1} and the electron binding energy in eV are given in parentheses; see references 10, 11, 55, and 56. ^b Standard deviation of at least three measurements. ^c Reaction rate constants represent an upper bound value, see experimental section.

Table 6.02: Product ion distributions for the reactions of $CXY^{\bullet-}$ with CS_2 , COS , CO_2 , and O_2 .

Neutral reagent	Product ions	$CH_2^{\bullet-}$ ^b (407.4; 0.652) ^a	$CHCl^{\bullet-}$ (384.8; 1.210)	$CHBr^{\bullet-}$ (380.7; 1.454)	$CF_2^{\bullet-}$ (377.4; 0.180)	$CCl_2^{\bullet-}$ (364.2; 1.590)	$CBrCl^{\bullet-}$ ^c (361; 1.84)	
CS_2	X^-		0.07	0.50		1.00	Cl^- , Br^-	
	$X_2^{\bullet-}$						$BrCl^{\bullet-}$	
	$S^{\bullet-}$	+						
	SH^-	+						
	$CS_2^{\bullet-}$	+				1.00		
	C_2HS^-	+						
	$C_2S_2^{\bullet-}$			0.02	0.01			+
	$CXS^{\bullet-}$			0.18	0.37			
	$CYXS^{\bullet-}$	+		0.73	0.12			
e^-	+							
COS	X^-		0.90	1.00		0.94	Cl^- , Br^-	
	$X_2^{\bullet-}$						$BrCl^{\bullet-}$	
	$S^{\bullet-}$	+						
	$C_2OS^{\bullet-}$			0.03	trace			
	$CXYS^{\bullet-}$	+		0.07		1.00	0.06	
	e^-	+						
CO_2	X^-		0.94	1.00	0.20			
	$CYXO^{\bullet-}$		0.06					
	$C_2X_2O_2^{\bullet-}$				0.80			
	e^-	+						
O_2	X^-		0.60	0.90	0.30	0.58	Cl^-	
	$X_2^{\bullet-}$				0.02	0.24	$BrCl^{\bullet-}$	
	$O^{\bullet-}$	+	0.32	0.07	0.40	0.12	+	
	OH^-		0.05	0.03				
	$O_2^{\bullet-}$				0.28			
	OX^-		0.03			0.04	ClO^-	
	$CX_2O^{\bullet-}$					0.02		

The + sign indicates that the ion was formed. For the $CH_2^{\bullet-}$ ion, X and Y=H; for the $CHCl^{\bullet-}$ and $CHBr^{\bullet-}$ anions, X=halogen and Y=H; for the $CF_2^{\bullet-}$, $CCl_2^{\bullet-}$, and $CBrCl^{\bullet-}$ anion both X and Y=halogen. ^a The enthalpy of protonation in kcal mol⁻¹ and the electron binding energy in eV are given in parentheses; see references 10, 11, 55, and 56. ^b The product ions formed from the reactions of $CH_2^{\bullet-}$ with CS_2 , COS , CO_2 , and O_2 are taken from reference 70. ^c Product branching ratios are not determined because the $CHBrCl^{\bullet-}$ ion was also present in the reaction flow tube.

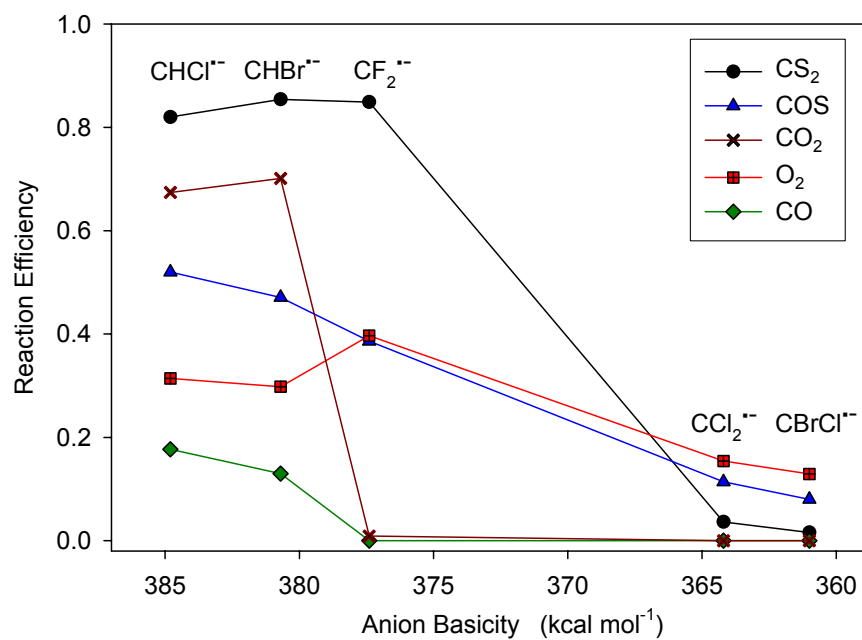


Figure 6.01: Reaction efficiency versus anion basicity. (Lines are only intended to guide eye.)

Table 6.03: Calculated and experimental reaction exothermicities (kcal mol⁻¹) for the reactions of CHCl⁻, CCl₂⁻, and CF₂⁻.

Reaction	calc ^a	exp ^b	BR ^c
CHCl ⁻ + CS ₂ → Cl ⁻ + C ₂ HS ₂ [•]	0		0.07
→ C ₂ S ₂ ^{•-} + HCl	-64		0.02
→ CHClS ^{•-} + CS	-11		0.73
→ CCIS ⁻ + HCS [•]	-6		0.18
CHCl ⁻ + COS → Cl ⁻ + C ₂ HOS [•]	-48		0.90
→ C ₂ OS ^{•-} + HCl	-41		0.03
→ CHClS ^{•-} + CO	-42		0.07
→ CCIS ⁻ + HCO [•]	-4		not obs.
CHCl ⁻ + CO ₂ → Cl ⁻ + C ₂ HO ₂ [•]	-25		0.94
→ C ₂ O ₂ ^{•-} + HCl	-10		not obs.
→ CHClO ^{•-} + CO	-37		0.06
→ CClO ⁻ + HCO [•]	-29	-33	not obs.
CHCl ⁻ + O ₂ → O ^{•-} + CHClO	-66		0.32
→ OH ⁻ + COCl [•]	-88	-91	0.05
→ Cl ⁻ + CHO ₂ [•]	-134	-137	0.60
→ ClO ⁻ + CHO [•]	-68	-70	0.03
CHCl ⁻ + CO → Cl ⁻ + [•] C ₂ HO	-33	-11	>0.99
→ C ₂ O ^{•-} + HCl	-7	-10	Trace
CHCl ⁻ + N ₂ O → CHClN ⁻ + NO [•]	-94	-94	not obs.
→ Cl ⁻ + HCN + NO [•]	-71	-72	not obs.
CCl ₂ ⁻ + CS ₂ → Cl ⁻ + C ₂ ClS ₂ [•]	-26		1.00
→ Cl ₂ ^{•-} + C ₂ S ₂	-5		not obs.
→ CCl ₂ S ^{•-} + CS	+5		not obs.
→ CCIS ⁻ + CCIS [•]	+15		not obs.
CCl ₂ ⁻ + COS → Cl ⁻ + C ₂ ClOS [•]	-21		0.94
→ Cl ₂ ^{•-} + C ₂ OS	+13		not obs.
→ CCl ₂ S ^{•-} + CO	-27		0.06
→ CCIS ⁻ + CClO [•]	+11		not obs.
CCl ₂ ⁻ + CO ₂ → Cl ⁻ + C ₂ ClO ₂ [•]	-6		not obs.
→ Cl ₂ ^{•-} + 2 CO	-32		not obs.
→ CCl ₂ O ^{•-} + CO	-29		not obs.
→ CClO ⁻ + ClCO [•]	-13		not obs.

$\text{CCl}_2^{\bullet-} + \text{O}_2 \rightarrow \text{O}^{\bullet-} + \text{CCl}_2\text{O}$	-44		0.12
$\rightarrow \text{Cl}^- + \text{CClO}_2^{\bullet}$	-116	-140	0.58
$\rightarrow \text{ClO}^- + \text{CClO}^{\bullet}$	-52	-63	0.04
$\rightarrow \text{CCl}_2\text{O}^{\bullet-} + \text{O}$	-39		0.02
$\rightarrow \text{Cl}_2^{\bullet-} + \text{CO}_2$	-171	-170	0.24
$\text{CCl}_2^{\bullet-} + \text{CO} \rightarrow \text{Cl}^- + \text{}^{\bullet}\text{C}_2\text{ClO}$	-5		not obs.
$\rightarrow \text{Cl}_2^{\bullet-} + \text{C}_2\text{O}$	+62		not obs.
$\text{CCl}_2^{\bullet-} + \text{N}_2\text{O} \rightarrow \text{CCl}_2\text{N}^- + \text{NO}^{\bullet}$	-59		not obs.
$\rightarrow \text{Cl}^- + \text{ClCN} + \text{NO}^{\bullet}$	-40	-40	not obs.
$\text{CF}_2^{\bullet-} + \text{CS}_2 \rightarrow \text{CS}_2^{\bullet-} + \text{CF}_2$	-5	-10	1.00
$\rightarrow \text{F}^- + \text{C}_2\text{FS}_2^{\bullet}$	+68		not obs.
$\rightarrow \text{F}_2^{\bullet-} + \text{C}_2\text{S}_2$	+52		not obs.
$\rightarrow \text{CF}_2\text{S}^{\bullet-} + \text{CS}$	-2		not obs.
$\rightarrow \text{CFS}^- + \text{FCS}^{\bullet}$	+25		not obs.
$\text{CF}_2^{\bullet-} + \text{COS} \rightarrow \text{CF}_2\text{S}^{\bullet-} + \text{CO}$	-34		1.00
$\rightarrow \text{F}^- + \text{C}_2\text{FOS}^{\bullet}$	+74		not obs.
$\rightarrow \text{F}_2^{\bullet-} + \text{C}_2\text{OS}$	+69		not obs.
$\rightarrow \text{CFS}^- + \text{FCO}^{\bullet}$	+20		not obs.
$\text{CF}_2^{\bullet-} + \text{CO}_2 \rightarrow \text{F}^- + \text{}^{\bullet}\text{C}_2\text{FO}_2$	+80		not obs.
$\rightarrow \text{F}_2^{\bullet-} + 2 \text{CO}$	+24		not obs.
$\rightarrow \text{CF}_2\text{O}^{\bullet-} + \text{CO}$	-26		not obs.
$\rightarrow \text{CFO}^- + \text{CFO}^{\bullet}$	+6		not obs.
$\rightarrow \text{C}_2\text{F}_2\text{O}_2^{\bullet-}$	-36		1.00
$\text{CF}_2^{\bullet-} + \text{O}_2 \rightarrow \text{O}^{\bullet-} + \text{CF}_2\text{O}$	-68		0.40
$\rightarrow \text{F}^- + \text{}^{\bullet}\text{CFO}_2$	-97		0.30
$\rightarrow \text{O}_2^{\bullet-} + \text{CF}_2$	-5	-7	0.28
$\rightarrow \text{F}_2^{\bullet-} + \text{CO}_2$	-114	-116	0.02
$\text{CF}_2^{\bullet-} + \text{CO} \rightarrow \text{F}^- + \text{}^{\bullet}\text{C}_2\text{FO}$	<i>d</i>		not obs.
$\rightarrow \text{F}_2^{\bullet-} + \text{C}_2\text{O}$	+118		not obs.
$\text{CF}_2^{\bullet-} + \text{N}_2\text{O} \rightarrow \text{CF}_2\text{N}^- + \text{NO}^{\bullet}$	-43	<-4	0.90
$\rightarrow \text{F}^- + \text{FCN} + \text{NO}^{\bullet}$	-7	-10	0.10

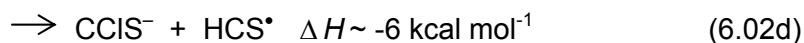
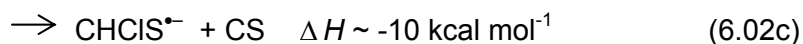
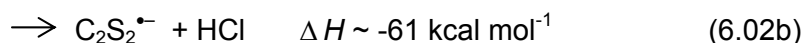
^a G3 calculated reaction enthalpies. ^b Enthalpies of formation are determined from the thermochemical data on the NIST webbook⁷⁹ or from the JANAF thermochemical tables.⁸⁰ ^c This work. ^d Undetermined; the calculation for $^{\bullet}\text{C}_2\text{FO}$ would not converge.

significantly lower electron binding energy than the other ions studied here and, in general, other fluoro-anions typically display distinct reactivity.⁸¹

As demonstrated in Figure 6.01 and by the formation of multiple product ions (Table 6.02), the reactivity of these carbene anions is complex. To be able to address these reactivity trends, we must first discuss the likely reaction mechanisms. In the following sections the reactivity of the $\text{CHCl}^{\bullet-}$, $\text{CHBr}^{\bullet-}$, $\text{CCl}_2^{\bullet-}$, and $\text{CBrCl}^{\bullet-}$ anions will be discussed together while the reactivity of the $\text{CF}_2^{\bullet-}$ anion will be discussed separately. Since our experimental setup does not allow for neutral product detection, the neutral products are inferred from the ionic products, and the structures of the neutral and ionic products are based on molecular stability and on the occurrence of reasonable reaction mechanisms. Electronic structure calculations are used as a guide in determining these structures and mechanisms. The G3 calculated exothermicities for the observed fluorinated and chlorinated reactions are provided throughout the text and in Table 6.03. The calculated results are compared to experimental values when possible.

Reactions of $\text{CHX}^{\bullet-}$ and $\text{CCIX}^{\bullet-}$ ($X=\text{Cl}$ and Br)

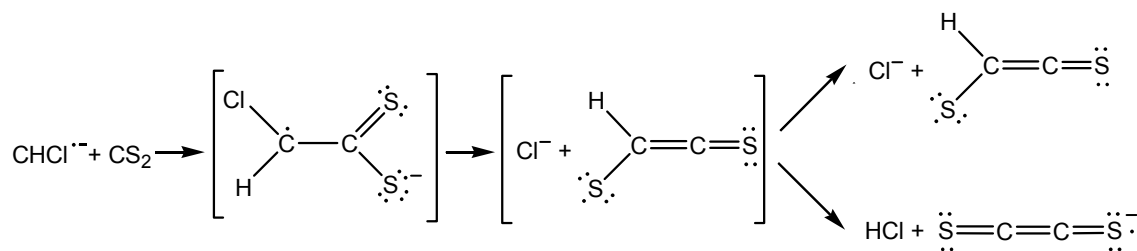
The reactions of $\text{CHX}^{\bullet-}$ ($X=\text{Cl}$ and Br) with CS_2 produce X^- , $\text{C}_2\text{S}_2^{\bullet-}$, $\text{CHXS}^{\bullet-}$, and CXS^- , as shown below for $\text{CHCl}^{\bullet-} + \text{CS}_2$.



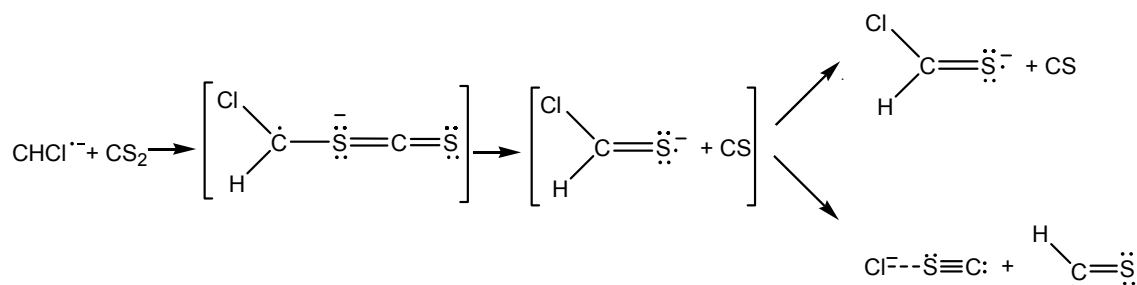
Reactions 6.02a and 6.02b presumably proceed by anion attack on the carbon atom of CS_2 , as shown in Scheme 6.01. These two reactions proceed through an

$[\text{HCIC-CS}_2]^\ominus$ intermediate followed by an intramolecular $\text{S}_\text{N}2$ reaction, where the sulfur atom attacks the β carbon atom to displace Cl^- . A trace amount of $\text{C}_2\text{S}_2^\ominus$ is detected, which is the result of proton transfer before the initial products from 6.02a separate. While proton transfer to form $\text{C}_2\text{S}_2^\ominus$ is thermodynamically favored, it is a minor product whose formation is likely influenced by kinetic or dynamic factors within the product ion-molecule complex. Reactions 6.02c and 6.02d most likely proceed by carbanion attack on the sulfur atom of CS_2 , as shown in Scheme 6.02. Reaction 6.02c is the result of the displacement of neutral CS . The CCIS^- ion (6.02d) is formed from hydrogen atom transfer before the initial products of 6.02c separate; G3 calculations predict that this ion is a $[\text{Cl}^- \bullet \text{S} \equiv \text{C}]$ ion-dipole bound complex.

Scheme 6.01



Scheme 6.02



The reactions of CHX^\ominus ($\text{X} = \text{Cl}$ or Br) with COS and CO_2 proceed similarly to the corresponding reactions with CS_2 ; such parallels in reactivity of anions with these three neutral reactants have previously been reported in the literature.^{64,65} The

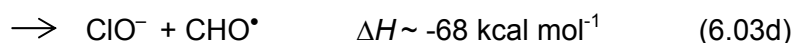
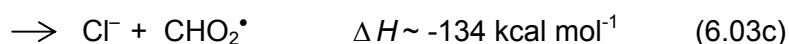
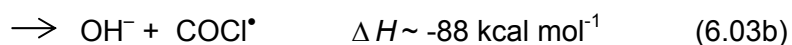
product ions formed are consistent with either attack on the neutral reagent carbon atom, analogous to the mechanism shown in Scheme 6.01, or attack on neutral reagent sulfur (or oxygen) atom, analogous to the mechanism shown in Scheme 6.02. As the neutral reagent is changed from CS₂ to COS and CO₂, sulfur/oxygen atom attack becomes the minor pathway for the CHCl^{•-} anion and is not observed for the CHBr^{•-} anion.

The product ions formed in the reactions of CCl₂^{•-} and CBrCl^{•-} with CS₂ are consistent with a mechanism that is analogous to Scheme 6.01 only. For the reactions of CBrCl^{•-} with CS₂, either Cl⁻ or Br⁻ can be displaced by an intramolecular S_N2 reaction. The formation of BrCl^{•-} is due to halogen atom abstraction, in contrast to proton transfer, before the initial products separate; in some encounters, the electron remains with C₂S₂. Both of these dihalo anions react with COS but do not react with CO₂ within our detection limits. The reaction of CCl₂^{•-} with COS primarily proceeds by anion attack on the carbon atom of COS; additionally, a minor channel of anion attack on the sulfur atom of COS is also observed. The CBrCl^{•-} anion reacts with COS exclusively by attack on carbon.

An interesting observation is that the reaction efficiencies (Figure 6.01) for the mono- and dihalocarbene anions do not mirror each other. For the CHCl^{•-} and CHBr^{•-} anions, the reaction with CS₂ is most efficient, followed by CO₂, then by COS. In contrast for these three neutral reactants, the efficiency is greatest for the reactions of CCl₂^{•-} and CBrCl^{•-} with COS, followed by CS₂, while CO₂ is below our detection limit. As established above, these carbene anions primarily react with this neutral series by nucleophilic attack on the neutral reagent carbon atom; with the exception of CHX^{•-} with CS₂, anion attack on the neutral reagent sulfur/oxygen atom is at most a minor pathway. This mechanism (shown in Scheme 6.01) is complex

and multiple factors influence the observed reaction efficiency. If we consider the first step of the reaction mechanism, we would expect the reactivity to increase as the number of oxygen atoms in the neutral reagent increases, since in CO₂ there is a greater partial positive charge on the carbon atom as compared to CS₂. However, while oxygen is more electronegative, sulfur can expand its valence and therefore more readily accept the negative charge. Following the anion attack on the carbon atom of the neutral reagent, halide displacement occurs as a result of an intramolecular S_N2 reaction. Here we must consider two further factors, the nature of the leaving group (Cl⁻ or Br⁻) and of the nucleophile (S or O). It is known that Br⁻ is a better leaving group than Cl⁻ and in the gas-phase the nucleophilicity of sulfur anions are comparable to oxygen anions.⁸² Since multiple factors must be considered, predicting the reaction efficiency trend is not straightforward. Furthermore, it is likely that the individual factors may have a different overall net effect for different anions, and hence the observed trends for the mono- and dihalocarbene anions differ from one another.

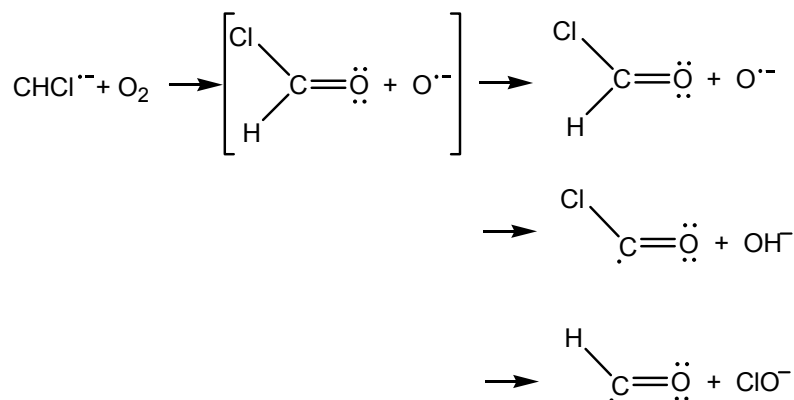
Both CHCl⁻ and CHBr⁻ react with O₂ with the same efficiency to produce analogous products. The reaction of CHCl⁻ with O₂ produces O⁻, OH⁻, Cl⁻, and ClO⁻.



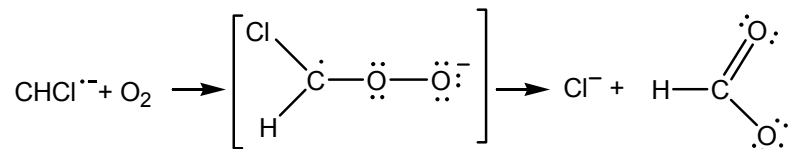
Reaction 6.03a proceeds by an S_N2 reaction with anion attack at the oxygen to displace O⁻. Before the product ion-molecule complex dissociates, O⁻ can abstract either a hydrogen or chlorine atom to form OH⁻ (6.03b) or ClO⁻ (6.03d), respectively

(Scheme 6.03). The formation of Cl^- in 6.03c is the major product. Analogous to the above reactions with CS_2 , COS , and CO_2 , where the displaced halide is also observed, this reaction most likely proceeds through an $[\text{HCIC-O-O}]^{\bullet-}$ intermediate followed by an intra-molecular $\text{S}_{\text{N}}2$ reaction where, in a concerted step, the terminal O atom attacks the carbon to displace Cl^- (Scheme 6.04).

Scheme 6.03



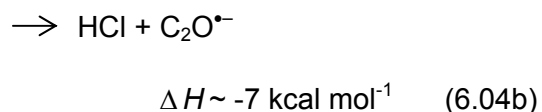
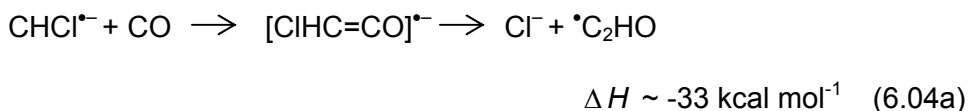
Scheme 6.04



The dihalocarbanions, $\text{CCl}_2^{\bullet-}$ and $\text{CBrCl}^{\bullet-}$, react with O_2 to form similar product ions as the corresponding reactions of $\text{CHX}^{\bullet-}$ ($\text{X} = \text{Cl}$ and Br) with O_2 , the majority of which can be explained by the above mechanisms. The reaction of $\text{CCl}_2^{\bullet-}$ with O_2 additionally produces minor amounts of $\text{CCl}_2\text{O}^{\bullet-}$, which is due to electron transfer from $\text{O}^{\bullet-}$ within the product ion-molecule complex. The reactions of $\text{CCl}_2^{\bullet-}$ and $\text{CBrCl}^{\bullet-}$ with O_2 also produce the dihalide anions. These dihalide anions could be formed from a mechanism similar to Scheme 6.04, where X atom abstraction occurs within the product ion-molecule complex before the initial products separate to form $\text{XY}^{\bullet-}$ and CO_2 . Interestingly, the product ions formed in the

reactions of $\text{CCl}_2^{\bullet-}$ and $\text{CBrCl}^{\bullet-}$ with O_2 are comparable to the carbene cation reaction of $\text{CBr}_2^{\bullet+}$ with O_2 , which has previously been studied by Cooks and co-workers.⁸³ In that work, the authors speculate that this reaction proceeds through a $\text{Br}_2\text{CO}_2^{\bullet+}$ intermediate, which can eliminate CO_2 to form $\text{Br}_2^{\bullet+}$. This intermediate can also rearrange to form BrCO^+ and BrO^\bullet and, in a competitive process, BrCO^\bullet and BrO^+ .

Both $\text{CHCl}^{\bullet-}$ and $\text{CHBr}^{\bullet-}$ react with CO to primarily produce the displaced halide (6.04a). For the reaction of $\text{CHCl}^{\bullet-}$, a trace amount of $\text{C}_2\text{O}^{\bullet-}$ is also formed (6.04b), while for the reaction of $\text{CHBr}^{\bullet-}$ a trace amount of $\text{C}_2\text{HO}^\bullet$ is detected.



The formation of these products is consistent with a mechanism where the anion attacks the carbon atom of CO . In an analogous manner to the other reactions discussed thus far, Cl^- could be displaced by an intramolecular $\text{S}_{\text{N}}2$ mechanism where the O atom attacks the carbon atom in the β position. However, if this were indeed the case, the resulting neutral species is probably not stable. Instead, if the addition of $\text{CHCl}^{\bullet-}$ to CO is sufficiently exothermic, the C-Cl bond could break to produce very stable products, Cl^- and $\text{H-C}\equiv\text{C-O}^\bullet$. Alternatively, the initially formed intermediate, may undergo a retro-carbene reaction to make HCl and $:\text{C}=\text{C}=\text{O}^{\bullet-}$ directly; proton transfer within the product ion-molecule complex then would form Cl^- and HCCO^\bullet . In this case, both mechanisms are feasible; however, neither one likely occurs for the other reactions discussed above that also produce the displaced

halide as less energy is required to form a C=O bond from a C≡O bond, than to form a C-O bond from a C=O bond. Neither $\text{CCl}_2^{\bullet-}$ nor $\text{CBrCl}^{\bullet-}$ react with CO, consistent with calculations, which predict the reaction of $\text{CCl}_2^{\bullet-}$ with CO to be endothermic.

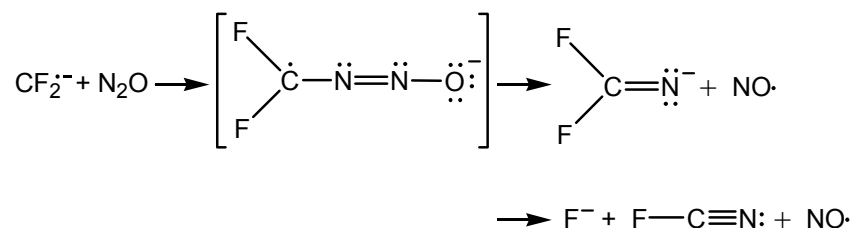
Reactions of $\text{CF}_2^{\bullet-}$

The reactivity of the $\text{CF}_2^{\bullet-}$ anion is different from that of other carbene anions, due in part, to its lower electron binding energy ($\text{eBE}(\text{CF}_2^{\bullet-})=0.180 \text{ eV}$).¹⁰ As a result, this anion can react by electron transfer. This is the case for the reaction of $\text{CF}_2^{\bullet-}$ with CS_2 , where electron transfer is the only pathway observed, consistent with calculations, which predict that electron transfer is the only exothermic pathway. The reactions of $\text{CF}_2^{\bullet-}$ with COS, CO_2 , and O_2 show some similarities and some differences to the other anions discussed above. For example, $\text{CF}_2^{\bullet-}$ reacts with COS via anion attack on the sulfur atom of COS to exclusively produce CF_2S^- , analogous to Scheme 6.02. A mechanism analogous to Scheme 6.01 to form F^- is predicted to be endothermic. The reaction of $\text{CF}_2^{\bullet-}$ with CO_2 exclusively forms $\text{C}_2\text{F}_2\text{O}_2^{\bullet-}$. This is most likely the result of anion addition to the carbon atom of CO_2 , similar to the addition reaction of OH^- with CO_2 ,⁸⁴ rather than from a clustering process. For the reaction of $\text{CF}_2^{\bullet-}$ with O_2 , electron transfer is exothermic and this pathway is viable as evident by the formation of $\text{O}_2^{\bullet-}$. Additionally this reaction produces $\text{O}^{\bullet-}$, F^- , and $\text{F}_2^{\bullet-}$, which are analogous to the products formed from $\text{CClX}^{\bullet-}$ ($\text{X}=\text{Cl}$ and Br) with O_2 .

It has previously been demonstrated that neither $\text{CHCl}^{\bullet-}$ nor $\text{CHBr}^{\bullet-}$ react with N_2O ,⁵⁵ even though the reaction of $\text{CHCl}^{\bullet-}$ with N_2O is predicted to be exothermic. As would be expected, $\text{CCl}_2^{\bullet-}$ and $\text{CBrCl}^{\bullet-}$ also do not react with N_2O . $\text{CF}_2^{\bullet-}$, however, does react with N_2O to produce CF_2N^- and F^- in a 0.90 to 0.10 branching

fraction, respectively. This reaction most likely proceeds by attack of the anion on the terminal nitrogen atom of N_2O , as shown in Scheme 6.05. The addition of $\text{CF}_2^{\bullet-}$ is sufficiently exothermic ($\Delta_{\text{rxn}}H \sim -43 \text{ kcal mol}^{-1}$) such that F^- can be displaced. In this case, addition-dissociation is similar to the reaction of $\text{CHX}^{\bullet-}$ with CO , where X^- is displaced. The $\text{CF}_2^{\bullet-}$ anion, however, does not react with CO ; this reaction is predicted to be endothermic. Similar nitrogen atom transfer reactions have previously been observed for reactions of radical anions and N_2O .^{67,85}

Scheme 6.05

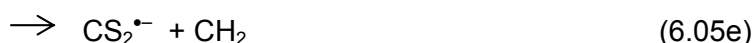
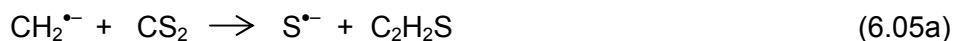


So far we have discussed the differences in the reactivity of $\text{CF}_2^{\bullet-}$ in terms of its lower electron binding energy. Several groups have attributed the stability of the neutral halocarbene singlet state (and destabilization of the triplet state) to two factors, the electronegativity of the substituents and the ability of the halogen to donate electron density to the carbon through π -backbonding.^{11,54} These two effects are magnified in the case of neutral CF_2 , since fluorine is the most electronegative halogen and since the C-F bond is shorter than the C-Cl and C-Br bonds and, therefore, there is good overlap between the carbon and fluorine atom π -orbitals. As a result, the electron binding energy of $\text{CF}_2^{\bullet-}$ (and $\text{CHF}^{\bullet-}$) is significantly lower than that of the chloro and bromo carbene anions ($\text{eBE}(\text{CHCl}^{\bullet-}) = 1.210 \text{ eV}$; $\text{eBE}(\text{CHBr}^{\bullet-}) = 1.454 \text{ eV}$; $\text{eBE}(\text{CCl}_2^{\bullet-}) = 1.590 \text{ eV}$; $\text{eBE}(\text{CBrCl}^{\bullet-}) = 1.84 \text{ eV}$).^{10,11,56} While this explanation accounts for its propensity to undergo electron transfer, it clearly does not explain every difference among $\text{CF}_2^{\bullet-}$ and the other anions studied here.

In general, for these carbene anions, the reaction efficiency increases as the anion basicity increases. It is not surprising that $\text{CF}_2^{\bullet-}$ is considerably more basic than $\text{CCl}_2^{\bullet-}$ and $\text{CBrCl}^{\bullet-}$; thus, due to its basicity and its electron binding energy, we would expect $\text{CF}_2^{\bullet-}$ to be highly reactive; this expectation is experimentally observed in some instances. Additionally, $\text{CF}_2^{\bullet-}$ is a hard base due to its small size; typically hard bases are good nucleophiles. However, since fluorine is so electronegative, the fluorine substituents inductively withdraw electron density from the carbon σ -orbital, decreasing the nucleophilicity of the anion. As a result, $\text{CF}_2^{\bullet-}$ reacts with COS fairly efficiently by sulfur atom transfer but does not react with CO.

Comparison to the $\text{CH}_2^{\bullet-}$ anion

The product ions formed in the reactions of $\text{CH}_2^{\bullet-}$ with CS_2 , COS, CO_2 , O_2 , CO, and N_2O have been previously documented.⁷⁰ The ionic products formed in the reactions with CS_2 , COS, CO_2 , and O_2 are included in Table 6.02. The reaction of $\text{CH}_2^{\bullet-}$ with CS_2 shows some similarities to the reactions of $\text{CXY}^{\bullet-}$ studied here.



Evidence of anion addition to the carbon atom of CS_2 is observed in 6.05a-c; however, instead of the sulfur atom attacking the β carbon atom in an intramolecular $\text{S}_\text{N}2$ reaction, $\text{S}^{\bullet-}$ is displaced. The product ions formed in 6.05b and c are the result of hydrogen atom or proton transfer within the product ion-molecule complex of 6.05a before the initial products separate. In contrast, sulfur anion displacement is

not observed for the reactions of $\text{CHX}^{\bullet-}$ and $\text{CCIX}^{\bullet-}$ ($\text{X} = \text{Cl}$ and Br) with CS_2 since halides are better leaving groups. Reaction 6.05d is the result of carbanion attack on the sulfur atom of CS_2 followed by loss of CS , analogous to Scheme 6.02.

Reaction 6.05e proceeds by electron transfer, which parallels the reaction of $\text{CF}_2^{\bullet-}$ with CS_2 , again due to the low electron binding energy of $\text{CH}_2^{\bullet-}$. The $\text{CH}_2^{\bullet-}$ and $\text{CF}_2^{\bullet-}$ anions show additional parallels in reactivity. For example, both anions react with N_2O by attack on the terminal nitrogen. A notable difference in the reactivity of $\text{CH}_2^{\bullet-}$ is that this anion has a propensity to react via associative or reactive electron detachment. In fact, electron detachment is the major channel for the reaction of $\text{CH}_2^{\bullet-}$ with CS_2 (6.05f) and the sole channel for reactions with CO_2 and CO . While we cannot fully exclude the possibility of electron detachment in the present study of $\text{CF}_2^{\bullet-}$, it is at most a minor process.

6.3.2) Reactions of $\text{CHX}^{\bullet-}$ and $\text{CCIX}^{\bullet-}$ ($\text{X} = \text{Cl}$ and Br) with Halogenated Species

Table 6.04 displays the experimentally measured reaction rate constants for the reactions of $\text{CXY}^{\bullet-}$ with each halogenated neutral reagent. Table 6.05 presents product ion branching fractions for the reactions of $\text{CXY}^{\bullet-}$ with CCl_4 , CHCl_3 , and CH_2Cl_2 ; for the reactions of $\text{CXY}^{\bullet-}$ with CH_3Cl , CH_3Br , and $(\text{CH}_3)_3\text{CBr}$ the displaced halide is the sole ionic product. As demonstrated in Table 6.05 by the number of ionic products formed, these anions display diverse chemistry. In order to elucidate the likely reaction mechanisms, a detailed isotopic labeling study was performed for the reactions of $\text{CHCl}^{\bullet-}$.

Reactions of $\text{CHCl}^{\bullet-}$ with CCl_4 , CHCl_3 , CH_2Cl_2 , and CH_3Cl

For the reactions of $\text{CHCl}^{\bullet-}$ with CCl_4 , CHCl_3 , CH_2Cl_2 , and CH_3Cl , both the $\text{CH}^{35}\text{Cl}^{\bullet-}$ and $\text{CH}^{37}\text{Cl}^{\bullet-}$ isotopomers were separately mass selected and injected into

Table 6.04: Reaction rate constants ($10^{-10} \text{ cm}^3 \text{ s}^{-1}$) for the reactions of $\text{CXY}^{\bullet-}$ with CCl_4 , CHCl_3 , CH_2Cl_2 , CH_3Cl , CH_3Br , and $(\text{CH}_3)_3\text{CBr}$.

	$\text{CHCl}_2^{\bullet-}$ (384.8; 1.210) ^a	$\text{CHBr}_2^{\bullet-}$ (380.7; 1.454)	$\text{CF}_2^{\bullet-}$ (377.4; 0.180)	$\text{CCl}_2^{\bullet-}$ (364.2; 1.59)	$\text{CBrCl}^{\bullet-}$ (361; 1.84)
CCl_4	9.26 ± 0.12^b	7.98 ± 0.11	9.11 ± 0.14	5.62 ± 0.10	4.39 ± 0.18
CHCl_3	11.3 ± 0.4	8.04 ± 0.11	9.60 ± 0.10	5.31 ± 0.07	3.82 ± 0.14
CH_2Cl_2	11.8 ± 0.4	8.01 ± 0.17	4.52 ± 0.07	<0.001	<0.001
CH_3Cl	2.62 ± 0.10	0.933 ± 0.015	3.03 ± 0.02	0.003 ± 0.001	<0.001
CH_3Br	7.46 ± 0.06	4.98 ± 0.14	6.99 ± 0.09	0.665 ± 0.11	0.183 ± 0.002
<i>d-KIE</i>	0.99 ± 0.03	1.00 ± 0.04	1.01 ± 0.02	1.01 ± 0.02	1.01 ± 0.06
$(\text{CH}_3)_3\text{CBr}$	10.1 ± 0.1	5.78 ± 0.14	6.75 ± 0.02	<0.001	<0.001
<i>d-KIE</i>	1.14 ± 0.04	1.86 ± 0.08	1.37 ± 0.04	-	-

^a The anion basicity in kcal mol^{-1} and the electron binding energy in eV are given in parentheses; see references 10, 11, 55, and 56. ^b Standard deviation of at least three measurements.

Table 6.05: Product ion branching fractions for the reactions of $CXY^{\bullet-}$ with CCl_4 , $CHCl_3$, and CH_2Cl_2 .

neutral reagent	Product ions	$CHCl^{\bullet-}$ (384.8; 1.210) ^a	$CHBr^{\bullet-}$ (380.7; 1.454)	$CF_2^{\bullet-}$ (377.4; 0.180)	$CCl_2^{\bullet-}$ (364.2; 1.59)	$CBrCl^{\bullet-}$ ^b (361; 1.84)
CCl_4	Cl^-			0.97	0.06	+
	$Cl_2^{\bullet-}$				0.04	+
	$CHCl_2^-$	trace				
	CCl_3^-	1.00	1.00	0.03	0.90	+
	$CBrCl_2^-$					+
$CHCl_3$	Cl^-	trace		0.43	0.23	+
	$Cl_2^{\bullet-}$	trace			0.03	+
	$CHCl_2^-$	0.21				
	CCl_3^-	0.79	1.00	0.57	0.74	+
	Br^-					+
	$BrCl^{\bullet-}$					+
CH_2Cl_2	Cl^-	0.10	0.23	0.96		
	$Cl_2^{\bullet-}$	trace		0.03		
	$CHCl_2^-$	0.90	0.67	0.01		
	Br^-		0.08			
	$BrCl^{\bullet-}$		0.02			

^a The enthalpy of protonation in kcal mol^{-1} and the electron binding energy in eV are given in parentheses; see references 10, 11, 55, and 56. The + sign indicates that the ion was formed. ^b Product branching ratios are not determined because the $CHBrCl^-$ ion was also present in the reaction flow tube.

Table 6.06: Reaction rate constants ($10^{-10} \text{ cm}^3 \text{ s}^{-1}$) and product ion branching ratios for the reactions of $\text{CH}^{35}\text{Cl}^{\bullet-}$ with $\text{CH}_n\text{Cl}_{4-n}$ ($n=0-3$) and product ion isotope distributions for the reactions of $\text{CH}^{35}\text{Cl}^{\bullet-}$ and $\text{CH}^{37}\text{Cl}^{\bullet-}$ with $\text{CH}_n\text{Cl}_{4-n}$ ($n=0-3$).

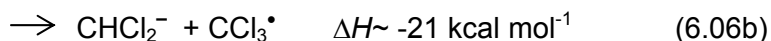
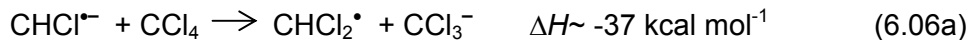
$\text{CH}_n\text{Cl}_{4-n}$	k	ionic products	branching fraction ^a	product ion isotope distributions ^b	
				injection of $\text{CH}^{35}\text{Cl}^{\bullet-}$	injection of $\text{CH}^{37}\text{Cl}^{\bullet-}$
CH_3Cl	2.62 ± 0.10	Cl^-	1.00	78:22	70:30
CH_2Cl_2	11.8 ± 0.4	Cl^-	0.10	78:22	68:32
		$\text{Cl}_2^{\bullet-}$	trace	73:22:5	26:57:17
		CHCl_2^-	0.90	57:37:6	57:37:6
CHCl_3	11.3 ± 0.4	Cl^-	0.05	81:19	59:41
		$\text{Cl}_2^{\bullet-}$	trace	71:25:4	28:55:17
		CHCl_2^-	0.15	60:35:5	49:44:7
		CCl_3^-	0.80	44:43:12:1	45:42:12:1
CCl_4	9.26 ± 0.12	CHCl_2^-	trace	68:28:4	8:64:28
		CCl_3^-	1.00	45:41:13:1	44:42:13:1

^a The errors for the product ion branching fractions are $\pm 30\%$. ^b The error associated with the product ion isotope distributions is ± 0.05 for Cl^- and $\text{Cl}_2^{\bullet-}$ and ± 0.02 for CHCl_2^- and CCl_3^- . The natural abundance isotope distributions are: Cl^- (76:24); $\text{Cl}_2^{\bullet-}$ (57:37:6); CHCl_2^- (57:37:6); CCl_3^- (44:42:13:1).

the reaction flow tube while monitoring the product ion isotope distributions.

Reaction rate constants, product ion branching fractions, and product ion isotope distributions are provided in Table 6.06.

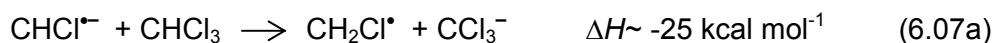
The $\text{CHCl}^{\bullet-}$ anion reacts with CCl_4 to primarily produce CCl_3^- and a trace amount of CHCl_2^- , as shown in 6.06a-b.



The formation of these products is consistent with attack on chlorine causing displacement of CCl_3^- or chlorine atom transfer to form CHCl_2^- ; for both pathways, electron transfer can occur before the initial products separate. Similar reactivity has been reported for the reactions of other open and closed shell anions with CCl_4 .^{74,86,87}

As predicted by this mechanism, the CCl_3^- ion is produced with an isotope distribution that reflects the natural Cl atom abundance in CCl_3 (44:42:13:1); hence this distribution does not change for different reactant ion isotopomers. In contrast, the CHCl_2^- product isotope distribution is skewed toward the reactant ion isotopomer.

The reactions of $\text{CHCl}^{\bullet-}$ with CHCl_3 and CH_2Cl_2 primarily occur via proton transfer (6.07a and 6.08) to produce CCl_3^- and CHCl_2^- , respectively. As expected, the isotope distributions of these product ions are not altered upon changing the reactant ion isotopomer.

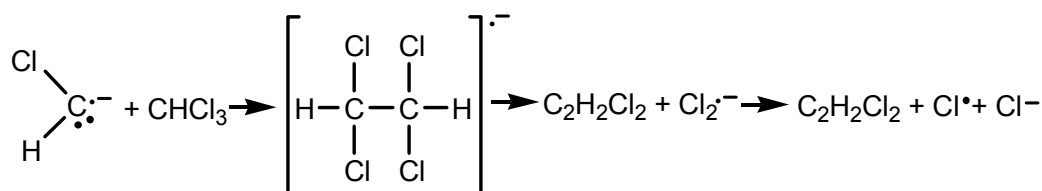


The reaction of $\text{CHCl}^{\bullet-}$ with CHCl_3 (6.07b) additionally proceeds by anion attack on Cl to produce CHCl_2^- (analogous to 6.06a). The isotope distribution of this product ion changes when the reactant ion isotopomer is changed, consistent with

thermoneutral electron transfer within the product ion-molecule complex. An intriguing result of these reactions is the formation of $\text{Cl}_2^{\bullet-}$ and Cl^- ions, and that changing the $\text{CHCl}^{\bullet-}$ isotopomers affects the isotope distributions of both of these product ions. For example, when $\text{CH}^{37}\text{Cl}^{\bullet-}$ is allowed to react with CHCl_3 , all three isotopomers of $\text{Cl}_2^{\bullet-}$ are detected, however the isotope distribution is skewed to reflect incorporation of ^{37}Cl . Likewise although both Cl^- isotopes are detected, $^{37}\text{Cl}^-$ exceeds the natural abundance. These observations suggest that the products must result from a mechanism that partially scrambles the reactant ion and neutral reagent Cl atoms.

The formation of both $\text{Cl}_2^{\bullet-}$ and Cl^- is consistent with an insertion-elimination mechanism, shown below in Scheme 6.06 for the reaction of $\text{CHCl}^{\bullet-}$ with CHCl_3 .

Scheme 6.06

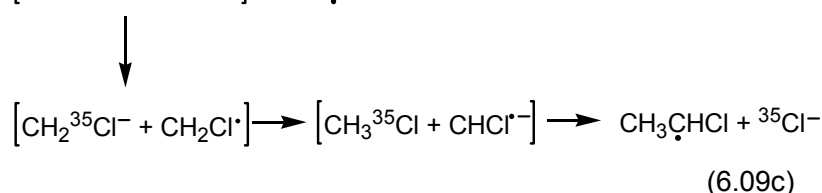
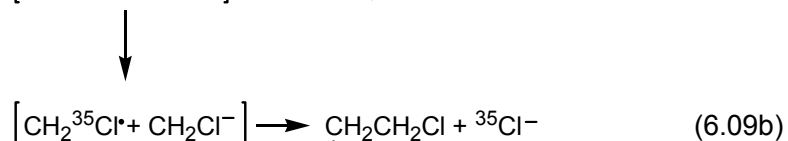
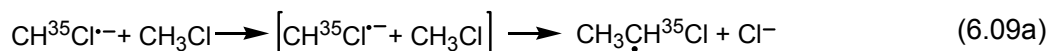


Presumably the first step of this reaction involves the formation of a σ - π complex, where the singly occupied π -orbital of the anion overlaps with the C-Cl σ -bond of the neutral species to transfer an electron. Neutral $:\text{CHCl}$ then inserts into the Cl-C bond in a concerted step, which proceeds through a three-centered transition state where the Cl atom of CHCl_3 attacks the carbene C atom and the carbene lone pair attacks the C atom of CHCl_3 . Insertion of $:\text{CHCl}$ forms the $[\text{CHCl}_2\text{CHCl}_2]^{\bullet-}$ intermediate, where the extra electron is localized on a Cl atom in a low-lying σ -type orbital. This intermediate is unstable, and eliminates $\text{Cl}_2^{\bullet-}$; the overall reaction is sufficiently exothermic ($\Delta H \sim -80 \text{ kcal mol}^{-1}$) such that $\text{Cl}_2^{\bullet-}$ can dissociate into Cl^{\bullet}

and Cl^- . Insertion of $:\text{CH}^{35}\text{Cl}$ into a $\text{Cl}-\text{C}$ bond results in a Cl^- (82:18) and $\text{Cl}_2^{\bullet-}$ (67:30:3) isotope distribution, while insertion of $:\text{CH}^{37}\text{Cl}$ results in a Cl^- (57:43) and $\text{Cl}_2^{\bullet-}$ (29:56:15) isotope distribution. These predictions are in agreement with the measured Cl^- and $\text{Cl}_2^{\bullet-}$ isotope distributions for the reaction of $\text{CHCl}_2^{\bullet-}$ with CHCl_3 . The predictions fall slightly outside of the experimental error bars for the reaction of $\text{CHCl}_2^{\bullet-}$ with CH_2Cl_2 ; however, the occurrence of minor amounts of $\text{S}_{\text{N}}2$ substitution would influence the Cl isotope distribution. Despite this, the predicted distributions for an insertion-elimination mechanism provide the best agreement with experiment compared to other possible mechanisms. Furthermore, these results indicate that insertion occurs into a $\text{C}-\text{Cl}$ bond rather than into a $\text{C}-\text{H}$ bond. (Insertion into a $\text{C}-\text{H}$ bond results in a Cl^- (88:12) and $\text{Cl}_2^{\bullet-}$ (76:24:0) isotope distribution for the reaction of $\text{CH}^{35}\text{Cl}_2^{\bullet-}$ and a Cl^- (38:62) and $\text{Cl}_2^{\bullet-}$ (0:76:24) isotope distribution for the reaction of $\text{CH}^{37}\text{Cl}_2^{\bullet-}$.) In solution carbenes typically insert into $\text{C}-\text{H}$ bonds; however, in the gas-phase insertion into a $\text{C}-\text{Cl}$ bond is favored since the addition of an extra electron increases the nucleophilicity of the Cl atom.

The reaction of $\text{CHCl}_2^{\bullet-}$ with CH_3Cl exclusively produces Cl^- . These results are in excellent agreement with the work of Nibbering and co-workers, which show a slightly skewed Cl^- isotope distribution for the reaction of $\text{CH}^{35}\text{Cl}_2^{\bullet-}$ with CH_3Cl (3% deviation from the $^{35}\text{Cl}:$ ^{37}Cl natural abundance of 76:24),⁵⁶ however, we propose an alternate, energetically favorable mechanism to explain the skewed Cl isotope distribution. The authors proposed that this reaction proceeds by two pathways, as shown in 6.09a and 6.09b. We agree that the primary path (6.09a) is a traditional $\text{S}_{\text{N}}2$ reaction to produce Cl^- and the $\text{CH}_3\text{CH}^{35}\text{Cl}^{\bullet}$ radical, where the displaced halide ion is produced with an isotope distribution representative of the Cl atom natural isotope abundance. Additionally, it was suggested that this reaction proceeds by a

minor second path (6.09b), where the anion abstracts a proton from methyl chloride prior to S_N2 substitution; the result of this pathway is the formation of ³⁵Cl⁻ and ClCH₂CH₂[•]. Instead, we propose a mechanism (6.09c) in which the chlorine atoms are scrambled by two proton exchanges. In this process, CH³⁵Cl⁻ and CH₃Cl enter a



long-lived ion-dipole complex which typically contains ~15-20 kcal mol⁻¹ excess energy.⁸⁸ The first step of the exchange, the proton transfer reaction of CH³⁵Cl⁻ with CH₃Cl, is endothermic (~15 kcal mol⁻¹) and consumes most of the complexation energy; thus, it seems unlikely that the S_N2 reaction of CH₂³⁵Cl[•] with CH₂Cl⁻ (6.09b) could proceed past an S_N2 reaction barrier despite the fact that the overall reaction is exothermic. Instead, back transfer of a proton to form [CH₃³⁵Cl + CHCl^{•-}] restores the complexation energy, scrambles the Cl atoms, and allows for an S_N2 reaction to occur. Reaction 6.09c produces different isotopomers of the reactants and products in 6.09a through an energetically favorable mechanism.

Reactions of CXY⁻ with CCl₄, CHCl₃, CH₂Cl₂, and CH₃Cl

Although the reactions of CCl₂⁻, CHBr⁻, and CBrCl⁻ have not been explicitly discussed, all of the observed ionic products (Table 6.05) can be explained by the previously outlined mechanisms. Additionally, isotopic labeling studies for the reactions of CCl₂⁻ with this neutral series were performed by alternately SIFT-injecting the C³⁵Cl³⁵Cl⁻ and C³⁷Cl³⁷Cl⁻ isotopomers while monitoring the change in

the product ion isotope distributions. While only a qualitative study was performed, these results are in agreement with the previously discussed mechanisms. Notably, the reactions of $\text{CCl}_2^{\bullet-}$ with CCl_4 and CHCl_3 produce minor amounts of Cl^- and $\text{Cl}_2^{\bullet-}$, analogous to the reactions of $\text{CHCl}^{\bullet-}$ with CHCl_3 and CH_2Cl_2 . Similarly, for both reactant ions, the isotopic distributions for the Cl^- and $\text{Cl}_2^{\bullet-}$ product ions differ when different isotopomers of the reactant anion are allowed to react, reflecting the incorporation of the reactant anion chlorine atoms; this observation is consistent the occurrence of an insertion-elimination mechanism.

One further interesting observation is that the reaction of $\text{CCl}_2^{\bullet-}$ with CCl_4 (eq 6.10) produces CCl_3^- with an isotope distribution that reflects the natural Cl atom abundance in CCl_4 .



This reaction is analogous to reactions of $\text{CHCl}^{\bullet-}$ with CCl_4 and CHCl_3 (6.06a and 6.07b); however, these results allow us to assign an $\text{S}_{\text{N}}2$ type mechanism, where the $\text{CCl}_2^{\bullet-}$ anion attacks a Cl atom of CCl_4 to displace CCl_3^- rather than a mechanism, where the $\text{CCl}_2^{\bullet-}$ anion abstracts a neutral Cl atom from CCl_4 . Additionally, in contrast to 6.06a and 6.07b, thermoneutral electron transfer does not occur within the product ion-molecule complex; this may reflect the large geometry differences, and hence poor Franck-Condon overlap, between the CCl_3 anion and radical.

The $\text{CF}_2^{\bullet-}$ anion displays unique reactivity as apparent in the reported reaction efficiencies and product ion distributions (Tables 6.04 and 6.05). As previously discussed, this difference is partially due to the lower electron binding energy of the $\text{CF}_2^{\bullet-}$ anion. As a result, dissociative electron transfer to produce Cl^- is also possible and is observed for the reactions of $\text{CF}_2^{\bullet-}$ with CCl_4 and CHCl_3 . Additionally the $\text{CF}_2^{\bullet-}$ anion displays increased nucleophilicity as demonstrated in the

reaction of CF_2^{\ominus} with methyl chloride. The CF_2^{\ominus} anion is $\sim 7.5 \text{ kcal mol}^{-1}$ less basic than the CHCl^{\ominus} anion, however, both anions react at approximately the same reaction efficiency; typically nucleophilicity scales with anion basicity. This is consistent with CF_2^{\ominus} being a hard base and hence a good nucleophile. This idea, however, is in contrast to the fact that fluorine atoms are electronegative, and thus the fluorine substituents on CF_2^{\ominus} inductively withdraw electron density from the carbon σ -orbital, decreasing the nucleophilic character (as observed in the above section for the reactions of CF_2^{\ominus} with sulfur and oxygen containing species). These studies illuminate the complexity of the CF_2^{\ominus} anion nucleophilicity and, due to the importance of $\text{S}_{\text{N}}2$ reactions, this aspect remains a clear target for further experimental and theoretical study.

Figure 6.02 is a plot of reaction efficiency versus the number of chlorine atoms in the neutral reagent series, CCl_4 , CHCl_3 , CH_2Cl_2 , and CH_3Cl . In general the reaction efficiency increases as the number of chlorine atoms in the neutral substrate increases. This trend is not apparent upon inspection of the overall reaction rate constants in Table 6.04, since the reactions with nonpolar CCl_4 have a smaller collisional component than the other reactions studied here. In contrast, the reaction efficiency decreases as the number of chlorine atoms in the anion increases as evident for the reactions of CHCl^{\ominus} , CHBr^{\ominus} , CCl_2^{\ominus} , and CBrCl^{\ominus} . This trend simply reflects the relative stability of the reactant anions.

The reactions of CXY^{\ominus} with CH_3Cl are the least efficient of the series studied here. These reactions exclusively proceed via an $\text{S}_{\text{N}}2$ reaction on carbon to displace Cl^- . Substitution reactions of this type have been the focus of intense study.⁸⁹⁻⁹¹ It is well established that the rates of these reactions are controlled by the crossing of a central barrier; as a result, exothermic reactions can proceed at a rate slower than

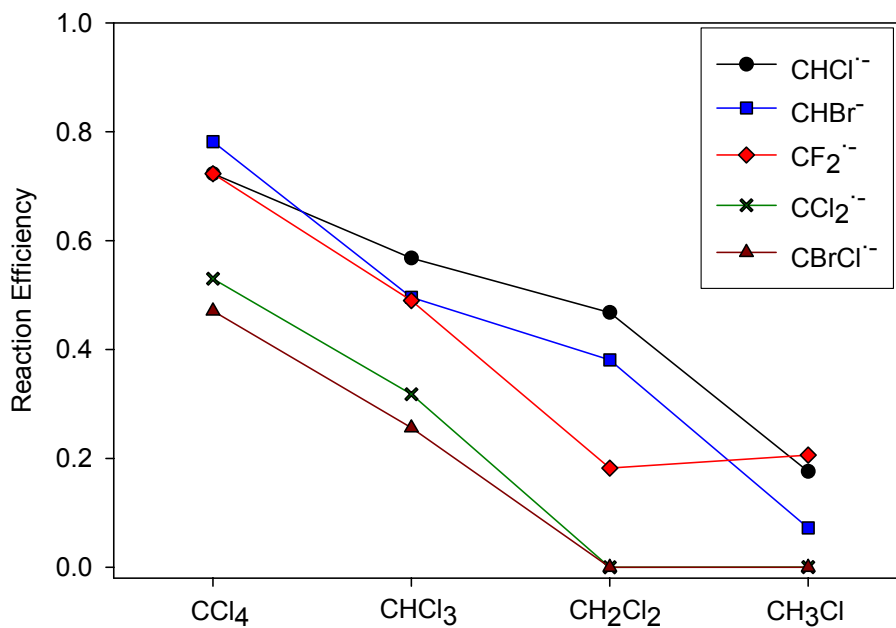


Figure 6.02: Reaction efficiency versus the number of chlorine atoms in the neutral reagent. (Lines are only intended to guide eye.)

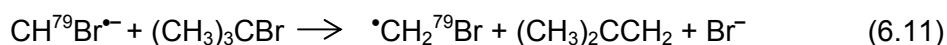
the collision rate. The reactions of CXY^{\ominus} with CCl_4 are the most efficient of the series studied here. With the exception of the reaction of CF_2^{\ominus} with CCl_4 , these reactions primarily proceed by an S_N2 reaction on chlorine. It is expected that these reactions do not have a large central barrier since there are fewer steric restrictions due the absence of an inversion center in the transition state and the presence of four chlorine atoms in CCl_4 . As the number of chlorine atoms in the neutral reagent increases, the likelihood that an S_N2 reaction on carbon occurs decreases, while the likelihood that an S_N2 reaction on chlorine increases. For the reactions of CXY^{\ominus} with $CHCl_3$ and CH_2Cl_2 it is unclear if a carbon centered S_N2 reaction occurs; however, if this reaction does occur, it is in minor amounts. Additionally for these reactions, chlorine centered S_N2 substitution is only observed for the reaction of $CHCl_3^{\ominus}$ with $CHCl_3$. Instead the reactions of CXY^{\ominus} with $CHCl_3$ and CH_2Cl_2 primarily proceed by proton transfer, and as expected the reactions with $CHCl_3$ are more efficient than those with CH_2Cl_2 , since $CHCl_3$ is more acidic than CH_2Cl_2 . Proton transfer is not observed in the reactions of CCl_2^{\ominus} and $CBrCl^{\ominus}$ with CH_2Cl_2 since this pathway is endothermic.

Reactions of CXY^{\ominus} with CH_3Br and $(CH_3)_3CBr$

Reaction rate constants and deuterium kinetic isotope effects for the reactions of CXY^{\ominus} with CH_3Br and with $(CH_3)_3CBr$ are given in Table 6.04; for these reactions, the halide (Br^-) is the sole ionic product. Deuterium kinetic isotope effects are the ratio of perprotio to perdeuterio reaction rate constants ($KIE = k_H/k_D$). For reactions that proceed below the collision rate, kinetic isotope effects can provide a sensitive probe of the transition state structure. For S_N2 reactions inverse KIEs ($k_H/k_D < 1$) are observed, while for E2 reactions normal KIEs ($k_H/k_D > 1$) are observed. A detailed explanation of the origin of these effects is given in Chapter 5.

It has previously been established that reactions of $\text{CXY}^{\bullet-}$ with methyl halides proceed via an $\text{S}_{\text{N}}2$ mechanism. Analogous to the above reaction of $\text{CHCl}^{\bullet-}$ with CH_3Cl , our results are consistent with those of Nibbering and co-workers, which report a slightly skewed Br^- isotope distribution for the reaction of $\text{CH}^{79}\text{Br}^{\bullet-}$ with CH_3Br (2% deviation from the $^{79}\text{Br}:^{81}\text{Br}$ natural abundance of 49:51).⁵⁶ As explained above, we attribute this skewed isotope distribution to H atom transfer within the reactant ion-molecule complex, rather than the previously suggested mechanism of proton transfer followed by an $\text{S}_{\text{N}}2$ reaction (see the analogous reactions 6.09a-c). Typically deuterium kinetic isotope effects for $\text{S}_{\text{N}}2$ reactions are less than one; however, for the reactions measured here, deuteration of the neutral reagent does not change the reaction rate. The absence of an isotope effect is most likely due to the large size of the nucleophile, resulting in a “loose” transition state structure. Similarly, kinetic isotope effects are typically not observed for $\text{S}_{\text{N}}2$ reactions of sulfur anion nucleophiles.⁹²

The reaction of $\text{CHBr}^{\bullet-}$ with $(\text{CH}_3)_3\text{CBr}$ proceeds via an E2 reaction⁸² where the displaced halide is the sole ionic product of the reaction, as shown in eq 6.11.

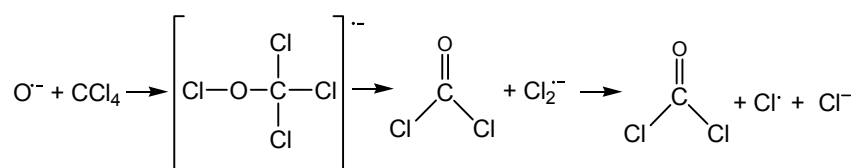


In this reaction, the isotope distribution of Br^- is the bromine atom natural abundance, consistent with a pure E2 mechanism. Additionally, the measured deuterium kinetic isotope effects are greater than one; similar effects have been reported for E2 reactions in the literature.^{93,94} For $\text{CHCl}^{\bullet-}$, $\text{CHBr}^{\bullet-}$, and $\text{CF}_2^{\bullet-}$ elimination occurs fairly efficiently while for $\text{CCl}_2^{\bullet-}$ and $\text{CBrCl}^{\bullet-}$, no reaction occurs. This is most likely because the $\text{CCl}_2^{\bullet-}$ and $\text{CBrCl}^{\bullet-}$ anions are too weakly basic.

Comparison of O^{•-} and CH₂^{•-} with halogenated neutral reagents.

Mayhew and co-workers⁸⁷ and Nibbering and co-workers⁷⁴ have previously investigated the reactions of O^{•-} with chloromethanes; both studies report the formation of Cl⁻ and Cl₂^{•-}. In light of the results presented here, these two products may be formed from an analogous insertion-elimination mechanism, as shown in Scheme 6.07 for the reaction of O^{•-} with CCl₄.

Scheme 6.07



In a similar manner to Scheme 6.06, the first step of the mechanism involves the formation of a σ - π complex, where the singly occupied π -orbital of O^{•-} overlaps with the C-Cl σ -bond of the neutral species to transfer an electron. Neutral oxygen atom then insertion into the Cl-C bond then occurs forming the [ClOCCl₃]^{•-} intermediate, which is unstable and eliminates Cl₂^{•-} or Cl[•] and Cl⁻. Insertion reactions of oxygen atoms into single bonds have previously been reported in the literature.⁹⁵

The halogenated carbene anions studied here exclusively react with methylhalides via S_N2 substitution to displace a halide ion. The reactions of CH₂^{•-} and O^{•-} also react with methyl halides via S_N2 substitution, as shown for the reaction with CH₃Cl (6.12a and 6.13a) in addition to proton transfer (6.12b and 6.13b).^{70,74,96}



In addition, the reaction of $\text{O}^{\bullet-}$ forms $\text{CHCl}^{\bullet-}$ via an $\text{H}_2^{\bullet+}$ abstraction (6.13c).⁷⁴ This unique reaction pathway, not exhibited by $\text{CH}_2^{\bullet-}$ or the carbene anions studied here, reflects the high stability of the H_2O product molecule.

6.4) Conclusions

The carbene radical anions studied here display diverse reactivity as demonstrated by the reaction trends and the number of product ions formed. The reactions of $\text{CXY}^{\bullet-}$ with CS_2 , COS , and CO_2 proceed by two main pathways. The first is carbanion attack on the neutral reactant carbon atom to displace the halide ion while the second is carbanion attack on the neutral reactant sulfur/oxygen atom resulting in sulfur/oxygen atom transfer. The reactions of O_2 occur by carbanion attack on the oxygen to yield $\text{O}^{\bullet-}$, the halide ion, and other minor product ions. The reactions of CO solely produce the halide ion. The $\text{CF}_2^{\bullet-}$ anion displays remarkably different reactivity; these differences are discussed in terms of its lower electron binding energy and the effect of the electronegative fluorine substituents.

The reactivity studies of $\text{CXY}^{\bullet-}$ with halogenated species show that these carbene anions can act as prototypical anions in that they undergo proton transfer, substitution, and elimination reactions. In addition to these classic transformations, the product ion isotope distributions for the reaction of $\text{CHCl}^{\bullet-}$ with CHCl_3 and CH_2Cl_2 provide convincing support for the occurrence of an insertion-elimination mechanism. Neutral and cationic carbenes are known to insert into single bonds;^{1,2,97-99} however, the results presented here are the first report of such gas-phase anion reactivity.

6.5) Acknowledgments

This work would not have been possible without the contributions of Ms. Nicole Eyet, Prof. Veronica M. Bierbaum, and Prof. Charles H. DePuy. Additionally, gratitude is expressed to Prof. W. Carl Lineberger and Prof. Tarek

Sammakia. Financial support is provided by AFOSR (FA9550-06-1-006) and NSF (CHE-0647088). The computational results are based upon work supported by the NSF under the following NSF programs: Partnerships for Advanced Computational Infrastructure, Distributed Terascale Facility (DTF) and Terascale Extensions: Enhancements to the Extensible Terascale Facility.

6.6) Chapter 6 References

- (1) Kirmse, W. Carbene Chemistry; Academic Press: New York, 1971.
- (2) Jones, M.; Moss, R. A. Carbenes; John Wiley and Sons: New York, 1973.
- (3) Jones, M.; Moss, R. A. Carbenes; John Wiley and Sons: New York, 1975.
- (4) Moss, R. A.; Jones, M. Reactive Intermediates; John Wiley and Sons: New York, 1978.
- (5) Hoffmann, R.; Zeiss, G. D.; Vandine, G. W. Electronic Structure of Methylenes. *Journal of the American Chemical Society* **1968**, *90*, 1485-1499.
- (6) Baird, N. C.; Taylor, K. F. Multiplicity of Ground-State and Magnitude of T1-S0 Gap in Substituted Carbenes. *Journal of the American Chemical Society* **1978**, *100*, 1333-1338.
- (7) Harrison, J. F.; Liedtke, R. C.; Liebman, J. F. Multiplicity of Substituted Acyclic Carbenes and Related Molecules. *Journal of the American Chemical Society* **1979**, *101*, 7162-7168.
- (8) Mueller, P. H.; Rondan, N. G.; Houk, K. N.; Harrison, J. F.; Hooper, D.; Willen, B. H.; Liebman, J. F. Carbene Singlet-Triplet Gaps - Linear Correlations with Substituent π Donation. *Journal of the American Chemical Society* **1981**, *103*, 5049-5052.
- (9) Murray, K. K.; Leopold, D. G.; Miller, T. M.; Lineberger, W. C. Photoelectron-Spectroscopy of the Halocarbene Anions HCF^- , HCCl^- , HCB^- , HCl^- , CF_2^- , and CCl_2^- . *Journal of Chemical Physics* **1988**, *89*, 5442-5453.
- (10) Gilles, M. K.; Ervin, K. M.; Ho, J.; Lineberger, W. C. Negative-Ion Photoelectron-Spectroscopy of HCF^- , HCCl^- , HCB^- , and HCl^- - Photoelectron Angular-Distributions and Neutral Triplet Excitation-Energies. *Journal of Physical Chemistry* **1992**, *96*, 1130-1141.
- (11) Schwartz, R. L.; Davico, G. E.; Ramond, T. M.; Lineberger, W. C. Singlet-Triplet Splittings in CX_2 (X = F, Cl, Br, I) Dihalocarbenes via Negative Ion Photoelectron Spectroscopy. *Journal of Physical Chemistry A* **1999**, *103*, 8213-8221.
- (12) Chowdhury, P. K. IR Multiphoton Dissociation Dynamics of Octafluorocyclopentene - Time-Resolved Observation of Concerted Products - CF_2 and Hexafluorobutadiene. *Journal of Physical Chemistry* **1995**, *99*, 12084-12089.
- (13) Felder, P.; Demuth, C. Photodissociation of CFCl_3 at 193 nm Investigated by Photofragment Translational Spectroscopy. *Chemical Physics Letters* **1993**, *208*, 21-26.

- (14) Ibuki, T.; Hiraya, A.; Shobatake, K. Vacuum Ultraviolet-Absorption Spectra and Photodissociative Excitation of CHBr_2Cl and CHBrCl_2 . *Journal of Chemical Physics* **1992**, *96*, 8793-8798.
- (15) Martinez, R.; Merelas, I.; Rayo, M. N. S.; Castano, F. Analysis of the Optical-Emission ($\lambda=400\text{-}900\text{ nm}$) of Fragments Produced by Electron-Impact on CF_2Br_2 . *Journal of Physics B: Atomic Molecular and Optical Physics* **1995**, *28*, 4563-4575.
- (16) DeZarate, A. O.; Martinez, R.; Rayo, M. N. S.; Castano, F.; Hancock, G. Preparation of $\text{Chf}(X^1a')$ by Infrared Multiphoton Dissociation and Reactions with Alkenes. *Journal of the Chemical Society-Faraday Transactions* **1992**, *88*, 535-541.
- (17) Finlayson-Pitts, B. J.; Pitts, J. N. J. Atmospheric Chemistry: Fundamentals and Experimental Techniques; Wiley: New York, 1986.
- (18) McConnell, J. C.; Templeton, E. M. J.; Henderson, G. S.; Evans, W. F. J. Potential Effects of Halons on Stratospheric O_3 Based on the Montreal Protocol. *Atmosphere-Ocean* **1990**, *28*, 177-188.
- (19) Molina, M. J.; Rowland, F. S. Stratospheric Sink for Chlorofluoromethanes - Chlorine Atom-Catalyzed Destruction of Ozone. *Nature* **1974**, *249*, 810-812.
- (20) McConnell, J. C.; Henderson, G. S.; Barrie, L.; Bottenheim, J.; Niki, H.; Langford, C. H.; Templeton, E. M. J. Photochemical Bromine Production Implicated in Arctic Boundary-Layer Ozone Depletion. *Nature* **1992**, *355*, 150-152.
- (21) Suzuki, C.; Sasaki, K.; Kadota, K. Rate Coefficient for Self-Association Reaction of CF_2 Radicals Determined in the Afterglow of Low-Pressure C_4F_8 Plasmas. *Plasma Chemistry and Plasma Processing* **2001**, *21*, 139-147.
- (22) Miller, W. T.; Kim, C. S. Y. Reactions of Alkylolithiums with Polyhalides. *Journal of the American Chemical Society* **1959**, *81*, 5008-5009.
- (23) Kofron, W. G.; Hauser, C. R.; Kirby, F. B. Reactions of Tetrahalomethanes with Potassium *t*-Butoxide and Potassium Amide. *Journal of Organic Chemistry* **1963**, *28*, 873-875.
- (24) Franzen, V. Reaktionen Mit Difluorcarben. *Angewandte Chemie-International Edition* **1960**, *72*, 566-566.
- (25) Tao, C.; Mukarakate, C.; Reid, S. A. Electronic spectroscopy of the $A^1A''\text{-}X^1A'$ system of CDCl . *Journal of Molecular Spectroscopy* **2007**, *241*, 143-150.
- (26) Mukarakate, C.; Mishchenko, Y.; Brusse, D.; Tao, C.; Reid, S. A. Probing Spin-Orbit Mixing and the Singlet-Triplet Gap in Dichloromethylene via K_a Sorted Emission Spectra. *Physical Chemistry Chemical Physics* **2006**, *8*, 4320-4326.

- (27) Deselnicu, M.; Tao, C.; Mukarakate, C.; Reid, S. A. Fluorescence Excitation and Emission Spectroscopy of the $A^1A''-X^1A'$ System of CHBr. *Journal of Chemical Physics* **2006**, *124*, 134302/1-134302/11.
- (28) Chang, W. Z.; Hsu, H. J.; Chang, B. C. New Dispersed Fluorescence Spectra of HCB_r and DCB_r. *Chemical Physics Letters* **2005**, *413*, 25-30.
- (29) Tarczay, G.; Miller, T. A.; Czako, G.; Csaszar, A. G. Accurate *Ab Initio* Determination of Spectroscopic and Thermochemical Properties of Mono- and Dichlorocarbenes. *Physical Chemistry Chemical Physics* **2005**, *7*, 2881-2893.
- (30) Hsu, H. J.; Chang, W. Z.; Chang, B. C. Dispersed Fluorescence Spectroscopy of the CBr₂ $A^1B_1-X^1A_1$ Transition. *Physical Chemistry Chemical Physics* **2005**, *7*, 2468-2473.
- (31) Fan, H. Y.; Mukarakate, C.; Deselnicu, M.; Tao, C.; Reid, S. A. Dispersed Fluorescence Spectroscopy of Jet-Cooled HCF and DCF: Vibrational Structure of the X^1A' State. *Journal of Chemical Physics* **2005**, *123*, 014314/1-014314/7.
- (32) Guss, J. S.; Richmond, C. A.; Nauta, K.; Kable, S. H. Laser-Induced Fluorescence Excitation and Dispersed Fluorescence Spectroscopy of the $A^1B_1-X^1A_1$ Transition of Dichlorocarbene. *Physical Chemistry Chemical Physics* **2005**, *7*, 100-108.
- (33) Lin, C. S.; Chen, Y. E.; Chang, B. C. New Electronic Spectra of the HCCI and DCCI A-X Vibronic Bands. *Journal of Chemical Physics* **2004**, *121*, 4164-4170.
- (34) Lee, C. L.; Liu, M. L.; Chang, B. C. Electronic Spectroscopy of Bromomethylenes in a Supersonic Free Jet Expansion. *Physical Chemistry Chemical Physics* **2003**, *5*, 3859-3863.
- (35) Richmond, C. A.; Guss, J. S.; Nauta, K.; Kable, S. H. Rovibronic Spectroscopy of the $A^1A'-X^1A''$ Transition in the Bromochloromethylene Radical. *Journal of Molecular Spectroscopy* **2003**, *220*, 137-149.
- (36) Liu, M. L.; Lee, C. L.; Bezant, A.; Tarczay, G.; Clark, R. J.; Miller, T. A.; Chang, B. C. Dispersed Fluorescence Spectra of the CCl₂ A-X Vibronic Bands. *Physical Chemistry Chemical Physics* **2003**, *5*, 1352-1358.
- (37) Chang, B. C.; Guss, J.; Sears, T. J. Hot Bands in the A-X Spectrum of HCB_r. *Journal of Molecular Spectroscopy* **2003**, *219*, 136-144.
- (38) Yu, H. G.; Gonzalez-Lezana, T.; Marr, A. J.; Muckerman, J. T.; Sears, T. J. Experimental and Theoretical Studies of the Near-Infrared Spectrum of Bromomethylene. *Journal of Chemical Physics* **2001**, *115*, 5433-5444.
- (39) Tsai, T. C.; Chen, C. W.; Chang, B. C. Laser Excitation and Dispersed Fluorescence Spectra of the HCB_r A-X Vibronic Transition. *Journal of Chemical Physics* **2001**, *115*, 766-770.

- (40) Schwartz, M.; Marshall, P. An *ab initio* Investigation of Halocarbenes. *Journal of Physical Chemistry A* **1999**, *103*, 7900-7906.
- (41) Irikura, K. K.; Hudgens, J. W.; Johnson, R. D. Spectroscopy of the Fluoromethylene Radicals HCF and DCF by 2+1 Resonance-Enhanced Multiphoton Ionization Spectroscopy and by *Ab-Initio* Calculation. *Journal of Chemical Physics* **1995**, *103*, 1303-1308.
- (42) Qian, H. B.; Davies, P. B. Infrared-Laser Spectroscopy of the ν_2 Band of Difluorocarbene (CF_2). *Journal of Molecular Spectroscopy* **1995**, *169*, 201-210.
- (43) Kohn, D. W.; Robles, E. S. J.; Logan, C. F.; Chen, P. Photoelectron-Spectrum, Ionization-Potential, and Heat of Formation of CCl_2 . *Journal of Physical Chemistry* **1993**, *97*, 4936-4940.
- (44) Russo, N.; Sicilia, E.; Toscano, M. Geometries, Singlet-Triplet Separations, Dipole-Moments, Ionization-Potentials, and Vibrational Frequencies in Methylene (CH_2) and Halocarbenes (CHF , CF_2 , CCl_2 , CBr_2 , and Cl_2). *Journal of Chemical Physics* **1992**, *97*, 5031-5036.
- (45) Irikura, K. K.; Goddard, W. A.; Beauchamp, J. L. Singlet Triplet Gaps in Substituted Carbenes CXY ($X, Y = \text{H}, \text{F}, \text{Cl}, \text{Br}, \text{I}, \text{SiH}_3$). *Journal of the American Chemical Society* **1992**, *114*, 48-51.
- (46) Gutsev, G. L.; Ziegler, T. Theoretical-Study on Neutral and Anionic Halocarbynes and Halocarbenes. *Journal of Physical Chemistry* **1991**, *95*, 7220-7228.
- (47) Wormhoudt, J.; McCurdy, K. E.; Burkholder, J. B. Measurements of the Strengths of Infrared Bands of CF_2 . *Chemical Physics Letters* **1989**, *158*, 480-485.
- (48) Burkholder, J. B.; Howard, C. J.; Hamilton, P. A. Fourier-Transform Spectroscopy of the ν_1 and ν_3 Fundamental Bands of CF_2 . *Journal of Molecular Spectroscopy* **1988**, *127*, 362-369.
- (49) Dyke, J. M.; Lee, E. P. F.; Mok, D. K. W.; Chau, F. T. A Combined *Ab Initio*/Franck-Condon Study of the A-X Single-Vibronic-Level Emission Spectrum of CCl_2 and the Photodetachment Spectrum of CCl_2^- . *ChemPhysChem* **2005**, *6*, 2046-2059.
- (50) McKee, M. L.; Michl, J. A Possible Reinterpretation of the Photoelectron Spectra of CCl_2^- , CBr_2^- , and Cl_2^- : A Role for Quartet Iso-dihalocarbene or Dihalocarbene Radical Anions? *Journal of Physical Chemistry A* **2002**, *106*, 8495-8497.
- (51) Carter, E. A.; Goddard, W. A. New Predictions for Singlet Triplet Gaps of Substituted Carbenes. *Journal of Physical Chemistry* **1987**, *91*, 4651-4652.

- (52) Chau, F. T.; Mok, D. K. W.; Lee, E. P. F.; Dyke, J. M. The Singlet-Triplet Separation in CF_2 : State of the Art *Ab Initio* Calculations and Franck-Condon Simulations Including Anharmonicity. *ChemPhysChem* **2005**, *6*, 2037-2045.
- (53) Paulino, J. A.; Squires, R. R. Carbene Thermochemistry from Collision-Induced Dissociation Threshold Energy Measurements in a Flowing Afterglow-Triple Quadrupole Instrument. *Abstracts of Papers of the American Chemical Society* **1991**, *201*, 196-PHYS.
- (54) Poutsma, J. C.; Paulino, J. A.; Squires, R. R. Absolute Heats of Formation of CHCl , CHF , and CClF . A Gas-Phase Experimental and G2 Theoretical Study. *Journal of Physical Chemistry A* **1997**, *101*, 5327-5336.
- (55) Born, M.; Ingemann, S.; Nibbering, N. M. M. Heats of Formation of Mono-Halogen-Substituted Carbenes - Stability and Reactivity of CHX^- (X=F, Cl, Pr, and I) Radical-Anions. *Journal of the American Chemical Society* **1994**, *116*, 7210-7217.
- (56) Born, M.; Ingemann, S.; Nibbering, N. M. M. Thermochemical Properties of Halogen-Substituted Methanes, Methyl Radicals, and Carbenes in the Gas Phase. *International Journal of Mass Spectrometry* **2000**, *194*, 103-113.
- (57) Lias, S. G.; Karpas, Z.; Liebman, J. F. Halomethylenes: Effects of Halogen Substitution on Absolute Heats of Formation. *Journal of the American Chemical Society* **1985**, *107*, 6089-6096.
- (58) Ferguson, E. E.; Fehsenfeld, F. C.; Albritton, D. L. Gas-Phase Ion Chemistry; Academic Press: New York, 1979.
- (59) Jennings, K. R. Gas-Phase Ion Chemistry; Academic Press: New York, 1979.
- (60) Harrison, A. G. Chemical Ionization Mass Spectrometry; CRC Press: Boca Raton, 1983.
- (61) Grimsrud, E. P. Electron Capture Elsevier: New York, 1981.
- (62) Born, M.; Ingemann, S.; Nibbering, N. M. M. Reactivity of Mono-Halogen Carbene Radical Anions (CHX^- ; X=F, Cl and Br) and the Corresponding Carbanions (CH_2X^- ; X=Cl and Br) in the Gas Phase. *Journal of the Chemical Society-Perkin Transactions 2* **1996**, 2537-2547.
- (63) Villano, S. M.; Eyet, N.; Lineberger, W. C.; Bierbaum, V. M. Gas-Phase Reactions of Halogenated Radical Carbene Anions with Sulfur and Oxygen Containing Species. *International Journal of Mass Spectrometry* **2009**, *In Press*.
- (64) DePuy, C. H.; Bierbaum, V. M.; Robinson, M. S.; Davico, G. E.; Gareyev, R. The Gas-Phase Reactions of the Allenyl Anion with CS_2 , COS and CO_2 . *Tetrahedron* **1997**, *53*, 9847-9856.

- (65) Robinson, M. S.; Davico, G. E.; Bierbaum, V. M.; DePuy, C. H. The Gas-Phase Ion/Molecule Chemistry of the ^{13}C Labeled Ketenyl and Methyl Ketenyl Anions with CS_2 , COS , and CO_2 . *International Journal of Mass Spectrometry and Ion Processes* **1994**, *137*, 107-119.
- (66) DePuy, C. H.; Bierbaum, V. M. Gas-Phase Sulfur Anions - Synthesis and Reactions of H_2NS^- and Related Ions. *Tetrahedron Letters* **1981**, *22*, 5129-5130.
- (67) Kass, S. R.; Filley, J.; Van Doren, J. M.; DePuy, C. H. Nitrous-Oxide in Gas-Phase Ion Molecule Chemistry - A Versatile Reagent for the Determination of Carbanion Structure. *Journal of the American Chemical Society* **1986**, *108*, 2849-2852.
- (68) Bierbaum, V. M.; DePuy, C. H.; Shapiro, R. H. Gas-Phase Reactions of Anions with Nitrous-Oxide and Carbon-Dioxide. *Journal of the American Chemical Society* **1977**, *99*, 5800-5802.
- (69) O'Hair, R. A. J.; DePuy, C. H.; Bierbaum, V. M. Gas-Phase Chemistry and Thermochemistry of the Hydroxysulfide Anion, HOS^- . *Journal of Physical Chemistry* **1993**, *97*, 7955-7961.
- (70) DePuy, C. H.; Barlow, S. E.; Van Doren, J. M.; Roberts, C. R.; Bierbaum, V. M. Gas-Phase Chemistry of CH_2^- . *Journal of the American Chemical Society* **1987**, *109*, 4414-4415.
- (71) Van Doren, J. M.; Barlow, S. E.; DePuy, C. H.; Bierbaum, V. M. Tandem Flowing Afterglow-Selected Ion Flow Tube and Its Application to the Thermal-Energy Reactions of $^{18}\text{O}^-$. *Journal of the American Chemical Society* **1987**, *109*, 4412-4414.
- (72) Bierbaum, V. M.; Grabowski, J. J.; DePuy, C. H. Gas-Phase Synthesis and Reactions of Nitrogen-Containing and Sulfur-Containing Anions. *Journal of Physical Chemistry* **1984**, *88*, 1389-1393.
- (73) Villano, S. M.; Eyet, N.; Lineberger, W. C.; Bierbaum, V. M. Gas-Phase Carbene Radical Anions: New Mechanistic Insight. *Journal of the American Chemical Society* **2008**, *130*, 7214-7215.
- (74) Staneke, P. O.; Kauw, J.; Born, M.; Ingemann, S.; Nibbering, N. M. M. Low Pressure Gas-Phase Reactions of the Atomic Oxygen Radical Anion with Halomethanes Studied using Fourier Transform Ion Cyclotron Resonance. *Rapid Communications in Mass Spectrometry* **1997**, *11*, 124-132.
- (75) Lee, J.; Grabowski, J. J. Reactions of the Atomic Oxygen Radical Anion and the Synthesis of Organic Reactive Intermediates. *Chemical Reviews* **1992**, *92*, 1611-1647.
- (76) Su, T.; Chesnavich, W. J. Parametrization of the Ion-Polar Molecule Collision Rate-Constant by Trajectory Calculations. *Journal of Chemical Physics* **1982**, *76*, 5183-5185.

(77) Curtiss, L. A.; Raghavachari, K.; Redfern, P. C.; Rassolov, V.; Pople, J. A. Gaussian-3 (G3) Theory for Molecules Containing First and Second-Row Atoms. *Journal of Chemical Physics* **1998**, *109*, 7764-7776.

(78) Frisch, M. J.; Trucks, G. W.; Schlegel, H. B.; Scuseria, G. E.; Robb, M. A.; Cheeseman, J. R.; Montgomery, J. A.; Vreven, T.; Kudin, K. N.; Burant, J. C.; Millam, J. M.; Iyengar, S. S.; Tomasi, J.; Barone, V.; Mennucci, B.; Cossi, M.; Scalmani, G.; Rega, N.; Petersson, G. A.; Nakatsuji, H.; Hada, M.; Ehara, M.; Toyota, K.; Fukuda, R.; Hasegawa, J.; Ishida, M.; Nakajima, T.; Honda, Y.; Kitao, O.; Nakai, H.; Klene, M.; Li, X.; Knox, J. E.; Hratchian, H. P.; Cross, J. B.; Adamo, C.; Jaramillo, J.; Gomperts, R.; Stratmann, R. E.; Yazyev, O.; Austin, A. J.; Cammi, R.; Pomelli, C.; Ochterski, J. W.; Ayala, P. Y.; Morokuma, K.; Voth, G. A.; Salvador, P.; Dannenberg, J. J.; Zakrzewski, V. G.; Dapprich, S.; Daniels, A. D.; Strain, M. C.; Farkas, O.; Malick, D. K.; Rabuck, A. D.; Raghavachari, K.; Foresman, J. B.; Ortiz, J. V.; Cui, Q.; Baboul, A. G.; Clifford, S.; Cioslowski, J.; Stefanov, B. B.; Liu, G.; Liashenko, A.; Piskorz, P.; Komaromi, I.; Martin, R. L.; Fox, D. J.; Keith, T.; Al-Laham, M. A.; C. Y. Peng; Nanayakkara, A.; Challacombe, M.; Gill, P. M. W.; Johnson, B.; Chen, W.; Wong, M. W.; Gonzalez, C.; Pople, J. A. Gaussian 03, revision B.05; I. Gaussian, Ed.; Gaussian, Inc.: Pittsburgh, PA, 2003.

(79) *NIST Chemistry WebBook, NIST Standard Reference Database Number 69*; Linstrom, P. J.; Mallard, W. G., Eds.; National Institute of Standards and Technology: Gaithersburg MD, 20899 June 2005 (<http://webbook.nist.gov>).

(80) Chase Jr., W. M.; Davies, C. A.; Downey, J. J. R.; Frurip, D. J.; McDonald, R. A.; Syverud, A. N. JANAF Thermochemical Tables, 3rd ed. Parts I and II. In *J. Phys. Chem. Ref. Data*; 3rd Parts I and II ed., 1985; pp Suppl 1.

(81) Clair, R. L.; McMahon, T. B. Ion-Cyclotron Resonance Study of Base-Induced Elimination-Reactions of Fluorinated Alcohols and Unimolecular Loss of HF from Chemically Activated Fluoroalkoxide Ions. *International Journal of Mass Spectrometry and Ion Processes* **1980**, *33*, 21-36.

(82) DePuy, C. H.; Gronert, S.; Mullin, A.; Bierbaum, V. M. Gas-Phase S_N2 and E2 Reactions of Alkyl-Halides. *Journal of the American Chemical Society* **1990**, *112*, 8650-8655.

(83) Pradeep, T.; Ma, S. G.; Shen, J. W.; Francisco, J. S.; Cooks, R. G. Activation of Dioxygen by Halocarbon Ions. *Journal of Physical Chemistry A* **2000**, *104*, 6804-6808.

(84) Grabowski, J. J. Studies of Gas Phase Ion-Molecule Reactions using a Selected Ion Flow Tube. Ph.D. Thesis, Department of Chemistry and Biochemistry, University of Colorado at Boulder 1983.

(85) Dawson, J. H. J.; Nibbering, N. M. M. Concerning $CH_2=C^-$ And Its Reaction with $^{14}N^{15}NO$. *Journal of the American Chemical Society* **1978**, *100*, 1928-1929.

(86) Staneke, P. O.; Groothuis, G.; Ingemann, S.; Nibbering, N. M. M. Competing Electron Transfer, Proton Abstraction and Nucleophilic Substitutions in

Gas-Phase Reactions of (Radical) Anions with Chloro- and Bromomethanes. *Journal of Physical Organic Chemistry* **1996**, 9, 471-486.

(87) Mayhew, C. A.; Peverall, R.; Watts, P. Gas-Phase Ionic Reactions of Freons and Related-Compounds - Reactions of Some Halogenated Methanes with O^- and O_2^- . *International Journal of Mass Spectrometry and Ion Processes* **1993**, 125, 81-93.

(88) DePuy, C. H.; Kato, S. H/D Exchange Reactions. In *Encyclopedia of Mass Spectrometry: Theory and Ion Chemistry*; P. B. Armentrout, Ed.; Elsevier: Amsterdam, 2003; Vol. 1; pp 670-674.

(89) Olmstead, W. N.; Brauman, J. I. Gas-phase Nucleophilic Displacement Reactions *Journal of the American Chemical Society* **1977**, 99, 4219-4228.

(90) Laerdahl, J. K.; Uggerud, E. Gas phase Nucleophilic Substitution. *International Journal of Mass Spectrometry* **2002**, 214, 277-314.

(91) Hase, W. L. Classical Trajectory Simulations. In *Encyclopedia of Mass Spectrometry: Chemistry and Physics of Gas-Phase Ions*; M. Gross and R. Caprioli, Eds.; Elsevier: New York, 2005; Vol. 4; pp 504.

(92) Gronert, S.; DePuy, C. H.; Bierbaum, V. M. Deuterium-Isotope Effects in Gas-Phase Reactions of Alkyl-Halides - Distinguishing E2 and S_N2 Pathways. *Journal of the American Chemical Society* **1991**, 113, 4009-4010.

(93) Bierbaum, V. M.; Filley, J.; DePuy, C. H.; Jarrold, M. F.; Bowers, M. T. Kinetic Isotope Effect in Gas-Phase Base-Induced Elimination-Reactions. *Journal of the American Chemical Society* **1985**, 107, 2818-2820.

(94) Dekoning, L. J.; Nibbering, N. M. M. On the Mechanism of Base-Induced Gas-Phase Elimination-Reactions of Ethers. *Journal of the American Chemical Society* **1987**, 109, 1715-1722.

(95) Shu, J.; Lin, J. J.; Wang, C. C.; Lee, Y. T.; Yang, X. M.; Nguyen, T. L.; Mebel, A. M. $O(^1D)$ Reaction with Cyclopropane: Evidence of O Atom Insertion into the C-C bond. *Journal of Chemical Physics* **2001**, 115, 7-10.

(96) Van Doren, J. M. Developments and Applications to Gas-Phase Ion Chemistry. Ph.D. Thesis, Department of Chemistry and Biochemistry, University of Colorado at Boulder, 1987.

(97) Birchall, J. M.; Haszeldine, R. N.; Tissington, P. *Journal of the Society of Perkins Transactions 1* **1975**, 1975, 1638.

(98) Bohme, D. K. Carbene Chemistry of Cations: The Chemistry of the Carbene Cation C_3H^+ in the Gas Phase *Journal of the American Chemical Society* **1983**, 105, 5481-5483.

(99) Julian, R. R.; May, J. A.; Stoltz, B. M.; Beauchamp, J. L. Biomimetic Approaches to Gas-Phase Peptide Chemistry: Combining Selective Binding Motifs with Reactive Carbene Precursors to Form Molecular Mousetraps. *International Journal of Mass Spectrometry* **2003**, 228, 851-864.

CHAPTER VII
SPECTROSCOPIC CHARACTERIZATION OF THE
c-C₄F₈⁻ AND SF₆⁻ ANIONS

7.1) Introduction

Both c-C₄F₈ and SF₆ have industrial applications as reagents in etching plasmas and as insulating gases for high voltage devices. In addition, both molecules have long lifetimes in the upper atmosphere and are considered greenhouse gases whose atmospheric lifetimes are, in part, controlled by electron attachment.¹ These two perfluorinated molecules are of fundamental interest since they have a propensity to nondissociatively attach low energy electrons, indicating that the corresponding anions have a very long lifetime with respect to autodetachment.^{2,3} One of the reasons for this slow autodetachment undoubtedly results from the change in structure of the molecular framework upon anion formation. For these reasons, both molecules have been the subject of many studies that have focused on the characterization of the neutral and the formation and reactivity of the anion;⁴⁻¹⁰ however, very few spectroscopic studies have addressed the structural aspects of the ions.

Various spectroscopic studies have shown that the geometry of neutral c-C₄F₈ is bent with D_{2d} symmetry and these studies have measured several vibrational frequencies.¹¹⁻¹⁸ High level CCSD(T)/CBS calculations were employed to map the double well potential surface to the low-frequency ring-puckering motion; the two minima were found to be separated by 132 cm⁻¹ barrier. Analysis of the c-C₄F₈ electron density suggests that the puckering barrier arises principally from the $\sigma_{cc} \rightarrow \sigma_{cf}^*$ hyper-conjugative interactions that are more strongly stabilizing in the puckered than in the planar form.¹⁸ Far less is known about the anion structure.

Recent ESR studies have shown that the anion structure is planar with D_{4h} symmetry¹⁹ and computational results predict that the added electron is delocalized in a 'p-like' orbital extending over the entire molecule, strengthening the four C–C bonds via π -bonding interactions, and weakening the eight C–F bonds via σ -anti-bonding interactions.^{19,20}

As with $c\text{-C}_4\text{F}_8$, there is a large geometry change upon attachment of an electron to SF_6 . This molecule has been the focus of intense study.²¹⁻³² The neutral SF_6 structure has been well characterized by several Raman and infrared studies.³³ Only two reports, however, have addressed the structural aspects of the ion through spectroscopy.^{34,35} An early study commented only on the lack of observed photo-detachment in the near ultraviolet,³⁴ far above the adiabatic threshold, while a matrix isolation study identified a single weak vibrational transition near 600 cm^{-1} .³⁵ More recently, computational results predict that the O_h symmetry of SF_6 is retained upon attachment of an electron; however, the S–F bonds are elongated by about 0.2 \AA .³⁶

The present study³⁷ investigates electron attachment to the closed shell perfluorinated molecules $c\text{-C}_4\text{F}_8$ and SF_6 . Spectroscopic studies of the SF_6^- and $c\text{-C}_4\text{F}_8^-$ anions are reported in order to provide experimental benchmarks for theoretical predictions of their structures and electron binding energies. The work presented here was done in collaboration with Prof. Mark A. Johnson's group at Yale University and Thomas M. Miller and A. A. Viggiano at Hanscom Air Force Research Laboratory. The photoelectron spectra of both the $c\text{-C}_4\text{F}_8^-$ anion and the "cooled" SF_6^- anion were collected at JILA. The photoelectron spectra of the SF_6^- anion was also collected at Yale University. The photoelectron spectra of both the $c\text{-C}_4\text{F}_8^-$ and SF_6^- anions are compared to the calculated results of Borrelli,^{38,39} which provide important insights into the observed spectroscopic character.

7.2) Experimental Methods

The 351.1 nm photoelectron spectra of both the $c\text{-C}_4\text{F}_8^-$ and SF_6^- anions were collected with a flowing afterglow-negative ion photoelectron spectrometer that was described in Chapter 4. The target anions were prepared by flowing He buffer gas seeded with a trace amount of SF_6 or $c\text{-C}_4\text{F}_8$ gas through a microwave discharge source. The SF_6^- anion was cooled by surrounding the flow tube with a liquid nitrogen jacket; prior experience with this arrangement suggests that the resulting ions are prepared in the 150–200 K range.⁴⁰ Negative ions were gently extracted from the source region and passed through a Wien filter for mass selection. The mass selected ion beam was then crossed with a 351.1 nm (3.531 eV) line from a cw argon-ion laser in an external build up cavity producing ~100 W of circulating power. Photoelectrons that are ejected perpendicular to the plane of the ion-photon interaction region are energy analyzed by a hemispherical kinetic energy analyzer coupled to position sensitive detector. The absolute energy scale is calibrated with the electron affinity (EA) of atomic oxygen⁴¹ in the measurements of the photoelectron spectrum, and a linear energy scale compression factor (< 1%), which is determined from the photoelectron spectrum of tungsten anion.⁴²

Optimized geometries and harmonic vibrational frequencies (not scaled) for the neutral molecules and corresponding anions are determined from density functional theory (DFT) calculations (B3LYP/6-31+G(3df))⁴³⁻⁴⁵ using the Gaussian 03 suite of programs.⁴⁶

7.3) Results and Discussion

7.3.1) Photoelectron Spectrum of the $c\text{-C}_4\text{F}_8^-$ Anion

Figure 7.01 shows the 351.1 nm photoelectron spectrum of the $c\text{-C}_4\text{F}_8^-$ anion. In this spectrum, the $c\text{-C}_4\text{F}_8^-$ anion has a room temperature vibrational and rotational distribution from collisions with He buffer gas (~ 0.5 torr, 3 –10 ms residence time)

prior to leaving the source region.⁴⁷ The arrow in Figure 7.01 indicates the value of the EA(*c*-C₄F₈), which was determined by flowing afterglow Langmuir probe studies, at 0.63 ± 0.05 eV;⁹ two other EA values have also been reported and will be elaborated on later.^{21,48} The absence of electron detachment at this energy indicates a large geometry change upon photodetachment of the *c*-C₄F₈⁻ anion. The observed spectrum consists of an extremely long progression composed of over fifty resolved peaks that are spaced by 355 cm⁻¹ and extend almost 2 eV into the vibrational manifold of the ground electronic state of *c*-C₄F₈. Based on the size of the molecule and the large geometry change between the anion and neutral, one might expect to see an extended Franck-Condon profile with virtually no resolved features. However, what is so striking is that the spectrum appears to display a single mode character that is rather 'diatomic-like' and remains harmonic across the entire spectrum.

It is known from electron diffraction and infrared studies that the carbon framework of the neutral is bent with D_{2d} symmetry,¹¹⁻¹⁷ while recent ESR studies have shown that the anion framework is planar with D_{4h} symmetry.¹⁹ Optimized structures (B3LYP/6-31+G(3df)) of the neutral and the anion are displayed in Figure 7.02. Detachment of an electron elongates the C–C bonds, shortens the C–F bonds, and increases the non-bonded F–F distance. This increase in symmetry for the anion has been predicted by computations which also show that the negative charge in the anion is a 'p-like' orbital that is delocalized over the entire molecule.^{19,20} This deformation corresponds to the ν_5 ring-breathing mode, calculated to be 360 cm⁻¹ at the MP2/TZVPP level of theory (Table 7.01). Thus, we expect this mode to be active in the photoelectron spectrum, and based on a cursory evaluation of the spectrum, the long progression appears to correspond to excitation of this mode.

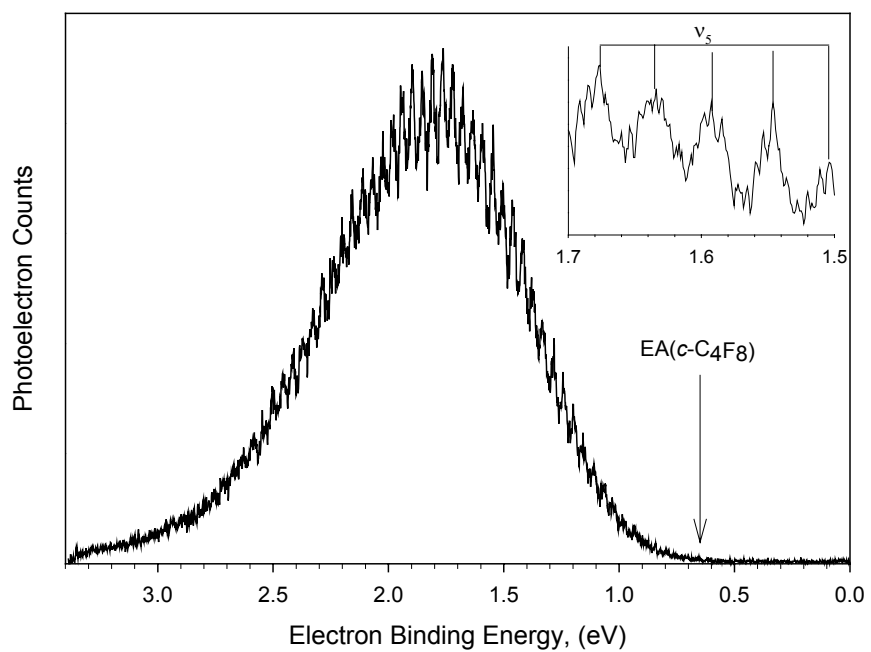


Figure 7.01: The 351.1 nm photodetachment spectrum of $c\text{-C}_4\text{F}_8^-$ taken at the magic angle. The $\text{EA}(c\text{-C}_4\text{F}_8)$ determined by Miller⁹ is indicated by a vertical arrow.

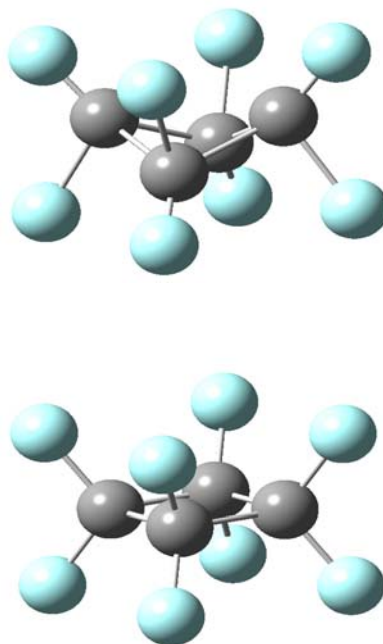


Figure 7.02: Calculated structures (B3LYP/6-31+G(3df)) of $c\text{-C}_4\text{F}_8$ neutral (top) and anion (bottom). The neutral structure is bent out of plane by 8.0° ; however, the figure is exaggerated for clarity. For $c\text{-C}_4\text{F}_8$, $R(\text{CC}) = 1.579 \text{ \AA}$, $R(\text{CF}) = 1.337 \text{ \AA}$, non-bonded $R(\text{FF}) = 2.189 \text{ \AA}$, $\angle(\text{FCF}) = 109.0^\circ$, $\angle(\text{CCC}) = 89.7^\circ$, $D(\text{CCCC}) = 8.0^\circ$. For $c\text{-C}_4\text{F}_8^-$, $R(\text{CC}) = 1.505 \text{ \AA}$, $R(\text{CF}) = 1.406 \text{ \AA}$, non-bonded $R(\text{FF}) = 2.170 \text{ \AA}$, $\angle(\text{FCF}) = 100.9^\circ$, $\angle(\text{CCC}) = 90.0^\circ$, $D(\text{CCCC}) = 0.0^\circ$.

Table 7.01: Theoretical frequencies (cm^{-1}), calculated using the MP2/TZVPP level of theory, for both $c\text{-C}_4\text{F}_8$ anion and neutral along with the experimental values for neutral $c\text{-C}_4\text{F}_8$.

Vibrational Mode		$c\text{-C}_4\text{F}_8$		$c\text{-C}_4\text{F}_8^-$	
		Theory ³⁹	Exp.		Theory ³⁹
ν_1	a_1	1448	1433 ^a	a_{1g}	1499
ν_2	a_1	1315	1413 ^a	b_{2u}	963
ν_3	a_1	715	700 ^a	a_{1g}	668
ν_4	a_1	618	607 ^a	a_{1g}	489
ν_5	a_1	370	359 ^a	b_{2u}	391
ν_6	a_1	58		b_{2u}	47
ν_7	a_2	893		a_{2g}	889
ν_8	a_2	220		b_{1u}	216
ν_9	b_1	1047	1010 ^a	b_{2g}	1203
ν_{10}	b_1	283		b_{2g}	253
ν_{11}	b_1	251		a_{1u}	206
ν_{12}	b_2	1323	1292 ^b	a_{2u}	872
ν_{13}	b_2	1264	1240 ^b	b_{1g}	1042
ν_{14}	b_2	669	659 ^b	b_{1g}	631
ν_{15}	b_2	360	348 ^b	b_{1g}	358
ν_{16}	b_2	197	195 ^b	a_{2u}	190
ν_{17}	e	1380	1343 ^b	e_g	1249
ν_{18}	e	1246	1223 ^b	e_u	847
ν_{19}	e	987	964 ^b	e_u	835
ν_{20}	e	581	569 ^b	e_u	559
ν_{21}	e	444	437 ^b	e_g	425
ν_{22}	e	289	283 ^b	e_g	271
ν_{23}	e	190		e_u	200

^a From reference 17 ^b From reference 18

This simple explanation, however, requires this mode to behave as a harmonic oscillator even at very high levels of vibrational excitation (up to fifty quanta) indicating a weak coupling of this mode to the rather large density of background states. Furthermore, a vibrational progression of fifty quanta would require a large, physical unrealistic displacement from the equilibrium geometry. Thus, a single mode explanation would be quite unusual and, therefore, this issue requires further investigation.

Borrelli and Peluso³⁹ have analyzed the photodetachment of the $c\text{-C}_4\text{F}_8^-$ anion in terms of the Franck-Condon factors between the ground state of the anion and neutral species. Their results show that excitation of only the ν_5 mode results in a much narrower spectral profile ($\sim 5,000\text{ cm}^{-1}$) than experimentally observed, with the maximum intensity corresponding to the 5_0^4 transition. Instead, consideration of both the ν_5 and the ν_1 ring-breathing modes results in a spectral profile in qualitative agreement with the experiment. This simulation (shown in Figure 7.03a) is composed of ~ 60 peaks that are spaced by approximately 370 cm^{-1} , resulting in an overall bandwidth of $\sim 23,000\text{ cm}^{-1}$. The spectrum is composed of a series of combination band progressions of the type $1_0^m 5_0^n$, where n and m are integers. Because the ratio of these two frequencies ($\omega_1 \approx 4\omega_5$) is very close to an integer (Table 7.01), transitions of the type $1_0^m 5_0^n$ and $1_0^{m-1} 5_0^{n+4}$ are not resolvable from one another; because of this accidental degeneracy all the peaks in the spectrum are equally spaced. Figure 7.03b displays the room temperature Franck-Condon simulation where all modes have been considered. The excellent quality of the simulation is readily apparent and the underlying continuum in the spectrum is due to the low-frequency ring-puckering mode (ν_6), which in the neutral species exhibits a double well potential energy surface. Minor contributions from the other totally

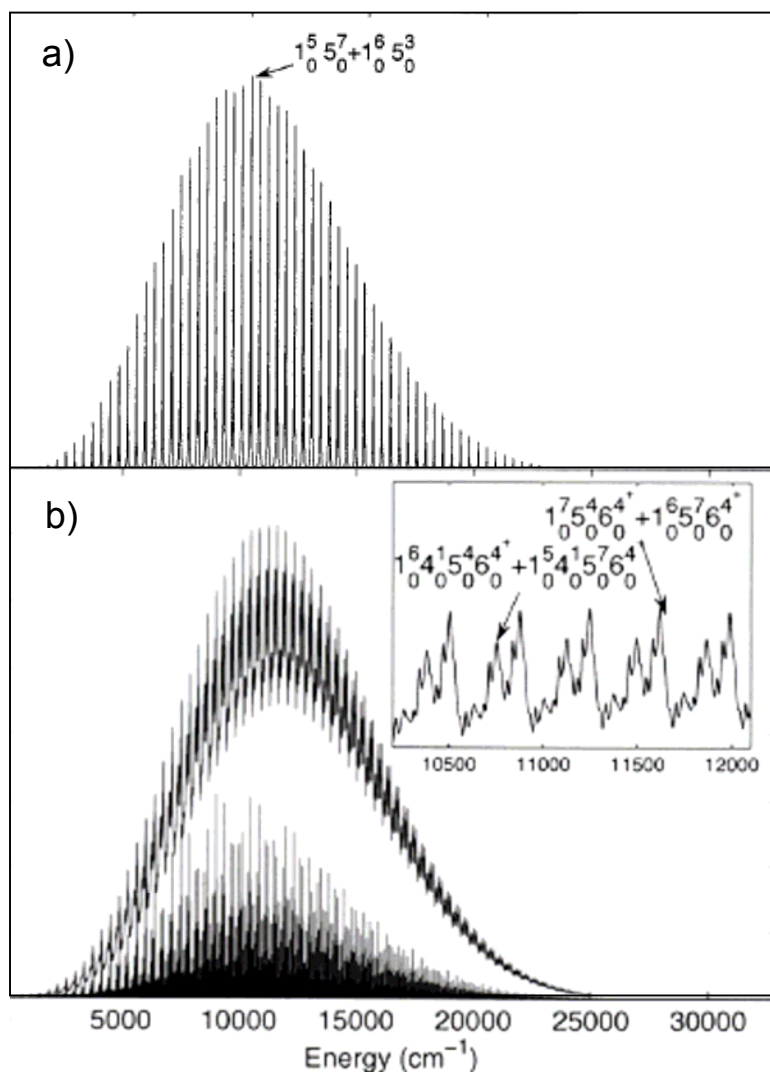


Figure 7.03: Calculated photoelectron spectra of the $c\text{-C}_4\text{F}_8^-$ anion reproduced from reference 39, with permission copyright 2008, American Institute of Physics, where a) only the ν_5 and ν_1 modes were considered and b) where all modes were considered. The Franck-Condon simulations are based on the equilibrium geometries and frequencies for the $c\text{-C}_4\text{F}_8^-$ anion and neutral calculated at the MP2/TZVPP level of theory. For both spectra, the raw Franck-Condon factors were convoluted with a 25 cm^{-1} fwhm Gaussian function. Note that in this figure the energy axis is reversed from Figure 7.01.

symmetric modes contribute to the underlying shape and to a complex fine structure shown in the inset of Figure 7.03b; these peaks are not resolvable within the instrument resolution.

As previously mentioned, other EA values have been reported in the literature.^{21,48} Although the photoelectron spectrum of $c\text{-C}_4\text{F}_8^-$ does not give a direct determination of this value, it does provide an upper bound of ~ 0.75 eV. Hiraoka and coworkers measured $\text{EA}(c\text{-C}_4\text{F}_8)$ relative to that of SF_6 , using a pulsed electron beam high pressure mass spectrometer.⁴⁸ They reported a value of 1.05 eV, which is incompatible with the photoelectron spectrum reported here. Hiraoka interpreted his observations to suggest the presence of an excited $c\text{-C}_4\text{F}_8^-$ isomer, which would form at elevated temperatures (above 350 K) and undergo electron detachment. The EA of this other isomer was reported to be 0.5 eV, based upon electron transfer equilibrium with O_2 . The coexistence of a second isomer, however, is not supported by photoelectron angular distribution measurements, which give a smooth minor progression of the anisotropy parameter (β) across the spectrum, or by Franck-Condon calculations, which effectively reproduce the observed spectrum by only considering a single isomer of the $c\text{-C}_4\text{F}_8^-$ anion. While these results do not provide a definitive EA determination, they do allow for a definitive choice between the two most reliable prior determinations. Thus we conclude that an $\text{EA}(c\text{-C}_4\text{F}_8)$ of 0.63 eV⁹ is both consistent with the data presented here, and the most reliable value available. A detailed discussion of all of the earlier determinations of $\text{EA}(c\text{-C}_4\text{F}_8)$ has been recently given by Miller *et al.*⁹

7.3.2) Photoelectron Spectrum of the SF_6^- Anion

Figure 7.04 presents the photoelectron spectrum of the SF_6^- ion collected under cold flow tube conditions where the anion temperature is estimated to be in the 150-200 K temperature range.⁴⁰ The most striking aspect of this spectrum is that,

despite the fact that the adiabatic electron affinity is reported to be 1.05 ± 0.1 eV,⁴⁹ significant photoelectron activity does not begin until almost 2 eV. The 3 eV location of the band maximum (vertical electron detachment energy, VDE), however, is qualitatively consistent with calculations (CCSD(T)/6-311+G(2df)) of the anion structure,³⁶ which predict that the anion retains the O_h symmetry of the neutral and that S–F bonds are elongated by ~ 0.2 Å. The spectrum is composed of two different progressions spaced by a constant frequency as indicated by solid lines and dashed lines in the inset of Figure 7.04. This spectrum is compared to the photoelectron spectrum of the bare SF_6^- anion and SF_6^- tagged with one argon atom collected using a double focusing tandem time of flight pulsed spectrometer at Yale University⁵⁰ in Figure 7.05. In these experiments the bare SF_6^- anion was generated by entraining trace SF_6 in an expansion of N_2 at a stagnation pressure of 5 atm. For both of the bare SF_6^- spectra (traces a and b), discernable vibrational fine structure appears with similar depth of modulation and location of the maxima, thus reflecting a robust property of the ion that is independent of the method of preparation. The spectrum of $\text{SF}_6^- \cdot \text{Ar}$ (trace c) displays significantly sharper peaks than either of the bare ion spectra (traces a and b), and the pattern appears uniformly shifted by ~ 52 meV towards higher binding energy. The tagged spectrum clearly displays the second series of interloper peaks with similar peak intensities as those evident in the bare ion. Thus, the Ar atom does not seem to significantly perturb the structure, but rather further quenches the SF_6^- subsystem into its ground vibrational state.

The main progression is remarkably harmonic and has a constant spacing of 750 ± 20 cm^{-1} , which is assigned to the symmetric a_{1g} S–F stretching mode (ν_1) in neutral SF_6 . Note that at lower levels of vibrational excitation accessible by direct absorption from the ground state neutral, high resolution spectroscopic analysis

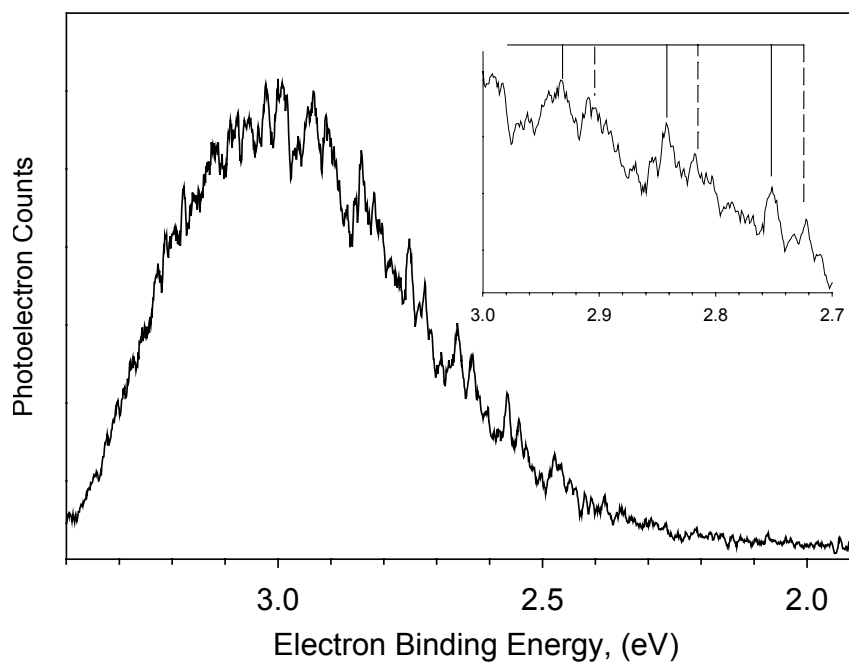


Figure 7.04: The 351.1 nm photodetachment spectrum of SF₆⁻ taken under cold flow tube conditions at the magic angle. A regular harmonic progression is present (solid line) with spacing corresponding to ν_1 frequency of $750 \pm 20 \text{ cm}^{-1}$ of the neutral molecule. A second progression is present (dashed lines) with the same character spacing; however, this second progression is displaced by $440 \pm 10 \text{ cm}^{-1}$ relative to the main features.

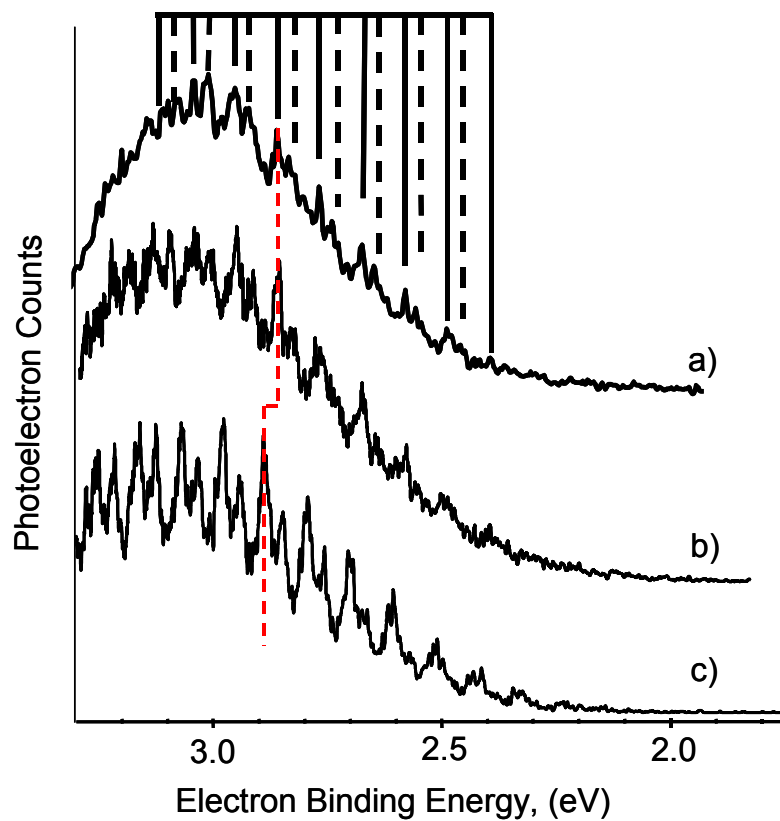


Figure 7.05: Comparison of the (a) 351.1 nm photodetachment spectrum of SF_6^- reproduced from Figure 7.04, and (b and c) the SF_6^- photoelectron spectrum taken by Mark A. Johnson's group at Yale University using a double focusing tandem time of flight pulsed spectrometer, where SF_6^- was generated by entraining trace SF_6 in an expansion of N_2 at a stagnation pressure of 5 atm. Trace b is a spectrum of the bare SF_6^- ion while trace c is a spectrum of $\text{SF}_6^- \cdot \text{Ar}$.

indicates that this mode indeed exhibits only rather small coupling constants in the anharmonic Hamiltonian. Inspection of the calculated spectrum suggests that the peak of the vibrational progression occurs at $v \sim 27$. This is consistent with the slightly smaller (by 26 cm^{-1}) observed spacing relative to the fundamental transition since $X_{11} = -0.896 \text{ cm}^{-1}$.³³

Assignment of the second active mode in the spectrum is less obvious. Since the spacing of the interloper peaks remains constant throughout the spectrum, it is unlikely that two different modes are activated upon photodetachment to give two different Gaussian-like progressions that originate from the same initial state of the anion. Additionally, it is unlikely that the interloper peaks are due to contributions from residual vibrational hot bands. As shown in Table 7.02, the calculated SF_6^- frequencies vary from 237 to 722 cm^{-1} , implying that there is plausible excitation of ν_4 , ν_5 , and ν_6 in the thermal ensemble; however, none of these frequencies matches the observed energy gap. Furthermore, as discussed above, the consistency of the spectra in different ion sources indicates that the second mode does not arise from excited vibrational levels of the anion ground electronic state. This second mode is systematically displaced by about $440 \pm 10 \text{ cm}^{-1}$ relative to the main features. This frequency does not correspond to any of the fundamental frequencies in neutral SF_6 (Table 7.02); thus, this second progression is not likely due to a combination band assignment based on one quantum of another vibrational mode. One further possibility is that the second progression is due to an overtone/combination band. The closest match to the observed splitting is $2\nu_4$ ($\sim 1220 \text{ cm}^{-1}$), which is a non-totally symmetric, IR active mode; therefore, we would only expect even quanta to be

Table 7.02: Theoretical frequencies (cm^{-1}), calculated using the MBPT(2) level of theory for SF_6 anion and neutral and the experimental values for SF_6 neutral.

Vibrational Mode		SF_6		SF_6^-
		Theory ³⁶	Exp. ⁵¹	Theory ³⁶
ν_1	a_{1g}	779	775	626
ν_2	t_g	655	643	447
ν_3	t_{1u}	965	948	722
ν_4	t_{1u}	611	615	306
ν_5	t_{2g}	519	524	336
ν_6	t_{2u}	346	348	237

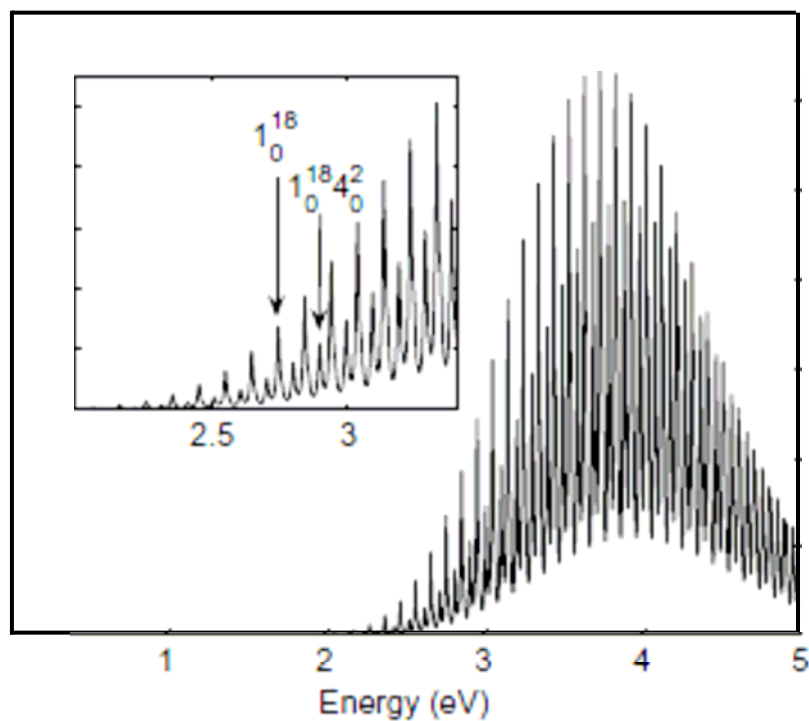


Figure 7.06: Calculated photoelectron spectra of the SF_6^- anion reproduced from reference 38 with permission copyright 2008, Elsevier. In this simulation the equilibrium geometries of the SF_6^- anion and neutral are determined from MP2/6-311G(2df) calculations. The raw Franck-Condon factors were convoluted with a 70 cm^{-1} Lorentzian function. Note that in this figure the energy axis is reversed from Figures 7.04 and 7.05.

populated in photodetachment. Based on this assignment, the ν_4 frequency would be $660 \pm 10 \text{ cm}^{-1}$.

This overtone/combination band assignment is confirmed by the Franck-Condon calculation of Borrelli (shown in Figure 7.06).³⁸ As expected, the calculated spectrum displays an extended 1_0^n progression, where n is an integer, with the maximum intensity corresponding to 1_0^{28} , in excellent agreement with experimental predictions. The interloper peaks are due to a progression of $1_0^n 4_0^2$. Thus for any given 1_0^x peak (where $n=x$), the interloper peak at 440 cm^{-1} higher energy corresponds a $1_0^{x-1} 4_0^2$ transition. The $0 \rightarrow 2$ transition of the ν_4 mode derives its intensity from the large change in vibrational frequencies upon photo-detachment. As revealed by Borrelli's calculations, the $t_{1u} \nu_4$ mode is triply degenerate and mixes with the $t_{1u} \nu_3$ mode; this mixing is observed in the Duschinsky matrix.

7.4) Conclusions

The photoelectron spectra of SF_6^- and $c\text{-C}_4\text{F}_8^-$ both display extended progressions in the ground electronic state manifold of the corresponding neutral. In both cases, there is no observable signal near the measured EA, which is consistent with a large change in geometry between the anionic and neutral species. The observed spectral features in $c\text{-C}_4\text{F}_8^-$ are primarily due to combination bands of two symmetric ring-breathing modes, ν_1 and ν_5 . Since the frequency ratio of these two modes is very close to an integer value, a very simple progression emerges that resembles a single-mode harmonic progression. The photoelectron spectrum of SF_6^- is dominated by a long progression in the ν_1 S-F stretching mode, with an envelope consistent with theoretical predictions that the anion preserves the O_h symmetry of the neutral, but has a longer S-F bond length. This main progression

occurs with an unexpectedly strong ν_1 and ν_4 overtone/combination band progression.

7.5) Acknowledgements

This work would not have been possible without the contributions from Mr. Scott W. Wren, Dr. Adam J. Gianola, and Prof. W. Carl Lineberger at JILA, Mr. Joseph C. Bopp, Mr. Joseph R. Roscioli, and Prof. Mark A. Johnson at Yale University, and Dr. Thomas M. Miller and Dr. A. A. Viggiano at Hanscom Air Force Research Laboratory. Furthermore, I wish to acknowledge the work of Raffaele Borrelli and Andrea Peluso, whose Franck-Condon calculations revealed flaws in our original interpretation of these data. This work was supported by the Air Force Office of Scientific Research (FA9550-06-1-006).

7.6) Chapter 7 References

- (1) Morris, R. A.; Miller, T. M.; Viggiano, A. A.; Paulson, J. F.; Solomon, S.; Reid, G. Effects of Electron and Ion Reactions on Atmospheric Lifetimes of Fully Fluorinated Compounds. *Journal of Geophysical Research Atmospheres* **1995**, *100*, 1287-1294.
- (2) Compton, R. N.; Christophorou, L. G.; Hurst, G. S.; Reinhardt, P. W. Nondissociative Electron Capture in Complex Molecules and Negative-Ion Lifetimes. *Journal of Chemical Physics* **1966**, *45*, 4634-4639.
- (3) Compton, R. N.; Hurst, G. S.; Christophorou, L. G.; Reinhardt, P. W. "ORNL-TM-1409," 1966.
- (4) Dehmer, J. L.; Siegel, J.; Dill, D. Shape Resonances in e-SF₆ Scattering. *Journal of Chemical Physics* **1978**, *69*, 5205-5206.
- (5) Field, D.; Jones, N. C.; Ziesel, J. P. Cold Electron Scattering in SF₆ and C₆F₆: Bound and Virtual State Channels. *Physical Review A* **2004**, *69*, 0527216/1-0527216/11.
- (6) Ferch, J.; Raith, W.; Schroder, K. Total Cross-Section Measurement for e-SF₆ Scattering Down to 0.036 eV. *Journal of Physics B: Atomic, Molecular and Optical Physics* **1982**, *15*, L175-L178.
- (7) Christophorou, L. G.; Olthoff, J. K. Electron Interactions with SF₆. *Journal of Physical and Chemical Reference Data* **2000**, *29*, 267-330.
- (8) Christophorou, L. G.; Olthoff, J. K. Electron Interactions with *c*-C₄F₈. *Journal of Physical and Chemical Reference Data* **2001**, *30*, 449-473.
- (9) Miller, T. M.; Friedman, J. F.; Viggiano, A. A. Electron Attachment and Detachment and the Electron Affinity of *cyclo*-C₄F₈. *Journal of Chemical Physics* **2004**, *120*, 7024-7028.
- (10) Braun, M.; Gruber, F.; Ruf, M.-W.; Kumar, S. V. K.; Illenberger, E.; Hotop, H. IR Photon Enhanced Dissociative Electron Attachment to SF₆: Dependence on Photon, Vibrational, and Electron Energy. *Chemical Physics* **2006**, *329*, 148-162.
- (11) Fischer, G.; Purchase, R. L.; Smith, D. M. The Ring-Puckering Motion in Perfluorocyclobutane. *Journal of Molecular Structure* **1997**, *405*, 159-167.
- (12) Bauman, R. P.; Bulkin, B. J. Spectra and Structure of Perfluorocyclobutane. *Journal of Chemical Physics* **1966**, *45*, 496-498.
- (13) Mao, C.; Nie, C. S.; Zhu, Z. Y. Normal Coordinate Analyses of C₄-C₆ Perfluorocycloparaffins. *Spectrochimica Acta, Part A: Molecular Spectroscopy* **1988**, *44*, 1093-1098.

- (14) Beagley, B.; Calladine, R.; Pritchard, R. G.; Taylor, S. F. The Molecular-Structure of Perfluoro-Thiirane in the Presence of Perfluoro-Cyclobutane - a Gas-Phase Electron-Diffraction Study. *Journal of Molecular Structure* **1987**, *158*, 309-314.
- (15) Chang, C. H.; Porter, R. F.; Bauer, S. H. Molecular Structures of Perfluorocyclobutane and Perfluorocyclobutene, Determined by Electron Diffraction. *Journal of Molecular Structure* **1971**, *7*, 89-99.
- (16) Lemaire, H. P.; Livingston, R. L. The Molecular Structures of Octafluorocyclobutane and of Methylcyclobutane. *Journal of the American Chemical Society* **1952**, *74*, 5732-5736.
- (17) Miller, F. A.; Capwell, R. J. The Infrared and Raman Spectra of Octachloro-, Octafluoro-, and Octahydroxycyclobutane. *Spectrochimica Acta, Part A: Molecular Spectroscopy* **1971**, *A 27*, 1113-1131.
- (18) Blake, T.; Glendening, E.; Sams, R.; Sharpe, S.; Xantheas, S. High-Resolution Infrared Spectroscopy in the 1200-1300 cm^{-1} Region and Accurate Theoretical Estimates for the Structure and Ring-Puckering Barrier of Perfluorocyclobutane. *Journal of Physical Chemistry A* **2007**, *111*, 11328-11341.
- (19) El'Sohly, A. M.; Tschumper, G. S.; Crocombe, R. A.; Wang, J. T.; Williams, F. Computational and ESR studies of electron attachment to decafluorocyclopentane, octafluorocyclobutane, and hexafluorocyclopropane: Electron affinities of the molecules and the structures of their stable negative ions as determined from C-13 and F-19 hyperfine coupling constants. *Journal of the American Chemical Society* **2005**, *127*, 10573-10583.
- (20) Gallup, G. A. The Structures of $c\text{-C}_4\text{F}_8$ and $c\text{-C}_4\text{F}_8^-$ and the Adiabatic Electron Affinity of $c\text{-C}_4\text{F}_8$. *Chemical Physics Letters* **2004**, *399*, 206-209.
- (21) Lifshitz, C.; Tiernan, T. O.; Hughes, B. M. Electron Affinities from Endothermic Negative-Ion Charge-Transfer Reactions. IV. SF_6 , Selected Fluorocarbons and Other Polyatomic-Molecules. *Journal of Chemical Physics* **1973**, *59*, 3182-3192.
- (22) Compton, R. N.; Reinhardt, P. W.; Cooper, C. D. Collisional Ionization Between Fast Alkali Atoms and Selected Hexafluoride Molecules. *Journal of Chemical Physics* **1978**, *68*, 2023-2036.
- (23) Babcock, L. M.; Streit, G. E. Ion-Molecule Reactions of SF_6^- : Determination of I.P.(SF_5), A.P.($\text{SF}_5^+/\text{SF}_6$), and D($\text{SF}_5\text{-F}$). *Journal of Chemical Physics* **1981**, *74*, 5700-5706.
- (24) Hay, P. J. The Relative Energies of SF_6^- and SF_6 as a Function of Geometry. *Journal of Chemical Physics* **1982**, *76*, 502-504.
- (25) Streit, G. E. Gas-Phase Reactions of O^- and O_2^- with a Variety of Halogenated Compounds. *Journal of Physical Chemistry* **1982**, *86*, 2321-2324.

- (26) Christophorou, L. G. Electron-Molecule Interactions and Their Applications; Ed.; Academic: New York, 1984.
- (27) Klobukowski, M.; Barandiaran, Z.; Seijo, L.; Huzinaga, S. Towards HF SCF Value of Electron-Affinity of SF₆. *Journal of Chemical Physics* **1987**, *86*, 1637-1638.
- (28) Mock, R. S.; Grimsrud, E. P. Electron Photodetachment of the Molecular Anions of SF₆ and Several Perfluorinated Hydrocarbons. *Chemical Physics Letters* **1991**, *184*, 99-101.
- (29) Datskos, P. G.; Carter, J. G.; Christophorou, L. G. Photodetachment of SF₆⁻. *Chemical Physics Letters* **1995**, *239*, 38-43.
- (30) Gianturco, F. A.; Lucchese, R. R. Electron Scattering From Gaseous SF₆: Comparing Calculations with Experiments. *Journal of Chemical Physics* **2001**, *114*, 3429-3439.
- (31) Tachikawa, H. *Ab initio* MO Calculations of Structures and Electronic States of SF₆ and SF₆⁻. *Journal of Physics B: Atomic, Molecular and Optical Physics* **2002**, *35*, 55-60.
- (32) Braun, M.; Ruf, M. W.; Hotop, H.; Allan, M. Low-Energy Electron Attachment to SF₆ Molecules: Vibrational Structure in the Cross-Section for SF₅⁻ Formation Up to 1 eV. *Chemical Physics Letters* **2006**, *419*, 517-522.
- (33) McDowell, R. S.; Krohn, B. J. Vibrational Levels and Anharmonicity in SF₆. II. Anharmonic and Potential Constants. *Spectrochimica Acta, Part A: Molecular Spectroscopy* **1986**, *42*, 371-385.
- (34) Drzaic, P. S.; Brauman, J. I. Electron Photodetachment Study of Sulfur-Hexafluoride Anion - Comments on the Structure of SF₆⁻. *Journal of the American Chemical Society* **1982**, *104*, 13-19.
- (35) Lugez, C. L.; Jacox, M. E.; King, R. A.; Schaefer, H. F. Experimental and *ab initio* Study of the Infrared Spectra of Ionic Species Derived from SF₆ and SF₄ and Trapped in Solid Neon. *Journal of Chemical Physics* **1998**, *108*, 9639-9650.
- (36) Gutsev, G. L.; Bartlett, R. J. Adiabatic Electron Affinities of PF₅ and SF₆: A Coupled-Cluster Study. *Molecular Physics* **1998**, *94*, 121-125.
- (37) Bopp, J. C.; Roscioli, J. R.; Johnson, M. A.; Miller, T. M.; Viggiano, A. A.; Villano, S. M.; Wren, S. W.; Lineberger, W. C. Spectroscopic Characterization of the Isolated SF₆⁻ and C₄F₈⁻ Anions: Observation of Very Long Harmonic Progressions in Asymmetric Deformation Modes Upon Photodetachment. *Journal of Physical Chemistry A* **2007**, *111*, 1214-1221.
- (38) Borrelli, R. Franck-Condon Analysis of the SF₆⁻ Electron Photodetachment Spectrum. *Chemical Physics Letters* **2007**, *445*, 84-88.

(39) Borrelli, R.; Peluso, A. The Electron Photodetachment Spectrum of $c\text{-C}_4\text{F}_8^-$: A Test Case for the Computation of Franck-Condon Factors of Highly Flexible Molecules. *The Journal of Chemical Physics* **2008**, *128*, 044303/1-044303/7.

(40) Wenthold, P. G.; Polak, M. L.; Lineberger, W. C. Photoelectron Spectroscopy of the Allyl and 2-Methylallyl Anions. *Journal of Physical Chemistry* **1996**, *100*, 6920-6926.

(41) Neumark, D. M.; Lykke, K. R.; Andersen, T.; Lineberger, W. C. Laser Photodetachment Measurement of the Electron-Affinity of Atomic Oxygen. *Physical Review A* **1985**, *32*, 1890-1892.

(42) Moore, C. E. "Atomic Energy Levels," 1952.

(43) Becke, A. D. Density-Functional Thermochemistry. III. The Role of Exact Exchange. *Journal of Chemical Physics* **1993**, *98*, 5648-5652.

(44) Lee, C. T.; Yang, W. T.; Parr, R. G. Development of the Colle-Salvetti Correlation-Energy Formula into a Functional of the Electron-Density. *Physical Review B* **1988**, *37*, 785-789.

(45) Krishnan, R.; Binkley, J. S.; Seeger, R.; Pople, J. A. Self-Consistent Molecular-Orbital Methods. II. Basis Set for Correlated Wave-Functions. *Journal of Chemical Physics* **1980**, *72*, 650-654.

(46) Frisch, M. J.; Trucks, G. W.; Schlegel, H. B.; Scuseria, G. E.; Robb, M. A.; Cheeseman, J. R.; Montgomery, J. A.; Vreven, T.; Kudin, K. N.; Burant, J. C.; Millam, J. M.; Iyengar, S. S.; Tomasi, J.; Barone, V.; Mennucci, B.; Cossi, M.; Scalmani, G.; Rega, N.; Petersson, G. A.; Nakatsuji, H.; Hada, M.; Ehara, M.; Toyota, K.; Fukuda, R.; Hasegawa, J.; Ishida, M.; Nakajima, T.; Honda, Y.; Kitao, O.; Nakai, H.; Klene, M.; Li, X.; Knox, J. E.; Hratchian, H. P.; Cross, J. B.; Adamo, C.; Jaramillo, J.; Gomperts, R.; Stratmann, R. E.; Yazyev, O.; Austin, A. J.; Cammi, R.; Pomelli, C.; Ochterski, J. W.; Ayala, P. Y.; Morokuma, K.; Voth, G. A.; Salvador, P.; Dannenberg, J. J.; Zakrzewski, V. G.; Dapprich, S.; Daniels, A. D.; Strain, M. C.; Farkas, O.; Malick, D. K.; Rabuck, A. D.; Raghavachari, K.; Foresman, J. B.; Ortiz, J. V.; Cui, Q.; Baboul, A. G.; Clifford, S.; Cioslowski, J.; Stefanov, B. B.; Liu, G.; Liashenko, A.; Piskorz, P.; Komaromi, I.; Martin, R. L.; Fox, D. J.; Keith, T.; Al-Laham, M. A.; C. Y. Peng; Nanayakkara, A.; Challacombe, M.; Gill, P. M. W.; Johnson, B.; Chen, W.; Wong, M. W.; Gonzalez, C.; Pople, J. A. Gaussian 03, revision B.05; I. Gaussian, Ed. Pittsburgh, PA, 2003.

(47) Leopold, D. G.; Murray, K. K.; Miller, A. E. S.; Lineberger, W. C. Methylene: A Study of the X^3B_1 and a 1a_1 States by Photoelectron-Spectroscopy of CH_2^- and CD_2^- . *Journal of Chemical Physics* **1985**, *83*, 4849-4865.

(48) Hiraoka, K.; Mizuno, T.; Eguchi, D.; Takao, K.; Iino, T.; Yamabe, S. Gas-phase Ion/Molecule Reactions in Octafluorocyclobutane. *Journal of Chemical Physics* **2002**, *116*, 7574-7582.

(49) Grimsrud, E. P.; Chowdhury, S.; Kebarle, P. Electron-Affinity of SF_6 and Perfluoromethylcyclohexane - The Unusual Kinetics of Electron-Transfer

Reactions $A^+ + B = A + B^+$, Where $A = SF_6$ or Perfluorinated Cyclo-Alkanes. *Journal of Chemical Physics* **1985**, *83*, 1059-1068.

(50) Johnson, M. A.; Lineberger, W. C. Pulsed Methods for Cluster Ion Spectroscopy. In *Techniques for the Study of Ion-Molecule Reactions*; J. M. Farrar and J. W. H. Saunders, Eds.; Wiley: New York, 1988; Vol. 20; pp 591-635.

(51) McDowell, R. S.; Krohn, B. J.; Flicker, H.; Vasquez, M. C. Vibrational Levels and Anharmonicity in SF_6 . I. Vibrational Band Analysis. *Spectrochimica Acta, Part A: Molecular Spectroscopy* **1986**, *42*, 351-369.

CHAPTER VIII

THERMOCHEMICAL STUDIES OF *N*-METHYLPYRAZOLE AND *N*-METHYLIMIDAZOLE

8.1) Introduction

Azoles are nitrogen-containing five-membered ring heteroaromatic compounds whose structures are analogous to cyclopentadiene, C_5H_6 , where an N atom has replaced one or more C-H groups. These compounds constitute an important class of heterocycles whose structures appear as fundamental units in biomolecules,¹ pharmaceuticals,^{2,3} ionic liquids,^{4,5} dyes,^{6,7} explosives,⁸ and fuels.⁹⁻¹¹ Sound knowledge of the thermochemistry, especially the bond dissociation energies (BDEs), of these compounds is important to fields such as combustion chemistry¹² and transition metal coordination chemistry.¹³⁻¹⁶

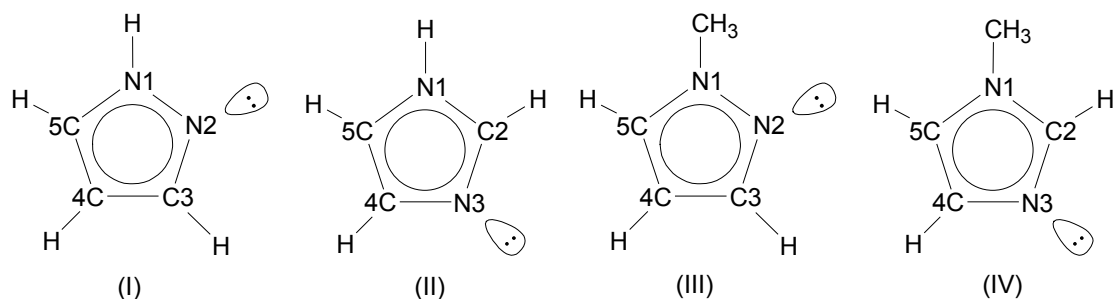
The vast majority of information in the literature about azoles has focused on pyrrole, C_4NH_5 . It is postulated that the thermal decomposition of pyrrole, along with other N-heterocycles that are contained in coal, leads to the formation of NO_x species in the atmosphere.^{17,18} The thermal decomposition of pyrrole has been investigated by two groups using shock tube pyrolysis.^{19,20} The initial decomposition step proceeds by a hydrogen-atom transfer from the nitrogen to the adjacent carbon (C2 carbon) to form pyrrolenine, followed by the cleavage of the C2-N bond to produce an acyclic structure.^{19,21} This acyclic structure further decomposes by C-C bond cleavage. In contrast, there is evidence that thermal decomposition of pyridine, the six-membered heterocycle that contains one nitrogen atom, is initiated by the cleavage of the C2-H bond.²² The difference between these two initiation steps, in part, may be attributed to the difference in C-H bond strengths of the five- and six-membered heterocycles. The C2-H and N-H bond strengths of pyrrole were

measured by Lee *et al.*²³ using photofragment translational spectroscopy to be $112.5 \pm 1 \text{ kcal mol}^{-1}$ and $88 \pm 2 \text{ kcal mol}^{-1}$, respectively. Later experiments,^{24,25} however, have not observed a C-H bond dissociation process in the photochemistry of pyrrole and find the N-H BDE to be higher, $93.92 \pm 0.11 \text{ kcal mol}^{-1}$. In contrast, the corresponding C2-H BDE of pyridine is reported to be much lower at $105 \text{ kcal mol}^{-1}$; for the C-H bonds that do not have an adjacent nitrogen atom (C3 and C4 carbons), the BDEs increase to $112 \text{ kcal mol}^{-1}$.²⁶ In contrast to this extensive knowledge of these mononitrogen heterocycles, much less is known about the nitrogen heterocycles that contain additional nitrogen atoms in the ring.

Our research program has utilized negative ion spectroscopy along with gas-phase ion chemistry to study several azoles.²⁷⁻³¹ Negative ion spectroscopy provides thermodynamic information such as electron affinities and term energies, allows for the measurement of vibrational frequencies, and gives insight into the molecular structure of both the anion and radical species.³² Gas-phase ion chemistry studies include the measurement of the forward and reverse proton transfer reaction rate constants in order to determine the gas-phase acidity relative to a reference acid. These techniques are complementary since the electron affinity (EA) of the neutral radical can be combined with the gas-phase acidity ($\Delta_a G_{298}$) to determine the bond dissociation energy (BDE) using a negative ion thermochemical cycle.^{33,34}

Using these techniques we have previously investigated the thermodynamic properties of pyrazole (I)^{29,30} and imidazole (II).²⁸ In that work, the 1-azolide anion was formed by deprotonation of the azole by hydroxide at the most acidic site, the N-H bond. Photoelectron spectra of the 1-azolide anions were reported along with a discussion of the electronic structure of the corresponding radical. The gas-phase acidity of the N-H bond was measured using proton transfer equilibrium

measurements and the N-H BDE was obtained. In addition to deprotonation at the nitrogen, deprotonation also occurred at the next acidic site, the carbon adjacent to the N-H group (C5 carbon), allowing for the assignment of the electron affinity of the C5 radical. In both the pyrazolide and the imidazolide anion spectra, C5 deprotonation was only observed when the azolide anion was prepared by proton transfer to hydroxide. When the azole anion was prepared by proton transfer to O^{\ominus} , only the 1-azolide anion spectra were seen. The acidity ($\Delta_a G_{298}$) of the C5-H bond was bracketed between that of water and the hydroxy radical at $380 \pm 4 \text{ kcal mol}^{-1}$. The C5-H BDE was then determined to be $121 \pm 4 \text{ kcal mol}^{-1}$ for pyrazole and $119 \pm 4 \text{ kcal mol}^{-1}$ for imidazole. The large error bars reflect the acidity gap between water and hydroxy radical. However, even when suitable reference acids are available, quantitative determination of the gas-phase acidities and C-H bond dissociation energies is difficult when there are multiple acidic sites in the molecule.



Measurements of gas-phase proton transfer reactions generally determine the gas-phase acidity (and hence the BDE) of only the most acidic site of a hydrocarbon. This limitation, in part, is due to the inherent difficulty in independently preparing the more basic anion from neutral precursors. One commonly used method to probe the acidity of the less acidic site is fluorodesilylation of substituted trimethylsilanes.³⁵⁻⁴⁰ This method allows for the preparation of regiospecific carbanions whose acidity can then be bracketed between two reference acids.

A second technique that allows for acidity measurements on molecules with multiple acidic sites uses a dual-cell Fourier transform mass spectrometer.^{41,42} In this method a mixture of isomeric anions is formed in the source region. To prevent catalyzed isomerization of the more basic anion to the less basic species, the ion mixture is extracted into a second chamber, which is free of neutral precursors. Using this technique, a lower bound acidity can be found for the less acidic proton. This method has recently been applied to determine the acidities of the N1 and N3 sites of uracil⁴¹ and the N9 and N10 sites of adenine and adenine derivatives.⁴² This technique, however, requires a sufficient difference in the acidity of the two sites so that bracketing experiments can be used; moreover, the timescale for ion extraction must be shorter than for ion isomerization.

The principal motivation of this work is to improve the precision of the C5-H BDE of pyrazole and imidazole through the investigation of the corresponding *N*-methylated species (III and IV). *N*-methylation of pyrazole and imidazole blocks the nitrogen site and makes the C5 position the most acidic site, without significantly changing the C-H bond energetics (as discussed below). Here we report the photoelectron spectra of *N*-methylpyrazolide anion and *N*-methylimidazolidide anion, as well as electronic structure calculations, which aid in the interpretation and assignment of the spectra. The gas-phase acidities of the C5 positions in *N*-methylpyrazole and *N*-methylimidazole were measured, and these measurements are used to determine the C5-H BDE.

8.2) Experimental Methods

8.2.1) Negative Ion Photoelectron Spectroscopy

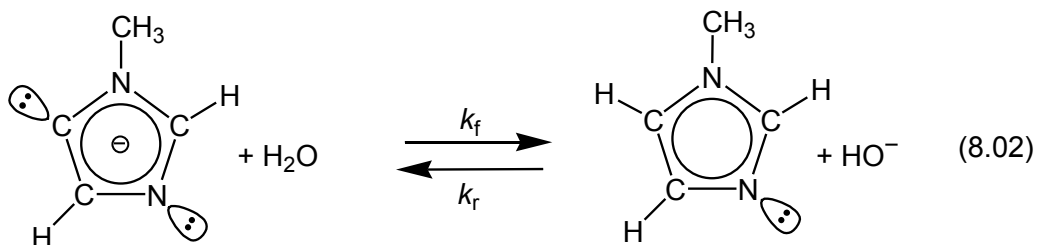
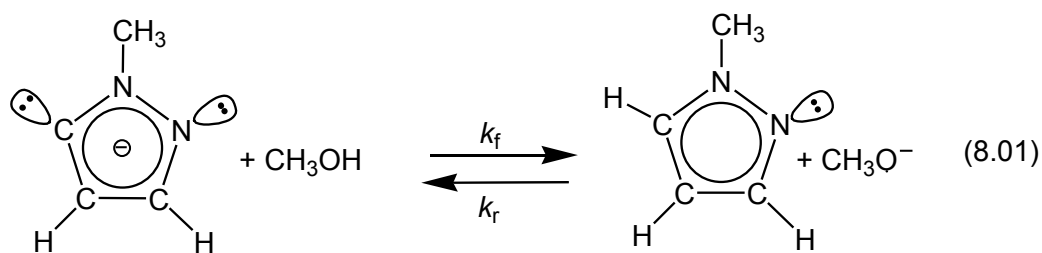
The 351.1 nm photoelectron spectra of the *N*-methylpyrazolide anion and the *N*-methylimidazolidide anion were obtained with a flowing afterglow-negative ion photoelectron spectrometer that was described in Chapter 4. The *N*-methyl-

pyrazolide and *N*-methylimidazolide anions are prepared by proton abstraction from *N*-methylpyrazole and *N*-methylimidazole, respectively, using hydroxide (OH⁻) as a base, downstream of a microwave discharge source under room temperature and liquid nitrogen conditions. Negative ions were gently extracted from the source region and passed through a Wien filter for mass selection. The mass selected ion beam was then crossed with a 351.1 nm (3.531 eV) line from a cw argon-ion laser in an external build up cavity producing ~100 W of circulating power. Photoelectrons that are ejected perpendicular to the plane of the ion-photon interaction region are energy analyzed by a hemispherical kinetic energy analyzer coupled to a position sensitive detector. The absolute energy scale is calibrated with the electron affinity (EA) of atomic oxygen⁴³ in the measurements of the photoelectron spectra, and a linear energy scale compression factor (< 1%), which is measured from the photoelectron spectra of reference ions S⁻,⁴⁴ I⁻,⁴⁵ and O⁻ using the EAs of the corresponding atoms.

Optimized geometries and harmonic vibrational frequencies (not scaled) for the neutral parent, anion, and radical are determined from density functional theory (DFT) calculations (B3LYP/6-311++G(d,p))⁴⁶⁻⁴⁸ using the Gaussian 03 suite of programs.⁴⁹ Simulated photoelectron spectra were obtained by calculating the Franck-Condon (FC) factors at a vibrational temperature of 300 K with the PESCAL program,⁵⁰ using calculated geometries, normal modes, and electron binding energies for the anion and radical. The methyl torsional mode is excluded from the simulation because of the incompatibility with the harmonic assumption used in the simulation.⁵¹

8.2.2) Flowing Afterglow-Selected Ion Flow Tube (FA-SIFT) Measurements

Gas-phase acidity ($\Delta_a G_{298}$) measurements of *N*-methylpyrazole and *N*-methylimidazole were obtained using a tandem flowing afterglow-selected ion flow tube instrument, FA-SIFT, described in Chapter 3. The acidity of *N*-methylpyrazole is determined relative to methanol [$\Delta_a G_{298}(\text{CH}_3\text{OH}) = 375.5 \pm 0.6 \text{ kcal mol}^{-1}$],⁵² shown in reaction 8.01, while the acidity of *N*-methylimidazole was determined relative to water [$\Delta_a G_{298}(\text{H}_2\text{O}) = 383.68 \pm 0.02 \text{ kcal mol}^{-1}$]⁵², shown in reaction 8.02. The photoelectron spectra collected for both isomers suggest that the C5 position is the most acidic site and therefore the acidity measurements represent the acidity of the C5-H bond (see discussion below).



The reactant ions, *N*-methyl-5-pyrazolide, *N*-methyl-5-imidazolide and CH_3O^- , were formed by proton abstraction from the corresponding neutrals by OH^- , mass selection, and injection into the reaction flow tube with minimal energy to reduce fragmentation from collision-induced dissociation. For all of the reactions studied, with the exception of the reverse reaction 8.02, neutral reagent flows were determined by measuring a change in pressure versus time in a calibrated volume; reagents were added to the flow tube through a manifold of inlets. This technique

was not used for the reaction of hydroxide with *N*-methylimidazole due to its low volatility. Instead a regulated but unknown flow of *N*-methylimidazole was introduced into the reaction flow tube at one position. A relative reaction rate was measured by alternately injecting NH_2^- and OH^- for reaction with the constant reactant flow. The neutral reagent concentration and the reaction rate constant were extracted from the relative rate measurement^{27,28} by assuming that the highly exothermic proton transfer reaction of NH_2^- with *N*-methylimidazole proceeds at $90 \pm 10\%$ of the calculated collision rate⁵³ ($k_{\text{col}} = 5.7 \cdot 10^{-9} \text{ cm}^3 \text{ s}^{-1}$).

The forward direction of reaction 8.01 and the reverse direction of reaction 8.02 are exothermic and proton transfer is the only observed pathway. For the corresponding endothermic reactions, adduct formation is observed in addition to proton transfer. The rate constant for proton transfer is determined from the overall rate constant and the proton transfer branching ratio. An experimental complication in measuring the proton transfer branching ratio is the occurrence of a secondary switching reaction between the adduct and water.⁵⁴ This reaction does not affect the overall rate constant but must be considered in determining the proton transfer branching ratio. This ratio was measured by monitoring the branching ratio at various reaction times and extrapolating to zero time, where there is no depletion of the adduct due to secondary reaction. Efforts were made to minimize mass discrimination, however, it was necessary to estimate the relative detection sensitivities when calculating the proton transfer branching ratio. The relative detection sensitivity was estimated by examining a series of exothermic ion-molecule reactions where only one ionic product was formed and the reactant and product ions were similar in mass to the ions of interest.

The absolute uncertainty of each rate constant measurement is generally $\pm 20\%$, but $\pm 50\%$ for reactions where branching ratios must be evaluated. The absolute error in the gas-phase acidity is smaller because some systematic errors (pressure, temperature, He flow rate, etc.) cancel in the rate ratio. Collision rate constants were calculated using parametrized trajectory collision rate theory.⁵³

8.3) Results and Discussion

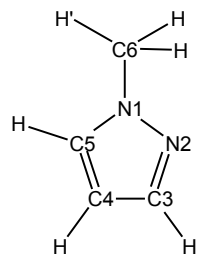
8.3.1) Computational Results

The B3LYP/6-311++G(d,p) optimized geometries of *N*-methylpyrazole, *N*-methyl-5-pyrazolide anion, *N*-methyl-5-pyrazolyl radical, *N*-methylimidazole, *N*-methyl-5-imidazolide anion, and *N*-methyl-5-imidazolyl radical along with the harmonic vibrational frequencies for the above anions and radicals are presented in Tables 8.01-8.04. Examination of the DFT optimized geometries shows that, for both *N*-methyl-5-pyrazolide anion and *N*-methyl-5-imidazolide anion, there are significant geometry differences between the anion and the $^2A'$ state of the radical. Similar ring distortions are predicted for both isomers; the most dramatic changes are seen in the shortening of the C4-C5 and N1-C5 bonds and in the decrease of the N1-C5-C4 bond angle. It is therefore expected that vibrational modes, which contain significant ring distortion along these coordinates, will be activated upon photodetachment.

8.3.2) Photoelectron Spectra of *N*-methyl-5-pyrazolide Anion

The 351.1 nm magic angle photoelectron spectrum of the *N*-methylpyrazolide anion, generated from the reaction of OH^- with *N*-methylpyrazole, is shown in Figure 8.01a. Electronic structure calculations were used to evaluate the acidity of *N*-methylpyrazole; these results are summarized in Table 8.05. DFT calculations predict that the C5 carbon is the most acidic site and therefore it is most likely that deprotonation by OH^- will occur at this site. Peak *a* is assigned as the electronic

Table 8.01: B3LYP/6-311++G(d,p) Optimized Geometries for *N*-methylpyrazole, *N*-methyl-5-pyrazolide and *N*-methyl-5-pyrazolyl.



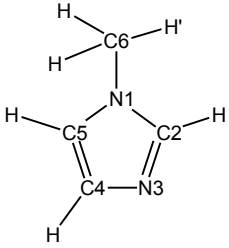
	<i>N</i> -methyl- pyrazole	<i>N</i> -methyl-5- pyrazolide	<i>N</i> -methyl-5-pyrazolyl	
	(\tilde{X}^1A')	(\tilde{X}^1A')	(\tilde{X}^2A')	(\tilde{A}^2A'')
N1–N2	1.348	1.380	1.362	1.450
N2–C3	1.332	1.335	1.335	1.313
C3–C4	1.410	1.412	1.413	1.418
C4–C5	1.382	1.416	1.377	1.490
C5–N1	1.358	1.374	1.340	1.318
N1–C6	1.451	1.442	1.451	1.453
C6–H'	1.090	1.089	1.089	1.087
C6–H	1.091	1.098	1.091	1.092
C5–H	1.078	-	-	-
C3–H	1.080	1.0859	1.0803	1.081
C4–H	1.078	1.0835	1.0759	1.081
∠N1–N2–C3	105.0	102.4	105.1	103.6
∠N2–C3–C4	111.7	111.5	112.6	110.8
∠C3–C4–C5	104.3	108.3	101.9	108.3
∠C4–C5–N1	106.8	100.7	110.5	100.3
∠C5–N1–N2	112.2	117.1	109.9	116.9
∠C5–N1–C6	119.7	125.8	129.4	128.0
∠N1–C6–H'	108.8	107.5	108.4	107.6
∠N1–C6–H	121.6	111.2	109.9	109.9
∠N1–C5–H	121.6	-	-	-
∠N2–C3–H	119.6	118.9	119.2	120.0
∠C5–C4–H	127.3	125.6	128.6	124.8

Bond lengths are in Angstroms and bond angles are in degrees.

Table 8.02: B3LYP/6-311++G(d,p) Harmonic Frequencies (cm⁻¹) of *N*-methyl-5-pyrazolide and *N*-methyl-5-pyrazolyl.

ν	symmetry	<i>N</i> -methyl-5-pyrazolide (\tilde{X}^1A')	<i>N</i> -methyl-5-pyrazolyl (\tilde{X}^2A')	<i>N</i> -methyl-5-pyrazolyl (\tilde{A}^2A'')
1	A'	3176	3276	3238
2		3145	3227	3223
3		3121	3145	3166
4		2976	3050	3045
5		1504	1530	1518
6		1464	1508	1476
7		1420	1470	1439
8		1380	1444	1417
9		1368	1377	1321
10		1249	1299	1208
11		1232	1257	1194
12		1153	1205	1084
13		1062	1081	1008
14		999	1020	979
15		935	964	916
16		911	899	680
17		707	685	553
18		388	360	377
19	A''	3007	3116	3106
20		1477	1478	1481
21		1136	1145	1156
22		836	877	898
23		749	754	759
24		654	659	671
25		615	523	499
26		222	199	233
27		81	34	145

Table 8.03: B3LYP/6-311++G(d,p) Optimized Geometries for *N*-methylimidazole, *N*-methyl-5-imidazolide and *N*-methyl-5-imidazolyl.



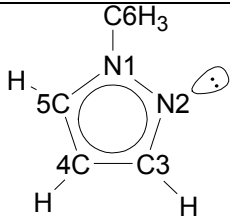
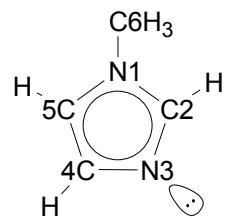
	<i>N</i> -methylimidazole (\tilde{X}^1A')	<i>N</i> -methyl-5- imidazolide (\tilde{X}^1A') (TS)	<i>N</i> -methyl-5-imidazolyl (\tilde{X}^2A')	(\tilde{A}^2A'')
N1–C2	1.367	1.378	1.368	1.390
C2–N3	1.314	1.316	1.318	1.330
N3–C4	1.375	1.395	1.382	1.345
C4–C5	1.372	1.398	1.365	1.487
C5–N1	1.380	1.402	1.370	1.362
N1–C6	1.454	1.444	1.455	1.461
C6–H'	1.090	1.097	1.090	1.087
C6–H	1.092	1.095	1.092	1.093
C5–H	1.078	-	-	-
C2–H	1.080	1.084	1.080	1.083
C4–H	1.079	1.084	1.076	1.082
\angle N1–C2–N3	112.3	111.0	111.9	112.1
\angle C2–N3–C4	105.2	103.6	106.9	103.4
\angle N3–C4–C5	110.5	114.8	107.3	114.5
\angle C4–C5–N1	105.7	99.6	109.1	98.9
\angle C5–N1–C2	106.4	110.9	104.9	111.1
\angle C5–N1–C6	126.7	124.5	127.0	123.9
\angle N1–C6–H'	108.9	110.9	108.7	107.3
\angle N1–C6–H	110.7	109.9	110.5	110.6
\angle N1–C2–H	121.8	123.1	122.6	123.2
\angle N1–C5–H	122.0	-	-	-
\angle C5–C4–H	128.0	126.3	130.1	124.8

Bond lengths are in Angstroms and bond angles are in degrees.

Table 8.04: B3LYP/6-311++G(d,p) Harmonic Frequencies (cm⁻¹) of *N*-methyl-5-imidazolide and *N*-methyl-5-imidazolyl.

ν	symmetry	N-methyl-5- imidazolide (\tilde{X}^1A')	N-methyl-5- imidazolyl (\tilde{X}^2A')	N-methyl-5- imidazolyl (\tilde{A}^2A'')
1	A'	3166	3273	3218
2		3159	3233	3212
3		3051	3134	3160
4		2991	3045	3039
5		1515	1519	1511
6		1501	1508	1490
7		1434	1473	1441
8		1404	1436	1373
9		1331	1365	1279
10		1272	1348	1264
11		1222	1261	1182
12		1188	1239	1169
13		1095	1101	1068
14		1025	1067	1015
15		971	1028	974
16		915	865	823
17		687	672	673
18		366	344	365
19	A''	3041	3108	3100
20		1466	1485	1499
21		1133	1144	1225
22		788	811	1124
23		679	780	831
24		673	663	706
25		616	488	550
26		215	201	237
27		57i	60	80

Table 8.05: B3LYP/6-311++G(d,p) $\Delta_a G_{298}$ and BDE of *N*-methylpyrazole and *N*-methylimidazole and the EA of the corresponding radicals.

		$\Delta_a G_{298}$ (kcal mol ⁻¹)	EA (eV)	D_0 (kcal mol ⁻¹)
<i>N</i> -methylpyrazole				
	C3-H	394.3	1.254	115.5
	C4-H	390.9	1.544	118.8
	C5-H	377.6	2.045	117.5
	C6-H	384.0	0.635	90.9
<i>N</i> -methylimidazole				
	C2-H	381.7	1.751	114.8
	C4-H	397.9	1.058	115.1
	C5-H	380.8	1.965	118.1
	C6-H	381.0	0.785	91.4

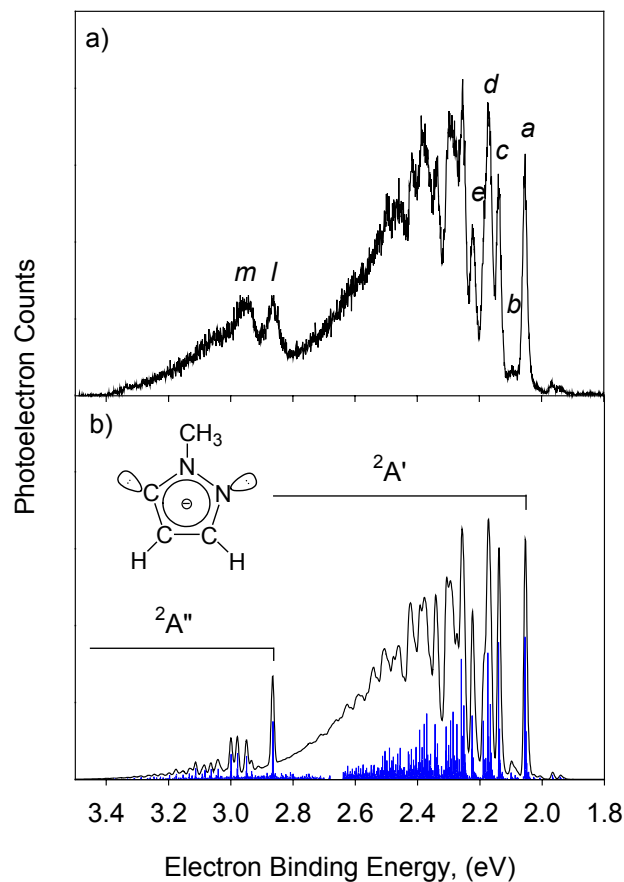


Figure 8.01: a) The 351.1 nm magic-angle photoelectron spectrum of the *N*-methyl-5-pyrazolide anion. b) Simulations of the spectrum based on optimized geometries and normal modes from B3LYP/6-311++G(d,p) calculations. The sticks (blue) are the raw Franck-Condon factors and the solid line is the 10 meV fwhm Gaussian convolutions for transitions from \tilde{X}^1A' *N*-methyl-5-pyrazolide anion to \tilde{X}^2A' and \tilde{A}^2A'' *N*-methyl-5-pyrazolyl radical. In the simulated spectra the positions and intensities were set to match those observed in the experimental spectrum.

band origin at 2.054 ± 0.006 eV, which corresponds to the EA of the *N*-methyl-5-pyrazolyl radical. The peaks observed at higher eBE correspond to excited vibrational levels of the *N*-methyl-5-pyrazolyl radical. The photoelectron angular distribution was measured and the anisotropy parameter (β) is ~ 0.5 at the origin but gradually decreases to ~ 0.1 at 2.8 eV. Beyond 2.8 eV, β rapidly decreases and is -0.4 for peaks *l* and *m*. DFT calculations find minima with C_s symmetry for both the anion and radical. The in-plane C-H bond of the methyl group is trans to the N1-N2 bond for both states. The electronic ground state of the *N*-methyl-5-pyrazolide anion is predicted to be \tilde{X}^1A' , while that of the *N*-methyl-5-pyrazolyl radical is predicted to be \tilde{X}^2A' . The calculated EA of the *N*-methyl-5-pyrazolyl radical is 2.045 eV, in good agreement with the assignment of the origin above. DFT calculations predict that there is an excited state, \tilde{A}^2A'' , with a term energy (T_e) of 0.768 eV.

FC factors were computed for the transition from the \tilde{X}^1A' state of the *N*-methyl-5-pyrazolide anion to both the \tilde{X}^2A' and \tilde{A}^2A'' states of the *N*-methyl-5-pyrazolyl radical. The stick spectra and the spectrum resulting from convoluting the stick spectrum with a 10 meV fwhm Gaussian function, which represents the instrument resolution, are shown in Figure 8.01b. The binding energies for both radical states have been slightly shifted (< 40 meV) and the intensities normalized to match the experimental spectrum. The simulated spectrum is in excellent agreement with the experimental spectrum, and it confirms that the spectrum is solely due to the C5 deprotonated anion.

Using the FC simulation, several vibrations of the \tilde{X}^2A' state of the *N*-methyl-5-pyrazolyl radical can be assigned. The low intensity peak *b* is the fundamental of an in-plane methyl rocking with a frequency of 345 ± 45 cm^{-1} . Peaks *c* and *e* are the fundamental and first overtone of an in-plane a' N2-N1-C5 bend with a frequency of

$680 \pm 35 \text{ cm}^{-1}$. The three in-plane ring distortion modes (ring bending, N1-N2 stretch, and N1-C5 stretch) contribute to peak *d* and cannot be resolved within our instrumental resolution. A large number of combination bands of these modes contribute to the spectral features at higher eBE. The atomic displacements for these normal modes, as well as the positions of all the peaks observed in the experimental spectrum, are provided in Figure 8.02. The simulation tends to underestimate the intensity toward the higher eBE, which may be a result of neglecting the methyl torsion levels (see the above section). The EA of the *N*-methyl-5-pyrazolyl radical is very close to that of the 5-pyrazolyl radical, $2.104 \pm 0.005 \text{ eV}$.²⁹ Introduction of the methyl group at the N1 position leads to more complication and congestion in the vibronic features, compared to the rather simple, extensive vibrational progression for a ring bending mode observed in the 5-pyrazolide anion spectrum.²⁹

The sharp change in β at 2.8 eV is consistent with the presence of another electronic state, seen in the spectrum peaks *l* and *m*. Both peaks *l* and *m* have a negative β value, which is distinct from the feature for the \tilde{X}^2A' state where positive β values are found. Positive β values are often observed for low kinetic energy photoelectrons detached from the in-plane orbitals of aromatic systems.^{29,55} This is consistent with electron detachment from the C5-centered in-plane σ -orbital of the \tilde{X}^1A' anion to form the \tilde{X}^2A' radical. In contrast, negative β values are often signatures of electrons detached from aromatic π orbitals.^{27-29,55} The negative β value for peaks *l* and *m* may suggest that the detachment takes place from a π orbital to form the \tilde{A}^2A'' state. This observation is consistent with DFT calculations, which find an $^2A''$ excited state of the *N*-methyl-5-pyrazolyl radical with a calculated T_e of 0.768 eV. The simulated spectrum (shown in Figure 8.01b at eBE > 2.8 eV) qualitatively resembles the experimental spectrum, however the observed spectrum

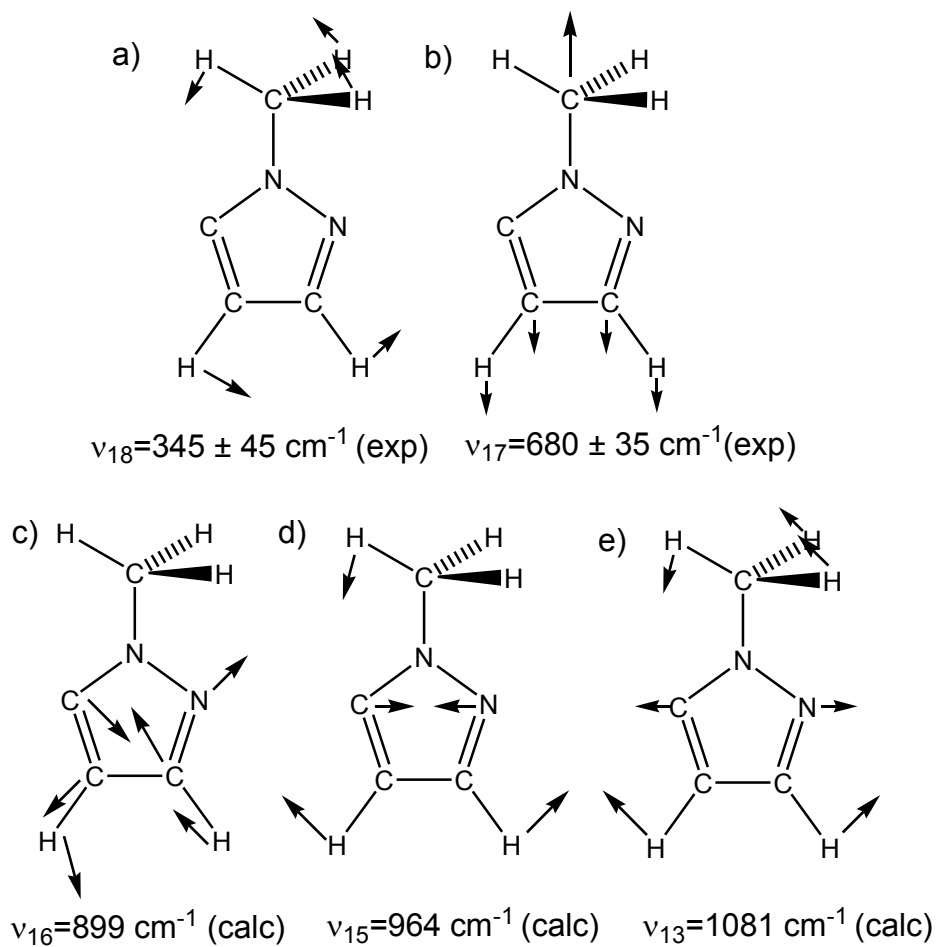


Figure 8.02: Relative atomic displacements in the activated normal modes of the \tilde{X}^2A' state of *N*-methyl-5-pyrazolyl and their frequencies. (Frequencies a and b are experimentally determined while frequencies c-e are calculated.)

is considerably broader than predicted. We attribute the observed broad feature of peaks *l* and *m* to the vibronic coupling between the \tilde{X}^2A' and \tilde{A}^2A'' states. Vibronic coupling can generate a large number of vibronic levels among which transition intensities are distributed, resulting in broadening.⁵⁶ Such broadening has been observed, for instance, in the photoionization of pyrrole.⁵⁷ Thus, we conclude that peaks *l* and *m* represent the \tilde{A}^2A'' vibronic levels, and the T_e is determined to be 0.807 ± 0.009 eV. The EA for the \tilde{A}^2A'' state of the *N*-methyl-5-pyrazolyl radical is 2.861 ± 0.007 eV, which is close to the EA of the 1-pyrazolyl radical, 2.938 ± 0.005 eV, where photodetachment takes place from a π orbital of the 1-pyrazolide ion.²⁹ It should be noted that vibronic coupling can also lend some intensity to the highly excited vibronic levels of the \tilde{X}^2A' state, which may explain some of the discrepancy between the observed spectrum and the simulation for the \tilde{X}^2A' state shown in Figure 8.01b. The observed gradual decrease of the β value toward the higher eBE in the \tilde{X}^2A' spectrum may reflect the nonadiabatic effects.

8.3.3) Photoelectron Spectra of *N*-methylimidazolidine Anion

The 351.1 nm magic angle photoelectron spectrum of the *N*-methylimidazolidine anion is shown in Figure 8.03. This ion was formed from the reaction of OH^- with *N*-methylimidazole. Analogous to *N*-methylpyrazole, DFT calculations (Table 8.05) predict that the C5 position is the most acidic site. However, deprotonation by OH^- at the methyl carbon and at the C2 carbon is also exothermic and therefore, we might expect to see all three isomers in the experimental spectrum. Instead, there appears to be one dominant FC envelope beginning with peak *a* at 1.987 ± 0.008 eV, an electronic band origin. The photoelectron angular distribution was measured and β is approximately 0.5 at the origin and smoothly decreases to -0.2 at 3.0 eV. At energies lower than the

electronic band origin there are several peaks and a broad band which extends ~1 eV. When the spectrum is collected under cold flow tube conditions (not shown) these lower binding energy peaks are absent, supporting the assignment of the origin.

To aid in the assignment of the experimental spectrum, FC simulations were performed for all three isomeric anions (C5, C2 and methyl anions) and their corresponding ground state neutral radicals. The unadjusted stick spectra and the spectra that result from convoluting the stick spectra with a 10 meV fwhm Gaussian function are shown in Figure 8.04b-8.04d, along with the experimental spectrum (8.04a). It is clear that the spectral features for *N*-imidazolylmethyl anion and the methyl-2-imidazolidine anion are not observed in the experimental spectrum. However, the EA, spectral profile, and even the individual resolved transitions for the *N*-methyl-5-imidazolidine anion simulated spectrum are in excellent agreement with the experimental spectrum. Figure 8.05 shows the lower eBE portion of the C5 anion FC simulation overlaid on the experimental data. In Figure 8.05 the origin of the simulated spectrum (red trace) has been slightly shifted (< 25 meV) to match the experimental data (black trace). This figure further demonstrates that within 300 meV from the origin, where the simulation is most reliable, the predicted relative intensities match the experimental spectrum, confirming that the signal in this region is primarily due to one species. Thus, we conclude that under our experimental conditions deprotonation of *N*-methylimidazole by OH⁻ almost exclusively occurs at the C5 position.

The calculated EA of the *N*-methyl-5-imidazolyl radical is 1.965 eV, which is close to the assigned origin (peak *a*). Using the FC simulation, four vibrations of the \tilde{X}^2A' state of the *N*-methyl-5-imidazolyl radical can be assigned. The small intensity

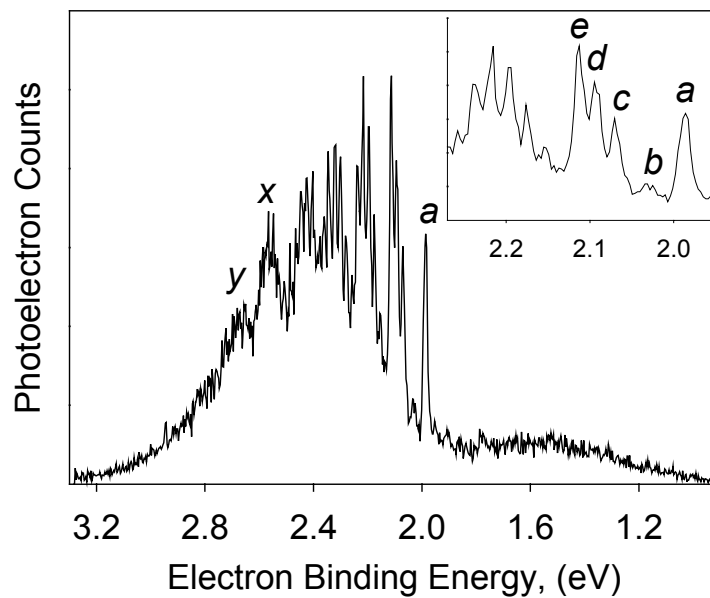


Figure 8.03: The 351.1 nm magic-angle photoelectron spectrum of the *N*-methylimidazolidide anion. A portion of the spectrum near peak *a* is expanded in the inset.

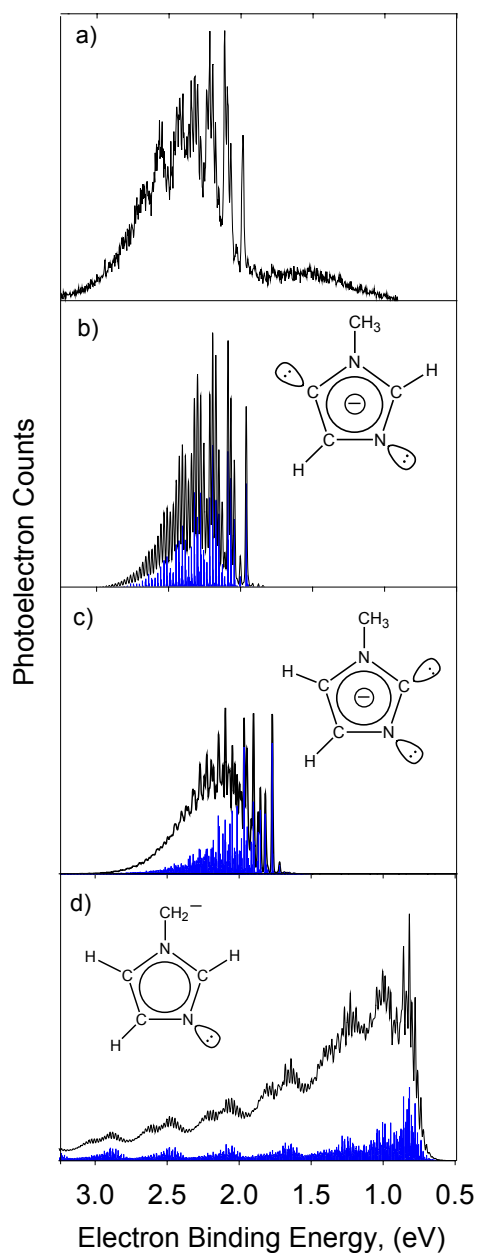


Figure 8.04: a) The 351.1 nm magic-angle photoelectron spectrum of the *N*-methylimidazolidine anion, reproduced from Figure 8.03. Simulations of the spectrum based on optimized geometries and normal modes from B3LYP/6-311++G(d,p) calculations. The sticks (blue) are the raw Franck-Condon factors and the solid line is the 10 meV fwhm Gaussian convolutions for transitions of b) \tilde{X}^1A' *N*-methyl-5-imidazolidine to \tilde{X}^2A' *N*-methyl-5-imidazolyl, c) \tilde{X}^1A' *N*-methyl-2-imidazolidine to \tilde{X}^2A' *N*-methyl-2-imidazolyl, and d) \tilde{X}^1A' *N*-imidazolymethyl anion to \tilde{X}^2A' *N*-imidazolymethyl radical.

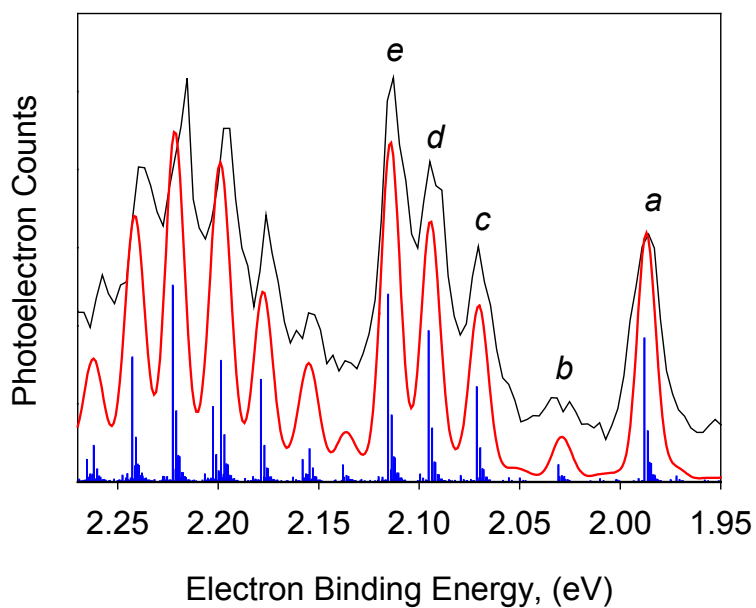


Figure 8.05: The 351.1 nm magic-angle photoelectron spectrum of the *N*-methylimidazolidine anion (black), reproduced from Figure 8.03 and the simulated 10 meV Gaussian convoluted (red) and stick (blue) spectra, reproduced from Figure 8.04b. The eBE of the origin for the simulated spectra was set to match the eBE of peak *a* in the experimental spectrum.

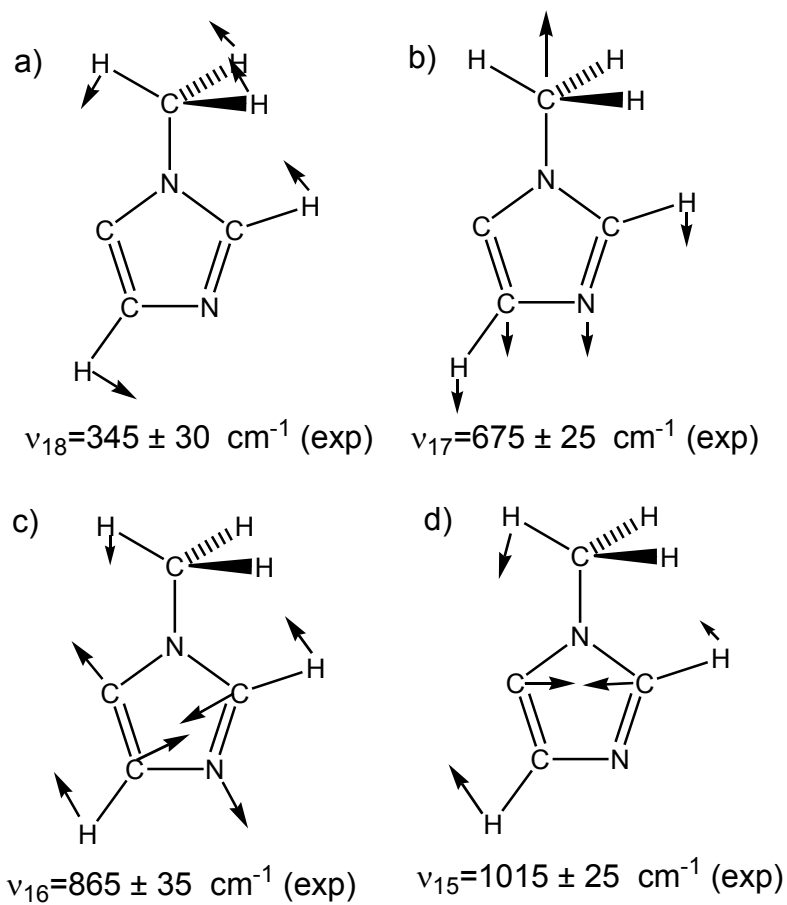


Figure 8.06: Relative atomic displacements in the activated normal modes for the \tilde{X}^2A' state of *N*-methyl-5-imidazolyl.

peak *b* is assigned to a methyl rocking mode with a frequency of $345 \pm 30 \text{ cm}^{-1}$. Peaks *c*, *d*, and *e* are partially resolved fundamentals of in-plane ring distortion modes. Peak *c* corresponds to a C2-N1-C5 bend with a frequency of $675 \pm 25 \text{ cm}^{-1}$, peak *d* to a C2-N3-C4 bend with a frequency of $865 \pm 35 \text{ cm}^{-1}$, and peak *e* to C4-C5-N1 bend with a frequency of $1015 \pm 25 \text{ cm}^{-1}$. Combination bands of these modes are observed in the larger eBE region. The atomic displacements for these normal modes are shown in Figure 8.06. The same bending modes are active in the photoelectron spectrum of the 5-imidazolidine anion.

Following the analysis of the *N*-methyl-5-pyrazolidine anion spectrum, we consider photodetachment to the \tilde{A}^2A'' state of the *N*-methyl-5-imidazolyl radical. DFT calculations predict the T_e to be 0.452 eV. This T_e corresponds to the broad band *x* in Figure 8.03. Analogous to the *N*-methyl-5-pyrazolyl radical system, vibronic coupling between the \tilde{X}^2A' and \tilde{A}^2A'' states is expected for the *N*-methyl-5-imidazolyl radical, which can broaden the spectral profile. In the previous section, we noted the similarity between the eBE for the detachment to the \tilde{A}^2A'' state of *N*-methyl-5-pyrazolyl and the EA of the 1-pyrazolyl radical. In this sense, because the EA of the 1-imidazolyl radical is $2.613 \pm 0.006 \text{ eV}$,²⁷ the broad band *y* in Figure 8.03 seems to correspond to the vibrational origin of the \tilde{A}^2A'' *N*-methyl-5-imidazolyl radical. Rigorous assignment is impossible in the present study, but it is most likely that some of the spectral features at eBE > 2.4 eV represents the \tilde{A}^2A'' state of the radical. Gradual decrease of the β value toward the higher eBE is consistent with this conclusion. The broad background at eBE > 2.0 eV may be a manifestation of the nonadiabatic effects as well.

As mentioned above, deprotonation of *N*-methylimidazole at the methyl and C2 sites by hydroxide is predicted to be exothermic. Nonetheless the spectral

features for these two anions are absent in the experimental spectrum, suggesting that these isomers are not formed in any significant amounts. This notion, however, should be taken with caution, because the identity of the low-intensity, broad feature observed at $eBE < 2.0$ eV is uncertain. This feature is absent when the ions are synthesized in a flow tube cooled with liquid nitrogen. There may be an isomerization process (i.e., ring-opening) when OH^- interacts with a H atom at C2, C4, or the methyl group.

8.3.4) Gas-Phase Acidity Measurements

The gas-phase acidity of *N*-methylpyrazole was measured relative to methanol⁵² (shown in reaction 8.01). For the forward reaction, the *N*-methylpyrazolide anion is prepared from a proton transfer reaction of *N*-methylpyrazole with OH^- in the source. The photoelectron spectrum of *N*-methylpyrazolide, where the anion was prepared from proton transfer to hydroxide, shows that deprotonation only occurs on the C5 site. The forward reaction of the *N*-methyl-5-pyrazolide anion with CH_3OH is exothermic and the reaction proceeds exclusively by proton transfer. The rate constant is measured to be $1.3 \pm 0.1 \times 10^{-9} \text{ cm}^3 \text{ s}^{-1}$ (0.68 efficiency). The reverse reaction of CH_3O^- with *N*-methylpyrazole is endothermic, and significant adduct formation is observed in addition to proton transfer. The overall rate constant is $5.5 \pm 0.4 \times 10^{-10} \text{ cm}^3 \text{ s}^{-1}$ (0.19 efficiency). The proton transfer rate constant was determined from the overall rate constant and the proton transfer branching ratio to be $1.2 \pm 0.3 \times 10^{-10} \text{ cm}^3 \text{ s}^{-1}$.

Combining the forward and reverse proton transfer rate constants, the gas-phase-acidity ($\Delta_a G_{298}$) of *N*-methylpyrazole is determined to be $376.9 \pm 0.7 \text{ kcal mol}^{-1}$, which is in exact agreement with the calculated value of $376.9 \text{ kcal mol}^{-1}$. The

DFT entropy of deprotonation, $\Delta_a S_{298} = 23.7 \text{ cal mol}^{-1} \text{ K}^{-1}$, is used with $\Delta_a G_{298}$ to calculate the enthalpy of deprotonation ($\Delta_a H_{298}$) to be $384.0 \pm 0.7 \text{ kcal mol}^{-1}$.

The gas-phase acidity of *N*-methylimidazole was measured relative to water (shown in reaction 8.02). In both the forward and reverse reactions the *N*-methylimidazolate anion is formed from deprotonation of the neutral by OH^- . (For the forward reaction, this step occurs in the source.) As discussed in the analysis of the *N*-methylimidazolate anion photoelectron spectrum, deprotonation of *N*-methylimidazole by OH^- almost exclusively occurs at the C5 site. If the methyl and C2 isomers are present they are in minor amounts and therefore would not significantly affect the experimental gas-phase acidity value.

The forward reaction of the *N*-methylimidazolate anion with H_2O is endothermic, and significant adduct formation is observed in addition to proton transfer. The overall rate constant is found to be $1.0 \pm 0.3 \times 10^{-10} \text{ cm}^3 \text{ s}^{-1}$ (0.04 efficiency). Kinetic plots for this reaction were measured as a function of SIFT injection potential (over a 50 V range) and are observed to be linear, which supports the conclusion that other isomeric ions are not present in significant amounts. The proton transfer rate constant is determined from the overall rate constant and the proton transfer branching ratio to be $1.3 \pm 0.3 \times 10^{-11} \text{ cm}^3 \text{ s}^{-1}$. The reverse reaction of OH^- with *N*-methylimidazole is exothermic and proton transfer is the only reaction pathway observed. The proton transfer reaction rate constant was determined relative to that for the reaction of *N*-methylimidazole with NH_2^- , which is highly exothermic, assuming that this reaction proceeds at $90 \pm 10\%$ of the collision rate. This assumption is validated by measurements of the proton transfer rate constant for the reaction of NH_2^- with *N*-methylpyrazole, which is slightly more exothermic and

found to occur at the collision rate. The proton transfer rate constant for *N*-methylimidazole with OH⁻ is determined to be $4.6 \pm 0.5 \times 10^{-9} \text{ cm}^3 \text{ s}^{-1}$ (eff = 0.82).

Combining the forward and reverse proton transfer rate constants, the gas-phase-acidity ($\Delta_a G_{298}$) of *N*-methylimidazole is determined to be $380.2 \pm 1.0 \text{ kcal mol}^{-1}$. Although the gas-phase acidity of H₂O is known to within $\pm 0.02 \text{ kcal mol}^{-1}$, we have assigned more conservative error bars to the gas-phase acidity of *N*-methylimidazole to account for the possibility that another, more basic isomer may be present.⁵⁸ The experimental gas-phase acidity is in good agreement with the calculated value of $380.8 \text{ kcal mol}^{-1}$. The DFT calculated $\Delta_a S_{298} = 26.5 \text{ cal mol}^{-1} \text{ K}^{-1}$; therefore, $\Delta_a H_{298}$ is determined to be $388.1 \pm 1.0 \text{ kcal mol}^{-1}$.

8.3.5) H/D Exchange of *N*-methylimidazolidide Anion

The observation that deprotonation of *N*-methylimidazole by OH⁻ results in almost exclusively the C5 anion has prompted us to investigate the H/D exchange reaction of the *N*-methylimidazolidide anion with D₂O and ND₃. H/D exchange experiments have proven to be a useful probe for determining anion structures and for studies of the structure and dynamics of ion-dipole complexes.⁵⁹ In this process, the ion and deuterated reagent enter a long-lived complex, which typically contains $\sim 15\text{-}20 \text{ kcal mol}^{-1}$ excess energy.⁵⁹ During the lifetime of this ion-dipole complex, proton-deuteron scrambling can occur before the ion and neutral separate.

D₂O and ND₃ are useful exchange reagents in that they can both exchange more than one deuteron in an encounter. These two exchange reagents differ from one another in that ion-molecule complexes with ND₃ typically contain less energy than ion-molecule complexes with D₂O.⁶⁰ When *N*-methylimidazolidide anion is allowed to react with ND₃ four exchanges are observed. Assuming that the initial anionic site is at the C5 position, three exchanges are due to the methyl group and

one exchange is from a ring proton (either C2 or C4 protons). The first step of the exchange, the deuteron transfer reaction of *N*-methyl-5-imidazolide anion with ND₃, is sufficiently endothermic (~15 kcal mol⁻¹) and consumes almost all of the complexation energy. Using the DFT calculated acidities as a guide (Table 8.05), back transfer of a proton to ND₂⁻ from the methyl or C2 position is energetically favored, while proton transfer from the C4 position would consume an additional ~2 kcal mol⁻¹ of the complexation energy. Any subsequent exchange, therefore, is most likely to occur at the methyl or C2 position. When D₂O is used as an exchange reagent four exchanges are also observed. Despite the fact that ion-molecule complexes with D₂O have larger excess energy than complexes with ND₃ and that the initial deuteron transfer is less endothermic, exchange at the C4 position is not observed. These results are consistent with computations, which predict that the C4 proton is significantly less acidic than other sites in the molecule. Furthermore, these results indicate that the methyl and C2 positions are accessible.

8.3.6) Thermochemistry

The C5-H BDE (D_0) of *N*-methylpyrazole and *N*-methylimidazole can be determined from the electron affinity measurements and the enthalpy of deprotonation using a negative ion thermochemical cycle,^{33,34} as discussed in Chapter 1. In *N*-methylpyrazole, where the two nitrogen atoms are adjacent, the $D_0(\text{C5-H})$ is determined to be 116.4 ± 0.7 kcal mol⁻¹. In *N*-methylimidazole, where the two nitrogen atoms are separated by one carbon atom, the $D_0(\text{C5-H})$ is determined to be 119.0 ± 1.0 kcal mol⁻¹. The uncertainty in the BDE measurements is largely due to the error in the gas-phase acidity measurements. Table 8.06 summarizes these BDEs as well as other thermodynamic values reported in this work. The BDE is the energy required to break the C-H bond to form the radical and

an H atom. The difference in the BDE of the two isomers is $2.6 \text{ kcal mol}^{-1}$, indicating that the location of the remote (β position) nitrogen atom in the ring does not significantly change the strength of the C5-H bond. This subtle difference, however, does indicate that the *N*-methyl-5-pyrazolyl radical is slightly more stable than the *N*-methyl-5-imidazolyl radical relative to their respective neutral azoles. Similarly, gas-phase acidity measurements indicate that the *N*-methyl-5-pyrazolide anion is more stable than the *N*-methyl-5-imidazolide anion when compared to the corresponding neutral azoles.

The heat of formation of both *N*-methylazoles, $\Delta_f H_{298}(\text{AH})$, has previously been determined ($\Delta_f H_{298}(\text{N-methylpyrazole}) = 37.4 \pm 0.5 \text{ kcal mol}^{-1}$ and $\Delta_f H_{298}(\text{N-methylimidazole}) = 32.9 \pm 1.0 \text{ kcal mol}^{-1}$). Using the BDEs reported here for the *N*-methylazoles, the heat of formation of the *N*-methylazolyl radicals, $\Delta_f H_{298}(\text{A})$, can be determined (also discussed in Chapter 1). The heat of formation is determined to be $103.1 \pm 1.5 \text{ kcal mol}^{-1}$ for the *N*-methyl-5-pyrazolyl radical and $101.2 \pm 3.1 \text{ kcal mol}^{-1}$ for the *N*-methyl-5-imidazolyl radical.

If the methyl group does not significantly change the C-H bond energetics, the thermochemical properties measured here should be consistent with those of pyrazole and imidazole. For imidazole, the previously measured C5-H bond strength ($119 \pm 4 \text{ kcal mol}^{-1}$) is similar to the value reported here for *N*-methylimidazole ($119.0 \pm 1.0 \text{ kcal mol}^{-1}$), which has much greater precision. In addition, the EA and gas-phase acidity reported here are also similar to those for imidazole ($\Delta_a G_{298}(\text{C5-H, imidazole}) = 380 \pm 4 \text{ kcal mol}^{-1}$, $\text{EA}(5\text{-imidazolyl}) = 1.992 \pm 0.010 \text{ eV}$).²⁷ The previously measured bond strength of pyrazole ($121 \pm 4 \text{ kcal mol}^{-1}$), on the other hand, is $4.6 \text{ kcal mol}^{-1}$ higher than the value reported here for *N*-methylpyrazole.

Table 8.06: Thermochemical Parameters.

<i>N-methylpyrazole and N-methyl-5-pyrazolyl radical</i>	
EA(<i>N</i> -methyl-5-pyrazolyl) ^a	2.054 ± 0.006 eV
T _e (<i>N</i> -methyl-5-pyrazolyl) ^a	0.807 ± 0.009 eV
Δ _a G ₂₉₈ (C5-H, <i>N</i> -methylpyrazole) ^a	376.9 ± 0.7 kcal mol ⁻¹
Δ _a S ₂₉₈ (C5-H, <i>N</i> -methylpyrazole) ^b	23.7 cal mol ⁻¹ K ⁻¹
Δ _a H ₂₉₈ (C5-H, <i>N</i> -methylpyrazole) ^c	384.0 ± 0.7 kcal mol ⁻¹
Δ _a H ₀ (C5-H, <i>N</i> -methylpyrazole) ^d	382.6 ± 0.7 kcal mol ⁻¹
D ₀ (C5-H, <i>N</i> -methylpyrazole) ^e	116.4 ± 0.7 kcal mol ⁻¹
Δ _f H ₂₉₈ (<i>N</i> -methylpyrazole) ^f	37.4 ± 0.5 kcal mol ⁻¹
Δ _f H ₂₉₈ (<i>N</i> -methyl-5-pyrazolyl) ^g	103.1 ± 1.5 kcal mol ⁻¹
<i>N-methylimidazole and N-methyl-5-imidazolyl radical</i>	
EA(<i>N</i> -methyl-5-imidazolyl) ^a	1.987 ± 0.008 eV
Δ _a G ₂₉₈ (C5-H, <i>N</i> -methylimidazole) ^a	380.2 ± 1.0 kcal mol ⁻¹
Δ _a S ₂₉₈ (C5-H, <i>N</i> -methylimidazole) ^b	26.5 cal mol ⁻¹ K ⁻¹
Δ _a H ₂₉₈ (C5-H, <i>N</i> -methylimidazole) ^c	388.1 ± 1.0 kcal mol ⁻¹
Δ _a H ₀ (C5-H, <i>N</i> -methylimidazole) ^d	386.8 ± 1.1 kcal mol ⁻¹
D ₀ (C5-H, <i>N</i> -methylimidazole) ^e	119.0 ± 1.0 kcal mol ⁻¹
Δ _f H ₂₉₈ (<i>N</i> -methylimidazole) ^f	32.9 ± 1.0 kcal mol ⁻¹
Δ _f H ₂₉₈ (<i>N</i> -methyl-5-imidazolyl) ^g	101.2 ± 3.1 kcal mol ⁻¹

^a Experimentally determined in this study. ^b Determined from B3LYP/ 6-311++G(d,p) calculations. ^c Calculated from Δ_aG₂₉₈ and Δ_aS₂₉₈. ^d Calculated from Δ_aH₂₉₈. ^e Calculated using the EA and Δ_aH₀ in addition to the IE(H). ^f Value taken from reference 64 ^g Calculated from Δ_fH₂₉₈(H), Δ_fH₂₉₈(RH) and D₂₉₈(RH).

The difference in bond strength is primarily due to the difference in the measured acidity, 4 kcal mol^{-1} ($\Delta_a G_{298}(\text{C5-H, pyrazole}) = 380 \pm 4 \text{ kcal mol}^{-1}$, $\text{EA}(5\text{-pyrazolyl}) = 2.104 \pm 0.005 \text{ eV}$). It seems unlikely that the substitution of a methyl group on pyrazole would significantly perturb the energetics of the C-H bonds, especially since there is no significant effect for *N*-methylimidazole. More likely it seems that the difference in BDEs of pyrazole and *N*-methylpyrazole reflects the difficulties in determining the C5-H acidity of pyrazole.⁶¹ Thus, the C5-H BDE values reported in this work, at the present time, represent the most accurate C-H BDE values for the family of azoles.

The C5-H BDEs of *N*-methylpyrazole and *N*-methylimidazole determined in this work are significantly larger than the C-H BDE of benzene ($D_0(\text{C-H}) = 112.0 \pm 0.6 \text{ kcal mol}^{-1}$), a benchmark C-H bond strength for aromatic compounds.⁶² Generally, C-H BDEs in five-membered ring aromatic compounds are predicted theoretically to be larger than those in six-membered aromatics; this has been discussed with respect to the difference in the molecular structure.¹² The inherently smaller interior angle in a five-membered ring makes the corresponding C-H bond stronger because the 2s orbital of the C atom contributes more to the C-H bonding orbital. While our experimental findings are consistent with this argument, the reported C-H BDE of another five-membered ring compound, the cyclopentadienyl radical (C_5H_5),⁶³ $D_{298} = 105 \pm 3.4 \text{ kcal mol}^{-1}$, is much lower than the C5-H BDEs of the *N*-methylazoles and the C-H BDE of benzene. In this case, however, the cyclopentadienyl radical is not a $4n+2$ Hückel system.⁶⁴ Following C-H bond fission, the resultant cyclopentadienylidene would maintain an unpaired electron in the π (b_1) orbital in the electronic ground state (3B_1), inducing a static Jahn-Teller stabilization, which may explain the low C-H BDE of the cyclopentadienyl radical.

In order to extend the knowledge of the C-H BDEs of azoles, we have performed preliminary experiments on *N*-methylpyrrole. It is difficult, however, to determine the C2-H BDE (which is equivalent to the C5-H BDE by symmetry) using the same experimental technique employed in this study, because *N*-methylation of pyrrole does not make the C2 carbon the most acidic location.⁶⁵ The C2-H BDE of pyrrole has been reported to be $112.5 \pm 1 \text{ kcal mol}^{-1}$ according to a photofragment translational spectroscopic study.²³ It should be mentioned, however, that more recent studies^{24,25} have not observed a C-H bond dissociation process in the photochemistry of pyrrole. In light of the discrepancy in the N-H BDE of pyrrole, there are some questions about the reported C2-H BDE of pyrrole in the aforementioned study. It should also be noted that a photofragment velocity map imaging technique has been ineffective to explore the C-H BDE of *N*-methylpyrrole.²⁴ In light of the C5-H BDEs determined here for *N*-methylpyrazole and *N*-methylimidazole, it seems likely that the photofragment translational spectroscopic study underestimates the C2-H BDE of *N*-methylpyrrole.

8.4) Conclusions

The 351.1 nm photoelectron spectrum of the *N*-methyl-5-pyrazolide anion was measured and is in excellent agreement with the calculated FC factors for the transition from the \tilde{X}^1A' state of the anion to the \tilde{X}^2A' and \tilde{A}^2A'' states of the *N*-methyl-5-pyrazolyl radical. The EA of the radical is $2.054 \pm 0.006 \text{ eV}$ and the T_e of the \tilde{A}^2A'' state is $0.807 \pm 0.009 \text{ eV}$. Fundamental vibrational frequencies of $345 \pm 45 \text{ cm}^{-1}$ and $680 \pm 35 \text{ cm}^{-1}$ are found for an in-plane methyl rocking and C5-N1-N2 bending modes of the \tilde{X}^2A' state of the *N*-methyl-5-pyrazolyl radical, respectively. The gas-phase acidity of *N*-methylpyrazole was measured relative to methanol, $\Delta_a G_{298}(N\text{-methylpyrazole}) = 376.9 \pm 0.7 \text{ kcal mol}^{-1}$ and $\Delta_a H_{298}(N\text{-methylpyrazole}) =$

384.0 ± 0.7 kcal mol⁻¹. Using a negative ion thermodynamic cycle the C5-H BDE was determined to be $D_0(N\text{-methylpyrazole}) = 116.4 \pm 0.7$ kcal mol⁻¹ and $\Delta_f H_{298}(N\text{-methylpyrazole}) = 103.1 \pm 1.5$ kcal mol⁻¹.

The 351.1 nm photoelectron spectrum of the *N*-methyl-5-imidazolide anion was measured and is in good agreement with the calculated FC factors for the \tilde{X}^1A' state of the anion to the \tilde{X}^2A' state of the *N*-methyl-5-imidazolyl radical. The EA of the radical is 1.987 ± 0.008 eV. Fundamental frequencies of four in-plane modes are 345 ± 30 cm⁻¹ (methyl rocking), 675 ± 25 cm⁻¹ (C5-N1-C2), 865 ± 35 cm⁻¹ (C2-N3-C4), and 1015 ± 25 cm⁻¹ (C4-C5-N1) for the \tilde{X}^2A' state of the *N*-methyl-5-imidazolyl radical. The gas-phase acidity of *N*-methylimidazole was measured relative to water, $\Delta_a G_{298}(N\text{-methylimidazole}) = 380.2 \pm 1.0$ kcal mol⁻¹ and $\Delta_a H_{298}(N\text{-methylimidazole}) = 388.1 \pm 1.0$ kcal mol⁻¹. Using a negative ion thermodynamic cycle the C5-H BDE and the heat of formation of the *N*-methyl-5-imidazolyl radical were determined to be 119.0 ± 1.0 kcal mol⁻¹ and 101.2 ± 3.1 kcal mol⁻¹, respectively.

8.5) Acknowledgements

This work would not have been possible without the help of Dr. Adam J. Gianola, Ms. Nicole Eyet, Dr. Takatoshi Ichino, Dr. Shuji Kato, Prof. Veronica M. Bierbaum, and Prof. W. Carl Lineberger. In addition, thanks is given to Prof. Charles H. DePuy for his useful comments, Mr. Todd B. Kreutzian for determining the water content of the neutral reagents, and Prof. Paul G. Wenthold and Prof. Jeehiun K. Lee for sharing their unpublished work with us. This work was funded by the AFOSR (FA9550-06-1-006) and NSF (CHE0512188, PHY0551010, and CHE0349937).

8.6) Chapter 8 References

- (1) Abeles, R. H.; Frey, P. A.; Jencks, W. P. *Biochemistry*; 1st ed.; Jones and Bartlett: Boston, MA., 1992.
- (2) Toribio, L.; del Nozal, M. J.; Bernal, J.; Alonso, C.; Jimenez, J., L. Enantiomeric Separation of Several Antimycotic Azole Drugs using Supercritical Fluid Chromatography. *Journal of Chromatography A* **2007**, *1144*, 255-261.
- (3) Ahmad, Z.; Sharma, S.; Khuller, G. K. Azole Antifungals as Novel Chemotherapeutic Agents Against Murine Tuberculosis. *FEMS Microbiol. Lett.* **2006**, *261*, 181-186.
- (4) Ogihara, W.; Yoshizawa, M.; Ohno, H. Novel Ionic Liquids Composed of Only Azole Ions. *Chemistry Letters* **2004**, *33*, 1022-1023.
- (5) Jorapur, Y. R.; Jeong, J. M.; Chi, D. Y. Potassium Carbonate as a Base for the N-alkylation of Indole and Pyrrole in Ionic Liquids. *Tetrahedron Letters* **2006**, *47*, 2435-2438.
- (6) Raposo, M. M. M.; Sousa, A. M. R. C.; Fonseca, A. M. C.; Kirsch, G. Donor-Acceptor Substituted Thienylpyrrole Azo Dyes: Synthesis, Solvatochromic and Electrochemical Properties. *Advanced Materials Forum Iii, Pts 1 and 2* **2006**, *514-516*, 103-107.
- (7) Zhao, W.; Carreira, E. M. Conformationally Restricted Aza-BODIPY: Highly Fluorescent, Stable Near-Infrared Absorbing Dyes. *Chemistry--A European Journal* **2006**, *12*, 7254-7263.
- (8) Williams, G. K.; Palopoli, S. F.; Brill, T. B. Thermal-Decomposition of Energetic Materials .65. Conversion of Insensitive Explosives (Nto, Anta) and Related-Compounds to Polymeric Melon-Like Cyclic Azine Burn-Rate Suppressants. *Combustion and Flame* **1994**, *98*, 197-204.
- (9) Knicker, H.; Hatcher, P. G.; Scaroni, A. W. Solid-State ¹⁵N NMR-Spectroscopy of Coal. *Energy & Fuels* **1995**, *9*, 999-1002.
- (10) Okumara, Y.; Sugiyama, Y.; Okazaki, K. Evolution Prediction of Coal-Nitrogen in High Pressure Pyrolysis Processes. *Fuel* **2002**, *81*, 2317-2324.
- (11) Snyder, L. R. Nitrogen and Oxygen Compound Types in Petroleum - Total Analysis of a 400-700° F Distillate from a California Crude Oil. *Analytical Chemistry* **1969**, *41*, 314-323.
- (12) Barckholtz, C.; Barckholtz, T. A.; Hadad, C. M. C-H and N-H Bond Dissociation Energies of Small Aromatic Hydrocarbons. *Journal of the American Chemical Society* **1999**, *121*, 491-500.
- (13) Shapley, J. R.; Samkoff, D. E.; Bueno, C.; Churchill, M. R. Reaction of OS₃(CO)₁₀(NCCH₃)₂ with Imidazole and Related Aromatic Heterocycles - Crystal and

Molecular-Structure of $(\mu\text{-H})\text{OS}_3(\text{CO})_{10}(\mu\text{-}3,4\text{-Eta-}2\text{-}\eta^2\text{C}_3\text{H}_3)$. *Inorganic Chemistry* **1982**, *21*, 634-639.

(14) Jones, W. D.; Dong, L. Z.; Myers, A. W. Bond-Cleavage Reactions in Oxygen and Nitrogen-Heterocycles by a Rhodium Phosphine Complex. *Organometallics* **1995**, *14*, 855-861.

(15) Agarwala, R.; Azam, K. A.; Dilshad, R.; Kabir, S. E.; Miah, R.; Shahiduzzaman, M.; Hardcastle, K. I.; Rosenberg, E.; Hursthouse, M. B.; Malik, K. M. A. Triosmium and Triruthenium Clusters Containing Diazaheterocycles. *Journal of Organometallic Chemistry* **1995**, *492*, 135-144.

(16) Musaev, D. G.; Morokuma, K. *Ab-Initio* Molecular-Orbital Study of the Mechanism of H-H, C-H, N-H, O-H, and Si-H Bond Activation on Transient Cyclopentadienylcarbonylrhodium. *Journal of the American Chemical Society* **1995**, *117*, 799-805.

(17) Xie, K. C.; Lin, J. Y.; Li, W. Y.; Chang, L. P.; Feng, J.; Zhao, W. Formation of HCN and NH_3 During Coal Macerals Pyrolysis and Gasification with CO_2 . *Fuel* **2005**, *84*, 271-277.

(18) Babich, I. V.; Seshan, K.; Lefferts, L. Nature of Nitrogen Species in Coke and Their Role in NO_x Formation During FCC Catalyst Regeneration. *Applied Catalysis B-Environmental* **2005**, *59*, 205-211.

(19) Mackie, J. C.; Colket, M. B.; Nelson, P. F.; Esler, M. Shock-Tube Pyrolysis of Pyrrole and Kinetic Modeling. *International Journal of Chemical Kinetics* **1991**, *23*, 733-760.

(20) Lifshitz, A.; Tamburu, C.; Suslensky, A. Isomerization and Decomposition of Pyrrole at Elevated-Temperatures - Studies with a Single-Pulse Shock-Tube. *Journal of Physical Chemistry* **1989**, *93*, 5802-5808.

(21) Dubnikova, F.; Lifshitz, A. Isomerization of Pyrrole. Quantum Chemical Calculations and Kinetic Modeling. *Journal of Physical Chemistry A* **1998**, *102*, 10880-10888.

(22) Mackie, J. C.; Colket, M. B.; Nelson, P. F. Shock Tube Pyrolysis of Pyridine. *Journal of Physical Chemistry* **1990**, *94*, 4099-4106.

(23) Blank, D. A.; North, S. W.; Lee, Y. T. The Ultraviolet Photodissociation Dynamics of Pyrrole. *Chemical Physics* **1994**, *187*, 35-47.

(24) Wei, J.; Kuczmann, A.; Riedel, J.; Renth, F.; Temps, F. Photofragment Velocity Map Imaging of H Atom Elimination in the First Excited State of Pyrrole. *Physical Chemistry Chemical Physics* **2003**, *5*, 315-320.

(25) Cronin, B.; Nix, M. G. D.; Qadiri, R. H.; Ashfold, M. N. R. High Resolution Photofragment Translational Spectroscopy Studies of the Near Ultraviolet Photolysis of Pyrrole. *Physical Chemistry Chemical Physics* **2004**, *6*, 5031-5041.

- (26) Kiefer, J. H.; Zhang, Q.; Kern, R. D.; Yao, J.; Jursic, B. Pyrolyses of Aromatic Azines: Pyrazine, Pyrimidine, and Pyridine. *Journal of Physical Chemistry A* **1997**, *101*, 7061-7073.
- (27) Gianola, A. J.; Ichino, T.; Hoenigman, R. L.; Kato, S.; Bierbaum, V. M.; Lineberger, W. C. Photoelectron Spectra and Ion Chemistry of Imidazolidine. *Journal of Physical Chemistry A* **2005**, *109*, 11504-11514.
- (28) Gianola, A. J.; Ichino, T.; Hoenigman, R. L.; Kato, S.; Bierbaum, V. M.; Lineberger, W. C. Thermochemistry and Electronic Structure of the Pyrrolyl Radical. *Journal of Physical Chemistry A* **2004**, *108*, 10326-10335.
- (29) Gianola, A. J.; Ichino, T.; Kato, S.; Bierbaum, V. M.; Lineberger, W. C. Thermochemical Studies of Pyrazolide. *Journal of Physical Chemistry A* **2006**, *110*, 8457-8466.
- (30) Ichino, T.; Gianola, A. J.; Lineberger, W. C.; Stanton, J. F. Nonadiabatic Effects in the Photoelectron Spectrum of the Pyrazolide- d_3 Anion: Three-State Interactions in the Pyrazolyl- d_3 Radical. *Journal of Chemical Physics* **2006**, *125*, 084312-084333.
- (31) Ichino, T.; Andrews, D. H.; Rathbone, G. J.; Misaizu, F.; Calvi, R. M. D.; Wren, S. W.; Kato, S.; Bierbaum, V. M.; Lineberger, W. C. Ion Chemistry of 1H-1,2,3-Triazole. *Journal of Physical Chemistry B* **2008**, *112*, 545-557.
- (32) Ervin, K. M.; Lineberger, W. C. In *Gas Phase Ion Chemistry*; N. C. Adams and L. M. Babcock, Eds.; JAI Press: Greenwich, 1992; Vol. 1; pp 121.
- (33) Blanksby, S. J.; Ellison, G. B. Bond Dissociation Energies of Organic Molecules. *Accounts of Chemical Research* **2003**, *36*, 255-263.
- (34) Berkowitz, J.; Ellison, G. B.; Gutman, D. Three Methods to Measure RH Bond-Energies. *Journal of Physical Chemistry* **1994**, *98*, 2744-2765.
- (35) O'Hair, R. A. J.; Gronert, S.; DePuy, C. H.; Bowie, J. H. Gas-Phase Ion Chemistry of the Acetic-Acid Enolate Anion $[\text{CH}_2\text{CO}_2\text{H}]^-$. *Journal of the American Chemical Society* **1989**, *111*, 3105-3106.
- (36) Hare, M. C.; Marimanikkuppam, S. S.; Kass, S. R. Acetamide Enolate: Formation, Reactivity, and Proton Affinity. *International Journal of Mass Spectrometry* **2001**, *210*, 153-163.
- (37) Baschky, M. C.; Peterson, K. C.; Kass, S. R. Stereospecificity in the Gas-Phase - Formation and Characterization of Configurationally Stable Cyclopropyl Anions. *Journal of the American Chemical Society* **1994**, *116*, 7218-7224.
- (38) Chou, P. K.; Kass, S. R. E-Vinyl and Z-Vinyl Anions - the Formation and Characterization of Regioisomers and Stereoisomers in the Gas-Phase. *Journal of the American Chemical Society* **1991**, *113*, 4357-4359.

- (39) Wenthold, P. G.; Squires, R. R. Biradical Thermochemistry from Collision-Induced Dissociation Threshold Energy Measurements - Absolute Heats of Formation of Ortho-Benzyne, Meta-Benzyne, and Para-Benzyne. *Journal of the American Chemical Society* **1994**, *116*, 6401-6412.
- (40) Grabowski, J. J.; Cheng, X. H. Gas-Phase Formation of the Enolate Monoanion of Acetic-Acid by Proton Abstraction. *Journal of the American Chemical Society* **1989**, *111*, 3106-3108.
- (41) Kurinovich, M. A.; Lee, J. K. The Acidity of Uracil from the Gas Phase to Solution: The Coalescence of the N1 and N3 Sites and Implications for Biological Glycosylation. *Journal of the American Chemical Society* **2000**, *122*, 6258-6262.
- (42) Sharma, S.; Lee, J. K. Acidity of Adenine and Adenine Derivatives and Biological Implications. A Computational and Experimental Gas-Phase Study. *Journal of Organic Chemistry* **2002**, *67*, 8360-8365.
- (43) Neumark, D. M.; Lykke, K. R.; Andersen, T.; Lineberger, W. C. Laser Photodetachment Measurement of the Electron-Affinity of Atomic Oxygen. *Physical Review A* **1985**, *32*, 1890-1892.
- (44) Hotop, H.; Lineberger, W. C. Binding-Energies in Atomic Negative-Ions II. *Journal of Physical and Chemical Reference Data* **1985**, *14*, 731-750.
- (45) Hanstorp, D.; Gustafsson, M. Determination of the Electron-Affinity of Iodine. *Journal of Physics B-Atomic Molecular and Optical Physics* **1992**, *25*, 1773-1783.
- (46) Becke, A. D. Density-Functional Thermochemistry. III. The Role of Exact Exchange. *Journal of Chemical Physics* **1993**, *98*, 5648-5652.
- (47) Lee, C. T.; Yang, W. T.; Parr, R. G. Development of the Colle-Salvetti Correlation-Energy Formula into a Functional of the Electron-Density. *Physical Review B* **1988**, *37*, 785-789.
- (48) Krishnan, R.; Binkley, J. S.; Seeger, R.; Pople, J. A. Self-Consistent Molecular-Orbital Methods. XX. Basis Set for Correlated Wave-Functions. *Journal of Chemical Physics* **1980**, *72*, 650-654.
- (49) Frisch, M. J.; Trucks, G. W.; Schlegel, H. B.; Scuseria, G. E.; Robb, M. A.; Cheeseman, J. R.; Montgomery, J. A.; Vreven, T.; Kudin, K. N.; Burant, J. C.; Millam, J. M.; Iyengar, S. S.; Tomasi, J.; Barone, V.; Mennucci, B.; Cossi, M.; Scalmani, G.; Rega, N.; Petersson, G. A.; Nakatsuji, H.; Hada, M.; Ehara, M.; Toyota, K.; Fukuda, R.; Hasegawa, J.; Ishida, M.; Nakajima, T.; Honda, Y.; Kitao, O.; Nakai, H.; Klene, M.; Li, X.; Knox, J. E.; Hratchian, H. P.; Cross, J. B.; Adamo, C.; Jaramillo, J.; Gomperts, R.; Stratmann, R. E.; Yazyev, O.; Austin, A. J.; Cammi, R.; Pomelli, C.; Ochterski, J. W.; Ayala, P. Y.; Morokuma, K.; Voth, G. A.; Salvador, P.; Dannenberg, J. J.; Zakrzewski, V. G.; Dapprich, S.; Daniels, A. D.; Strain, M. C.; Farkas, O.; Malick, D. K.; Rabuck, A. D.; Raghavachari, K.; Foresman, J. B.; Ortiz, J. V.; Cui, Q.; Baboul, A. G.; Clifford, S.; Cioslowski, J.; Stefanov, B. B.; Liu, G.; Liashenko, A.; Piskorz, P.; Komaromi, I.; Martin, R. L.; Fox, D. J.; Keith, T.; Al-

Laham, M. A.; C. Y. Peng; Nanayakkara, A.; Challacombe, M.; Gill, P. M. W.; Johnson, B.; Chen, W.; Wong, M. W.; Gonzalez, C.; Pople, J. A. Gaussian 03, revision B.05; I. Gaussian, Ed. Pittsburgh, PA, 2003.

(50) Ervin, K. M.; Ramond, T. M.; Davico, G. E.; Schwartz, R. L.; Casey, S. M.; Lineberger, W. C. Naphthyl Radical: Negative Ion Photoelectron Spectroscopy, Franck-Condon Simulation, and Thermochemistry. *Journal of Physical Chemistry A* **2001**, *105*, 10822-10831.

(51) The B3LYP/6-311++G(d,p) calculations predict that the three-fold barriers for the methyl torsion are 247 and 105 cm^{-1} for *N*-methyl-5-pyrazolide and *N*-methyl-5-pyrazolyl, respectively. They are 47 and 111 cm^{-1} for *N*-methyl-5-imidazolide and *N*-methyl-5-imidazolyl, respectively.

(52) Ervin, K. M.; DeTuro, V. F. Anchoring the Gas-Phase Acidity Scale. *Journal of Physical Chemistry A* **2002**, *106*, 9947-9956.

(53) Su, T.; Chesnavich, W. J. Parametrization of the Ion-Polar Molecule Collision Rate-Constant by Trajectory Calculations. *Journal of Chemical Physics* **1982**, *76*, 5183-5185.

(54) For the reverse direction in reaction 2, water was present as trace amounts in the *N*-methylpyrazole. The amount of water contained in the neutral reagent was determined by Carl Fisher titration to be 1.48 wt. %, however the percent of water in the vapor phase is estimated to be higher than in the liquid phase. It is unlikely that a direct association between methoxide and water is occurring because this reaction is known to be slow ($k^{\text{II}} = 1.0 \times 10^{-11} \text{ cm}^3 \text{ s}^{-1}$ at 0.5 torr He). [Kato, S.; Dang, T. T.; Barlow, S. E.; DePuy, C. H.; Bierbaum, V. M. Gas-phase association reactions of hydroxide, methoxide, ethoxide, and their deuterated analogs, *International Journal of Mass Spectrometry* **2000**, *196*, 625-638.] For the forward direction in reaction 6, water is present as the neutral reagent ($[\text{N}] \sim 5 \times 10^{12} \text{ molecules cm}^{-3}$). Again it is unlikely that direct association of hydroxide with water is the major contribution to the hydroxide-water adduct formation, because the rate constant for this process is known to be small ($k^{\text{II}} = 1.2 \times 10^{-12} \text{ cm}^3 \text{ s}^{-1}$ in 0.5 torr of He). [see above Kato *et al.*].

(55) Gunion, R. F.; Gilles, M. K.; Polak, M. L.; Lineberger, W. C. Ultraviolet Photoelectron-Spectroscopy of the Phenide, Benzyl and Phenoxide Anions, with *ab initio* Calculations. *International Journal of Mass Spectrometry and Ion Processes* **1992**, *117*, 601-620.

(56) Koppel, H.; Domcke, W.; Cederbaum, L. S. Multimode Molecular-Dynamics Beyond the Born-Oppenheimer Approximation. *Advances in Chemical Physics* **1984**, *57*, 59-246.

(57) Trofimov, A. B.; Koppel, H.; Schirmer, J. Vibronic Structure of the Valence π -Photoelectron Bands in Furan, Pyrrole, and Thiophene. *Journal of Chemical Physics* **1998**, *109*, 1025-1040.

(58) The largest source of experimental error is due to the measurement of k_r . The presence of a more basic anion would artificially raise the rate constant and

proton transfer branching ratio for the reaction of *N*-methylimidazolidine with water and therefore, the reported proton transfer rate constant represents an upper bound measurement.

(59) DePuy, C. H.; Kato, S. H/D Exchange Reactions. In *The Encyclopedia of Mass Spectrometry: Theory and Ion Chemistry*; P. B. Armentrout, Ed.; Elsevier: Amsterdam, 2003; Vol. 1; pp 670-674.

(60) *NIST Chemistry WebBook, NIST Standard Reference Database Number 69*; Linstrom, P. J.; Mallard, W. G., Eds.; National Institute of Standards and Technology: Gaithersburg MD, 20899 June 2005 (<http://webbook.nist.gov>).

(61) B3LYP/6-311++G(d,p) calculations predict that $\Delta_{\text{acid}}G_{298}(\text{C5-H, pyrazole}) = 376.8 \text{ kcal mol}^{-1}$ and $D_0(\text{C5-H, pyrazole}) = 118.1 \text{ kcal mol}^{-1}$. These values are close to the measured values of *N*-methylpyrazole reported here.

(62) Davico, G. E.; Bierbaum, V. M.; DePuy, C. H.; Ellison, G. B.; Squires, R. R. The C-H Bond-Energy of Benzene. *Journal of the American Chemical Society* **1995**, *117*, 2590-2599.

(63) McDonald, R. N.; Bianchina, E. J.; Tung, C. C. Electron Photodetachment of Cyclopentadienylidene Anion Radical in a Flowing Afterglow Apparatus - EA and ΔH_f° of Cyclopentadienylidene. *Journal of the American Chemical Society* **1991**, *113*, 7115-7121.

(64) The cyclopentadienyl radical is stabilized by delocalization but the species lacks one electron in the π system for aromaticity under the $4n+2$ Huckel's rule.

(65) DePuy, C. H.; Kass, S. R.; Bean, G. P. Formation and Reactions of Heteroaromatic Anions in the Gas-Phase. *Journal of Organic Chemistry* **1988**, *53*, 4427-4433.

CHAPTER IX

THERMOCHEMICAL STUDIES OF THE PEROXYFORMYL AND PEROXYACETYL RADICALS

9.1) Introduction

Organic peroxy radicals (RO_2) play an integral role in the chemistry of the troposphere.¹⁻³ These radicals are formed as a result of OH-initiated oxidation of volatile organic compounds (RH) emitted from biogenic and anthropogenic sources; this process efficiently removes hydrocarbons from the atmosphere and serves as an important sink for the OH radical. Once formed alkyl radicals, R, rapidly combine with atmospheric O_2 via a three-body reaction to produce organic peroxy radicals.



Peroxy radicals react with the NO_x and HO_x radical families. In urban areas, reactions with NO_x species (NO and NO_2) dominate. By oxidizing NO to NO_2 , peroxy radicals directly influence tropospheric ozone formation, since the photolysis of NO_2 forms $\text{O}(^3\text{P})$, which rapidly reacts with O_2 to form O_3 (eq 9.03-9.05).^{4,5}



In areas of low NO_x , organic peroxy radicals primarily react with other peroxy radicals (mainly HO_2), propagating chain reactions that eventually lead to the removal of radicals from the atmosphere.

Due to their significance in the atmosphere, the structure and thermochemistry of these radicals is of great interest. This work focuses on two very important peroxy radicals, the peroxyformyl radical (HC(O)OO) and the peroxyacetyl

radical ($\text{CH}_3\text{C}(\text{O})\text{OO}\cdot$). In particular, the latter species is one of the most abundant peroxy radicals in the atmosphere. In polluted environments, this radical reacts with NO_2 to form peroxyacetyl nitrate (PAN).^{6,7}



PAN is a key component in photochemical smog, it is a respiratory and eye irritant, and can damage vegetation. Due to its stability relative to other peroxy nitrates, PAN acts as a temporary reservoir for NO_x species and can undergo long-range transport from areas of high pollution to areas of low pollution, where subsequent thermal decomposition releases the reactive radicals. In addition to their atmospheric relevance, these two species are of fundamental structural interest since they have two distinct conformations (*cis* and *trans*), which differ dramatically in their reactivity and thermochemical properties.

The peroxyacetyl radical has been the focus of many spectroscopic and kinetic studies, the vast majority of which probe the strong UV $\tilde{B} - \tilde{X}$ transition.⁸⁻¹² However, due to the repulsive nature of the \tilde{B} state, this transition is broad and featureless, providing few structural details about the radical.¹ In contrast, the low-lying $\tilde{A} - \tilde{X}$ transition displays rotational and vibrational structure; however, due to its relatively small absorption cross section this transition requires use of sensitive spectroscopic techniques. Zalyubovsky *et al.*¹³ recorded the gas-phase absorption spectrum of the peroxyacetyl radical produced from photolysis of $(\text{COCl})_2$ in a $\text{CH}_3\text{CHO}/\text{O}_2/\text{N}_2$ mixture using cavity ringdown spectroscopy. More recently, Hu *et al.*^{14,15} employed near-IR/VUV ion enhancement spectroscopy to record the spectrum of peroxyacetyl radical produced from the thermal decomposition of PAN in a pyrolysis/supersonic pulsed nozzle. The results of these experiments are in excellent agreement with one another. The vibronic features were found to

correspond to the *trans*-conformer of the radical, the \tilde{A} - \tilde{X} term energy splitting was determined to be $5582.5 \pm 0.5 \text{ cm}^{-1}$, and several \tilde{A} state vibrational modes were identified.

The IR spectrum of the peroxyacetyl radical has been reported in a noble gas matrix from the flash thermolysis of PAN.¹⁶ The primary decomposition pathway of PAN was shown to occur by O-N bond fission yielding the peroxyacetyl radical. The resulting IR features were attributed to both the *cis*- and *trans*-conformers of the peroxyacetyl radical for which several IR and Raman active vibrational modes were identified. The peroxyformyl radical has also been observed using matrix isolation IR-spectroscopy. In an early study, this radical was produced by the photolysis of formaldehyde in a solid oxygen matrix.^{17,18} The assignment of the spectral features, however, was complicated by the presence of the HO₂ radical, which was likely present in the photolysis cage. More recently, the isolated *trans*-peroxyformyl radical was studied by the discharge production and deposition of the formyl radical onto a solid argon matrix followed by an association reaction with oxygen.¹⁹ The spectral assignments were confirmed by ¹⁸O isotopic labeling and by electronic structure calculations.

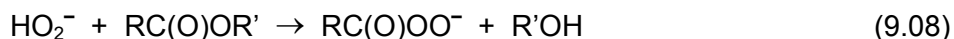
In this work we report the negative ion photoelectron spectrum of the peroxyformate (HC(O)OO⁻) and peroxyacetate anions (CH₃C(O)OO⁻). This technique provides access to the two lowest electronic states of the acylperoxy radical species through photodetachment of an electron from the corresponding anion. Analysis of the kinetic energy of the detached electron allows for the determination of electron affinities, term energy splitting, and vibrational frequencies, and gives insight into the molecular structure of both the anion and radical species. Additionally, the gas-phase acidities of peroxyformic acid and peroxyacetic acid were

determined from ion-molecule bracketing experiments and the collision-induced dissociation of the corresponding anions was investigated. Combining of the peracid gas-phase acidity with the peroxy radical electron affinity (EA) in a negative ion thermochemical cycle allows for the determination of the O-H bond dissociation energy (BDE).

9.2) Experimental Methods

9.2.1) Negative Ion Photoelectron Spectroscopy (NIPES)

A detailed description of the anion photoelectron spectrometer that was used in these studies is provided in Chapter 4. Acylperoxy ions ($\text{RC}(\text{O})\text{OO}^-$, $\text{R} = \text{H}$ and CH_3) were synthesized in a flowing afterglow source from a series of ion-molecule reactions (eq 9.07 and 9.08) that occur downstream of a microwave discharge source.



Equation 9.08 is a gas-phase Baeyer-Villiger reaction, which was previously reported by Bowie *et al.*²⁰ Due to the number of collisions in the source region, ions are prepared with a ~298 K rotational and vibrational Maxwell-Boltzmann distribution. Negative ions were gently extracted from the source region and passed through a Wien filter for mass selection. The mass selected ion beam was then crossed with a 351.1 nm (3.531 eV) line from a cw argon-ion laser in an external build up cavity producing ~100 W of circulating power. Photoelectrons that are ejected perpendicular to the plane of the ion-photon interaction region are energy analyzed by a hemispherical kinetic energy analyzer coupled to a position sensitive detector.

The electron energy resolution ranges from 8-15 meV fwhm. The absolute energy scale is calibrated with the well-known electron affinity (EA) of the sulfur

atom²¹ and a linear energy scale compression factor (< 1%), which is measured from the photoelectron spectra of reference ions S⁻,²¹ I⁻,²² and O⁻²³ using the EAs of the corresponding atoms. Angular distribution measurements were conducted by changing the angle (θ) between the electric field vector of the laser beam and the photoelectron collection axis.

9.2.2) Flowing Afterglow-Selected Ion Flow Tube (FA-SIFT) Measurements

Collision-induced dissociation (CID) studies and gas-phase acidity ($\Delta_a G$) measurements were conducted using a tandem flowing afterglow-selected ion flow tube instrument (FA-SIFT), which was described in Chapter 3. Acylperoxy ions were formed in a flowing afterglow source using the same synthesis scheme as in the above photodetachment experiments (eq 9.07 and 9.08). Peroxy ions were extracted from the source flow tube, focused into a quadrupole for mass selection, and injected into a second flow tube where the flow of He buffer gas is maintained at 12 SLPM and a pressure of ~0.5 torr. Ions injected into the flow tube undergo multiple collisions with the He buffer gas and a percentage of the ions fragment due to CID in the vicinity of the injection orifice that connects the quadrupole region to the second tube. Further downstream from the injection orifice, the ions are collisionally cooled to a ~298 K rotational and vibrational Maxwell-Boltzmann distribution. Measured flows of neutral reagents were introduced into the reaction flow tube through a manifold of inlets and the reactant and product ions were analyzed using a quadrupole mass filter coupled to an electron multiplier.

SIFT-CID^{24,25} studies were performed by changing the injection potential (E_{lab}) while monitoring the parent and daughter ion intensities. The SIFT-injection potential is defined as the voltage differential between the source flow tube and the second flow tube injector. The center of mass energy (E_{com}) is calculated from eq 9.09:

$$E_{\text{com}} = \frac{E_{\text{lab}} \times M_{\text{He}}}{M_{\text{He}} + M_{\text{ion}}} \quad (9.09)$$

where M_{He} is the mass of helium and M_{ion} is the mass of the parent ion. Since CID occurs under multiple collision conditions, large ions tend to store energy and fragment at a lower energy than the true threshold energy. Thus, the fragmentation energies determined in this technique are lower bounds to the true threshold energy.

The gas-phase acidities of both acyl peroxides were obtained using a ion-molecule bracketing technique, where the acyl peroxy ion was SIFT-injected and allowed to react with several reference acids of known acidity. If rapid proton transfer is observed then the acidity of the reference acid is a lower bound to the unknown acidity. If proton transfer is not observed then the acidity of the reference acid is an upper bound to the unknown acidity. One experimental complication in these bracketing experiments is that, despite injecting these peroxy ions with minimal energy, fragment ions due to CID were also present in the second flow tube. Since some of these fragment ions are more basic than the acyl peroxy ion, the M-H peak of the reference was always observed even when its acidity is below that of the acyl peroxide. Additionally, depletion of the parent acyl peroxy ion was also generally observed since it reacts by neutral O atom loss. In order to determine whether proton transfer between acyl peroxy ion and the reference acid occurs, the intensities of all ions were monitored as a function of time and the contribution from the fragment ions to the reference acid M-H signal was removed.

9.2.3) Electronic Structure Calculations

Two different theoretical models, both provided in the Gaussian 03 suite of programs,²⁶ are used to evaluate structural and energetic aspects of the alkyl peroxy ions. DFT calculations (B3LYP/6-311++G(d,p))²⁷⁻²⁹ were used to calculate optimized geometries, harmonic vibrational frequencies (not scaled), and the rotational

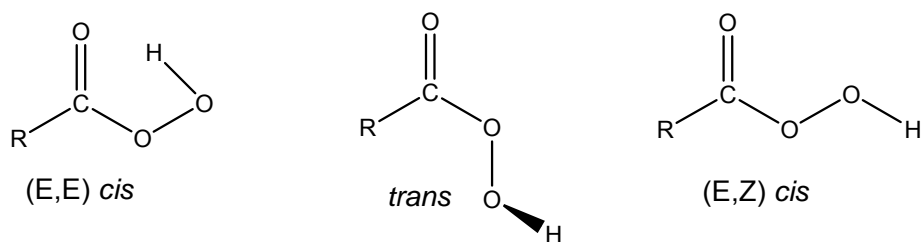
constants. This level of theory was chosen since it is known to provide reliable molecular structures. The G3MP2B3 composite technique³⁰ was used to investigate various thermodynamic properties of these species. In this technique geometries and zero point energies are calculated at the B3LYP/6-31G(d) level of theory followed by a series of well-defined *ab-initio* single-point energy calculations. This method has been tested,³⁰ and the average deviation from experiment is 1.25 kcal mol⁻¹. The accuracy of this method was independently evaluated in this work with a test group of molecules that was chosen based on their similarity to the compounds studied here; the average deviation from experiment for the test group was 1.42 kcal mol⁻¹ (see Table 9.01). Simulated photoelectron spectra were obtained by calculating the Franck-Condon (FC) factors at a vibrational temperature of 300 K with the PESCAL program.³¹ These Franck-Condon simulations are based on optimized geometries and normal modes from the DFT calculations and electron binding energies from the G3MP2B3 calculations.

9.3) Results and Discussion

9.3.1) Computational Results

It has been shown both experimentally^{32,33} and theoretically³⁴ that the lowest energy structure of these peroxyacids is the *cis*-planar conformer (E,E) where the peroxy hydrogen atom is hydrogen bonded to the carbonyl oxygen atom. At the G3MP2B3 level of theory this hydrogen bond is calculated to be 1.92 Å in peroxyformic acid and 1.86 Å in peroxyacetic acid. Rotation by 180° about the OCOO dihedral angle gives a higher energy *trans*-conformation, where the peroxy hydrogen atom points out of the plane of symmetry. In peroxyacetic acid, rotation about the OCOO dihedral angle coincides with the rotation of the methyl group; in the *cis*-structure the in-plane methyl hydrogen points towards the peroxy group, while in the *trans*-structure it points towards the carbonyl oxygen atom. In peroxyformic

acid rotation by 180° about the COOH dihedral angle gives one further conformer, a (E,Z) *cis*-planar form, which is the highest energy conformer.



The potential energy curves for rotation about the OCOO dihedral angle, which interconvert the *trans*- and (E,E) *cis*-structures of peroxyformic acid and peroxyacetic acid, were calculated using G3MP2B3 theory. This method was shown to reproduce the thermochemical quantities relevant to this study reasonably well for a test group of molecules (see Table 9.01). For peroxyformic acid, the *trans*-conformer is $\sim 3.4 \text{ kcal mol}^{-1}$ higher in energy than the *cis*-conformer; these two minima are connected by a $\sim 11.1 \text{ kcal mol}^{-1}$ (*trans* to *cis*) zero point energy corrected barrier. The difference in energies of the *cis*- and *trans*-conformers reflects the strength of the internal hydrogen bond. For peroxyacetic acid, the energy difference between the *trans*- and *cis*-conformer increases to $\sim 5.5 \text{ kcal mol}^{-1}$ and a $\sim 8.6 \text{ kcal mol}^{-1}$ (*trans* to *cis*) barrier connects the two minima. These results are summarized in Table 9.02 and the DFT optimized geometries are provided in Tables 9.03 and 9.04.

There are also two stable conformers for the acylperoxy anion and radical defined by the OCOO dihedral angle. In the *trans*-configuration the in-plane O-O bond is *trans* to the C=O bond with respect to the C-O bond. Rotation by 180° about the OCOO dihedral angle results in the *cis* configuration, where the in-plane O-O bond is *cis* to the C=O group. In the peroxyformate anion, the *trans*-structure is stabilized relative to the *cis*-structure by $\sim 5.0 \text{ kcal mol}^{-1}$; the *trans*-structure is connected to the *cis*-structure by a $\sim 18.3 \text{ kcal mol}^{-1}$ barrier as shown in Figure 9.01. In the formylradical the *trans*-structure is only $\sim 2.3 \text{ kcal mol}^{-1}$ lower in energy than

Table 9.01: Experimental and Calculated (G3MP2B3) Electron Affinities, Enthalpies of Deprotonation and Bond Dissociation Enthalpies for Alkyl Peroxides and Carboxylic Acids. The calculated values are in parentheses.

R'OH	EA(R'O) eV	$\Delta_a H_0(\text{R}'\text{O}-\text{H})$ kcal mol ⁻¹	$D_0(\text{R}'\text{O}-\text{H})$ kcal mol ⁻¹
HOOH ^a	1.076 ± 0.006 (1.061)	375.3 ± 0.8 (377.1)	86.7 ± 0.8 (88.0)
CH ₃ OOH ^b	1.161 ± 0.004 (1.168)	372.6 ± 1.0 (373.2)	86.9 ± 1.0 (86.6)
C ₂ H ₅ OOH ^b	1.186 ± 0.005 (1.175)	369.9 ± 2.2 (372.8)	83.9 ± 2.2 (86.4)
HC(O)OH ^c	3.498 ± 0.015 (3.575)	345.5 ± 0.5 (342.8)	112.8 ± 1.2 (113.1)
CH ₃ C(O)OH ^d	3.449 ± 0.010 (3.296)	348.9 ± 0.5 (348.0)	112 ± 3 (110.4)

^aReference 35. ^bReference 36. ^cReference 37 and 38. ^dReference 39 and 38.

Table 9.02: Relative Energies (kcal mol⁻¹) of the *trans*- and *cis*-conformers (going from the *trans*- to the *cis*-structure) calculated at the G3MP2B3 level of theory.

	$\Delta_0 E$	$\Delta_{298} H$	$\Delta_{298} G$	$E^\ddagger (E+E_{zpt})$
Peroxyformic Acid	-3.1	-3.4	-2.8	11.1
Peroxyformate Anion	5.1	5.0	5.1	18.3
Peroxyformyl Radical	2.4	2.3	2.3	8.9
Peroxyacetic Acid	-5.2	-5.5	-5.3	8.6
Peroxyacetate Anion	5.7	5.8	5.5	17.0
Peroxyacetyl Radical	0.7	0.8	0.3	5.9

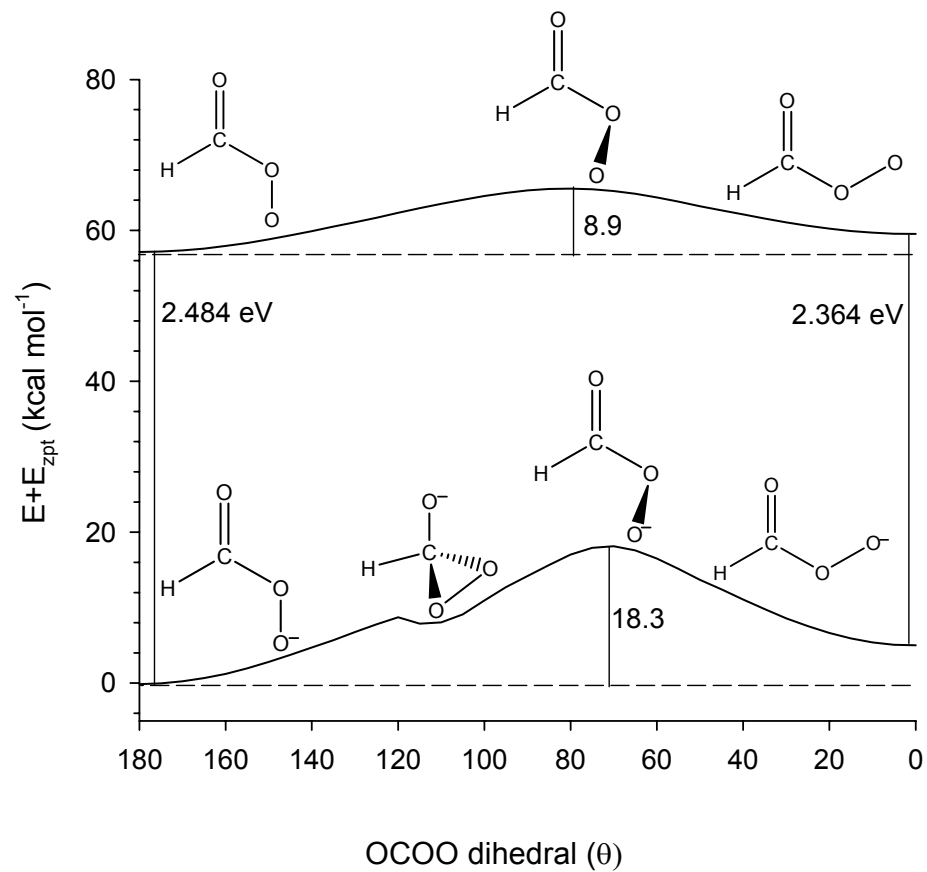


Figure 9.01: Potential energy surface ($E + E_{zpt}$) calculated at the G3MP2B3 level of theory for the *trans*- to *cis*-isomerization of the peroxyformate anion (bottom) and the formylperoxy radical (top)

Table 9.03: B3LYP/6-311++G(d,p) Optimized Geometries for Peroxyformic Acid, Peroxyformate Anion and Peroxyformyl Radical.

	Peroxyformic Acid (\tilde{X}^1A')		Peroxyformate Anion (\tilde{X}^1A')		Peroxyformyl Radical (\tilde{X}^2A'')		Peroxyformyl Radical (\tilde{A}^2A')	
	<i>cis</i>	<i>trans</i>	<i>cis</i>	<i>trans</i>	<i>cis</i>	<i>trans</i>	<i>cis</i>	<i>trans</i>
C-H	1.096	1.099	1.119	1.105	1.097	1.099	1.096	1.095
C=O	1.202	1.190	1.222	1.227	1.178	1.179	1.185	1.184
C-O	1.341	1.368	1.308	1.304	1.422	1.427	1.387	1.397
O-O	1.441	1.455	1.455	1.480	1.326	1.328	1.365	1.369
O-H	0.982	0.969	-	-	-	-	-	-
\angle H-C=O	127.3	127.9	122.1	124.0	129.2	130.4	129.0	128.1
\angle H-C-O	108.2	112.1	106.6	111.6	105.5	109.7	104.8	112.1
\angle O=C-O	124.4	120.1	131.3	124.4	125.3	119.9	125.3	119.8
\angle C-O-O	111.8	108.8	117.7	112.5	114.1	111.1	114.1	116.6
\angle O-O-H	101.6	99.7	-	-	-	-	-	-

Bond lengths are in Angstroms and bond angles are in degrees.

Table 9.04: B3LYP/6-311++G(d,p) Optimized Geometries for Peroxyacetic Acid, Peroxyacetate Anion and Peroxyacetyl Radical.

	Peroxyacetic Acid (\tilde{X}^1A')		Peroxyacetate Anion (\tilde{X}^1A')		Peroxyacetyl Radical			
					(\tilde{X}^2A'')		(\tilde{A}^2A')	
	<i>cis</i>	<i>trans</i>	<i>cis</i>	<i>trans</i>	<i>cis</i>	<i>trans</i>	<i>cis</i>	<i>trans</i>
C-H'	1.099	1.088	1.092	1.092	1.088	1.088	1.088	1.087
C-H	1.092	1.092	1.095	1.092	1.092	1.091	1.092	1.093
C-C	1.500	1.501	1.513	1.513	1.496	1.495	1.503	1.497
C=O	1.209	1.198	1.223	1.234	1.182	1.856	1.189	1.187
C-O	1.355	1.380	1.313	1.314	1.458	1.454	1.406	1.420
O-O	1.440	1.462	1.452	1.471	1.320	1.322	1.364	1.366
O-H	0.984	0.968	-	-	-	-	-	-
$\angle H'-C-C$	111.8	108.0	112.1	108.9	109.2	107.9	112.2	109.5
$\angle H-C-C$	108.6	110.5	109.1	109.6	109.9	110.4	108.3	109.3
$\angle C-C=O$	127.2	127.0	121.2	122.6	130.6	129.5	128.8	129.1
$\angle C-C-O$	111.0	117.6	109.7	116.7	107.5	115.8	108.1	113.9
$\angle O=C-O$	121.8	115.4	129.0	120.6	121.9	114.6	123.2	117.0
$\angle C-O-O$	111.6	117.8	117.6	115.5	113.8	114.6	117.1	117.0
$\angle O-O-H$	100.9	98.5	-	-	-	-	-	-

Bond lengths are in Angstroms and bond angles are in degrees.

the *cis*-structure and the isomerization barrier (*trans* to *cis*) is ~ 8.9 kcal mol⁻¹. In the peroxyacetate anion, the *trans*-structure is stabilized relative to the *cis*-structure by ~ 5.8 kcal mol⁻¹. Rotation about the OCOO dihedral angle coincides with the rotation of the methyl group and a barrier of ~ 17.0 kcal mol⁻¹ (*trans* to *cis*) separates the two conformers. In the radical the *cis*- and *trans*-structures lie within 1 kcal mol⁻¹ of each other, with the *trans*-structure being slightly more stable; a barrier of 5.9 kcal mol⁻¹ separates the two structures. These results are also summarized in Table 9.02 and the DFT optimized geometries are provided in Tables 9.03 and 9.04.

For both the peroxyformate and peroxyacetate anions, there is a shallow well (< 1.6 kcal mol⁻¹) along the isomerization path, which corresponds to a quasi-stable dioxirane intermediate. Under our experimental conditions, it is expected that this species does not exist in any appreciable concentration. However, it is interesting to note that this observation is consistent with the condensed-phase work of Porter *et al.*,⁴⁰ where the base-promoted interchange of the oxygen atoms of peroxybenzoate anion (C₆H₅C(O)OO⁻) indicates that the corresponding dioxirane structure is accessible from the anion.

9.3.2) Photoelectron Spectra of the Peroxyformate Ion

The 351.1 nm magic angle photoelectron spectrum of the *m/z*~61 ion produced from the reaction of HO₂⁻ with ethylformate is shown in Figure 9.02a. The same spectral profile is observed when the *m/z*~61 ion is produced from the reaction of HO₂⁻ with methylformate. In agreement with the ion-chemistry studies of Bowie *et al.*²⁰, the bicarbonate anion is not the likely product of this reaction, since the EA of the bicarbonate radical is ~ 3.9 eV,⁴¹ which is outside the range of the laser photon energy and, therefore, cannot contribute to the observed spectrum. The photoelectron angular distribution was measured and the anisotropy parameter (β) is

negative across the entire spectrum, consistent with photodetachment from a π -type orbital.^{35,36} The most striking feature of the spectrum is the series of intense peaks (*b*, *e*, *g*, *h*, *i*, *j*, *k*, and *m*), which are spaced by $\sim 990\text{ cm}^{-1}$. With the exception of peak *b*, the width of these peaks is $\sim 50\text{ meV}$ (fwhm), substantially greater than the instrument resolution (12-14 meV in Figure 9.02a), indicating that each band is composed of multiple transitions. To confirm this, the same spectrum was collected with a slightly better resolution of 8-9 meV but lower signal to noise ratio; the lower binding energy portion of this spectrum is shown in Figure 9.02b. With this slightly higher resolution, a subtle splitting of peaks *e*, *g*, and *h* is observed.

As mentioned above, the *trans*-conformer of the peroxyformate anion is predicted to lie $\sim 5\text{ kcal mol}^{-1}$ lower in energy than the *cis*-conformer. The Baeyer-Villiger reaction of HO_2^- and ethylformate is predicted to be sufficiently exothermic such that the *cis* to *trans* isomerization barrier lies below the total energy of the reaction. Based on this, the thermal population of peroxyformate anions in our source is expected to overwhelmingly consist of the *trans*-configuration; thus, photodetachment should result in the *trans*-form of the radical. In accordance with this, the calculated EA of the *trans*-form of the peroxyformyl radical is 2.484 eV, very close to the position of peak *b*. In contrast the EA of the *cis*-form of the peroxyformyl radical is predicted to be 2.364 eV, which is lower in energy than the observed spectral features. Using the DFT optimized geometries and harmonic frequencies (Tables 9.03 and 9.05, respectively) Franck-Condon simulations were performed for photodetachment from the \tilde{X}^1A' state of the *trans*-peroxyformate anion to the \tilde{X}^2A'' state of the *trans*-peroxyformyl radical. Figures 9.02c and 9.02d show the simulated stick spectra in blue while the red traces are the result of convoluting the stick

spectra with a 13 meV or a 9 meV fwhm Gaussian function, respectively. The simulation adequately predicts the main features of the experimental spectrum. That is, the simulation is composed of a series of clustered transitions, which correspond to the positions and intensities of the broad series of peaks (*b*, *e*, *g*, *h*, *i*, *j*, *k*, and *m*). While the simulation predicts that there are more resolvable transitions than are actually observed, it captures the essence of the spectral features including the relative intensities of the partially resolved peaks at lower electron binding energies (Figure 9.02b). Thus, the spectrum shown in Figures 9.02a and 9.02b is attributed to photodetachment of the *trans*-form of the peroxyformate anion. It should be noted that the spectrum for the *cis*-conformer was also simulated (Figure 9.03b) and is inconsistent with the experimental data.

Using the FC simulation as a guide, the vibronic features of the \tilde{X}^2A'' state of the peroxyformyl radical are assigned. Peak *b* at 2.493 ± 0.006 eV is the electronic band origin, which corresponds to the EA of the peroxyformyl radical. The partially resolved peaks *e1* and *e2* are due to the fundamental of the in-plane OCOO backbone deformation (ν_5) and to the fundamental of an O-O stretch (ν_4), respectively. The first and second overtones of ν_5 appear in the spectrum as peaks *g1* and *h1*. Peaks *g2* and *h2* are due to one and two quanta of ν_5 on the ν_4 fundamental ($\nu_5 + \nu_4$ and $2\nu_5 + \nu_4$, respectively), while peak *h3* is due to two quanta of ν_4 on the ν_5 fundamental ($2\nu_4 + \nu_5$). The extended progressions in these two modes enable a more accurate determination of fundamental vibrational frequencies, as well as crude measurements of the anharmonicity of each mode. Using eq 9.10 we can estimate the harmonic frequencies (ω) and anharmonicity constants (χ) for these two modes; here, $g(n)-g(0)$ is the energy difference between *n* and 0 quanta of a given mode.

Table 9.05: B3LYP/6-311++G(d,p) Harmonic Frequencies (cm⁻¹) of Peroxyformate Anion and Peroxyformyl Radical. Experimental values are provided in parentheses.

ν	symmetry	Peroxyformate Anion (\tilde{X}^1A')	Peroxyformyl Radical (\tilde{X}^2A'')	(\tilde{A}^2A')
1	A'	2952	3053	3080
2		1690	1889	(1821.5 ^a) 1851
3		1335	1335	1379
4		1286	1146	(1078 ^b) 1016
5		866	954	(957.3 ^a ; 966 ^b) 954
6		607	586	(574 ^b) 586
7		370	404	333
8	A''	1043	1009	997
9		220	175	195

^a Ar Matrix: reference 19. ^b Gas-phase: this work.

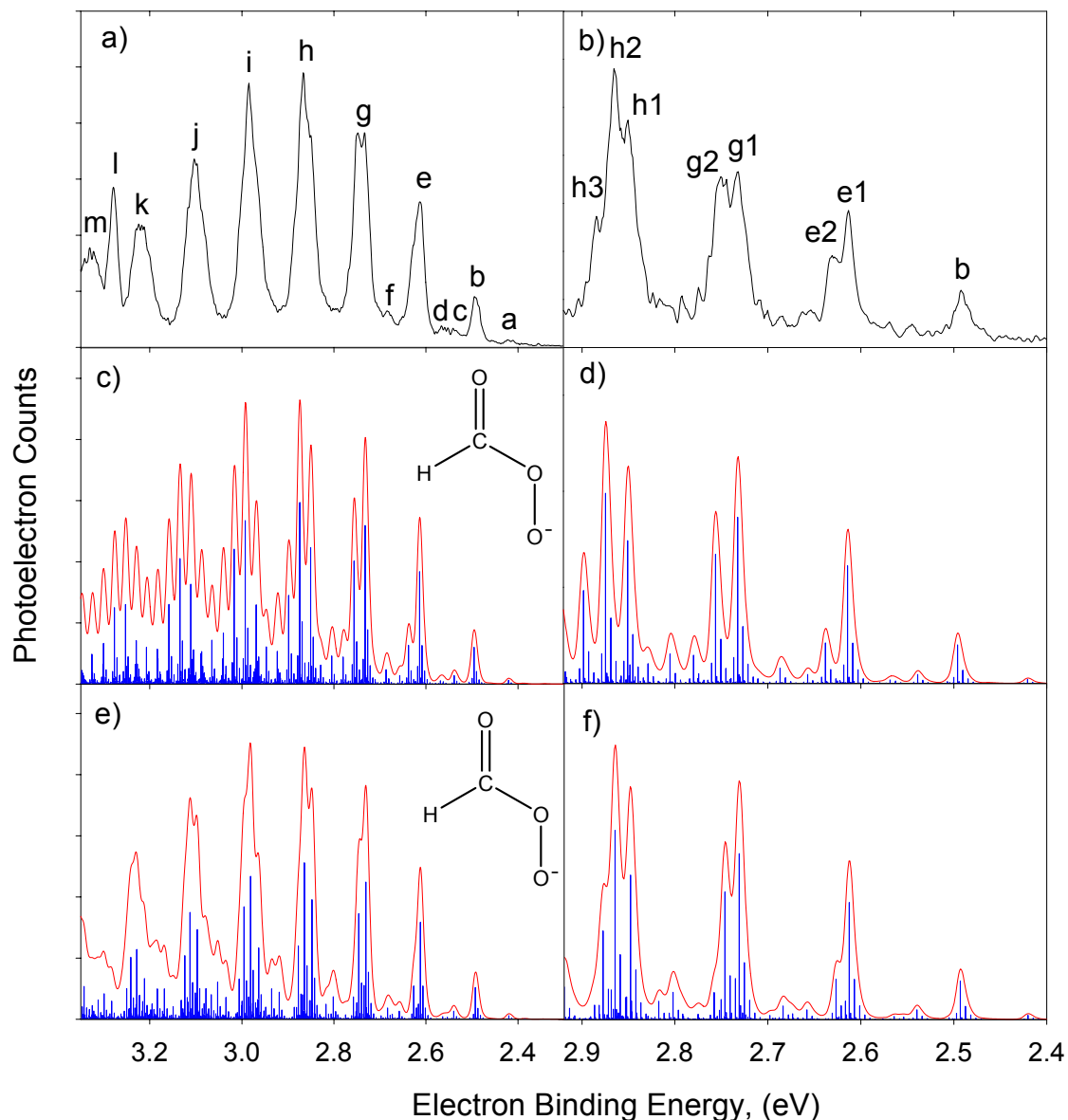


Figure 9.02: a-b) The 351.1 nm magic-angle photoelectron spectrum of the peroxyformate anion. c-f) Franck-Condon simulations for transitions from \tilde{X}^1A' state of the *trans*-peroxyformate anion to the \tilde{X}^2A'' state of the *trans*-peroxyformyl radical. The sticks are the raw Franck-Condon factors and the solid lines are the 13 meV (left) and 9 meV (right) fwhm Gaussian convolutions. In c-d) the simulation is based on the B3LYP/6-311++G(d,p) optimized geometries and harmonic frequencies and the origin position is determined by G3MP2B3 calculations. In e-f) the simulation is based on the above optimized geometries and harmonic frequencies with the exception of ν_4 , ν_5 , and ν_6 in the radical where the experimental frequencies and anharmonicities were used; the calculated EA was slightly shifted (<10 meV) to match the experiment.

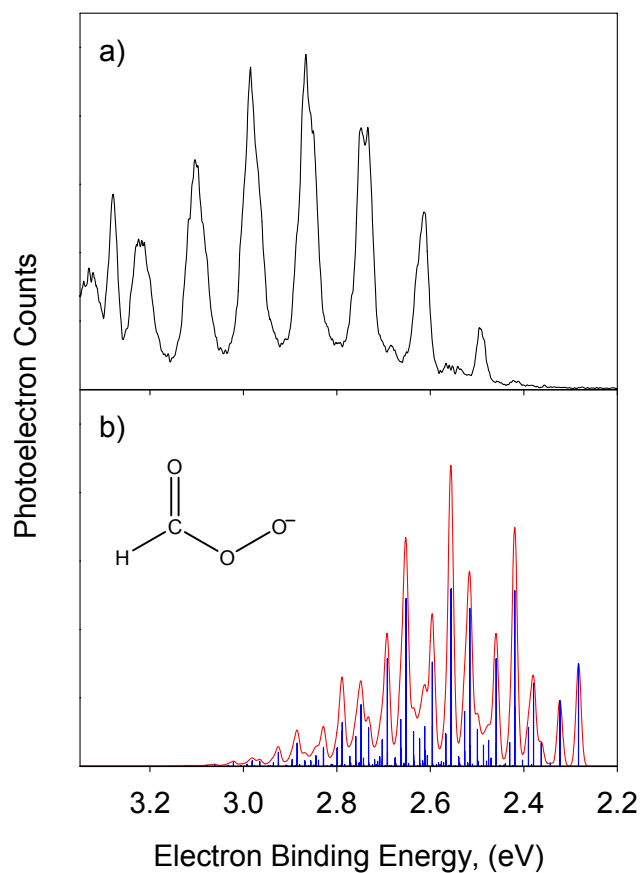


Figure 9.03: a) The 351.1 nm magic-angle photoelectron spectrum of the peroxyformate anion reproduced from Figure 9.02a. b) Franck-Condon simulation based on the B3LYP/6-311++G(d,p) optimized geometries and harmonic frequencies for transitions from \tilde{X}^1A' state of the *cis*-peroxyformate anion to the \tilde{X}^2A'' state of the *cis*-peroxyformyl radical. The sticks are the raw Franck-Condon factors and the solid lines are the 13 meV fwhm Gaussian convolutions. The position of the origin is determined by G3MP2B3 calculations.

$$g(n) - g(0) = \omega(n + \frac{1}{2}) - \chi(n + \frac{1}{2})^2 - \frac{1}{2}\omega + \frac{1}{4}\chi \quad (9.10)$$

The harmonic frequency and anharmonicity constant for the OCOO backbone deformation (ν_5) were found using the 5_0^n ($n=0-3$) and $5_0^1 4_0^1$ ($n=0-2$) progressions to be $\omega_5 = 973 \pm 20 \text{ cm}^{-1}$ and $\chi_5 = 4 \pm 3 \text{ cm}^{-1}$. The harmonic frequency and anharmonicity term for the O-O stretch (ν_4) were found using the $5_0^1 4_0^n$ ($n=0-2$) progression to be $\omega_4 = 1098 \pm 20 \text{ cm}^{-1}$ and $\chi_4 = 10 \pm 5 \text{ cm}^{-1}$. Using these parameters, the ν_5 and ν_4 fundamental frequencies were determined to be $966 \pm 20 \text{ cm}^{-1}$ and $1078 \pm 20 \text{ cm}^{-1}$, respectively. The low intensity peak *d* is the fundamental of the ν_6 OCO bend at $574 \pm 35 \text{ cm}^{-1}$, while peaks *f* and *h* are due to combination bands of one quanta of the ν_6 OCO bend on the ν_5 progression. Peaks *a* and *c* are due to excited anion vibrations. Peak *a* is the fundamental of the anion ν_6 OCO bend at $587 \pm 30 \text{ cm}^{-1}$, while peak *c* is a sequence band of one quanta of the anion ν_6 OCO bend with the radical ν_5 OCOO backbone deformation. Combination bands of these three modes contribute to the intensity at higher binding energies. The intense, broad series of peaks primarily derives its intensity from an extended progression in the ν_5 OCOO backbone deformation 5_0^n , along with two combination band progressions, $5_0^n 4_0^1$ and $5_0^n 4_0^2$. At higher binding energies higher order combination bands ($5_0^n 4_0^m$) congest the spectrum.

Following the analysis of the $\tilde{X}^2 A''$ state vibronic features, it appears that the discrepancy between the simulated and the experimental spectrum largely stems from the overestimate of the O-O stretching frequency. In actuality, the frequencies of O-O stretch and OCOO backbone deformation are closer to one another than predicted and, therefore, these two modes are only partially resolved. Additionally, at higher binding energies anharmonic effects are manifested and the harmonic

simulation overestimates the peak positions. Using the experimentally determined frequencies and anharmonicity constants in the Franck-Condon simulation (shown in Figure 9.02e and 9.02f) greatly improves its quality and the main series emerges. Additionally, the calculated binding energy was slightly shifted (< 10 meV) to match the experimental spectrum. Peak *l* is notably absent in the simulation. This peak is likely due to photodetachment to a low-lying electronic state of the radical. The position of this peak relative to the \tilde{X}^2A'' origin (peak *b*) is consistent with G3MP2B3 calculations, which find an \tilde{A}^2A' excited state of the peroxyformyl radical with a calculated T_e of 0.791 eV, which is comparable to the $\tilde{X} - \tilde{A}$ energy splittings of other peroxy radicals.^{13,24,35,42-44} Based on the simulated Franck-Condon profile for photodetachment from the \tilde{X}^1A' state of the anion to the \tilde{A}^2A' state of the radical (not shown), this feature is either the excited state electronic band origin or the ν_7 fundamental; thus, the T_e of the peroxyformyl radical is determined to be 0.784 ± 0.045 eV.

9.3.3) Photoelectron Spectra of the Peroxyacetate Ion

The 351.1 nm magic angle photoelectron spectrum of the $m/z \sim 75$ ion produced from the reaction of HO_2^- with ethylacetate is shown in Figure 9.04. The same spectral profile is observed when the $m/z \sim 75$ ion is produced from the reaction of HO_2^- with methylacetate and with 2,2-difluoroethylacetate. The anisotropy parameter (β) was measured and is negative across the entire spectrum, consistent with photodetachment from a π -type orbital.^{35,36} Since this ion is produced from a reaction analogous to that for peroxyformate anion formation, it is likely that the $m/z \sim 75$ ion is the peroxyacetate anion. To confirm this, Franck-Condon factors for the transition from the \tilde{X}^1A' state of the peroxyacetate anion to the \tilde{X}^2A'' and \tilde{A}^2A' states of the peroxyacetyl radical were computed. These results are shown in Figure

9.04b and the DFT optimized geometries and harmonic frequencies are provided in Tables 9.04 and 9.06. The calculated binding energies for both radical states have been slightly shifted (< 20 meV) and the intensities normalized to match the experimental spectrum. The simulation reproduces the observed spectral features reasonably well, especially considering the complicated nature of the spectrum. From this, we conclude that the observed spectral features are due to the *trans*-conformer of the peroxyacetate anion. It should be mentioned that the Franck-Condon factors for the *cis*-conformer of the peroxyacetate anion were also simulated (Figure 9.05b) and are inconsistent with the observed spectral features. Additionally, the possible formation of the hydrogenperoxide ethylenolate anion ($\text{CH}_2\text{C}(\text{O}^-)\text{OOH}$), which would result from deprotonation of peroxyacetic acid at the methyl group, was also investigated. While the deprotonation at the O-H site is favored thermodynamically (by ~ 5 kcal mol $^{-1}$), such lack of selectivity has previously been reported in the deprotonation of acetic acid.⁴⁵ The presence of this ion was also excluded by Franck-Condon simulations (Figure 9.05c), which were inconsistent with the experimental data.

Several features of the \tilde{X}^2A'' and \tilde{A}^2A' states of the peroxyacetyl radical can be assigned with assistance from the Franck-Condon simulation. Peak *a* at 2.381 ± 0.007 eV is the \tilde{X}^1A' electronic band origin, which corresponds to the EA of the peroxyacetyl radical. The peaks observed at higher binding energies represent excited vibrational levels of the peroxyacetyl radical. Introduction of the methyl group at the carbonyl center leads to more complication and congestion in the vibronic features, compared to the rather simple peroxyformate spectrum. The vibronic features in the peroxyacetate spectrum are attributed to five modes: an OO stretching mode (ν_7), OCOO backbone deformation (ν_8), CCOO backbone

Table 9.06: B3LYP/6-311++G(d,p) Harmonic Frequencies (cm^{-1}) of Peroxyacetate Anion and Peroxyacetyl Radical. Experimental values are provided in parentheses.

ν	symmetry	Peroxyacetate		Peroxyacetyl		
		Anion (\tilde{X}^1A')	(\tilde{X}^2A'')	Radical (\tilde{A}^2A')		
1	A'	3116	3164		3164	
2		3033	3061		3043	
3		1676	1898	(1850 ^a)	1883	
4		1450	1460	(1420 ^a)	1460	
5		1382	1399	(1367 ^a)	1391	
6		1325	1184	(1153 ^a)	1141	(1143.8 ^b)
7		1010	1121	(1099 ^a)	1005	(928.4 ^b ; 929 ^c ; 916 ^d)
8		934	978	(972 ^a)	984	(841.5 ^b)
9		792	726	(736 ^a)	751	(759.9 ^b)
10		562	540	(545 ^a)	541	(538.1 ^b ; 539 ^c)
11		500	505		476	(473.4 ^b ; 473 ^c)
12		327	322	(348 ^a)	272	(269.8 ^b)
13	A''	3097	3124		3105	
14		1443	1463	(1425 ^a)	1471	
15		1048	1045	(1029 ^a)	1062	
16		569	540	(500 ^a)	556	
17		205	145		180	
18		146	135		141	

^a Ne or Ar Matrix: reference 16. ^b Gas-phase: reference 15. ^c Gas-phase: reference 13. ^d Gas-phase: this work.

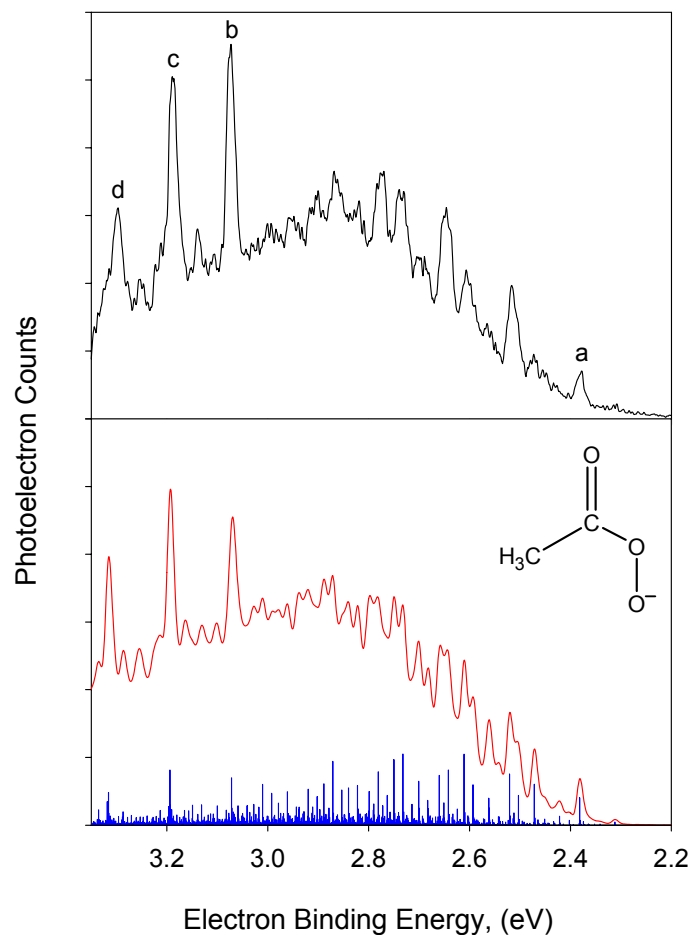


Figure 9.04: a) The 351.1 nm magic-angle photoelectron spectrum of the peroxyacetate anion. b) Franck-Condon simulations based on optimized geometries and normal modes from B3LYP/6-311++G(d,p) calculations for transitions from \tilde{X}^1A' *trans*-peroxyacetate anion to \tilde{X}^2A'' and \tilde{A}^2A' *trans*-peroxyacetyl radical. The sticks are the raw Franck-Condon factors and the solid line is the 13 meV fwhm Gaussian convolutions. The origin of each simulation was shifted (< 20 meV) and intensities normalized to correspond to the experimental spectrum.

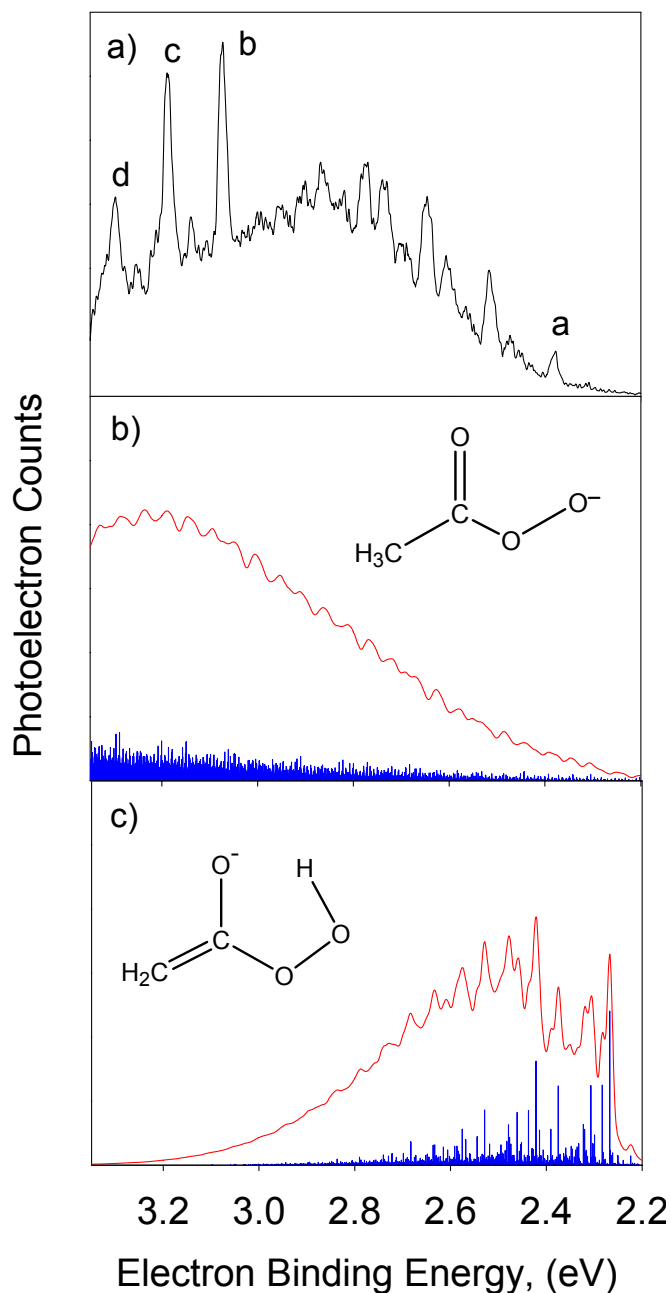


Figure 9.05: a) The 351.1 nm magic-angle photoelectron spectrum of the peroxyacetate anion reproduced from Figure 9.04a. Franck-Condon simulation based on the B3LYP/6-311++G(d,p) optimized geometries and harmonic frequencies for transitions from b) the \tilde{X}^1A' *cis*-peroxyacetate anion to the \tilde{X}^2A'' *cis*-peroxyacetyl radical and c) from the \tilde{X}^1A' state of the hydrogenperoxide ethylenolate anion to the \tilde{X}^2A'' state of the hydrogenperoxide ethylenolyl radical. The sticks are the raw Franck-Condon factors and the solid lines are the 13 meV fwhm Gaussian convolutions. The position of the origin is determined by G3MP2B3 calculations.

deformation (ν_9), OCO bend (ν_{10}), and CCOO breathing (ν_{12}). Combination bands of these five modes give rise to a multitude of transitions, which lead to congestion in the spectrum. The main spectral carriers are the OCOO and CCOO back bone deformations along with the O-O stretch. The frequencies of these modes have previously been determined using matrix isolation IR spectroscopy (see Table 9.06).¹⁶ Similar to the above peroxyformate spectrum, the O-O stretch and the OCOO frequencies are within 130 cm^{-1} of each other and, therefore, can only be partially resolved. This fact, combined with the extensive combination band progressions in the CCOO back bone deformation and O-O stretch, adds to the complexity of the spectrum.

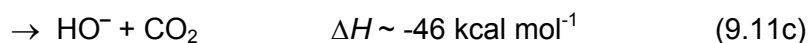
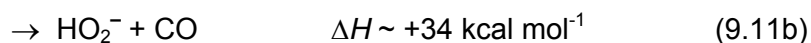
The intense narrow peaks appearing at higher electron binding energies are due to photodetachment to the low-lying \tilde{A}^2A' electronic state of the radical. Peak *b* is the \tilde{A}^2A' electronic band origin, giving a T_e of $0.691 \pm 0.009\text{ eV}$. Peaks *c* and *d* are the fundamental and first overtone of the \tilde{A}^2A' state OO stretch with a frequency of $916 \pm 45\text{ cm}^{-1}$. These peak assignments are confirmed by two prior independent measurements of the $\tilde{A}^2A' \leftarrow \tilde{X}^2A'$ transition.¹³⁻¹⁵

9.3.4) Collision-Induced Dissociation Studies

Measurement of ambient peroxide concentrations can provide insight into the extent of photochemical processing in a given air mass.⁴⁶ Mass spectrometry has become an increasingly important tool in the detection and quantification of trace species in the atmosphere. Since peroxy anions are easily formed from proton transfer to a moderate base, negative ion chemistry presents an alternative to more traditional positive ion chemical ionization methods. Furthermore, previous studies on decomposition pathways of organic peroxy anions indicate that collisional

activation of these ions gives characteristic fragment ions, which can assist in their analytical identification.²⁴

Figure 9.06a shows the relative yields of the fragment ions that result from the CID of the peroxyformate ion as a function of SIFT-injection energy. The primary dissociation pathway is the loss of an oxygen atom to form the formate ion. Minor amounts of OH⁻ and HO₂⁻ ions are also observed. The formation of these products is consistent with an intramolecular hydrogen atom transfer within the activated anion. The energetics of the various dissociation pathways were evaluated using electronic structure calculations (G3MP2B3) in eq 9.11a-c; the differences between these calculated exothermicities are in excellent agreement with the differences in the known heats of formation of the products.



The decomposition of peroxyformic acid by means of an intramolecular hydrogen atom transfer is analogous to the decomposition of the peroxyformyl radical. In the troposphere there is evidence that the association reaction of the formyl radical with oxygen forms a highly excited peroxyformyl radical intermediate, whose subsequent decomposition forms HO₂ + CO and HO + CO₂.^{17-19,47} Several potential decomposition mechanisms have been suggested including hydrogen atom transfer to the terminal oxygen atom of the peroxy group via a cyclic transition state.⁴⁷⁻⁴⁹ Electronic structure calculations (G3MP2B3) were employed to investigate the unimolecular rearrangement of the peroxyformate ion and a similar mechanism has been found, as shown in Scheme 9.01, where hydrogen atom transfer and C-O or O-O bond cleavage occur concomitantly. Due to the strained nature of these

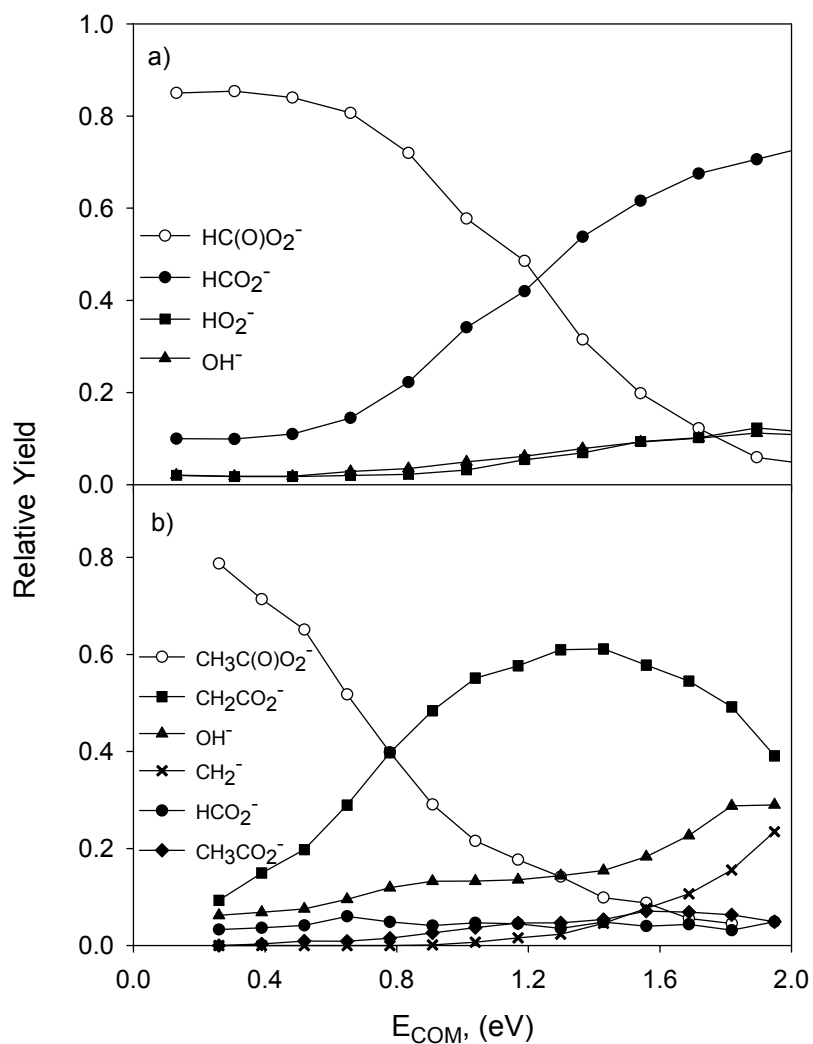
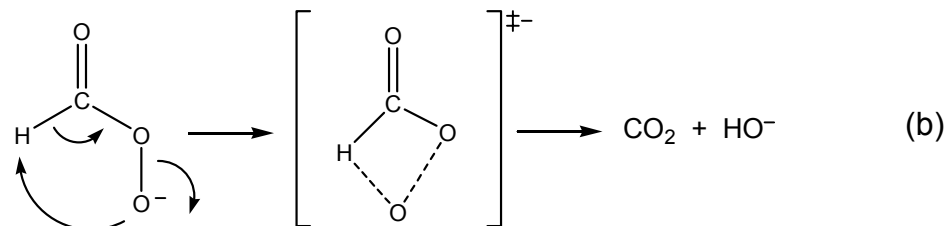
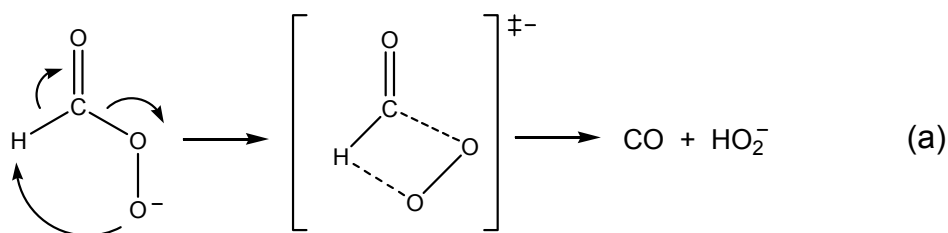


Figure 9.06: Collision Energy (E_{COM}) dependence of the relative yields of the parent and daughter ions in the CID of a) the peroxyformate anion and b) the peroxyacetate anion.

cyclic transition states, passage over the activation barrier is hindered by entropic effects. In path a, the $\angle\text{HCO}$ is 67.9° and $\angle\text{COO}$ is 103.9° in the transition state (compared to 110.7° and 112.5° in peroxyformic acid, respectively) while the CO bond increases 0.11 \AA . In path b the $\angle\text{HCO}$ is 75.9° and $\angle\text{COO}$ is 96.9° in the transition state while the OO bond increases 0.25 \AA . The barrier heights for the two channels are approximately equal, therefore, despite the difference in the reaction exothermicities, the branching fractions are approximately equal.

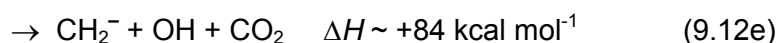
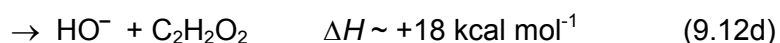
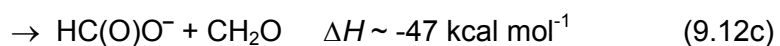
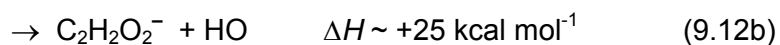
Scheme 9.01



The relative yields of the fragment ions that result from the CID of the peroxyacetate ion (eq 9.12a-e) are shown in Figure 9.06b. In analogy to the CID of the peroxy-formate ion, one would expect that the major fragmentation pathway would be O atom loss to form the acetate ion. While this pathway is observed (path 0.12a), it is a very minor process. Instead, the major ionic products formed are HO^- and $\text{C}_2\text{H}_2\text{O}_2^-$ (m/z 58), both of which result from an intramolecular hydrogen atom transfer. As the injection voltage is increased, the $\text{C}_2\text{H}_2\text{O}_2^-$ signal peaks around $E_{\text{COM}} = 1.4 \text{ eV}$ then decreases. The falloff of the $\text{C}_2\text{H}_2\text{O}_2^-$ anion correlates with the formation of CH_2^- , which is likely due to the elimination of CO_2 from the nascent

$C_2H_2O_2^-$ species. A minor amount of m/z 45 is observed, which presumably is the formate ion. The mechanism responsible for the formation of this ion is uncertain; however, one possibility is that the peroxyacetate ion rearranges to form the corresponding methyldioxiranol ion, which eliminates formaldehyde.

The calculated energetics of the various pathways are shown below:



In contrast to the CID of the peroxyformate ion, the decomposition of peroxyacetate ion primarily occurs by unimolecular rearrangement rather than by direct dissociation. In this case, intramolecular hydrogen atom transfer to the terminal oxygen atom of the peroxy group proceeds via a five-membered ring where there is considerably less strain than in the analogous four-membered cyclic-peroxyformate transition state. When entropic effects are considered, both cyclic-peroxyformate transition states are higher in energy than the direct dissociation channel. In contrast, the cyclic-peroxyacetate transition state is lower in energy than the direct dissociation channel, promoting the hydrogen atom transfer induced dissociation of the activated anion.

9.3.5) Gas-Phase Acidity Measurements

The gas-phase acidities of peroxyformic acid and peroxyacetic acid were determined by ion-molecule bracketing experiments. This method is employed when proton transfer equilibrium constant measurements are not feasible; in this case, the peracid neutral reagent is not available in pure form. In the ion-molecule bracketing

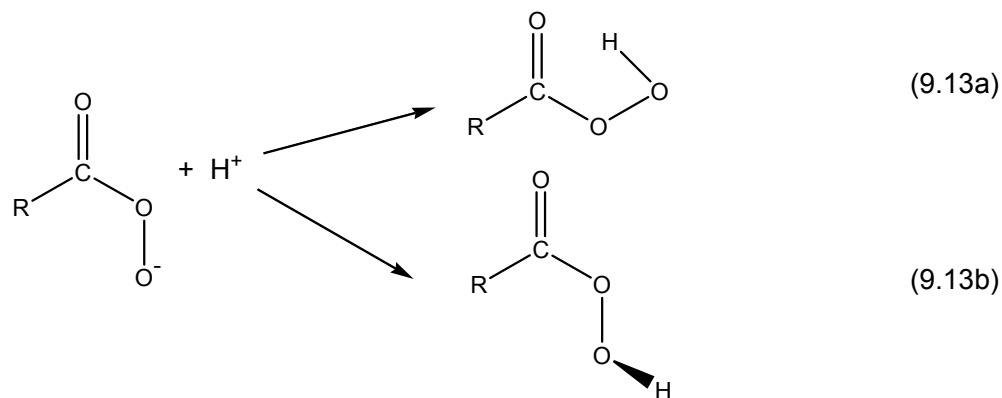
technique, the acyl peroxy anion is allowed to react with a series of reference acids and the occurrence or nonoccurrence of proton transfer sets a lower or upper bound on the unknown acidity, respectively. For these bracketing experiments, the acylperoxy anions were formed in the same manner as described above.

The gas-phase acidity of peroxyformic acid was bracketed against five reference acids: formic acid ($338.6 \pm 0.5 \text{ kcal mol}^{-1}$), acetic acid ($341.2 \pm 0.5 \text{ kcal mol}^{-1}$), hydrogen sulfide ($344.89 \pm 0.02 \text{ kcal mol}^{-1}$), *tert*-butylthiol ($344.3 \pm 3.3 \text{ kcal mol}^{-1}$), and *iso*-propylthiol ($348.4 \pm 0.5 \text{ kcal mol}^{-1}$).³⁸ For the reactions of peroxyformate anion with *tert*-butylthiol and *iso*-propylthiol, proton transfer did not occur; instead these reactions proceed exclusively by neutral O atom loss to form the formate anion. Proton transfer was the only pathway observed in the reactions of peroxyformate anion with formic acid and acetic acid. For the reaction with formic acid, proton transfer was confirmed by evaluating the reaction with formic acid-*d*1, DCO₂H. In this case, an observed increase in *m/z* 46 is due to proton transfer, whereas the absence of *m/z* 45 indicates that neutral O atom loss from the peroxyformate anion does not occur. The reaction with hydrogen sulfide primarily proceeds by O atom loss to form the formate ion. Only a minor amount of the proton transfer product, HS⁻, was observed, indicating that proton transfer pathway is slightly endothermic. Based on these results, the acidity of peroxyformic acid is found to be $\Delta_a G_{298} = 344.3 \pm 3.3 \text{ kcal mol}^{-1}$, between that of acetic acid and *tert*-butylthiol.

The gas-phase acidity of peroxyacetic acid was also bracketed against five reference acids: formic acid, acetic acid, hydrogen sulfide, *tert*-butylthiol, and ethanethiol ($348.4 \pm 0.5 \text{ kcal mol}^{-1}$).³⁸ Proton transfer was not observed in the reactions of peroxyacetate anion with *tert*-butylthiol and ethanethiol; instead these reactions proceed via neutral O atom loss to form the acetate anion. Proton transfer was observed in the reactions of formic acid and acetic acid. For the latter reaction,

the occurrence of proton transfer was confirmed by evaluating the reaction with acetic acid-*d*3, CD₃CO₂H, where the formation of *m/z* 62, instead of *m/z* 59, is consistent with proton transfer. The reaction with hydrogen sulfide produces small amounts of the proton transfer product in addition to the O atom transfer product, suggesting that this reaction is slightly endothermic. Similar to the acidity of peroxyformic acid, the acidity of peroxyacetic acid is determined to be between that of acetic acid and *tert*-butylthiol at $\Delta_a G_{298} = 344.3 \pm 3.3 \text{ kcal mol}^{-1}$.

While these acidity bracketing experiments are simple in their implementation, the interpretation of these results is complicated by the significant structural differences between the peroxy anion and the corresponding acid. As discussed above, the lowest energy structure of the peroxyacids is a *cis*-planar conformer where a strong intramolecular hydrogen bond exists between the peroxy hydrogen atom and the carbonyl oxygen atom.³²⁻³⁴ Rotation about the OCOO dihedral angle by 180° gives a higher energy *trans*-conformation, where the peroxy hydrogen atom points out of the plane of symmetry. In contrast, the *trans*-conformer of the anion is the lower energy structure, as was spectroscopically confirmed in the experiments described above. Thus, protonation of the anion initially forms the higher energy *trans*-conformation of the acid. Since a significant (*trans* to *cis*) isomerization barrier exists in these peroxyacids systems, the reaction may not contain enough energy for the acid to isomerize to the lower energy *cis*-conformer. Thus, it is not immediately clear whether the above gas-phase acidity measurements probe the *cis*- or *trans*-form of the acid, eq 9.13a and b, respectively.



Whether proton transfer leads to the formation of the *cis*- or *trans*-form of the acid depends on the size of the isomerization barrier and on the overall energetics of the proton transfer reaction; this is qualitatively demonstrated in Figure 9.07. For each potential energy surface the total energy of the reaction is given by the dotted line and the enthalpies of reaction for the *trans*- and *cis*-product channels are indicated. As the strength of the reference acid decreases in going from a to d in Figure 9.07, the reaction exothermicity decreases; however, the relative energetics of the two product channels remain constant. If proton transfer is sufficiently exothermic (a), then the *trans*-form of the acid can traverse the isomerization barrier to form the lower energy *cis*-structure. However, as the strength of the reference acid decreases (b), the reaction complex does not contain sufficient energy and the acid cannot surmount the isomerization barrier. In this scenario, proton transfer exclusively leads to the formation of the *trans*-form of the acid, even though the *cis*-product channel is more exothermic. Similarly, as the strength of the reference acid is further decreased such that the formation of the *trans*-form of the acid is endothermic (c), the reaction does not occur even though the *cis*-product channel is still exothermic. Of course, the reaction will also not occur if both product channels are endothermic (d).

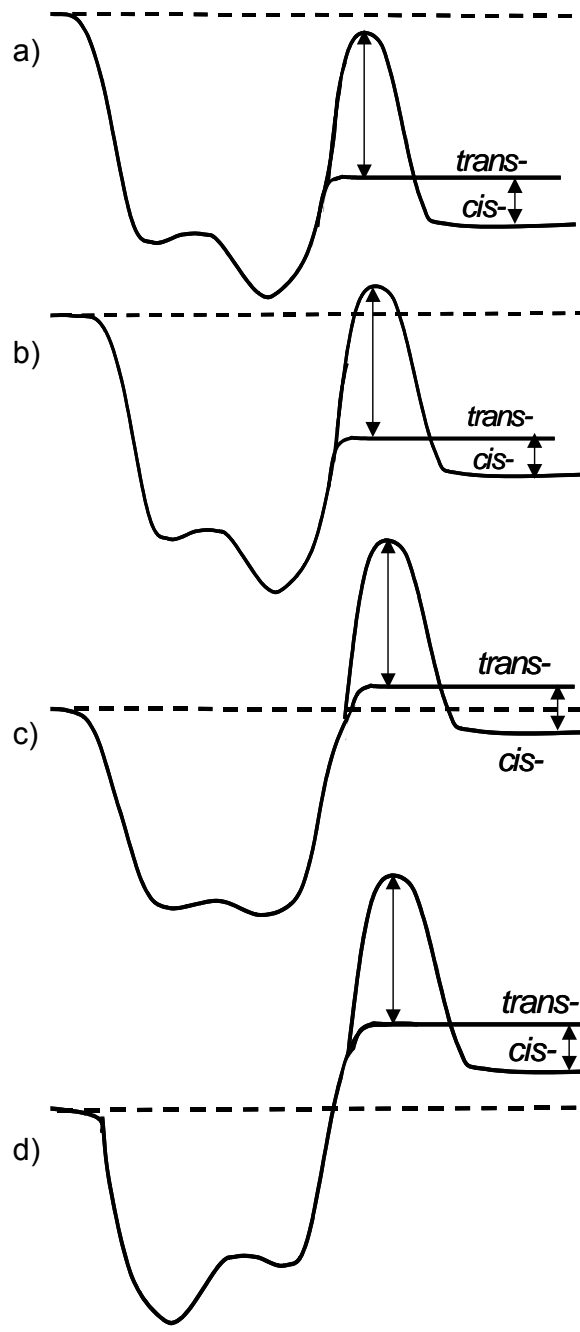


Figure 9.07: Representative potential energy surfaces for the proton transfer reaction of the *trans*-conformer of the acylperoxy ion with a reference acid where a) the reaction is exothermic and both the *trans*- and *cis*-peroxyacids are formed, b) the reaction is exothermic and only the *trans*-peroxyacid is formed, c) formation of the *cis*-peroxyacid is exothermic, however, no reaction occurs, and d) the reaction is endothermic.

For peroxyformic acid, the *trans*-conformer is 3.4 kcal mol⁻¹ higher in energy than the *cis*-conformer; these two minima are connected by a ~11.1 kcal mol⁻¹ (*trans* to *cis*) barrier (see Table 9.02). For peroxyacetic acid, the energy difference between the *trans*- and *cis*-conformer increases to 5.5 kcal mol⁻¹ and a ~8.6 kcal mol⁻¹ barrier connects the two minima. Since the difference in the acidities of the upper and lower bound reference acids is smaller than the isomerization barrier, the above acidity measurements of $\Delta_a G_{298} = 344.3 \pm 3.3$ kcal mol⁻¹ correspond to the *trans*-form of the acids. Thus, these bracketing experiments probe the gas-phase acidity of the higher energy conformer of the acylperoxy acids. This is consistent with computations, which find that the gas-phase acidity of *trans*-peroxyformic acid is 342.2 kcal mol⁻¹ while *trans*-peroxyacetic acid is 343.8 kcal mol⁻¹. The calculated acidities of the *cis*-conformers are 345.0 kcal mol⁻¹ and 349.1 kcal mol⁻¹, respectively, which are inconsistent with the experimental data.

It should be noted that a similar scenario would exist for the reverse gas-phase acidity bracket, where the pure neutral acylperoxy acid is reacted with a series of reference anions of known basicity. In this case, the acylperoxy acid is overwhelmingly in the *cis*-conformation.^{32,33} Proton abstraction would initially result in the formation of the *cis*-conformer of the anion, which then would have to surmount a significant isomerization barrier (Table 9.02) to form the lower energy *trans*-conformer. This acidity bracket would, therefore, probe the gas-phase basicity of the *cis*-conformer of the acylperoxy anion.

Given the complex nature of these acylperoxide systems it seems that the most feasible approach to determine the gas-phase acidity of the lower energy conformer of the *cis*-peroxy acid is through a calculated correction factor that reflects the relative stability of the *cis*- and *trans*-conformers (Table 9.02). In this case, computations are expected to accurately predict this relative stability since the

systematic errors from the *ab initio* method are likely similar for both conformers and, therefore, cancel out in the energy difference. Based on this, the gas-phase acidity is determined to be 347.1 ± 3.3 kcal mol⁻¹ for *cis*-peroxyformic acid and 349.6 ± 3.3 kcal mol⁻¹ for *cis*-peroxyacetic acid. Combining these results with the calculated entropies of deprotonation ($\Delta_a S_{298}$) allows for the determination of the enthalpy of deprotonation: $\Delta_a H_{298}(\textit{cis}\text{-HC(O)OOH}) = 354.7 \pm 3.3$ kcal mol⁻¹; $\Delta_a H_{298}(\textit{trans}\text{-HC(O)OOH}) = 351.3 \pm 3.3$ kcal mol⁻¹; $\Delta_a H_{298}(\textit{cis}\text{-CH}_3\text{C(O)OOH}) = 356.5 \pm 3.3$ kcal mol⁻¹; $\Delta_a H_{298}(\textit{trans}\text{-CH}_3\text{C(O)OOH}) = 351.0 \pm 3.3$ kcal mol⁻¹.

9.3.6) Thermochemistry

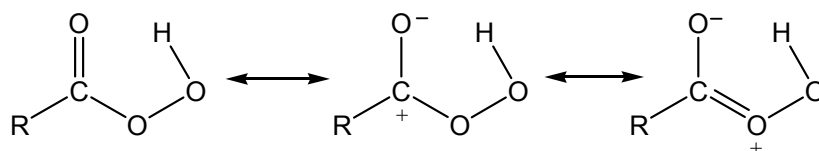
Sound knowledge of the peroxide O-H bond dissociation energies (BDE, D_0) is important to atmospheric and low-temperature combustion processes.^{50,51} The O-H BDE of peroxyformic acid and peroxyacetic acid can be determined from the above electron affinity and enthalpy of deprotonation measurements using a negative ion thermochemical cycle,^{52,53} eq 9.14, as discussed in Chapter 1.

$$D_0(\text{RC(O)OOH}) = \Delta_a H_0(\text{RC(O)OOH}) + \text{EA}(\text{RC(O)OO}) - \text{IE}(\text{H}) \quad (9.14)$$

Here, R = H and CH₃, $\Delta_a H_0(\text{RC(O)OOH})$ is the O-H deprotonation enthalpy of the peroxy acid at 0 K (a small conversion was applied to convert $\Delta_a H_0$ to $\Delta_a H_{298}$),⁵⁴ EA(RC(O)OO) is the electron affinity of the peroxy radical, and IE(H) is the ionization energy of the hydrogen atom (13.59844 eV).⁵⁵ From the data determined here, the BDEs of both the *cis*- and *trans*-conformers of the peroxyacids can be determined. For both cases, cleavage of the O-H bond results in the formation of the *trans*-form of the radical. The $D_0(\text{O-H})$ for the *cis*-conformer of peroxyformic acid and peroxyacetic acid is determined to be 98.0 ± 3.3 kcal mol⁻¹ and 97.5 ± 3.3 kcal mol⁻¹, respectively, while the BDEs for the *trans*-conformers were determined to be 95.7 ± 3.3 kcal mol⁻¹ and 93.0 ± 3.3 kcal mol⁻¹, respectively. The uncertainty in the BDE

measurements mainly reflects the error in the gas-phase acidity measurements. These BDEs, as well as other thermochemical values reported in this work, are summarized in Table 9.07.

The O-H BDEs of these peroxyacids are significantly larger than that of hydrogen peroxide and of alkyl peroxides, which range from 84-87 kcal mol⁻¹ (see Table 9.01). Simple peroxy radicals such as the hydrogen peroxy and methyl peroxy radicals have C_s symmetry. In the corresponding peroxide, the peroxy hydrogen atom points out of the ROO plane of symmetry, minimizing the repulsive interaction between the O-H bonding orbital and lone pair of electrons on the neighboring oxygen atom. In contrast, the lowest energy of peroxyacids is planar, due to the strong intramolecular hydrogen bond that is formed between the peroxy hydrogen atom and the carbonyl oxygen atom. The formation of this intramolecular hydrogen bond increases the O-H bond strength relative to that of alkyl peroxides, by ~3-4 kcal mol⁻¹; the difference between the *cis* and *trans* O-H BDEs reflects the strength of this hydrogen bond. Furthermore, the acyl peroxide is stabilized by the electron withdrawing effects of the carbonyl group. To illustrate this, consider a resonance structure, where there is a partial positive charge on the neighboring oxygen atom (shown below), which reduces the unfavorable lone pair-bond pair



interaction. Cleavage of the O-H bond not only breaks the hydrogen bond but also elongates the C-OO bond (by ~0.1 Å, see tables 9.03 and 9.04), reducing the C-OO double character. Thus, the increased bond strength of these peroxyacids is due to back-bonding and hydrogen bonding effects, which stabilize the peroxyacids relative to an alkyl peroxide. Similar back-bonding interaction stabilizes these acyl peroxy

Table 9.07: Thermochemical Parameters.

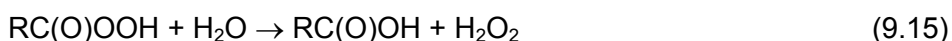
<i>Peroxyformyl Radical and Peroxyformic Acid</i>	
EA(HC(O)OO) ^a	2.493 ± 0.006 eV
T _e $\tilde{A} - \tilde{X}$ (HC(O)OO) ^a	0.784 ± 0.045 eV
$\Delta_a G_{298}(\textit{trans}\text{-HC(O)OO-H})^{b,c}$	344.3 ± 3.3 kcal mol ⁻¹
$\Delta_a G_{298}(\textit{cis}\text{-HC(O)OO-H})^{d,c}$	347.1 ± 3.3 kcal mol ⁻¹
$\Delta_a S_{298}(\textit{trans}\text{-HC(O)OO-H})^{e,c}$	23.7 cal mol ⁻¹ K ⁻¹
$\Delta_a S_{298}(\textit{cis}\text{-HC(O)OO-H})^{e,c}$	25.5 cal mol ⁻¹ K ⁻¹
$\Delta_a H_{298}(\textit{trans}\text{-HC(O)OO-H})^{f,c}$	351.3 ± 3.3 kcal mol ⁻¹
$\Delta_a H_{298}(\textit{cis}\text{-HC(O)OO-H})^{f,c}$	354.7 ± 3.3 kcal mol ⁻¹
$D_0(\textit{trans}\text{-HC(O)OO-H})^{g,c}$	95.7 ± 3.3 kcal mol ⁻¹
$D_0(\textit{cis}\text{-HC(O)OO-H})^{g,c}$	98.0 ± 3.3 kcal mol ⁻¹
<i>Peroxyacetyl Radical and Peroxyacetic Acid</i>	
EA(CH ₃ C(O)OO) ^a	2.381 ± 0.007 eV
T _e $\tilde{A} - \tilde{X}$ (CH ₃ C(O)OO) ^{a,h}	0.69214 ± 0.00006 eV
$\Delta_a G_{298}(\textit{trans}\text{-CH}_3\text{C(O)OO-H})^{b,c}$	344.3 ± 3.3 kcal mol ⁻¹
$\Delta_a G_{298}(\textit{cis}\text{-CH}_3\text{C(O)OO-H})^{d,c}$	349.6 ± 3.3 kcal mol ⁻¹
$\Delta_a S_{298}(\textit{trans}\text{-CH}_3\text{C(O)OO-H})^{e,c}$	22.4 cal mol ⁻¹ K ⁻¹
$\Delta_a S_{298}(\textit{cis}\text{-CH}_3\text{C(O)OO-H})^{e,c}$	23.1 cal mol ⁻¹ K ⁻¹
$\Delta_a H_{298}(\textit{trans}\text{-CH}_3\text{C(O)OO-H})^{f,c}$	351.0 ± 3.3 kcal mol ⁻¹
$\Delta_a H_{298}(\textit{cis}\text{-CH}_3\text{C(O)OO-H})^{f,c}$	356.5 ± 3.3 kcal mol ⁻¹
$D_0(\textit{trans}\text{-CH}_3\text{C(O)OO-H})^{g,c}$	93.0 ± 3.3 kcal mol ⁻¹
$D_0(\textit{cis}\text{-CH}_3\text{C(O)OO-H})^{g,c}$	97.5 ± 3.3 kcal mol ⁻¹

^a For *trans*-conformer of radical. ^b Bracketed between the acidity of acetic acid and *tert*-butylthiol. ^c Defined as the energy to go from the stated reactant to the lowest energy *trans*-conformer of the anion or radical. ^d Determined from the *trans*-peroxyacid acidity and a the calculated energy difference between *cis*- and *trans*-conformers. ^e Computationally determined. ^f Calculated from the corresponding $\Delta_a G_{298}$ and $\Delta_a S_{298}$. ^g Calculated using the EA, $\Delta_a H_{298}$, IE(H), and a small thermochemical correction (see reference 54) to bring the enthalpy of deprotonation to 0 K.

^h Reference 13; T_e $\tilde{A} - \tilde{X}$ = 0.691 ± 0.009 eV, this work.

anions relative to that of an alkyl peroxy anion. As a result, the enthalpy of deprotonation of these acyl peroxides is less than that of an alkyl peroxide while the electron affinity of these acyl peroxy radicals is higher than that of an alkyl peroxy radical.

It is surprising, given the importance of these peroxyacids, that their heats of formation have not been experimentally determined. Using G3MP2B3 calculations, we have calculated the heats of formation of peroxyformic acid and peroxyacetic acid from the following isodesmic reaction:



In eq 9.15, the heat of formation of the peroxyacid is determined from the calculated heat of reaction and the known heats of formation of the other three compounds.⁵⁶ Since the bonding environments in the reactants and products are similar, the systematic errors from the *ab initio* method cancel and, therefore, this method is expected to produce reasonably good heats of formation for closed shell species.

Using this method, the heat of formation at 298 K of *cis*-peroxyformic acid was determined to be $-69.0 \pm 1.2 \text{ kcal mol}^{-1}$. This value is slightly less than the CCSD(T)/CBS atomization energy calculation of Feller *et al.*;⁵⁷ however, the difference in these two values is equal to the relative stability of the *cis*- and *trans*-conformers and, therefore, it is unclear to which conformer Feller's value applies. The heat of formation of the *cis*-peroxyacetic acid was found to be $-83.2 \pm 1.2 \text{ kcal mol}^{-1}$, in good agreement with the calculations of Bozzelli *et al.*⁵⁸ and Benassi *et al.*⁵⁹ The heat of formation of the acyl peroxy radicals can be determined from the calculated heats of formation of the acyl peroxides and the above O-H BDEs measurements (see Chapter 1). The heat of formation of the formyl peroxy radical is determined to be $-22.5 \pm 4.5 \text{ kcal mol}^{-1}$ while the acetyl peroxy radical is found to be $-37.3 \pm 4.5 \text{ kcal mol}^{-1}$.

9.4) Conclusions

The 351.1 nm photoelectron spectrum of the peroxyformate anion was measured and the EA of the *trans*-peroxyformyl radical was determined to be 2.493 ± 0.006 eV and the T_e of the \tilde{A}^2A' state is 0.784 ± 0.045 eV. In the \tilde{X}^2A'' state of the peroxyformyl radical, the harmonic frequency and anharmonicity correction are $\omega_5 = 973 \pm 20$ cm⁻¹ and $\chi_5 = 4 \pm 3$ cm⁻¹ for the ν_5 OO stretch and $\omega_4 = 1098 \pm 20$ cm⁻¹ and $\chi_4 = 10 \pm 5$ cm⁻¹ for the ν_4 OCOO backbone deformation. The fundamental frequency of the in plane OCO bend is 574 ± 35 cm⁻¹. The gas-phase acidity of *trans*-peroxyformic acid was bracketed between the acidity of acetic acid and *tert*-butylthiol, $\Delta_a G_{298}(\textit{trans}\text{-peroxyformic acid}) = 344.3 \pm 3.3$ kcal mol⁻¹ and $\Delta_a H_{298}(\textit{trans}\text{-peroxyformic acid}) = 351.3 \pm 3.3$ kcal mol⁻¹. The gas-phase acidity of *cis*-peroxyformic acid was found from the *trans*-conformer acidity and a calculated energy correction to be $\Delta_a G_{298}(\textit{cis}\text{-peroxyformic acid}) = 347.1 \pm 3.3$ kcal mol⁻¹ and $\Delta_a H_{298}(\textit{cis}\text{-peroxyformic acid}) = 354.7 \pm 3.3$ kcal mol⁻¹. The O-H BDE for both the *cis*- and *trans*-conformers were determined using negative ion thermodynamic cycle to be $D_0(\textit{trans}\text{-peroxyformic acid}) = 95.7 \pm 3.3$ kcal mol⁻¹ and $D_0(\textit{cis}\text{-peroxyformic acid}) = 98.0 \pm 3.3$ kcal mol⁻¹.

The 351.1 nm photoelectron spectrum of the peroxyacetate anion was measured and is in good agreement with the calculated FC factors for the \tilde{X}^1A' state of the anion to the \tilde{X}^2A'' and \tilde{A}^2A' states of the peroxyacetyl radical. The EA of the radical is 2.381 ± 0.008 eV and the T_e of the \tilde{A}^2A' states is 0.691 ± 0.009 eV, which is in excellent agreement with two prior values.¹³⁻¹⁵ The gas-phase acidity of *trans*-peroxyacetic acid was bracketed between the acidity of acetic acid and *tert*-butylthiol, $\Delta_a G_{298}(\textit{trans}\text{-peroxyacetic acid}) = 344.3 \pm 3.3$ kcal mol⁻¹ and $\Delta_a H_{298}(\textit{trans}\text{-peroxyacetic acid}) = 351.0 \pm 3.3$ kcal mol⁻¹. The acidity of *cis*-peroxyacetic acid was

found by adding a calculated energy correction to the acidity of *trans*-conformer; $\Delta_a G_{298}(\text{cis-peroxyacetic acid}) = 349.6 \pm 3.3 \text{ kcal mol}^{-1}$ and $\Delta_a H_{298}(\text{cis-peroxyacetic acid}) = 356.5 \pm 3.3 \text{ kcal mol}^{-1}$. The O-H BDE for both conformers were determined using negative ion thermodynamic cycle to be $D_0(\text{trans-peroxyacetic acid}) = 93.0 \pm 3.3 \text{ kcal mol}^{-1}$ and $D_0(\text{cis-peroxyacetic acid}) = 97.5 \pm 3.3 \text{ kcal mol}^{-1}$.

9.5) Acknowledgements

This work benefited from the contributions of Ms. Nicole Eyet, Mr. Scott W. Wren, Ms. Kristen M Vogelhuber, Prof. Veronica M. Bierbaum, Prof. W. Carl Lineberger, and Prof. G. Barney Ellison. Additionally, I would like to thank Prof. Charles H. DePuy, Prof. Kent Ervin, Prof. John F. Stanton, Prof. Stephen J. Blanksby, Dr. Bradley A. Flowers, and Dr. Shuji Kato for providing useful comments. This work was supported by the AFOSR (FA9550-06-1-006). The computational results are based upon work supported by the National Science Foundation under the following NSF programs: Partnerships for Advanced Computational Infrastructure, Distributed Terascale Facility (DTF) and Terascale Extensions: Enhancements to the Extensible Terascale Facility.

9.6) Chapter 9 References

- (1) Lightfoot, P. D.; Cox, R. A.; Crowley, J. N.; Destriau, M.; Hayman, G. D.; Jenkin, M. E.; Moortgat, G. K.; Zabel, F. Organic Peroxy-Radicals - Kinetics, Spectroscopy and Tropospheric Chemistry. *Atmospheric Environment Part A-General Topics* **1992**, *26*, 1805-1961.
- (2) Madronich, S.; Greenberg, J.; Paulson, S. Atmospheric Chemistry and Global Change; G. P. Brasseur, J. J. Orlando and G. S. Tyndall, Eds.; Oxford University Press: New York, 1999; pp 325.
- (3) Le Bras, G. Chemical Processes in Atmospheric Oxidation G. Le Bras, Ed.; Springer: Berlin, 1997; pp 13.
- (4) Kirchner, F.; Stockwell, W. R. Effect of Peroxy Radical Reactions on the Predicted Concentrations of Ozone, Nitrogenous Compounds, and Radicals. *Journal of Geophysical Research-Atmospheres* **1996**, *101*, 21007-21022.
- (5) FinlaysonPitts, B. J.; Pitts, J. N. Tropospheric air pollution: Ozone, airborne toxics, polycyclic aromatic hydrocarbons, and particles. *Science* **1997**, *276*, 1045-1052.
- (6) Singh, H. B.; Herlth, D.; Ohara, D.; Zahnle, K.; Bradshaw, J. D.; Sandholm, S. T.; Talbot, R.; Crutzen, P. J.; Kanakidou, M. Relationship of Peroxyacetyl Nitrate to Active and Total Odd Nitrogen at Northern High-Latitudes - Influence of Reservoir Species on NO_x and O₃. *Journal of Geophysical Research-Atmospheres* **1992**, *97*, 16523-16530.
- (7) Roberts, J. M. The Atmospheric Chemistry of Organic Nitrates. *Atmospheric Environment Part A-General Topics* **1990**, *24*, 243-287.
- (8) Sehested, J.; Christensen, L. K.; Mogelberg, T.; Nielsen, O. J.; Wallington, T. J.; Guschin, A.; Orlando, J. J.; Tyndall, G. S. Absolute and relative rate constants for the reactions CH₃C(O)O₂ + NO and CH₃C(O)O₂ + NO₂ and thermal stability of CH₃C(O)O₂NO₂. *Journal of Physical Chemistry A* **1998**, *102*, 1779-1789.
- (9) Tomas, A.; Villenave, E.; Lesclaux, R. Reactions of the HO₂ radical with CH₃CHO and CH₃C(O)O₂ in the gas phase. *Journal of Physical Chemistry A* **2001**, *105*, 3505-3514.
- (10) Maricq, M. M.; Sente, J. J. The CH₃C(O)O₂ radical. Its UV Spectrum, Self-Reaction Kinetics, and Reaction with CH₃O₂. *Journal of Physical Chemistry* **1996**, *100*, 4507-4513.
- (11) Roehl, C. M.; Bauer, D.; Moortgat, G. K. Absorption Spectrum and Kinetics of the Acetylperoxy Radical. *Journal of Physical Chemistry* **1996**, *100*, 4038-4047.

- (12) Crawford, M. A.; Wallington, T. J.; Szente, J. J.; Maricq, M. M.; Francisco, J. S. Kinetics and Mechanism of the Acetylperoxy Plus HO₂ Reaction. *Journal of Physical Chemistry A* **1999**, *103*, 365-378.
- (13) Zalyubovsky, S. J.; Glover, B. G.; Miller, T. A. Cavity Ringdown Spectroscopy of the A-X Electronic Transition of the CH₃C(O)O₂ Radical. *Journal of Physical Chemistry A* **2003**, *107*, 7704-7712.
- (14) Hu, Y. J.; Fu, H. B.; Bernstein, E. R. Generation and Detection of the Peroxyacetyl Radical in the Pyrolysis of Peroxyacetyl Nitrate in a Supersonic Expansion. *Journal of Physical Chemistry A* **2006**, *110*, 2629-2633.
- (15) Hu, Y. J.; Fu, H. B.; Bernstein, E. R. Vibronic Spectroscopy of the Peroxyacetyl Radical in the Near IR. *Journal of Chemical Physics* **2006**, *124*, 114305/1-114305/6.
- (16) Von Ahsen, S.; Willner, H.; Francisco, J. S. Thermal Decomposition of Peroxy Acetyl Nitrate CH₃C(O)OONO₂. *Journal of Chemical Physics* **2004**, *121*, 2048-2057.
- (17) Tso, T. L.; Lee, E. K. C. Mechanism of Photooxidation of Glyoxal and Formaldehyde in Solid O₂ at 12-18 K. *Journal of Physical Chemistry* **1984**, *88*, 5465-5474.
- (18) Tso, T. L.; Diem, M.; Lee, E. K. C. Oxidation of Formyl Radical in Solid O₂ at 13 K - Formation of Formic-Acid and Formylperoxy Radical, HC(O)OO. *Chemical Physics Letters* **1982**, *91*, 339-342.
- (19) Yang, R. J.; Yu, L. A.; Zeng, A. H.; Zhou, M. F. Infrared Spectrum of the Formylperoxy Radical in Solid Argon. *Journal of Physical Chemistry A* **2004**, *108*, 4228-4231.
- (20) Bowie, J. H.; DePuy, C. H.; Sullivan, S. A.; Bierbaum, V. M. Gas-Phase Reactions of the Hydroperoxide and Peroxyformate Anions. *Canadian Journal of Chemistry-Revue Canadienne De Chimie* **1986**, *64*, 1046-1051.
- (21) Hotop, H.; Lineberger, W. C. Binding-Energies in Atomic Negative-Ions II. *Journal of Physical and Chemical Reference Data* **1985**, *14*, 731-750.
- (22) Hanstorp, D.; Gustafsson, M. Determination of the Electron-Affinity of Iodine. *Journal of Physics B-Atomic Molecular and Optical Physics* **1992**, *25*, 1773-1783.
- (23) Neumark, D. M.; Lykke, K. R.; Andersen, T.; Lineberger, W. C. Laser Photodetachment Measurement of the Electron-Affinity of Atomic Oxygen. *Physical Review A* **1985**, *32*, 1890-1892.
- (24) Blanksby, S. J.; Kato, S.; Bierbaum, V. M.; Ellison, G. B. Fragmentations of Deprotonated Alkyl Hydroperoxides (ROO⁻) Upon Collisional Activation: A Combined Experimental and Computational Study. *Australian Journal of Chemistry* **2003**, *56*, 459-472.

- (25) Kato, S.; Lineberger, W. C.; Bierbaum, V. M. Collision-Induced Dissociation of Fluoropyridinide Anions. *International Journal of Mass Spectrometry* **2007**, *266*, 166-179.
- (26) Frisch, M. J.; Trucks, G. W.; Schlegel, H. B.; Scuseria, G. E.; Robb, M. A.; Cheeseman, J. R.; Montgomery, J. A.; Vreven, T.; Kudin, K. N.; Burant, J. C.; Millam, J. M.; Iyengar, S. S.; Tomasi, J.; Barone, V.; Mennucci, B.; Cossi, M.; Scalmani, G.; Rega, N.; Petersson, G. A.; Nakatsuji, H.; Hada, M.; Ehara, M.; Toyota, K.; Fukuda, R.; Hasegawa, J.; Ishida, M.; Nakajima, T.; Honda, Y.; Kitao, O.; Nakai, H.; Klene, M.; Li, X.; Knox, J. E.; Hratchian, H. P.; Cross, J. B.; Adamo, C.; Jaramillo, J.; Gomperts, R.; Stratmann, R. E.; Yazyev, O.; Austin, A. J.; Cammi, R.; Pomelli, C.; Ochterski, J. W.; Ayala, P. Y.; Morokuma, K.; Voth, G. A.; Salvador, P.; Dannenberg, J. J.; Zakrzewski, V. G.; Dapprich, S.; Daniels, A. D.; Strain, M. C.; Farkas, O.; Malick, D. K.; Rabuck, A. D.; Raghavachari, K.; Foresman, J. B.; Ortiz, J. V.; Cui, Q.; Baboul, A. G.; Clifford, S.; Cioslowski, J.; Stefanov, B. B.; Liu, G.; Liashenko, A.; Piskorz, P.; Komaromi, I.; Martin, R. L.; Fox, D. J.; Keith, T.; Al-Laham, M. A.; C. Y. Peng; Nanayakkara, A.; Challacombe, M.; Gill, P. M. W.; Johnson, B.; Chen, W.; Wong, M. W.; Gonzalez, C.; Pople, J. A. Gaussian 03, revision B.05; I. Gaussian, Ed. Pittsburgh, PA, 2003.
- (27) Becke, A. D. Density-Functional Thermochemistry. III. The Role of Exact Exchange. *Journal of Chemical Physics* **1993**, *98*, 5648-5652.
- (28) Lee, C. T.; Yang, W. T.; Parr, R. G. Development of the Colle-Salvetti Correlation-Energy Formula into a Functional of the Electron-Density. *Physical Review B* **1988**, *37*, 785-789.
- (29) Krishnan, R.; Binkley, J. S.; Seeger, R.; Pople, J. A. Self-Consistent Molecular-Orbital Methods. XX. Basis Set for Correlated Wave-Functions. *Journal of Chemical Physics* **1980**, *72*, 650-654.
- (30) Baboul, A. G.; Curtiss, L. A.; Redfern, P. C.; Raghavachari, K. Gaussian-3 Theory Using Density Functional Geometries and Zero-Point Energies. *Journal of Chemical Physics* **1999**, *110*, 7650-7657.
- (31) Ervin, K. M.; Ramond, T. M.; Davico, G. E.; Schwartz, R. L.; Casey, S. M.; Lineberger, W. C. Naphthyl Radical: Negative Ion Photoelectron Spectroscopy, Franck-Condon Simulation, and Thermochemistry. *Journal of Physical Chemistry A* **2001**, *105*, 10822-10831.
- (32) Cugley, J. A.; Bossert, W.; Bauder, A.; Gunthard, H. H. Microwave-Spectrum, Dipole-Moment and Barrier to Internal-Rotation of Peroxyacetic Acid. *Chemical Physics* **1976**, *16*, 229-235.
- (33) Oldani, M.; Ha, T. K.; Bauder, A. Microwave-Spectrum, Dipole-Moment, and Substitution Structure of Peroxyformic Acid. *Journal of the American Chemical Society* **1983**, *105*, 360-365.
- (34) Langley, C. H.; Noe, E. A. *Ab Initio* Studies of the Conformations of Performic Acid, Peracetic Acid and Methyl Performate. *Journal of Molecular Structure-Theochem* **2004**, *682*, 215-224.

- (35) Ramond, T. M.; Blanksby, S. J.; Kato, S.; Bierbaum, V. M.; Davico, G. E.; Schwartz, R. L.; Lineberger, W. C.; Ellison, G. B. Heat of Formation of the Hydroperoxyl Radical HOO Via Negative Ion Studies. *Journal of Physical Chemistry A* **2002**, *106*, 9641-9647.
- (36) Blanksby, S. J.; Ramond, T. M.; Davico, G. E.; Nimlos, M. R.; Kato, S.; Bierbaum, V. M.; Lineberger, W. C.; Ellison, G. B.; Okumura, M. Negative-Ion Photoelectron Spectroscopy, Gas-Phase Acidity, and Thermochemistry of the Peroxyl Radicals CH₃OO and CH₃CH₂OO. *Journal of the American Chemical Society* **2001**, *123*, 9585-9596.
- (37) Kim, E. H.; Bradforth, S. E.; Arnold, D. W.; Metz, R. B.; Neumark, D. M. Study of HCO₂ and DCO₂ by Negative-Ion Photoelectron-Spectroscopy. *Journal of Chemical Physics* **1995**, *103*, 7801-7814.
- (38) Eyet, N.; Villano, S. M.; Bierbaum, V. M. Anchoring the Gas-Phase Acidity Scale: Formic Acid to Methanethiol. *International Journal of Mass Spectrometry* **2009**, *In Press*.
- (39) Wang, L. S.; Ding, C. F.; Wang, X. B.; Nicholas, J. B.; Nicholas, B. Probing the Potential Barriers and Intramolecular Electrostatic Interactions in Free Doubly Charged Anions. *Physical Review Letters* **1998**, *81*, 2667-2670.
- (40) Porter, N. A.; Yin, H. Y.; Pratt, D. A. The Peroxy Acid Dioxirane Equilibrium: Base-Promoted Exchange of Peroxy Acid Oxygens. *Journal of the American Chemical Society* **2000**, *122*, 11272-11273.
- (41) Squires, R. R. Gas-Phase Thermochemical Properties of the Bicarbonate and Bisulfite Ions. *International Journal of Mass Spectrometry and Ion Processes* **1992**, *117*, 565-600.
- (42) Pushkarsky, M. B.; Zalyubovsky, S. J.; Miller, T. A. Detection and Characterization of Alkyl Peroxy Radicals Using Cavity Ringdown Spectroscopy. *Journal of Chemical Physics* **2000**, *112*, 10695-10698.
- (43) Zalyubovsky, S. J.; Glover, B. G.; Miller, T. A.; Hayes, C.; Merle, J. K.; Hadad, C. M. Observation of the A-X Electronic Transition of the 1-C₃H₇O₂ and 2-C₃H₇O₂ Radicals Using Cavity Ringdown Spectroscopy. *Journal of Physical Chemistry A* **2005**, *109*, 1308-1315.
- (44) Just, G. M. P.; Sharp, E. N.; Zalyubovsky, S. J.; Miller, T. A. Cavity Ringdown Spectroscopy of the A-X Electronic Transition of the Phenyl Peroxy Radical. *Chemical Physics Letters* **2006**, *417*, 378-382.
- (45) Grabowski, J. J.; Cheng, X. H. Gas-Phase Formation of the Enolate Monoanion of Acetic-Acid by Proton Abstraction. *Journal of the American Chemical Society* **1989**, *111*, 3106-3108.
- (46) Reeves, C. E.; Penkett, S. A. Measurements of Peroxides and What They Tell Us. *Chemical Reviews* **2003**, *103*, 5199-5218.

- (47) Martinez-Avila, M.; Peiro-Garcia, J.; Ramirez-Ramirez, V. M.; Nebot-Gil, I. *Ab initio* study on the mechanism of the $\text{HCO} + \text{O}_2 \rightarrow \text{HO}_2 + \text{CO}$ reaction. *Chemical Physics Letters* **2003**, *370*, 313-318.
- (48) Yang, H. C.; Chen, H. L.; Ho, J. J. *Ab Initio* Study of Intramolecular Hydrogen transfer in Formylperoxy Radical. *Journal of Molecular Structure-Theochem* **2006**, *774*, 35-41.
- (49) Winter, N. W.; Goddard, W. A.; Bender, C. F. Theoretical Description of $^2\text{A}'$ and $^2\text{A}''$ States of Peroxyformyl Radical. *Chemical Physics Letters* **1975**, *33*, 25-29.
- (50) Carstensen, H. H.; Dean, A. M.; Deutschmann, O. Rate Constants for the H Abstraction from Alkanes (RH) by $\text{R}'\text{O}_2$ radicals: A Systematic Study on the Impact of R and R'. *Proceedings of the Combustion Institute* **2007**, *31*, 149-157.
- (51) Tyndall, G. S.; Cox, R. A.; Granier, C.; Lesclaux, R.; Moortgat, G. K.; Pilling, M. J.; Ravishankara, A. R.; Wallington, T. J. Atmospheric Chemistry of Small Organic Peroxy Radicals. *Journal of Geophysical Research-Atmospheres* **2001**, *106*, 12157-12182.
- (52) Blanksby, S. J.; Ellison, G. B. Bond Dissociation Energies of Organic Molecules. *Accounts of Chemical Research* **2003**, *36*, 255-263.
- (53) Berkowitz, J.; Ellison, G. B.; Gutman, D. Three Methods to Measure RH Bond-Energies. *Journal of Physical Chemistry* **1994**, *98*, 2744-2765.
- (54) Thermal Corrections for the conversion of $\Delta_a H_{298}$ to $\Delta_a H_0$: -0.44 kcal mol⁻¹ *trans*-peroxyformic acid; 0.58 kcal mol⁻¹ *cis*-peroxyformic acid; -0.65 kcal mol⁻¹ *trans*-peroxyacetic acid; 0.34 kcal mol⁻¹ *cis*-peroxyacetic acid. Thermal Corrections for the conversion of D_0 to D_{298} : -0.42 kcal mol⁻¹ *trans*-peroxyformic acid; -0.60 kcal mol⁻¹ *cis*-peroxyformic acid; -0.51 kcal mol⁻¹ *trans*-peroxyacetic acid; 0.48 kcal mol⁻¹ *cis*-peroxyacetic acid. .
- (55) *NIST Chemistry WebBook, NIST Standard Reference Database Number 69*; Linstrom, P. J.; Mallard, W. G., Eds.; National Institute of Standards and Technology: Gaithersburg MD, 20899 June 2005 (<http://webbook.nist.gov>).
- (56) $\Delta_f H_{298}(\text{H}_2\text{O}) = -57.7978 \pm 0.0096$ kcal mol⁻¹ [Cox, J.D.; Wagman, D.D.; Medvedev, V.A., CODATA Key Values for Thermodynamics, Hemisphere Publishing Corp., New York, 1984, 1.]; $\Delta_f H_{298}(\text{H}_2\text{O}_2) = -32.48 \pm 0.05$ kcal mol⁻¹ [Chase, M.W., Jr., NIST-JANAF Thermochemical Tables, Fourth Edition, J. Phys. Chem. Ref. Data, Monograph 9, 1998, 1-1951.]; $\Delta_f H_{298}(\text{HCO}_2\text{H}) = -90.51 \pm 0.60$ kcal mol⁻¹ [see Linstrom *et al.*]; $\Delta_f H_{298}(\text{CH}_3\text{CO}_2\text{H}) = -103.56 \pm 0.32$ kcal mol⁻¹ [see Linstrom *et al.*].
- (57) Feller, D.; Dixon, D. A.; Francisco, J. S. Coupled Cluster Theory Determination of the Heats of Formation of Combustion-Related Compounds: CO, HCO, CO₂, HCO₂, HOCO, HC(O)OH, and HC(O)OOH. *Journal of Physical Chemistry A* **2003**, *107*, 1604-1617.

(58) Bozzelli, J. W.; Sheng, C.; Chen, C. J.; Dean, A. M. Thermochemistry and Kinetics for Alkyl Plus O₂ Reactions in Hydrocarbon Oxidation. *Abstracts of Papers of the American Chemical Society* **2002**, 223, U571-U572.

(59) Benassi, R.; Taddei, E. Homolytic Bond Dissociation in Peroxides, Peroxyacids, Peroxyesters and Related Radicals - *Ab Initio* MO Calculations. *Tetrahedron* **1994**, 50, 4795-4810.

Bibliography:

- (1) Agarwala, R.; Azam, K. A.; Dilshad, R.; Kabir, S. E.; Miah, R.; Shahiduzzaman, M.; Hardcastle, K. I.; Rosenberg, E.; Hursthouse, M. B.; Malik, K. M. A. Triosmium and Triruthenium Clusters Containing Diazaheterocycles. *Journal of Organometallic Chemistry* **1995**, *492*, 135-144.
- (2) Ahmad, Z.; Sharma, S.; Khuller, G. K. Azole Antifungals as Novel Chemotherapeutic Agents Against Murine Tuberculosis. *FEMS Microbiol. Lett.* **2006**, *261*, 181-186.
- (3) Angel, L. A.; Ervin, K. M. Gas-phase S_N2 and Bromine Abstraction Reactions of Chloride Ion with Bromomethane: Reaction Cross Sections and Energy Disposal Into Products. *Journal of the American Chemical Society* **2003**, *125*, 1014-1027.
- (4) Babcock, L. M.; Streit, G. E. Ion-Molecule Reactions of SF₆⁻: Determination of I.P.(SF₅), A.P.(SF₅⁺/SF₆), and D(SF₅-F). *Journal of Chemical Physics* **1981**, *74*, 5700-5706.
- (5) Babich, I. V.; Seshan, K.; Lefferts, L. Nature of Nitrogen Species in Coke and Their Role in NO_x Formation During FCC Catalyst Regeneration. *Applied Catalysis B-Environmental* **2005**, *59*, 205-211.
- (6) Baboul, A. G.; Curtiss, L. A.; Redfern, P. C.; Raghavachari, K. Gaussian-3 Theory Using Density Functional Geometries and Zero-Point Energies. *Journal of Chemical Physics* **1999**, *110*, 7650-7657.
- (7) Baer, T.; Hase, W. L. Unimolecular Reaction Dynamics: Theory and Experiment; Oxford University Press: New York, 1996.
- (8) Baird, N. C.; Taylor, K. F. Multiplicity of Ground-State and Magnitude of T1-S0 Gap in Substituted Carbenes. *Journal of the American Chemical Society* **1978**, *100*, 1333-1338.
- (9) Barckholtz, C.; Barckholtz, T. A.; Hadad, C. M. C-H and N-H Bond Dissociation Energies of Small Aromatic Hydrocarbons. *Journal of the American Chemical Society* **1999**, *121*, 491-500.
- (10) Bartmess, J. E.; Hays, R. L.; Khatri, H. N.; Misra, R. N.; Wilson, S. R. Elimination, Fragmentation, and Proton-Transfer in 1,3-Dithianes and 1,3-Dithiolanes in the Gas-Phase. *Journal of the American Chemical Society* **1981**, *103*, 4746-4751.
- (11) Baschky, M. C.; Peterson, K. C.; Kass, S. R. Stereospecificity in the Gas-Phase - Formation and Characterization of Configurationally Stable Cyclopropyl Anions. *Journal of the American Chemical Society* **1994**, *116*, 7218-7224.

- (12) Bass, L.; Su, T.; Chesnavich, W. J.; Bowers, M. T. Ion-Polar Molecule Collisions - Modification of Average Dipole Orientation Theory: The $\cos\theta$ Model. *Chemical Physics Letters* **1975**, *34*, 119-122.
- (13) Bauman, R. P.; Bulkin, B. J. Spectra and Structure of Perfluorocyclobutane. *Journal of Chemical Physics* **1966**, *45*, 496-498.
- (14) Beagley, B.; Calladine, R.; Pritchard, R. G.; Taylor, S. F. The Molecular-Structure of Perfluoro-Thiirane in the Presence of Perfluoro-Cyclobutane - a Gas-Phase Electron-Diffraction Study. *Journal of Molecular Structure* **1987**, *158*, 309-314.
- (15) Becke, A. D. Density-Functional Thermochemistry. III. The Role of Exact Exchange. *Journal of Chemical Physics* **1993**, *98*, 5648-5652.
- (16) Benassi, R.; Taddei, E. Homolytic Bond Dissociation in Peroxides, Peroxyacids, Peroxyesters and Related Radicals - *Ab Initio* MO Calculations. *Tetrahedron* **1994**, *50*, 4795-4810.
- (17) Berkowitz, J.; Ellison, G. B.; Gutman, D. Three Methods to Measure RH Bond-Energies. *Journal of Physical Chemistry* **1994**, *98*, 2744-2765.
- (18) Bernath, P. F. Spectra of Atoms and Molecules; Oxford University Press: New York, 1995.
- (19) Bierbaum, V. M.; DePuy, C. H.; Shapiro, R. H. Gas-Phase Reactions of Anions with Nitrous-Oxide and Carbon-Dioxide. *Journal of the American Chemical Society* **1977**, *99*, 5800-5802.
- (20) Bierbaum, V. M.; Filley, J.; DePuy, C. H.; Jarrold, M. F.; Bowers, M. T. Kinetic Isotope Effect in Gas-Phase Base-Induced Elimination-Reactions. *Journal of the American Chemical Society* **1985**, *107*, 2818-2820.
- (21) Bierbaum, V. M.; Grabowski, J. J.; DePuy, C. H. Gas-Phase Synthesis and Reactions of Nitrogen-Containing and Sulfur-Containing Anions. *Journal of Physical Chemistry* **1984**, *88*, 1389-1393.
- (22) Birchall, J. M.; Haszeldine, R. N.; Tisington, P. *Journal of the Society of Perkins Transactions 1* **1975**, 1975, 1638.
- (23) Blake, T.; Glendening, E.; Sams, R.; Sharpe, S.; Xantheas, S. High-Resolution Infrared Spectroscopy in the 1200-1300 cm^{-1} Region and Accurate Theoretical Estimates for the Structure and Ring-Puckering Barrier of Perfluorocyclobutane. *Journal of Physical Chemistry A* **2007**, *111*, 11328-11341.
- (24) Blank, D. A.; North, S. W.; Lee, Y. T. The Ultraviolet Photodissociation Dynamics of Pyrrole. *Chemical Physics* **1994**, *187*, 35-47.

- (25) Blanksby, S. J.; Ellison, G. B. Bond Dissociation Energies of Organic Molecules. *Accounts of Chemical Research* **2003**, *36*, 255-263.
- (26) Blanksby, S. J.; Kato, S.; Bierbaum, V. M.; Ellison, G. B. Fragmentations of Deprotonated Alkyl Hydroperoxides (ROO⁻) Upon Collisional Activation: A Combined Experimental and Computational Study. *Australian Journal of Chemistry* **2003**, *56*, 459-472.
- (27) Blanksby, S. J.; Ramond, T. M.; Davico, G. E.; Nimlos, M. R.; Kato, S.; Bierbaum, V. M.; Lineberger, W. C.; Ellison, G. B.; Okumura, M. Negative-Ion Photoelectron Spectroscopy, Gas-Phase Acidity, and Thermochemistry of the Peroxyl Radicals CH₃OO and CH₃CH₂OO. *Journal of the American Chemical Society* **2001**, *123*, 9585-9596.
- (28) Bohme, D. K. Carbene Chemistry of Cations: The Chemistry of the Carbene Cation C₃H⁺ in the Gas Phase *Journal of the American Chemical Society* **1983**, *105*, 5481-5483.
- (29) Bohme, D. K.; Young, L. B. Kinetic Studies of Reactions of Oxide, Hydroxide, Alkoxide, Phenyl, and Benzylic Anions with Methyl Chloride in Gas Phase at 22.5°. *Journal of the American Chemical Society* **1970**, *92*, 7354-7358.
- (30) Bolden, R. C.; Hemsforth, R. S.; Shaw, M. J.; Twiddy, N. D. Measurements of Thermal-Energy Ion-Neutral Reaction Rate Coefficients for Rare-Gas Ions. *Journal of Physics Part B - Atomic and Molecular Optical Physics* **1970**, *3*, 45-60.
- (31) Bopp, J. C.; Roscioli, J. R.; Johnson, M. A.; Miller, T. M.; Viggiano, A. A.; Villano, S. M.; Wren, S. W.; Lineberger, W. C. Spectroscopic Characterization of the Isolated SF₆⁻ and C₄F₈⁻ Anions: Observation of Very Long Harmonic Progressions in Asymmetric Deformation Modes Upon Photodetachment. *Journal of Physical Chemistry A* **2007**, *111*, 1214-1221.
- (32) Born, M.; Ingemann, S.; Nibbering, N. M. M. Heats of Formation of Mono-Halogen-Substituted Carbenes - Stability and Reactivity of CHX⁻ (X=F, Cl, Pr, and I) Radical-Anions. *Journal of the American Chemical Society* **1994**, *116*, 7210-7217.
- (33) Born, M.; Ingemann, S.; Nibbering, N. M. M. Reactivity of Mono-Halogen Carbene Radical Anions (CHX⁻; X=F, Cl and Br) and the Corresponding Carbanions (CH₂X⁻; X=Cl and Br) in the Gas Phase. *Journal of the Chemical Society-Perkin Transactions 2* **1996**, 2537-2547.
- (34) Born, M.; Ingemann, S.; Nibbering, N. M. M. Thermochemical Properties of Halogen-Substituted Methanes, Methyl Radicals, and Carbenes in the Gas Phase. *International Journal of Mass Spectrometry* **2000**, *194*, 103-113.
- (35) Borrelli, R. Franck-Condon Analysis of the SF₆⁻ Electron Photodetachment Spectrum. *Chemical Physics Letters* **2007**, *445*, 84-88.

- (36) Borrelli, R.; Peluso, A. The Electron Photodetachment Spectrum of $c\text{-C}_4\text{F}_8^-$: A Test Case for the Computation of Franck-Condon Factors of Highly Flexible Molecules. *The Journal of Chemical Physics* **2008**, *128*, 044303/1-044303/7.
- (37) Botter, R.; Dibeler, V. H.; Walker, J. A.; Rosenstock, H. M. Experimental and Theoretical Studies of Photoionization-Efficiency Curves for C_2H_2 and C_2D_2 . *Journal of Chemical Physics* **1966**, *44*, 1298-1299.
- (38) Bowie, J. H.; DePuy, C. H.; Sullivan, S. A.; Bierbaum, V. M. Gas-Phase Reactions of the Hydroperoxide and Peroxyformate Anions. *Canadian Journal of Chemistry-Revue Canadienne De Chimie* **1986**, *64*, 1046-1051.
- (39) Bozzelli, J. W.; Sheng, C.; Chen, C. J.; Dean, A. M. Thermochemistry and Kinetics for Alkyl Plus O_2 Reactions in Hydrocarbon Oxidation. *Abstracts of Papers of the American Chemical Society* **2002**, *223*, U571-U572.
- (40) Brauman, J. I.; Blair, L. K. Gas-Phase Acidities of Alcohols. *Journal of the American Chemical Society* **1970**, *92*, 5986-5992.
- (41) Braun, M.; Gruber, F.; Ruf, M.-W.; Kumar, S. V. K.; Illenberger, E.; Hotop, H. IR Photon Enhanced Dissociative Electron Attachment to SF_6 : Dependence on Photon, Vibrational, and Electron Energy. *Chemical Physics* **2006**, *329*, 148-162.
- (42) Braun, M.; Ruf, M. W.; Hotop, H.; Allan, M. Low-Energy Electron Attachment to SF_6 Molecules: Vibrational Structure in the Cross-Section for SF_5^- Formation Up to 1 eV. *Chemical Physics Letters* **2006**, *419*, 517-522.
- (43) Brodbelt, J. S.; Isbell, J.; Goodman, J. M.; Secor, H. V.; Seeman, J. I. Gas Phase Versus Solution Chemistry: On the Reversal of Regiochemistry of Methylation of sp^2 - and sp^3 -Nitrogens. *Tetrahedron Letters* **2001**, *42*, 6949-6952.
- (44) Buncl, E.; Um, I.-H. The α -Effect and Its Modulation by Solvent. *Tetrahedron* **2004**, *60*, 7801-7825.
- (45) Buncl, E.; Wilson, H. R.; Chuaqui, C. Reaction-Selectivity Correlations. 4. The α -Effect in $\text{S}_{\text{N}}2$ Reactions at sp^3 Carbon. The Reactions of Hydrogen Peroxide Anion with Methyl Sulfates. *Journal of the American Chemical Society* **1982**, *1982*, 4896-4900.
- (46) Burkholder, J. B.; Howard, C. J.; Hamilton, P. A. Fourier-Transform Spectroscopy of the ν_1 and ν_3 Fundamental Bands of CF_2 . *Journal of Molecular Spectroscopy* **1988**, *127*, 362-369.
- (47) Carstensen, H. H.; Dean, A. M.; Deutschmann, O. Rate Constants for the H Abstraction from Alkanes (RH) by $\text{R}'\text{O}_2$ radicals: A Systematic Study on the Impact of R and R'. *Proceedings of the Combustion Institute* **2007**, *31*, 149-157.

- (48) Carter, E. A.; Goddard, W. A. New Predictions for Singlet Triplet Gaps of Substituted Carbenes. *Journal of Physical Chemistry* **1987**, *91*, 4651-4652.
- (49) Cernicharo, J.; Guelin, M.; Agundez, M.; Kawaguchi, K.; McCarthy, M.; Thaddeus, P. Astronomical Detection of C_4H^- , the Second Interstellar Anion. *Astronomy & Astrophysics* **2007**, *467*, L37-L40.
- (50) Chabinyk, M. L.; Craig, S. L.; Regan, C. K.; Brauman, J. I. Gas-Phase Ionic Reactions: Dynamics and Mechanism of Nucleophilic Displacements. *Science* **1998**, *279*, 1882-1886.
- (51) Chang, B. C.; Guss, J.; Sears, T. J. Hot Bands in the A-X Spectrum of HCB r . *Journal of Molecular Spectroscopy* **2003**, *219*, 136-144.
- (52) Chang, C. H.; Porter, R. F.; Bauer, S. H. Molecular Structures of Perfluorocyclobutane and Perfluorocyclobutene, Determined by Electron Diffraction. *Journal of Molecular Structure* **1971**, *7*, 89-99.
- (53) Chang, W. Z.; Hsu, H. J.; Chang, B. C. New Dispersed Fluorescence Spectra of HCB r and DCB r . *Chemical Physics Letters* **2005**, *413*, 25-30.
- (54) Chase Jr., M. W.; Davies, C. A.; Downey Jr., J. R.; Frurip, D. J.; McDonald, R. A.; Syverud, A. N. JANAF Thermochemical Tables, 3rd ed. *Journal of Physical and Chemical Reference Data* **1985**, *14*.
- (55) Chau, F. T.; Mok, D. K. W.; Lee, E. P. F.; Dyke, J. M. The Singlet-Triplet Separation in CF_2 : State of the Art *Ab Initio* Calculations and Franck-Condon Simulations Including Anharmonicity. *ChemPhysChem* **2005**, *6*, 2037-2045.
- (56) Chen, P. Photoelectron Spectroscopy of Reactive Intermediates. In *Unimolecular and Bimolecular Reaction Dynamics*; C. Y. Ng, T. Baer and I. Powis, Eds.; John Wiley and Sons: New York, 1994; pp 371-425.
- (57) Chen, P. Photoelectron Spectroscopy of Reactive Intermediates. In *Unimolecular and Bimolecular Reaction Dynamics*; C. Y. Ng, T. Baer and I. Powis, Eds.; John Wiley and Sons: New York, 1994; pp 371-425.
- (58) Chou, P. K.; Kass, S. R. E-Vinyl and Z-Vinyl Anions - the Formation and Characterization of Regioisomers and Stereoisomers in the Gas-Phase. *Journal of the American Chemical Society* **1991**, *113*, 4357-4359.
- (59) Chowdhury, P. K. IR Multiphoton Dissociation Dynamics of Octafluorocyclopentene - Time-Resolved Observation of Concerted Products - CF_2 and Hexafluorobutadiene. *Journal of Physical Chemistry* **1995**, *99*, 12084-12089.
- (60) Christophorou, L. G. Electron-Molecule Interactions and Their Applications; Ed.; Academic: New York, 1984.

- (61) Christophorou, L. G.; Olthoff, J. K. Electron Interactions with $c\text{-C}_4\text{F}_8$. *Journal of Physical and Chemical Reference Data* **2001**, *30*, 449-473.
- (62) Christophorou, L. G.; Olthoff, J. K. Electron Interactions with SF_6 . *Journal of Physical and Chemical Reference Data* **2000**, *29*, 267-330.
- (63) Clair, R. L.; McMahon, T. B. Ion-Cyclotron Resonance Study of Base-Induced Elimination-Reactions of Fluorinated Alcohols and Unimolecular Loss of HF from Chemically Activated Fluoroalkoxide Ions. *International Journal of Mass Spectrometry and Ion Processes* **1980**, *33*, 21-36.
- (64) Compton, R. N.; Christophorou, L. G.; Hurst, G. S.; Reinhardt, P. W. Nondissociative Electron Capture in Complex Molecules and Negative-Ion Lifetimes. *Journal of Chemical Physics* **1966**, *45*, 4634-4639.
- (65) Compton, R. N.; Hurst, G. S.; Christophorou, L. G.; Reinhardt, P. W. "ORNL-TM-1409," 1966.
- (66) Compton, R. N.; Reinhardt, P. W.; Cooper, C. D. Collisional Ionization Between Fast Alkali Atoms and Selected Hexafluoride Molecules. *Journal of Chemical Physics* **1978**, *68*, 2023-2036.
- (67) Cooper, J.; Zare, R. N. Angular Distributions of Photoelectrons. *Journal of Chemical Physics* **1968**, *48*, 942-943.
- (68) Crawford, M. A.; Wallington, T. J.; Szente, J. J.; Maricq, M. M.; Francisco, J. S. Kinetics and Mechanism of the Acetylperoxy Plus HO_2 Reaction. *Journal of Physical Chemistry A* **1999**, *103*, 365-378.
- (69) Cronin, B.; Nix, M. G. D.; Qadiri, R. H.; Ashfold, M. N. R. High Resolution Photofragment Translational Spectroscopy Studies of the Near Ultraviolet Photolysis of Pyrrole. *Physical Chemistry Chemical Physics* **2004**, *6*, 5031-5041.
- (70) Cugley, J. A.; Bossert, W.; Bauder, A.; Gunthard, H. H. Microwave-Spectrum, Dipole-Moment and Barrier to Internal-Rotation of Peroxyacetic Acid. *Chemical Physics* **1976**, *16*, 229-235.
- (71) Curtiss, L. A.; Raghavachari, K.; Redfern, P. C.; Rassolov, V.; Pople, J. A. Gaussian-3 (G3) Theory for Molecules Containing First and Second-Row Atoms. *Journal of Chemical Physics* **1998**, *109*, 7764-7776.
- (72) Datskos, P. G.; Carter, J. G.; Christophorou, L. G. Photodetachment of SF_6^- . *Chemical Physics Letters* **1995**, *239*, 38-43.
- (73) Davico, G. E.; Bierbaum, V. M.; DePuy, C. H.; Ellison, G. B.; Squires, R. R. The C-H Bond-Energy of Benzene. *Journal of the American Chemical Society* **1995**, *117*, 2590-2599.

- (74) Dawson, J. H. J.; Nibbering, N. M. M. Concerning $\text{CH}_2=\text{C}^-$ And Its Reaction with $^{14}\text{N}^{15}\text{NO}$. *Journal of the American Chemical Society* **1978**, *100*, 1928-1929.
- (75) Dehmer, J. L.; Siegel, J.; Dill, D. Shape Resonances in e-SF₆ Scattering. *Journal of Chemical Physics* **1978**, *69*, 5205-5206.
- (76) Dekoning, L. J.; Nibbering, N. M. M. On the Mechanism of Base-Induced Gas-Phase Elimination-Reactions of Ethers. *Journal of the American Chemical Society* **1987**, *109*, 1715-1722.
- (77) DePuy, C. H.; Barlow, S. E.; Van Doren, J. M.; Roberts, C. R.; Bierbaum, V. M. Gas-Phase Chemistry of CH_2^- . *Journal of the American Chemical Society* **1987**, *109*, 4414-4415.
- (78) DePuy, C. H.; Bierbaum, V. M. Gas-Phase Elimination-Reactions of Ethers Induced by Amide and Hydroxide Ions. *Journal of the American Chemical Society* **1981**, *103*, 5034-5038.
- (79) DePuy, C. H.; Bierbaum, V. M. Gas-Phase Sulfur Anions - Synthesis and Reactions of H_2NS^- and Related Ions. *Tetrahedron Letters* **1981**, *22*, 5129-5130.
- (80) DePuy, C. H.; Bierbaum, V. M.; Robinson, M. S.; Davico, G. E.; Gareyev, R. The Gas-Phase Reactions of the Allenyl Anion with CS_2 , COS and CO_2 . *Tetrahedron* **1997**, *53*, 9847-9856.
- (81) DePuy, C. H.; Della, E. W.; Filley, J.; Grabowski, J. J.; Bierbaum, V. M. Absence of an α -Effect in the Gas-Phase Nucleophilic Reactions of HOO^- . *Journal of the American Chemical Society* **1983**, *105*, 2481-2482.
- (82) DePuy, C. H.; Gronert, S.; Mullin, A.; Bierbaum, V. M. Gas-Phase $\text{S}_{\text{N}}2$ and E2 Reactions of Alkyl-Halides. *Journal of the American Chemical Society* **1990**, *112*, 8650-8655.
- (83) DePuy, C. H.; Kass, S. R.; Bean, G. P. Formation and Reactions of Heteroaromatic Anions in the Gas-Phase. *Journal of Organic Chemistry* **1988**, *53*, 4427-4433.
- (84) DePuy, C. H.; Kato, S. H/D Exchange Reactions. In *The Encyclopedia of Mass Spectrometry: Theory and Ion Chemistry*; P. B. Armentrout, Ed.; Elsevier: Amsterdam, 2003; Vol. 1; pp 670-674.
- (85) Deselnicu, M.; Tao, C.; Mukarakate, C.; Reid, S. A. Fluorescence Excitation and Emission Spectroscopy of the $\text{A}^1\text{A}''-\text{X}^1\text{A}'$ System of CHBr . *Journal of Chemical Physics* **2006**, *124*, 134302/1-134302/11.
- (86) DeZarate, A. O.; Martinez, R.; Rayo, M. N. S.; Castano, F.; Hancock, G. Preparation of Chf ($\text{X}^1\text{a}'$) by Infrared Multiphoton Dissociation and Reactions with Alkenes. *Journal of the Chemical Society-Faraday Transactions* **1992**, *88*, 535-541.

- (87) Dixon, J. E.; Bruice, T. C. α -Effect. IV. Additional Observation on the α -Effect Employing Malachite Green as Substrate. *Journal of the American Chemical Society* **1971**, *93*, 6592-6597.
- (88) Drzaic, P. S.; Brauman, J. I. Electron Photodetachment Study of Sulfur-Hexafluoride Anion - Comments on the Structure of SF₆⁻. *Journal of the American Chemical Society* **1982**, *104*, 13-19.
- (89) Dubnikova, F.; Lifshitz, A. Isomerization of Pyrrole. Quantum Chemical Calculations and Kinetic Modeling. *Journal of Physical Chemistry A* **1998**, *102*, 10880-10888.
- (90) Duncan, M. A.; Bierbaum, V. M.; Ellison, G. B.; Leone, S. R. Laser-Induced Fluorescence Studies of Ion Collisional Excitation in a Drift Field: Rotational Excitation of N₂⁺ in Helium. *Journal of Chemical Physics* **1983**, *79*, 5448-5456.
- (91) Dunkin, D. B.; Fehsenfeld, F. C.; Schmeltekopf, A. L.; Ferguson, E. E. Ion-Molecule Reaction Studies from 300 to 600 K in a Temperature-Controlled Flowing Afterglow System. *Journal of Chemical Physics* **1968**, *49*, 1365-1371.
- (92) Dupeyrat, G.; Rowe, B. R.; Fahey, D. W.; Albritton, D. L. Diagnostic Studies of Venturi Inlets for Flow Reactors. *International Journal of Mass Spectrometry and Ion Processes* **1982**, *44*, 1-18.
- (93) Dushman, S.; Lafferty, J. M. Scientific Foundations of Vacuum Techniques; John Wiley and Sons: New York, 1962.
- (94) Dyke, J. M.; Lee, E. P. F.; Mok, D. K. W.; Chau, F. T. A Combined *Ab Initio*/Franck-Condon Study of the A-X Single-Vibronic-Level Emission Spectrum of CCl₂ and the Photodetachment Spectrum of CCl₂⁻. *ChemPhysChem* **2005**, *6*, 2046-2059.
- (95) Edwards, J. O.; Pearson, R. G. Factors Determining Nucleophilic Reactivities. *Journal of the American Chemical Society* **1962**, *84*, 16-24.
- (96) Eland, J. H. D. Molecular Photoelectron Spectroscopy. *Journal of Physics E - Scientific Instruments* **1978**, *11*, 969-977.
- (97) El'Sohly, A. M.; Tschumper, G. S.; Crocombe, R. A.; Wang, J. T.; Williams, F. Computational and ESR studies of electron attachment to decafluorocyclopentane, octafluorocyclobutane, and hexafluorocyclopropane: Electron affinities of the molecules and the structures of their stable negative ions as determined from C-13 and F-19 hyperfine coupling constants. *Journal of the American Chemical Society* **2005**, *127*, 10573-10583.
- (98) Engelking, P. C. Approximate Rotational Band Shifts. *Journal of Physical Chemistry* **1986**, *90*, 4544-4545.

- (99) Ervin, K. M. FCFGAUS, Fortran program; University of Nevada, Reno, 2003.
- (100) Ervin, K. M. PESCAL, Fortran program; University of Nevada, Reno, 2008.
- (101) Ervin, K. M.; Anusiewicz, I.; Skurski, P.; Simon, J.; Lineberger, W. C. The Only Stable State of O_2^- is the $X^2\Pi_g$ Ground State and It (Still!) Has an Adiabatic Electron Detachment Energy of 0.45 eV. *Journal of Physical Chemistry A* **2003**, *107*, 8521-8529.
- (102) Ervin, K. M.; DeTuro, V. F. Anchoring the Gas-Phase Acidity Scale. *Journal of Physical Chemistry A* **2002**, *106*, 9947-9956.
- (103) Ervin, K. M.; Lineberger, W. C. In *Gas Phase Ion Chemistry*; N. C. Adams and L. M. Babcock, Eds.; JAI Press: Greenwich, 1992; Vol. 1; pp 121.
- (104) Ervin, K. M.; Lineberger, W. C. Photoelectron Spectroscopy of Negative Ions. In *Advances in Gas-Phase Ion Chemistry*; N. G. Adams and L. M. Babcock, Eds. Greenwich, 1992; pp 121-166.
- (105) Ervin, K. M.; Ramond, T. M.; Davico, G. E.; Schwartz, R. L.; Casey, S. M.; Lineberger, W. C. Naphthyl radical: Negative Ion Photoelectron Spectroscopy, Franck-Condon Simulation, and Thermochemistry. *Journal of Physical Chemistry A* **2001**, *105*, 10822-10831.
- (106) Espinosa-Garcia, J. Theoretical Enthalpies of Formation of ROX (R = H, CH₃; X = F, Cl, Br) Compounds. *Chemical Physics Letters* **1999**, *315*, 239-247.
- (107) Evanseck, J. D.; Blake, J. F.; Jorgensen, W. L. *Ab Initio* Study of the S_N2 Reactions of Hydroxide and Hydroperoxide with Chloromethane. *Journal of the American Chemical Society* **1987**, *109*, 2349-2353.
- (108) Eyet, N.; Villano, S. M.; Bierbaum, V. M. Anchoring the Gas-Phase Acidity Scale: Formic Acid to Methanethiol. *International Journal of Mass Spectrometry* **2009**, *In Press*.
- (109) Fan, H. Y.; Mukarakate, C.; Deselnicu, M.; Tao, C.; Reid, S. A. Dispersed Fluorescence Spectroscopy of Jet-Cooled HCF and DCF: Vibrational Structure of the X¹A' State. *Journal of Chemical Physics* **2005**, *123*, 014314/1-014314/7.
- (110) Fehsenfeld, F. C. Ion Reactions with Atomic Oxygen and Atomic Nitrogen of Astrophysical Importance. *Astrophysical Journal* **1976**, *209*, 638-639.
- (111) Fehsenfeld, F. C.; Albritton, D. L.; Bush, Y. A.; Fournier, P. G.; Govers, T. R.; Fournier, J. Ion-Atom Interchange Reactions Using Isotopic-Species. *Journal of Chemical Physics* **1974**, *61*, 2150-2155.

- (112) Fehsenfeld, F. C.; Evenson, K. M.; Broida, H. P. Microwave Discharge Cavities Operating at 2450 MHz. *Review of Scientific Instruments* **1965**, *36*, 294-298.
- (113) Fehsenfeld, F. C.; Schmeltekopf, A. L.; Goldan, H. I.; Schiff, H. I.; Ferguson, E. E. Thermal Energy Ion - Neutral Reaction Rates. I. Some Reactions of Helium Ions. *Journal of Chemical Physics* **1966**, *44*, 4087-4094.
- (114) Feigerle, C. S. Laser Photoelectron Spectroscopy Studies of Transition Metal Negative Ions. Ph.D. Thesis, Department of Chemical Physics, University of Colorado at Boulder, 1983.
- (115) Felder, P.; Demuth, C. Photodissociation of CFCl_3 at 193 nm Investigated by Photofragment Translational Spectroscopy. *Chemical Physics Letters* **1993**, *208*, 21-26.
- (116) Feller, D.; Dixon, D. A.; Francisco, J. S. Coupled Cluster Theory Determination of the Heats of Formation of Combustion-Related Compounds: CO, HCO, CO_2 , HCO_2 , HOCO, HC(O)OH , and HC(O)OOH . *Journal of Physical Chemistry A* **2003**, *107*, 1604-1617.
- (117) Ferch, J.; Raith, W.; Schroder, K. Total Cross-Section Measurement for e- SF_6 Scattering Down to 0.036 eV. *Journal of Physics B: Atomic, Molecular and Optical Physics* **1982**, *15*, L175-L178.
- (118) Ferguson, E. E.; Fehsenfeld, F. C.; Albritton, D. L. Gas-Phase Ion Chemistry; Academic Press: New York, 1979.
- (119) Ferguson, E. E.; Fehsenfeld, F. C.; Schmeltekopf, A. L. Flowing Afterglow Measurements of Ion-Neutral Reactions. In *Advances in Atomic and Molecular Physics*; Academic Press, Inc: New York, 1969; Vol. 5; pp 1-56.
- (120) Field, D.; Jones, N. C.; Ziesel, J. P. Cold Electron Scattering in SF_6 and C_6F_6 : Bound and Virtual State Channels. *Physical Review A* **2004**, *69*, 0527216/1-0527216/11.
- (121) Finlayson-Pitts, B. J.; Pitts, J. N. J. Atmospheric Chemistry: Fundamentals and Experimental Techniques; Wiley: New York, 1986.
- (122) Finlayson-Pitts, B. J.; Pitts, J. N. Tropospheric air pollution: Ozone, airborne toxics, polycyclic aromatic hydrocarbons, and particles. *Science* **1997**, *276*, 1045-1052.
- (123) Fischer, G.; Purchase, R. L.; Smith, D. M. The Ring-Puckering Motion in Perfluorocyclobutane. *Journal of Molecular Structure* **1997**, *405*, 159-167.
- (124) Fountain, K. R.; Felkerson, C. J.; Driskell, J. D.; Lamp, B. D. The α -Effect in Methyl Transfers from S-Methyldibenzothiophenium Fluoroborate to Substituted N-Methylbenzohydroxamates. *Journal of Organic Chemistry* **2003**, *68*, 1810-1814.

(125) Fountain, K. R.; Hutchinson, L. K.; Mulhearn, D. C.; Xu, Y. B. α -Effect in Menshutkin Alkylations. *Journal of Organic Chemistry* **1993**, *58*, 7883-7890.

(126) Fountain, K. R.; Tad-y, D. B.; Paul, T. W.; Golynskiy, M. V. The α -Effect in Benzyl Transfers from Benzylphenylmethyl Sulfonium Salts to *N*-Methylbenzohydroxamate Anions. *Journal of Organic Chemistry* **1999**, *64*, 6547-6553.

(127) Franzen, V. Reaktionen Mit Difluorcarben. *Angewandte Chemie-International Edition* **1960**, *72*, 566-566.

(128) Frisch, M. J.; Trucks, G. W.; Schlegel, H. B.; Scuseria, G. E.; Robb, M. A.; Cheeseman, J. R.; Montgomery, J. A.; Vreven, T.; Kudin, K. N.; Burant, J. C.; Millam, J. M.; Iyengar, S. S.; Tomasi, J.; Barone, V.; Mennucci, B.; Cossi, M.; Scalmani, G.; Rega, N.; Petersson, G. A.; Nakatsuji, H.; Hada, M.; Ehara, M.; Toyota, K.; Fukuda, R.; Hasegawa, J.; Ishida, M.; Nakajima, T.; Honda, Y.; Kitao, O.; Nakai, H.; Klene, M.; Li, X.; Knox, J. E.; Hratchian, H. P.; Cross, J. B.; Adamo, C.; Jaramillo, J.; Gomperts, R.; Stratmann, R. E.; Yazyev, O.; Austin, A. J.; Cammi, R.; Pomelli, C.; Ochterski, J. W.; Ayala, P. Y.; Morokuma, K.; Voth, G. A.; Salvador, P.; Dannenberg, J. J.; Zakrzewski, V. G.; Dapprich, S.; Daniels, A. D.; Strain, M. C.; Farkas, O.; Malick, D. K.; Rabuck, A. D.; Raghavachari, K.; Foresman, J. B.; Ortiz, J. V.; Cui, Q.; Baboul, A. G.; Clifford, S.; Cioslowski, J.; Stefanov, B. B.; Liu, G.; Liashenko, A.; Piskorz, P.; Komaromi, I.; Martin, R. L.; Fox, D. J.; Keith, T.; Al-Laham, M. A.; C. Y. Peng; Nanayakkara, A.; Challacombe, M.; Gill, P. M. W.; Johnson, B.; Chen, W.; Wong, M. W.; Gonzalez, C.; Pople, J. A. Gaussian 03, revision B.05; I. Gaussian, Ed. Pittsburgh, PA, 2003.

(129) Gallup, G. A. The Structures of $c\text{-C}_4\text{F}_8$ and $c\text{-C}_4\text{F}_8^-$ and the Adiabatic Electron Affinity of $c\text{-C}_4\text{F}_8$. *Chemical Physics Letters* **2004**, *399*, 206-209.

(130) Gianola, A. J.; Ichino, T.; Hoenigman, R. L.; Kato, S.; Bierbaum, V. M.; Lineberger, W. C. Photoelectron Spectra and Ion Chemistry of Imidazolid. *Journal of Physical Chemistry A* **2005**, *109*, 11504-11514.

(131) Gianola, A. J.; Ichino, T.; Hoenigman, R. L.; Kato, S.; Bierbaum, V. M.; Lineberger, W. C. Thermochemistry and Electronic Structure of the Pyrrolyl Radical. *Journal of Physical Chemistry A* **2004**, *108*, 10326-10335.

(132) Gianola, A. J.; Ichino, T.; Kato, S.; Bierbaum, V. M.; Lineberger, W. C. Thermochemical Studies of Pyrazolide. *Journal of Physical Chemistry A* **2006**, *110*, 8457-8466.

(133) Gianturco, F. A.; Lucchese, R. R. Electron Scattering From Gaseous SF_6 : Comparing Calculations with Experiments. *Journal of Chemical Physics* **2001**, *114*, 3429-3439.

- (134) Gilles, M. K.; Ervin, K. M.; Ho, J.; Lineberger, W. C. Negative-Ion Photoelectron-Spectroscopy of HCF^- , HCCl^- , HCB^- , and HCl^- - Photoelectron Angular-Distributions and Neutral Triplet Excitation-Energies. *Journal of Physical Chemistry* **1992**, *96*, 1130-1141.
- (135) Gioumoussis, G.; Stevenson, D. P. Reactions of Gaseous Molecule Ions with Gaseous Molecules .5. Theory. *Journal of Chemical Physics* **1958**, *29*, 294-299.
- (136) Grabowski, J. J. Studies of Gas Phase Ion-Molecule Reactions using a Selected Ion Flow Tube. Ph.D. Thesis, Department of Chemistry and Biochemistry, University of Colorado at Boulder 1983.
- (137) Grabowski, J. J.; Cheng, X. H. Gas-Phase Formation of the Enolate Monoanion of Acetic-Acid by Proton Abstraction. *Journal of the American Chemical Society* **1989**, *111*, 3106-3108.
- (138) Grabowski, J. J.; Cheng, X. H. Gas-Phase Formation of the Enolate Monoanion of Acetic-Acid by Proton Abstraction. *Journal of the American Chemical Society* **1989**, *111*, 3106-3108.
- (139) Graul, S. T.; Bowers, M. T. Vibrational-Excitation in Products of Nucleophilic-Substitution - The Dissociation of Metastable $\text{X}^-(\text{CH}_3\text{Y})$ in the Gas-Phase. *Journal of the American Chemical Society* **1994**, *116*, 3875-3883.
- (140) Gregory, M. J.; Bruice, T. C. Alpha Effect. II. Displacements on sp^3 Carbon. *Journal of the American Chemical Society* **1967**, *89*, 4400-4402.
- (141) Grimsrud, E. P. Electron Capture Elsevier: New York, 1981.
- (142) Grimsrud, E. P.; Chowdhury, S.; Kebarle, P. Electron-Affinity of SF_6 and Perfluoromethylcyclohexane - The Unusual Kinetics of Electron-Transfer Reactions $\text{A}^- + \text{B} = \text{A} + \text{B}^-$, Where $\text{A} = \text{SF}_6$ or Perfluorinated Cyclo-Alkanes. *Journal of Chemical Physics* **1985**, *83*, 1059-1068.
- (143) Gronert, S. Gas phase Studies of the Competition Between Substitution and Elimination Reactions. *Accounts of Chemical Research* **2003**, *36*, 848-857.
- (144) Gronert, S.; DePuy, C. H.; Bierbaum, V. M. Deuterium-Isotope Effects in Gas-Phase Reactions of Alkyl-Halides - Distinguishing E_2 and $\text{S}_{\text{N}}2$ Pathways. *Journal of the American Chemical Society* **1991**, *113*, 4009-4010.
- (145) Gronert, S.; Fagin, A. E.; Okamoto, K.; Mogali, S.; Pratt, L. M. Leaving Group Effects in Gas-Phase Substitutions and Eliminations. *Journal of the American Chemical Society* **2004**, *126*, 12977-12983.

- (146) Gronert, S.; Pratt, L. M.; Mogali, S. Substituent Effects in Gas-Phase Substitutions and Eliminations: β -Halo Substituents Solvation Reverses S_N2 Substituent Effects. *Journal of the American Chemical Society* **2001**, *123*, 3081-3091.
- (147) Gunion, R. F.; Gilles, M. K.; Polak, M. L.; Lineberger, W. C. Ultraviolet Photoelectron-Spectroscopy of the Phenide, Benzyl and Phenoxide Anions, with *Ab Initio* Calculations. *International Journal of Mass Spectrometry and Ion Processes* **1992**, *117*, 601-620.
- (148) Guss, J. S.; Richmond, C. A.; Nauta, K.; Kable, S. H. Laser-Induced Fluorescence Excitation and Dispersed Fluorescence Spectroscopy of the $A^1B_1-X^1A_1$ Transition of Dichlorocarbene. *Physical Chemistry Chemical Physics* **2005**, *7*, 100-108.
- (149) Gutsev, G. L.; Bartlett, R. J. Adiabatic Electron Affinities of PF_5 and SF_6 : A Coupled-Cluster Study. *Molecular Physics* **1998**, *94*, 121-125.
- (150) Gutsev, G. L.; Ziegler, T. Theoretical-Study on Neutral and Anionic Halocarbynes and Halocarbenes. *Journal of Physical Chemistry* **1991**, *95*, 7220-7228.
- (151) Hall, J. L.; Siegel, M. W. Angular Dependence of the Laser Photodetachment of the Negative Ions of Carbon, Oxygen, and Hydrogen. *Journal of Chemical Physics* **1968**, *48*, 943-945.
- (152) Hankin, J. J. Gas-Phase Chemistry of Silicon and Boron Ions. Ph.D. Thesis, Department of Chemistry and Biochemistry, University of Colorado at Boulder 1995.
- (153) Hanstorp, D.; Gustafsson, M. Determination of the Electron-Affinity of Iodine. *Journal of Physics B-Atomic Molecular and Optical Physics* **1992**, *25*, 1773-1783.
- (154) Hare, M. C.; Marimanikkuppam, S. S.; Kass, S. R. Acetamide Enolate: Formation, Reactivity, and Proton Affinity. *International Journal of Mass Spectrometry* **2001**, *210*, 153-163.
- (155) Harris, D. C.; Bertolucci, M. D. Symmetry and Spectroscopy: An Introduction to Vibrational and Electronic Spectroscopy; Oxford University Press: New York, 1978.
- (156) Harrison, A. G. Chemical Ionization Mass Spectrometry; CRC Press: Boca Raton, 1983.
- (157) Harrison, J. F.; Liedtke, R. C.; Liebman, J. F. Multiplicity of Substituted Acyclic Carbenes and Related Molecules. *Journal of the American Chemical Society* **1979**, *101*, 7162-7168.

- (158) Hase, W. L. Classical Trajectory Simulations. In *Encyclopedia of Mass Spectrometry: Chemistry and Physics of Gas-Phase Ions*; M. Gross and R. Caprioli, Eds.; Elsevier: New York, 2005; Vol. 4; pp 504.
- (159) Hay, P. J. The Relative Energies of SF₆⁻ and SF₆ as a Function of Geometry. *Journal of Chemical Physics* **1982**, *76*, 502-504.
- (160) Hehre, W. J.; Radom, L.; Schleyer, P. v. R.; Pople, J. A. *Ab Initio Molecular Orbital Theory*; Wiley: New York, 1986.
- (161) Hierl, P. M.; Friedman, J. F.; Miller, T. M.; Dotan, I.; Menendez-Barreto, M.; Seeley, J. V.; Williamson, J. S.; Dale, F.; Mundis, P. L.; Morris, R. A.; Paulson, J. F.; Viggiano, A. A. Flowing Afterglow Apparatus for the Study of Ion-Molecule Reactions at High Temperatures. *Review of Scientific Instruments* **1996**, *67*, 2142-2148.
- (162) Hiraoka, K.; Mizuno, T.; Eguchi, D.; Takao, K.; Iino, T.; Yamabe, S. Gas-phase Ion/Molecule Reactions in Octafluorocyclobutane. *Journal of Chemical Physics* **2002**, *116*, 7574-7582.
- (163) Ho, J. Negative Ion Laser Photoelectron Spectroscopy of Mass Selected Small Metal Clusters. Ph.D. Thesis, Department of Physics, University of Colorado at Boulder, 2001.
- (164) Hoffmann, R.; Zeiss, G. D.; Vandine, G. W. Electronic Structure of Methylenes. *Journal of the American Chemical Society* **1968**, *90*, 1485-1499.
- (165) Hotop, H.; Lineberger, W. C. Binding-Energies in Atomic Negative-Ions II. *Journal of Physical and Chemical Reference Data* **1985**, *14*, 731-750.
- (166) Hoz, S. The α -Effect - on the Origin of Transition-State Stabilization. *Journal of Organic Chemistry* **1982**, *47*, 3545-3547.
- (167) Hsu, H. J.; Chang, W. Z.; Chang, B. C. Dispersed Fluorescence Spectroscopy of the CBr₂ A¹B₁-X¹A₁ Transition. *Physical Chemistry Chemical Physics* **2005**, *7*, 2468-2473.
- (168) Hu, W. P.; Truhlar, D. G. Factors affecting competitive ion-molecule reactions: ClO⁻+C₂H₅Cl and C₂D₅Cl via E2 and S_N2 channels. *Journal of the American Chemical Society* **1996**, *118*, 860-869.
- (169) Hu, W. P.; Truhlar, D. G. Modeling Transition-State Solvation at the Single-Molecule Level - Test of Correlated *Ab-Initio* Predictions against Experiment for the Gas-Phase S_N2 Reaction of Microhydrated Fluoride with Methyl-Chloride. *Journal of the American Chemical Society* **1994**, *116*, 7797-7800.
- (170) Hu, Y. J.; Fu, H. B.; Bernstein, E. R. Vibronic Spectroscopy of the Peroxyacetyl Radical in the Near IR. *Journal of Chemical Physics* **2006**, *124*, 114305/1-114305/6.

- (171) Huggins, R. W.; Cahn, J. H. Metastable Measurements in Flowing Helium Afterglow. *Journal of Applied Physics* **1967**, *38*, 180-188.
- (172) Hupe, D. J.; Wu, D. The Effect of Solvation on Bronsted β Values for Proton Transfer Reactions. *Journal of the American Chemical Society* **1977**, *99*, 7653-7659.
- (173) Ibuki, T.; Hiraya, A.; Shobatake, K. Vacuum Ultraviolet-Absorption Spectra and Photodissociative Excitation of CHBr_2Cl and CHBrCl_2 . *Journal of Chemical Physics* **1992**, *96*, 8793-8798.
- (174) Ichino, T.; Andrews, D. H.; Rathbone, G. J.; Misaizu, F.; Calvi, R. M. D.; Wren, S. W.; Kato, S.; Bierbaum, V. M.; Lineberger, W. C. Ion Chemistry of 1H-1,2,3-Triazole. *Journal of Physical Chemistry B* **2008**, *112*, 545-557.
- (175) Ichino, T.; Gianola, A. J.; Lineberger, W. C.; Stanton, J. F. Nonadiabatic Effects in the Photoelectron Spectrum of the Pyrazolide- d_3 Anion: Three-State Interactions in the Pyrazolyl- d_3 Radical. *Journal of Chemical Physics* **2006**, *125*, 084312-084333.
- (176) Irikura, K. K.; Goddard, W. A.; Beauchamp, J. L. Singlet Triplet Gaps in Substituted Carbenes CXY ($X, Y = \text{H, F, Cl, Br, I, SiH}_3$). *Journal of the American Chemical Society* **1992**, *114*, 48-51.
- (177) Irikura, K. K.; Hudgens, J. W.; Johnson, R. D. Spectroscopy of the Fluoromethylene Radicals HCF and DCF by 2+1 Resonance-Enhanced Multiphoton Ionization Spectroscopy and by *Ab-Initio* Calculation. *Journal of Chemical Physics* **1995**, *103*, 1303-1308.
- (178) Jennings, K. R. Gas-Phase Ion Chemistry; Academic Press: New York, 1979.
- (179) Johnson, M. A.; Lineberger, W. C. Pulsed Methods for Cluster Ion Spectroscopy. In *Techniques for the Study of Ion-Molecule Reactions*; J. M. Farrar and J. W. H. Saunders, Eds.; Wiley: New York, 1988; Vol. 20; pp 591-635.
- (180) Jones, M. E.; Ellison, G. B. A Gas-Phase E2 Reaction - Methoxide Ion and Bromopropane. *Journal of the American Chemical Society* **1989**, *111*, 1645-1654.
- (181) Jones, M.; Moss, R. A. Carbenes; John Wiley and Sons: New York, 1973.
- (182) Jones, M.; Moss, R. A. Carbenes; John Wiley and Sons: New York, 1975.
- (183) Jones, W. D.; Dong, L. Z.; Myers, A. W. Bond-Cleavage Reactions in Oxygen and Nitrogen-Heterocycles by a Rhodium Phosphine Complex. *Organometallics* **1995**, *14*, 855-861.

- (184) Jorapur, Y. R.; Jeong, J. M.; Chi, D. Y. Potassium Carbonate as a Base for the N-alkylation of Indole and Pyrrole in Ionic Liquids. *Tetrahedron Letters* **2006**, *47*, 2435-2438.
- (185) Julian, R. R.; May, J. A.; Stoltz, B. M.; Beauchamp, J. L. Biomimetic Approaches to Gas-Phase Peptide Chemistry: Combining Selective Binding Motifs with Reactive Carbene Precursors to Form Molecular Mousetraps. *International Journal of Mass Spectrometry* **2003**, *228*, 851-864.
- (186) Just, G. M. P.; Sharp, E. N.; Zalyubovsky, S. J.; Miller, T. A. Cavity Ringdown Spectroscopy of the A-X Electronic Transition of the Phenyl Peroxy Radical. *Chemical Physics Letters* **2006**, *417*, 378-382.
- (187) Kass, S. R.; Filley, J.; Van Doren, J. M.; DePuy, C. H. Nitrous-Oxide in Gas-Phase Ion Molecule Chemistry - A Versatile Reagent for the Determination of Carbanion Structure. *Journal of the American Chemical Society* **1986**, *108*, 2849-2852.
- (188) Kato, S.; Davico, G. E.; Lee, H. S.; DePuy, C. H.; Bierbaum, V. M. Deuterium Kinetic Isotope Effects in Gas Phase S_N2 Reactions. *International Journal of Mass Spectrometry* **2001**, *210*, 223-229.
- (189) Kato, S.; Lineberger, W. C.; Bierbaum, V. M. Collision-Induced Dissociation of Fluoropyridinide Anions. *International Journal of Mass Spectrometry* **2007**, *266*, 166-179.
- (190) Kiefer, J. H.; Zhang, Q.; Kern, R. D.; Yao, J.; Jursic, B. Pyrolyses of Aromatic Azines: Pyrazine, Pyrimidine, and Pyridine. *Journal of Physical Chemistry A* **1997**, *101*, 7061-7073.
- (191) Kim, E. H.; Bradforth, S. E.; Arnold, D. W.; Metz, R. B.; Neumark, D. M. Study of HCO₂ and DCO₂ by Negative-Ion Photoelectron-Spectroscopy. *Journal of Chemical Physics* **1995**, *103*, 7801-7814.
- (192) King, G. K.; Maricq, M. M.; Bierbaum, V. M.; Depuy, C. H. Gas-Phase Reactions of Negative-Ions with Alkyl Nitrites. *Journal of the American Chemical Society* **1981**, *103*, 7133-7140.
- (193) Kirchner, F.; Stockwell, W. R. Effect of Peroxy Radical Reactions on the Predicted Concentrations of Ozone, Nitrogenous Compounds, and Radicals. *Journal of Geophysical Research-Atmospheres* **1996**, *101*, 21007-21022.
- (194) Kirmse, W. Carbene Chemistry; Academic Press: New York, 1971.
- (195) Klobukowski, M.; Barandiaran, Z.; Seijo, L.; Huzinaga, S. Towards HF SCF Value of Electron-Affinity of SF₆. *Journal of Chemical Physics* **1987**, *86*, 1637-1638.

- (196) Knicker, H.; Hatcher, P. G.; Scaroni, A. W. Solid-State ^{15}N NMR-Spectroscopy of Coal. *Energy & Fuels* **1995**, *9*, 999-1002.
- (197) Kofron, W. G.; Hauser, C. R.; Kirby, F. B. Reactions of Tetrahalomethanes with Potassium *t*-Butoxide and Potassium Amide. *Journal of Organic Chemistry* **1963**, *28*, 873-875.
- (198) Kohn, D. W.; Robles, E. S. J.; Logan, C. F.; Chen, P. Photoelectron-Spectrum, Ionization-Potential, and Heat of Formation of CCl_2 . *Journal of Physical Chemistry* **1993**, *97*, 4936-4940.
- (199) Koppel, H.; Domcke, W.; Cederbaum, L. S. Multimode Molecular-Dynamics Beyond the Born-Oppenheimer Approximation. *Advances in Chemical Physics* **1984**, *57*, 59-246.
- (200) Krishnan, R.; Binkley, J. S.; Seeger, R.; Pople, J. A. Self-Consistent Molecular-Orbital Methods. II. Basis Set for Correlated Wave-Functions. *Journal of Chemical Physics* **1980**, *72*, 650-654.
- (201) Kurinovich, M. A.; Lee, J. K. The Acidity of Uracil from the Gas Phase to Solution: The Coalescence of the N1 and N3 Sites and Implications for Biological Glycosylation. *Journal of the American Chemical Society* **2000**, *122*, 6258-6262.
- (202) Laerdahl, J. K.; Uggerud, E. Gas phase Nucleophilic Substitution. *International Journal of Mass Spectrometry* **2002**, *214*, 277-314.
- (203) Langevin, P. A Fundamental Formula of Kinetic Theory. *Annales De Chimie Et De Physique* **1905**, *5*, 245-288.
- (204) Langley, C. H.; Noe, E. A. *Ab Initio* Studies of the Conformations of Performic Acid, Peracetic Acid and Methyl Performate. *Journal of Molecular Structure-Theochem* **2004**, *682*, 215-224.
- (205) Le Bras, G. Chemical Processes in Atmospheric Oxidation G. Le Bras, Ed.; Springer: Berlin, 1997; pp 13.
- (206) Lee, C. L.; Liu, M. L.; Chang, B. C. Electronic Spectroscopy of Bromomethylenes in a Supersonic Free Jet Expansion. *Physical Chemistry Chemical Physics* **2003**, *5*, 3859-3863.
- (207) Lee, C. T.; Yang, W. T.; Parr, R. G. Development of the Colle-Salvetti Correlation-Energy Formula into a Functional of the Electron-Density. *Physical Review B* **1988**, *37*, 785-789.
- (208) Lee, J.; Grabowski, J. J. Reactions of the Atomic Oxygen Radical Anion and the Synthesis of Organic Reactive Intermediates. *Chemical Reviews* **1992**, *92*, 1611-1647.

- (209) Lemaire, H. P.; Livingston, R. L. The Molecular Structures of Octafluorocyclobutane and of Methylcyclobutane. *Journal of the American Chemical Society* **1952**, *74*, 5732-5736.
- (210) Leopold, D. G.; Murray, K. K.; Lineberger, W. C. Laser Photoelectron-Spectroscopy of Vibrationally Relaxed CH_2^- - A Reinvestigation of the Singlet Triplet Splitting in Methylene. *Journal of Chemical Physics* **1984**, *81*, 1048-1050.
- (211) Leopold, D. G.; Murray, K. K.; Miller, A. E. S.; Lineberger, W. C. Methylene: A Study of the X^3B_1 and a 1a_1 States by Photoelectron-Spectroscopy of CH_2^- and CD_2^- . *Journal of Chemical Physics* **1985**, *83*, 4849-4865.
- (212) Lias, S. G.; Karpas, Z.; Liebman, J. F. Halomethylenes: Effects of Halogen Substitution on Absolute Heats of Formation. *Journal of the American Chemical Society* **1985**, *107*, 6089-6096.
- (213) Lieder, C. A.; Brauman, J. I. Technique for Detection of Neutral Products in Gas-Phase, Ion-Molecule Reactions. *International Journal of Mass Spectrometry and Ion Processes* **1975**, *16*, 307-319.
- (214) Lifshitz, A.; Tamburu, C.; Suslensky, A. Isomerization and Decomposition of Pyrrole at Elevated-Temperatures - Studies with a Single-Pulse Shock-Tube. *Journal of Physical Chemistry* **1989**, *93*, 5802-5808.
- (215) Lifshitz, C.; Tiernan, T. O.; Hughes, B. M. Electron Affinities from Endothermic Negative-Ion Charge-Transfer Reactions. IV. SF_6 , Selected Fluorocarbons and Other Polyatomic-Molecules. *Journal of Chemical Physics* **1973**, *59*, 3182-3192.
- (216) Lightfoot, P. D.; Cox, R. A.; Crowley, J. N.; Destriau, M.; Hayman, G. D.; Jenkin, M. E.; Moortgat, G. K.; Zabel, F. Organic Peroxy-Radicals - Kinetics, Spectroscopy and Tropospheric Chemistry. *Atmospheric Environment Part A- General Topics* **1992**, *26*, 1805-1961.
- (217) Lin, C. S.; Chen, Y. E.; Chang, B. C. New Electronic Spectra of the HCCI and DCCI A-X Vibronic Bands. *Journal of Chemical Physics* **2004**, *121*, 4164-4170.
- (218) Liu, M. L.; Lee, C. L.; Bezant, A.; Tarczay, G.; Clark, R. J.; Miller, T. A.; Chang, B. C. Dispersed Fluorescence Spectra of the CCl_2 A-X Vibronic Bands. *Physical Chemistry Chemical Physics* **2003**, *5*, 1352-1358.
- (219) Lugez, C. L.; Jacox, M. E.; King, R. A.; Schaefer, H. F. Experimental and *ab initio* Study of the Infrared Spectra of Ionic Species Derived from SF_6 and SF_4 and Trapped in Solid Neon. *Journal of Chemical Physics* **1998**, *108*, 9639-9650.
- (220) Lum, R. C.; Grabowski, J. J. Substitution Competes with Elimination in a Gas-Phase Anion Molecule Reaction. *Journal of the American Chemical Society* **1988**, *110*, 8568-8570.

(221) Lum, R. C.; Grabowski, J. J. The Intrinsic Competition between Elimination and Substitution Mechanisms Is Controlled by Nucleophile Structure. *Journal of the American Chemical Society* **1992**, *114*, 9663-9665.

(222) Mackay, G. I.; Bohme, D. K. Bridging the Gap between Gas-Phase and Solution - Transition in Relative Acidity of Water and Methanol at 296 ± 2 K. *Journal of the American Chemical Society* **1978**, *100*, 327-329.

(223) Mackay, G. I.; Vlachos, G. D.; Bohme, D. K.; Schiff, H. I. Studies of Reactions Involving $C_2H_x^+$ Ions with HCN Using a Modified Selected Ion Flow Tube. *International Journal of Mass Spectrometry and Ion Physics* **1980**, *36*, 259-270.

(224) Mackie, J. C.; Colket, M. B.; Nelson, P. F. Shock Tube Pyrolysis of Pyridine. *Journal of Physical Chemistry* **1990**, *94*, 4099-4106.

(225) Mackie, J. C.; Colket, M. B.; Nelson, P. F.; Esler, M. Shock-Tube Pyrolysis of Pyrrole and Kinetic Modeling. *International Journal of Chemical Kinetics* **1991**, *23*, 733-760.

(226) Madronich, S.; Greenberg, J.; Paulson, S. Atmospheric Chemistry and Global Change; G. P. Brasseur, J. J. Orlando and G. S. Tyndall, Eds.; Oxford University Press: New York, 1999; pp 325

(227) Mao, C.; Nie, C. S.; Zhu, Z. Y. Normal Coordinate Analyses of C_4 - C_6 Perfluorocycloparaffins. *Spectrochimica Acta, Part A: Molecular Spectroscopy* **1988**, *44*, 1093-1098.

(228) Maricq, M. M.; Sente, J. J. The $CH_3C(O)O_2$ radical. Its UV Spectrum, Self-Reaction Kinetics, and Reaction with CH_3O_2 . *Journal of Physical Chemistry* **1996**, *100*, 4507-4513.

(229) Martinez, R.; Merelas, I.; Rayo, M. N. S.; Castano, F. Analysis of the Optical-Emission ($\lambda=400$ -900 nm) of Fragments Produced by Electron-Impact on CF_2Br_2 . *Journal of Physics B: Atomic Molecular and Optical Physics* **1995**, *28*, 4563-4575.

(230) Martinez-Avila, M.; Peiro-Garcia, J.; Ramirez-Ramirez, V. M.; Nebot-Gil, I. *Ab initio* study on the mechanism of the $HCO + O_2 \rightarrow HO_2 + CO$ reaction. *Chemical Physics Letters* **2003**, *370*, 313-318.

(231) Marynowski, M.; Franzen, W.; Elbatanouny, M. Analysis of the Properties of an Electrostatic Triplet Quadrupole Lens Used as an Electron-Beam Transport Device. *Review of Scientific Instruments* **1994**, *65*, 3718-3723.

(232) Mayhew, C. A.; Peverall, R.; Watts, P. Gas-Phase Ionic Reactions of Freons and Related-Compounds - Reactions of Some Halogenated Methanes with O^- and O_2^- . *International Journal of Mass Spectrometry and Ion Processes* **1993**, *125*, 81-93.

- (233) McAnoy, A. M.; Paine, M. R. L.; Blanksby, S. J. Reactions of the Hydroperoxide Anion with Dimethyl Methylphosphonate in an Ion Trap Mass Spectrometer: Evidence for a Gas-Phase α -Effect. *Organic and Biomolecular Chemistry* **2008**, *6*, 2316-2326.
- (234) McCarthy, M. C.; Gottlieb, C. A.; Gupta, H.; Thaddeus, P. Laboratory and Astronomical Identification of the Negative Molecular Ion C_6H^- . *Astrophysical Journal* **2006**, *652*, L141-L144.
- (235) McConnell, J. C.; Henderson, G. S.; Barrie, L.; Bottenheim, J.; Niki, H.; Langford, C. H.; Templeton, E. M. J. Photochemical Bromine Production Implicated in Arctic Boundary-Layer Ozone Depletion. *Nature* **1992**, *355*, 150-152.
- (236) McConnell, J. C.; Templeton, E. M. J.; Henderson, G. S.; Evans, W. F. J. Potential Effects of Halons on Stratospheric O_3 Based on the Montreal Protocol. *Atmosphere-Ocean* **1990**, *28*, 177-188.
- (237) McDonald, R. N.; Bianchina, E. J.; Tung, C. C. Electron Photodetachment of Cyclopentadienylidene Anion Radical in a Flowing Afterglow Apparatus - EA and ΔH_f° of Cyclopentadienylidene. *Journal of the American Chemical Society* **1991**, *113*, 7115-7121.
- (238) McDowell, R. S.; Krohn, B. J. Vibrational Levels and Anharmonicity in SF_6 . II. Anharmonic and Potential Constants. *Spectrochimica Acta, Part A: Molecular Spectroscopy* **1986**, *42*, 371-385.
- (239) McDowell, R. S.; Krohn, B. J.; Flicker, H.; Vasquez, M. C. Vibrational Levels and Anharmonicity in SF_6 . I. Vibrational Band Analysis. *Spectrochimica Acta, Part A: Molecular Spectroscopy* **1986**, *42*, 351-369.
- (240) McFarland, M.; Albritton, D. L.; Fehsenfeld, F. C.; Ferguson, E. E.; Schmeltekopf, A. L. Flow-Drift Technique for Ion Mobility and Ion-Molecule Reaction Rate Constant Measurements. I Apparatus and Mobility Measurements. *Journal of Chemical Physics* **1973**, *59*, 6610-6619.
- (241) McIsaac, J. E.; Mulhausen, H. A.; Behrman, E. J.; Subbaram, J.; Subbaram, L. R. Nucleophilic Reactivity of Peroxy Anions. *Journal of Organic Chemistry* **1972**, *37*, 1037-1041.
- (242) McKee, M. L.; Michl, J. A Possible Reinterpretation of the Photoelectron Spectra of CCl_2^- , CBr_2^- , and Cl_2^- : A Role for Quartet Iso-dihalocarbene or Dihalocarbene Radical Anions? *Journal of Physical Chemistry A* **2002**, *106*, 8495-8497.
- (243) Melander, L.; Saunders, J. H., Jr. Reaction Rates of Isotopic Molecules; John Wiley and Sons: New York, 1980.
- (244) Midey, A. J.; Viggiano, A. A. Rate Constants as a Function of Temperature and Kinetic Energy for the Reactions of Cl^- with C_2H_5Br and $n-C_3H_7Br$. *Journal of Physical Chemistry A* **200**, *104*, 6786-6790.

(245) Miller, F. A.; Capwell, R. J. The Infrared and Raman Spectra of Octachloro-, Octafluoro-, and Octahydroxycyclobutane. *Spectrochimica Acta, Part A: Molecular Spectroscopy* **1971**, *A 27*, 1113-1131.

(246) Miller, T. M.; Friedman, J. F.; Viggiano, A. A. Electron Attachment and Detachment and the Electron Affinity of *cyclo*-C₄F₈. *Journal of Chemical Physics* **2004**, *120*, 7024-7028.

(247) Miller, W. T.; Kim, C. S. Y. Reactions of Alkylolithiums with Polyhalides. *Journal of the American Chemical Society* **1959**, *81*, 5008-5009.

(248) Mock, R. S.; Grimsrud, E. P. Electron Photodetachment of the Molecular Anions of SF₆ and Several Perfluorinated Hydrocarbons. *Chemical Physics Letters* **1991**, *184*, 99-101.

(249) Molina, M. J.; Rowland, F. S. Stratospheric Sink for Chlorofluoromethanes - Chlorine Atom-Catalyzed Destruction of Ozone. *Nature* **1974**, *249*, 810-812.

(250) Moore, C. E. Atomic Energy Levels. NSRDS-NBS; Washington: US GPO Circular No. 467, 1952.

(251) Moran, T. F.; Hamill, W. H. Cross Sections of Ion-Permanent-Dipole Reactions by Mass Spectrometry. *Journal of Chemical Physics* **1963**, *39*, 1413-1422.

(252) Morris, R. A.; Miller, T. M.; Viggiano, A. A.; Paulson, J. F.; Solomon, S.; Reid, G. Effects of Electron and Ion Reactions on Atmospheric Lifetimes of Fully Fluorinated Compounds. *Journal of Geophysical Research Atmospheres* **1995**, *100*, 1287-1294.

(253) Morris, R. A.; Viggiano, A. A. Kinetics of the Reactions of F⁻ with CF₃Br and CF₃I as a Function of Temperature, Kinetic-Energy, Internal Temperature, and Pressure. *Journal of Physical Chemistry* **1994**, *98*, 3740-3746.

(254) Moss, R. A.; Jones, M. Reactive Intermediates; John Wiley and Sons: New York, 1978.

(255) Mueller, P. H.; Rondan, N. G.; Houk, K. N.; Harrison, J. F.; Hooper, D.; Willen, B. H.; Liebman, J. F. Carbene Singlet-Triplet Gaps - Linear Correlations with Substituent π Donation. *Journal of the American Chemical Society* **1981**, *103*, 5049-5052.

(256) Mukarakate, C.; Mishchenko, Y.; Brusse, D.; Tao, C.; Reid, S. A. Probing Spin-Orbit Mixing and the Singlet-Triplet Gap in Dichloromethylene via K_a Sorted Emission Spectra. *Physical Chemistry Chemical Physics* **2006**, *8*, 4320-4326.

- (257) Murray, K. K.; Leopold, D. G.; Miller, T. M.; Lineberger, W. C. Photoelectron-Spectroscopy of the Halocarbene Anions HCF^- , HCCl^- , HCB^- , HCl^- , CF_2^- , and CCl_2^- . *Journal of Chemical Physics* **1988**, *89*, 5442-5453.
- (258) Musaev, D. G.; Morokuma, K. *Ab-Initio* Molecular-Orbital Study of the Mechanism of H-H, C-H, N-H, O-H, and Si-H Bond Activation on Transient Cyclopentadienylcarbonylrhodium. *Journal of the American Chemical Society* **1995**, *117*, 799-805.
- (259) Neumark, D. M.; Lykke, K. R.; Andersen, T.; Lineberger, W. C. Laser Photodetachment Measurement of the Electron-Affinity of Atomic Oxygen. *Physical Review A* **1985**, *32*, 1890-1892.
- (260) NIST Chemistry WebBook, NIST Standard Reference Database Number 69; Linstrom, P. J.; Mallard, W. G., Eds.; National Institute of Standards and Technology: Gaithersburg MD, 20899 June 2005 (<http://webbook.nist.gov>).
- (261) Noest, A. J.; Nibbering, N. M. M. Negative Ion-Molecule Reactions of Aliphatic Nitrites Studied by Ion Cyclotron Resonance. *Advances in Mass Spectrometry* **1980**, *8*, 227-237.
- (262) Ogihara, W.; Yoshizawa, M.; Ohno, H. Novel Ionic Liquids Composed of Only Azole Ions. *Chemistry Letters* **2004**, *33*, 1022-1023.
- (263) O'Hair, R. A. J.; Davico, G. E.; Hacaloglu, J.; Dang, T. T.; DePuy, C. H.; Bierbaum, V. M. Measurements of Solvent and Secondary Kinetic Isotope Effects for the Gas-Phase $\text{S}_{\text{N}}2$ Reactions of Fluoride with Methyl Halides. *Journal of the American Chemical Society* **1994**, *116*, 3609-3610.
- (264) O'Hair, R. A. J.; DePuy, C. H.; Bierbaum, V. M. Gas-Phase Chemistry and Thermochemistry of the Hydroxysulfide Anion, HS^- . *Journal of Physical Chemistry* **1993**, *97*, 7955-7961.
- (265) O'Hair, R. A. J.; Gronert, S.; DePuy, C. H.; Bowie, J. H. Gas-Phase Ion Chemistry of the Acetic-Acid Enolate Anion $[\text{CH}_2\text{CO}_2\text{H}]^-$. *Journal of the American Chemical Society* **1989**, *111*, 3105-3106.
- (266) Okumara, Y.; Sugiyama, Y.; Okazaki, K. Evolution Prediction of Coal-Nitrogen in High Pressure Pyrolysis Processes. *Fuel* **2002**, *81*, 2317-2324.
- (267) Oldani, M.; Ha, T. K.; Bauder, A. Microwave-Spectrum, Dipole-Moment, and Substitution Structure of Peroxyformic Acid. *Journal of the American Chemical Society* **1983**, *105*, 360-365.
- (268) Olmstead, W. N.; Brauman, J. I. Gas-phase Nucleophilic Displacement Reactions *Journal of the American Chemical Society* **1977**, *99*, 4219-4228.

- (269) Ozkan, I. Franck-Condon Principle for Polyatomic-Molecules - Axis-Switching Effects and Transformation of Normal Coordinates. *Journal of Molecular Spectroscopy* **1990**, *139*, 147-162.
- (270) Patterson, E. V.; Fountain, K. R. On Gas Phase α -Effects. I. The Gas-Phase Manifestation and Potential SET Character. *Journal of Organic Chemistry* **2006**, *71*, 8121-8125.
- (271) Paulino, J. A.; Squires, R. R. Carbene Thermochemistry from Collision-Induced Dissociation Threshold Energy Measurements in a Flowing Afterglow-Triple Quadrupole Instrument. *Abstracts of Papers of the American Chemical Society* **1991**, *201*, 196-PHYS.
- (272) Poirier, R. A.; Wang, Y. L.; Westaway, K. C. A Theoretical-Study of the Relationship between Secondary α -Deuterium Kinetic Isotope Effects and the Structure of S_N2 Transition-States. *Journal of the American Chemical Society* **1994**, *116*, 2526-2533.
- (273) Porter, N. A.; Yin, H. Y.; Pratt, D. A. The Peroxy Acid Dioxirane Equilibrium: Base-Promoted Exchange of Peroxy Acid Oxygens. *Journal of the American Chemical Society* **2000**, *122*, 11272-11273.
- (274) Poutsma, J. C.; Paulino, J. A.; Squires, R. R. Absolute Heats of Formation of CHCl , CHF , and CClF . A Gas-Phase Experimental and G2 Theoretical Study. *Journal of Physical Chemistry A* **1997**, *101*, 5327-5336.
- (275) Pradeep, T.; Ma, S. G.; Shen, J. W.; Francisco, J. S.; Cooks, R. G. Activation of Dioxygen by Halocarbon Ions. *Journal of Physical Chemistry A* **2000**, *104*, 6804-6808.
- (276) Pushkarsky, M. B.; Zalyubovsky, S. J.; Miller, T. A. Detection and Characterization of Alkyl Peroxy Radicals Using Cavity Ringdown Spectroscopy. *Journal of Chemical Physics* **2000**, *112*, 10695-10698.
- (277) Qian, H. B.; Davies, P. B. Infrared-Laser Spectroscopy of the ν_2 Band of Difluorocarbene (CF_2). *Journal of Molecular Spectroscopy* **1995**, *169*, 201-210.
- (278) Ramond, T. M.; Blanksby, S. J.; Kato, S.; Bierbaum, V. M.; Davico, G. E.; Schwartz, R. L.; Lineberger, W. C.; Ellison, G. B. Heat of Formation of the Hydroperoxyl Radical HO_2 Via Negative Ion Studies. *Journal of Physical Chemistry A* **2002**, *106*, 9641-9647.
- (279) Ramond, T. Negative Ion Photoelectron Spectroscopy of Alkyl Peroxides, Alkoxides, and Group VIII Transition Metal Oxides. Ph.D. Thesis, Department of Physics, University of Colorado at Boulder, 2001.
- (280) Raposo, M. M. M.; Sousa, A. M. R. C.; Fonseca, A. M. C.; Kirsch, G. Donor-Acceptor Substituted Thienylpyrrole Azo Dyes: Synthesis, Solvatochromic and Electrochemical Properties. *Advanced Materials Forum* *lii*, Pts 1 and 2 **2006**, 514-516, 103-107.

- (281) Reeves, C. E.; Penkett, S. A. Measurements of Peroxides and What They Tell Us. *Chemical Reviews* **2003**, *103*, 5199-5218.
- (282) Ren, Y.; Yamataka, H. G2(+) Investigation on the α -Effect in the S_N2 Reactions at Saturated Carbon. *Chemistry-A European Journal* **2007**, *13*, 677-682.
- (283) Ren, Y.; Yamataka, H. The α -Effect in Gas-Phase S_N2 Reactions Revisited. *Organic Letters* **2005**, *8*, 119-121.
- (284) Ren, Y.; Yamataka, H. The α -Effect in Gas-Phase S_N2 Reactions: Existence and the Origin of the Effect. *Journal of Organic Chemistry* **2007**, *72*, 5660-5667.
- (285) Richmond, C. A.; Guss, J. S.; Nauta, K.; Kable, S. H. Rovibronic Spectroscopy of the A¹A'-X¹A" Transition in the Bromochloromethylene Radical. *Journal of Molecular Spectroscopy* **2003**, *220*, 137-149.
- (286) Roberts, J. M. The Atmospheric Chemistry of Organic Nitrates. *Atmospheric Environment Part A-General Topics* **1990**, *24*, 243-287.
- (287) Robinson, M. S.; Davico, G. E.; Bierbaum, V. M.; DePuy, C. H. The Gas-Phase Ion/Molecule Chemistry of the ¹³C Labeled Ketenyl and Methyl Ketenyl Anions with CS₂, COS, and CO₂. *International Journal of Mass Spectrometry and Ion Processes* **1994**, *137*, 107-119.
- (288) Roehl, C. M.; Bauer, D.; Moortgat, G. K. Absorption Spectrum and Kinetics of the Acetylperoxy Radical. *Journal of Physical Chemistry* **1996**, *100*, 4038-4047.
- (289) Russo, N.; Sicilia, E.; Toscano, M. Geometries, Singlet-Triplet Separations, Dipole-Moments, Ionization-Potentials, and Vibrational Frequencies in Methylene (CH₂) and Halocarbenes (CHF, CF₂, CCl₂, CBr₂, and Cl₂). *Journal of Chemical Physics* **1992**, *97*, 5031-5036.
- (290) Schmeltekopf, A. L.; Fehsenfeld, F. C. De-excitation Rate Constants for Helium Metastable Atoms with Several Atoms and Molecules. *Journal of Chemical Physics* **1970**, *53*, 3173-3177.
- (291) Schwartz, M.; Marshall, P. An *ab initio* Investigation of Halocarbenes. *Journal of Physical Chemistry A* **1999**, *103*, 7900-7906.
- (292) Schwartz, R. L.; Davico, G. E.; Ramond, T. M.; Lineberger, W. C. Singlet-Triplet Splittings in CX₂ (X = F, Cl, Br, I) Dihalocarbenes via Negative Ion Photoelectron Spectroscopy. *Journal of Physical Chemistry A* **1999**, *103*, 8213-8221.
- (293) Shapley, J. R.; Samkoff, D. E.; Bueno, C.; Churchill, M. R. Reaction of OS₃(CO)₁₀(NCCH₃)₂ with Imidazole and Related Aromatic Heterocycles - Crystal and Molecular-Structure of (μ-H)OS₃(CO)₁₀(μ-3,4-Eta-2-η²C₃H₃). *Inorganic Chemistry* **1982**, *21*, 634-639.

- (294) Sharma, S.; Lee, J. K. Acidity of Adenine and Adenine Derivatives and Biological Implications. A Computational and Experimental Gas-Phase Study. *Journal of Organic Chemistry* **2002**, *67*, 8360-8365.
- (295) Sharp, T. E.; Rosenstock, H. M. Franck-Condon Factors for Polyatomic Molecules. *Journal of Chemical Physics* **1964**, *41*, 3453-3463.
- (296) Shu, J.; Lin, J. J.; Wang, C. C.; Lee, Y. T.; Yang, X. M.; Nguyen, T. L.; Mebel, A. M. O(¹D) Reaction with Cyclopropane: Evidence of O Atom Insertion into the C-C bond. *Journal of Chemical Physics* **2001**, *115*, 7-10.
- (297) Simon, J. Molecular Anions. *Journal of Physical Chemistry A* **2008**, *112*, 6401-6511.
- (298) Singh, H. B.; Herlth, D.; Ohara, D.; Zahnle, K.; Bradshaw, J. D.; Sandholm, S. T.; Talbot, R.; Crutzen, P. J.; Kanakidou, M. Relationship of Peroxyacetyl Nitrate to Active and Total Odd Nitrogen at Northern High-Latitudes - Influence of Reservoir Species on NO_x and O₃. *Journal of Geophysical Research - Atmospheres* **1992**, *97*, 16523-16530.
- (299) Snyder, L. R. Nitrogen and Oxygen Compound Types in Petroleum - Total Analysis of a 400-700° F Distillate from a California Crude Oil. *Analytical Chemistry* **1969**, *41*, 314-323.
- (300) Squires, R. R. Gas-Phase Thermochemical Properties of the Bicarbonate and Bisulfite Ions. *International Journal of Mass Spectrometry and Ion Processes* **1992**, *117*, 565-600.
- (301) Staneke, P. O.; Groothuis, G.; Ingemann, S.; Nibbering, N. M. M. Competing Electron Transfer, Proton Abstraction and Nucleophilic Substitutions in Gas-Phase Reactions of (Radical) Anions with Chloro- and Bromomethanes. *Journal of Physical Organic Chemistry* **1996**, *9*, 471-486.
- (302) Staneke, P. O.; Kauw, J.; Born, M.; Ingemann, S.; Nibbering, N. M. M. Low Pressure Gas-Phase Reactions of the Atomic Oxygen Radical Anion with Halomethanes Studied using Fourier Transform Ion Cyclotron Resonance. *Rapid Communications in Mass Spectrometry* **1997**, *11*, 124-132.
- (303) Stock, H. M. P. Theory of Flowing Afterglow. *Journal of Physics B - Atomic Molecular and Optical Physics* **1973**, *6*, L86-L88.
- (304) Streit, G. E. Gas-Phase Reactions of O⁻ and O₂⁻ with a Variety of Halogenated Compounds. *Journal of Physical Chemistry* **1982**, *86*, 2321-2324.
- (305) Su, T.; Bowers, M. T. Theory of Ion-Polar Molecule Collisions - Comparison with Experimental Charge-Transfer Reactions of Rare-Gas Ions to Geometric Isomers of Difluorobenzene and Dichloroethylene. *Journal of Chemical Physics* **1973**, *58*, 3027-3037.

- (306) Su, T.; Chesnavich, W. J. Parametrization of the Ion-Polar Molecule Collision Rate-Constant by Trajectory Calculations. *Journal of Chemical Physics* **1982**, *76*, 5183-5185.
- (307) Sun, L.; Hase, W. L.; Song, K. Trajectory Studies of S_N2 Nucleophilic Substitution. 8. Central Barrier Dynamics for Gas-Phase Cl⁻+CH₃Cl. *Journal of the American Chemical Society* **2001**, *123*, 5753-5756.
- (308) Sun, L.; Song, K.; Hase, W. L. A S_N2 Reaction That Avoids Its Deep Potential Energy Minimum. *Science* **2002**, *296*.
- (309) Suzuki, C.; Sasaki, K.; Kadota, K. Rate Coefficient for Self-Association Reaction of CF₂ Radicals Determined in the Afterglow of Low-Pressure C₄F₈ Plasmas. *Plasma Chemistry and Plasma Processing* **2001**, *21*, 139-147.
- (310) Tachikawa, H. *Ab initio* MO Calculations of Structures and Electronic States of SF₆ and SF₆⁻. *Journal of Physics B: Atomic, Molecular and Optical Physics* **2002**, *35*, 55-60.
- (311) Tanaka, K.; Mackay, G. I.; Payzant, J. D.; Bohme, D. K. Gas-Phase Reactions of Anions with Halogenated Methanes at 297± 2 K. *Canadian Journal of Chemistry* **1976**, *54*, 1643-1659.
- (312) Tao, C.; Mukarakate, C.; Reid, S. A. Electronic spectroscopy of the A¹A''-X¹A' system of CCl. *Journal of Molecular Spectroscopy* **2007**, *241*, 143-150.
- (313) Tarczay, G.; Miller, T. A.; Czako, G.; Csaszar, A. G. Accurate *Ab Initio* Determination of Spectroscopic and Thermochemical Properties of Mono- and Dichlorocarbenes. *Physical Chemistry Chemical Physics* **2005**, *7*, 2881-2893.
- (314) Tomas, A.; Villenave, E.; Lesclaux, R. Reactions of the HO₂ radical with CH₃CHO and CH₃C(O)O₂ in the gas phase. *Journal of Physical Chemistry A* **2001**, *105*, 3505-3514.
- (315) Tonner, D. S.; McMahon, T. B. Non-statistical Effects in the Gas-Phase S_N2 Reaction. *Journal of the American Chemical Society* **2000**, *122*, 8783-8784.
- (316) Tritton, D. J. Physical Fluid Dynamics; Van Nostrand Reinhold Company: New York, 1977.
- (317) Trofimov, A. B.; Koppel, H.; Schirmer, J. Vibronic Structure of the Valence π-Photoelectron Bands in Furan, Pyrrole, and Thiophene. *Journal of Chemical Physics* **1998**, *109*, 1025-1040.
- (318) Tsai, T. C.; Chen, C. W.; Chang, B. C. Laser Excitation and Dispersed Fluorescence Spectra of the HCB^r A-X Vibronic Transition. *Journal of Chemical Physics* **2001**, *115*, 766-770.

- (319) Tso, T. L.; Diem, M.; Lee, E. K. C. Oxidation of Formyl Radical in Solid O₂ at 13 K - Formation of Formic-Acid and Formylperoxy Radical, HC(O)OO. *Chemical Physics Letters* **1982**, *91*, 339-342.
- (320) Tso, T. L.; Lee, E. K. C. Mechanism of Photooxidation of Glyoxal and Formaldehyde in Solid O₂ at 12-18 K. *Journal of Physical Chemistry* **1984**, *88*, 5465-5474.
- (321) Tyndall, G. S.; Cox, R. A.; Granier, C.; Lesclaux, R.; Moortgat, G. K.; Pilling, M. J.; Ravishankara, A. R.; Wallington, T. J. Atmospheric Chemistry of Small Organic Peroxy Radicals. *Journal of Geophysical Research-Atmospheres* **2001**, *106*, 12157-12182.
- (322) Van Doren, J. M. Developments and Applications to Gas-Phase Ion Chemistry. Ph.D. Thesis, Department of Chemistry and Biochemistry, University of Colorado at Boulder, 1987.
- (323) Van Doren, J. M.; Barlow, S. E.; DePuy, C. H.; Bierbaum, V. M. Tandem Flowing Afterglow-Selected Ion Flow Tube and Its Application to the Thermal-Energy Reactions of ¹⁸O⁻. *Journal of the American Chemical Society* **1987**, *109*, 4412-4414.
- (324) Van Doren, J. M.; Barlow, S. E.; DePuy, C. H.; Bierbaum, V. M. The Tandem Flowing Afterglow-SIFT-DRIFT. *International Journal of Mass Spectrometry and Ion Processes* **1987**, *81*, 85-100.
- (325) Van Doren, J. M.; DePuy, C. H.; Bierbaum, V. M. Gas-Phase Isotope-Exchange Reactions with Chloride-Ion. *Journal of Physical Chemistry* **1989**, *93*, 1130-1134.
- (326) Viggiano, A. A.; Howorka, F.; Albritton, D. L.; Fehsenfeld, F. C.; Adams, N. G.; Smith, D. Laboratory Studies of Some Ion-Atom Reactions Related to Interstellar Molecular Synthesis. *Astrophysical Journal* **1980**, *236*, 492-497.
- (327) Viggiano, A. A.; Morris, R. A.; Paschkewitz, J. S.; Paulsen, J. F. Kinetics of the Gas-Phase Reactions of Chloride Anion, Cl⁻ with CH₃Br and CD₃Br: Experimental Evidence for Nonstatistical Behavior? *Journal of the American Chemical Society* **1992**, *114*, 10477.
- (328) Villano, S. M.; Eyet, N.; Lineberger, W. C.; Bierbaum, V. M. Gas-Phase Carbene Radical Anions: New Mechanistic Insight. *Journal of the American Chemical Society* **2008**, *130*, 7214-7215.
- (329) Villano, S. M.; Eyet, N.; Lineberger, W. C.; Bierbaum, V. M. Reactions of α-Nucleophiles with Alkyl Chlorides: The Competition Between S_N2 and E2 Mechanisms and the Gas-Phase α-Effect. *Submitted to Journal of the American Chemical Society* **2009**.
- (330) Villano, S. M.; Eyet, N.; Lineberger, W. C.; Bierbaum, V. M. Gas-Phase Reactions of Halogenated Radical Carbene Anions with Sulfur and Oxygen Containing Species. *International Journal of Mass Spectrometry* **2009**, *In Press*.

(331) Villano, S. M.; Kato, S.; Bierbaum, V. M. Deuterium Kinetic Isotope Effects in Gas-Phase S_N2 and E2 Reactions: Comparison of Experiment and Theory. *Journal of the American Chemical Society* **2006**, *128*, 736-737.

(332) Von Ahsen, S.; Willner, H.; Francisco, J. S. Thermal Decomposition of Peroxy Acetyl Nitrate CH₃C(O)OONO₂. *Journal of Chemical Physics* **2004**, *121*, 2048-2057.

(333) Wang, L. S.; Ding, C. F.; Wang, X. B.; Nicholas, J. B.; Nicholas, B. Probing the Potential Barriers and Intramolecular Electrostatic Interactions in Free Doubly Charged Anions. *Physical Review Letters* **1998**, *81*, 2667-2670.

(334) Wayne, R. P. Chemistry of Atmospheres; Oxford: Clarendon, 1991.

(335) Wei, J.; Kuczmann, A.; Riedel, J.; Renth, F.; Temps, F. Photofragment Velocity Map Imaging of H Atom Elimination in the First Excited State of Pyrrole. *Physical Chemistry Chemical Physics* **2003**, *5*, 315-320.

(336) Wenthold, P. G.; Lineberger, W. C. Negative Ion Photoelectron Spectroscopy Studies of Organic Reactive Intermediates. *Accounts of Chemical Research* **1999**, *32*, 597-604.

(337) Wenthold, P. G.; Polak, M. L.; Lineberger, W. C. Photoelectron Spectroscopy of the Allyl and 2-Methylallyl Anions. *Journal of Physical Chemistry* **1996**, *100*, 6920-6926.

(338) Wenthold, P. G.; Squires, R. R. Biradical Thermochemistry from Collision-Induced Dissociation Threshold Energy Measurements - Absolute Heats of Formation of Ortho-Benzyne, Meta-Benzyne, and Para-Benzyne. *Journal of the American Chemical Society* **1994**, *116*, 6401-6412.

(339) Williams, G. K.; Palopoli, S. F.; Brill, T. B. Thermal-Decomposition of Energetic Materials .65. Conversion of Insensitive Explosives (Nto, Anta) and Related-Compounds to Polymeric Melon-Like Cyclic Azine Burn-Rate Suppressants. *Combustion and Flame* **1994**, *98*, 197-204.

(340) Winter, N. W.; Goddard, W. A.; Bender, C. F. Theoretical Description of ²A' and ²A" States of Peroxyformyl Radical. *Chemical Physics Letters* **1975**, *33*, 25-29.

(341) Wladkowski, B. D.; Brauman, J. I. Substitution Versus Elimination in Gas-Phase Ionic Reactions *Journal of the American Chemical Society* **1992**, *114*, 10643-10644.

(342) Woon, D. E.; Dunning, T. H. Gaussian-Basis Sets for Use in Correlated Molecular Calculations. III. The Atoms Aluminum through Argon. *Journal of Chemical Physics* **1993**, *98*, 1358-1371.

- (343) Wormhoudt, J.; McCurdy, K. E.; Burkholder, J. B. Measurements of the Strengths of Infrared Bands of CF₂. *Chemical Physics Letters* **1989**, *158*, 480-485.
- (344) Xie, K. C.; Lin, J. Y.; Li, W. Y.; Chang, L. P.; Feng, J.; Zhao, W. Formation of HCN and NH₃ During Coal Macerals Pyrolysis and Gasification with CO₂. *Fuel* **2005**, *84*, 271-277.
- (345) Yang, H. C.; Chen, H. L.; Ho, J. J. *Ab Initio* Study of Intramolecular Hydrogen transfer in Formylperoxy Radical. *Journal of Molecular Structure-Theochem* **2006**, *774*, 35-41.
- (346) Yang, R. J.; Yu, L. A.; Zeng, A. H.; Zhou, M. F. Infrared Spectrum of the Formylperoxy Radical in Solid Argon. *Journal of Physical Chemistry A* **2004**, *108*, 4228-4231.
- (347) Yu, H. G.; Gonzalez-Lezana, T.; Marr, A. J.; Muckerman, J. T.; Sears, T. J. Experimental and Theoretical Studies of the Near-Infrared Spectrum of Bromomethylene. *Journal of Chemical Physics* **2001**, *115*, 5433-5444.
- (348) Zalyubovsky, S. J.; Glover, B. G.; Miller, T. A. Cavity Ringdown Spectroscopy of the A-X Electronic Transition of the CH₃C(O)O₂ Radical. *Journal of Physical Chemistry A* **2003**, *107*, 7704-7712.
- (349) Zalyubovsky, S. J.; Glover, B. G.; Miller, T. A.; Hayes, C.; Merle, J. K.; Hadad, C. M. Observation of the A-X Electronic Transition of the 1-C₃H₇O₂ and 2-C₃H₇O₂ Radicals Using Cavity Ringdown Spectroscopy. *Journal of Physical Chemistry A* **2005**, *109*, 1308-1315.
- (350) Zhang, X.; Kato, S.; Bierbaum, V. M.; Nimlos, M. R.; Ellison, G. B. Use of a flowing afterglow SIFT apparatus to study the reactions of ions with organic radicals. *Journal of Physical Chemistry A* **2004**, *108*, 9733-9741.
- (351) Zhao, W.; Carreira, E. M. Conformationally Restricted Aza-BODIPY: Highly Fluorescent, Stable Near-Infrared Absorbing Dyes. *Chemistry--A European Journal* **2006**, *12*, 7254-7263.